

PHD THESIS

Monte Carlo methods on low and high energy atmospheric phenomena

Gabriel Sousa Diniz

Brasilia, March 2020

FICHA CATALOGRÁFICA

DINIZ, GABRIEL SOUSA

Monte Carlo methods on low and high energy atmospheric phenomena [Distrito Federal] 2020.

xvi, 143 p., 210 x 297 mm (IFD/UnB, Doutor, Doutorado em Física, 2020).

PhD thesis - Universidade de Brasília, Instituto de Física.

- | | |
|--------------|----------------------|
| 1. Leader | 2. Neutron Emission |
| 3. Gamma-ray | 4. Monte Carlo |
| I.IFD/UnB | II. Doutor em Física |

REFERÊNCIA BIBLIOGRÁFICA

DINIZ, G. (2020). *Monte Carlo methods on low and high energy atmospheric phenomena*. PhD thesis, Instituto de Física, Universidade de Brasília, Brasília, DF, 143 p.

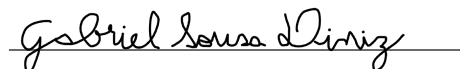
CESSÃO DE DIREITOS

AUTOR: Gabriel Sousa Diniz

TÍTULO: Monte Carlo methods on low and high energy atmospheric phenomena.

GRAU: Doutor em Física ANO: 2020

É concedida à Universidade de Brasília permissão para reproduzir cópias desta PhD thesis e para emprestar ou vender tais cópias somente para propósitos acadêmicos e científicos. Os autores reservam outros direitos de publicação e nenhuma parte dessa PhD thesis pode ser reproduzida sem autorização por escrito dos autores.



Gabriel Sousa Diniz

Instituto de Física - IFD

Universidade de Brasília (UnB)

Campus Darcy Ribeiro

CEP 70919-970 - Brasília - DF - Brasil

Meu Pai, tu és Rei na Umbanda.
O teu brado na pedreira é um trovão.
A ti, eu clamo por justiça.
Me ponho de joelhos pra falar em oração.
A ti, eu clamo, por justiça.
Me ponho de joelhos pra falar em oração.
Na terra, os homens brigam por vaidade.
Esquecem sua origem, esquecem sua missão.
De plantar na vida a caridade.
Que é o caminho da verdade.
Na Umbanda, a redenção.
Pois unidos, somos bem mais fortes.
Nós somos a voz de uma só nação.
De paz, amor e humildade.
Pra Xangô bato cabeça, pedindo orientação.
Caô Xangô, Xangô Caô.
Me mostre o caminho pra eu cumprir minha missão.
Caô Xangô, Xangô Caô.
Entrego a minha vida e meu destino em suas mãos.

Ponto de Xangô, composição popular.

Dedicatória

Para minhas avós, Zefinha e a falecida Edith; para meus pais, João França e Maria Lúcia; para minha tia e madrinha falecida, Rita; para o falecido Ti' Dão; para Maranguape, Itaporanga e para o P.sul; para o Cerrado.

Gabriel Sousa Diniz

Acknowledgements

I would like to acknowledge CAPES and the dutch project FOM project 12PR3041.

I would like to thank, first of all, my parents – João França and Maria Lúcia – for all the support and patience.

Natália Liberato, who would know? Against all the odds, we have found in each other better versions of one another. Thank you, with all my love, for making me a better human.

A warm thanks for my mentors, Ivan Soares Ferreira and Ute Ebert, without whom the work would not be possible. Both of you taught me what science can be and I am eternally grateful for that.

I send my cheers and regards for the crew of CWI's M.D. group.

To Casper Rutjes, who shared an immense amount of knowledge and laughter with me, a special thanks. There is, here, a dual part both as friend and mentor. I thank you for that.

To Christoph Köhn and David Sarria, two of my strong collaborators, thank you for sharing your time and knowledge with me.

Ashutosh, we both know that our chess games and our conversations always had a powerful effect on lighten the mood and the room; I've learned so much with you.

Rakesh! Amsterdam would not be itself without our drinking and joy!

To Behnaz, my thanks, you probably didn't even perceived but she taught me how to have a better life.

Andy Martinez! You helped me get through from hard calculations and ideas to joy at work. Our collaboration on the magical neutrons will still have fruits of its own.

Mandar, sharing the office with you was not only a cultural experience in which we exchange movies and musics but I will also never forget your help on scientific interpretation.

Adam Smith, my economist friend who is an astrophysicist, we both went through hell and high water together. May we always cheers with glasses high!

Gabriel Rübinger-Betti, I do not think you know how big is your influence in my thought and knowledge. As you once said, our work together is historical!

Paula Baqueiro, you know you are my moral compass! Thank you for the guidance.

I thank Adri, my former landlord and later friend, for all the talks, cooking, drinking, and mind organization that we've shared.

I thank Olaf Scholten and Brian Hare for always have an open door and open mind for me and possible collaborations.

Gabriel Sousa Diniz

RESUMO

Emissões de radiação e partículas com energia de até 100 MeV foram detectadas em solo e relacionadas com nuvens de tempestade. Este fenômeno envolve um conjunto de partículas, começando com elétrons acelerados que produzem fótons e; em combinação com estes fótons; resultam em uma avalanche de cargas elétricas e promovem descargas como o relâmpago ao mesmo tempo que produzem as emissões conhecidas como *Terrestrial Gamma ray Flashes*. Os fótons desse fenômeno estão em uma janela de energia a qual os permite interagir com as partículas do ar via *Giant Dipole Resonance*, o que resulta na emissão de nêutrons e prótons. Este trabalho pretende analisar os *Terrestrial Gamma ray Flashes* tanto por sua produção hadrônica, i.e. nêutrons e prótons, quanto pelo aceleração de elétrons que os originam. Através de simulações Monte Carlo, analisa-se os campos elétricos necessários para colocar um elétron em estado de *runaway*. Este estado significa que há maior ganho de energia pelo campo elétrico do que perda de energia pelas colisões, sendo condição necessária para a origem do *Terrestrial Gamma ray Flashes*. Aqui, verifica-se a possibilidade de *runaway* com campos elétricos mais baixos que anteriormente registrados. Por outro lado, simulações Monte Carlo, de feixes de fótons direcionados ao solo e com energia entre 10-100 MeV foram implementadas para comparar a detecção de nêutrons no solo com a literatura atual, assim como quantizar a produção dos nêutrons e prótons, estes últimos, ainda não detectados. Os resultados mostram que há uma produção de prótons comparável a de nêutrons, enquanto a detecção de nêutrons se concentra em 0,5 km de distância do eixo de simetria da fonte e produzem uma assinatura em fótons de energia ≈ 1 MeV no solo por causa das colisões com ar.

ABSTRACT

Particles and radiation emissions with energy up to 100 MeV were detected at ground and related to thunderclouds. A variety of particles is produced during these emissions, starting with accelerated electrons that emit photons and, together with the photons, are responsible for an avalanche of accelerated charges that result on discharges such as the lightning and the phenomenon known as Terrestrial Gamma ray Flashes. The energy of these photons cover the range of Giant Dipole Resonance, an interaction which results in the emission of neutrons and protons. This work analyzes the Terrestrial Gamma ray Flashes both by its hadronic production (neutrons and protons) and by the electron acceleration that originates them. Monte Carlo simulations are implemented to investigate the probability of low electric fields driving electrons to runaway state. Such state is characterized by a higher energy gain due to the electric field than energy loss by collisions. It is verified a possibility of runaway state with electric fields lower than it was previously observed. The investigation of the photonuclear reactions were through simulations with Monte Carlo techniques of monodirected beams of photons with energy between 10 and 100 MeV to compare the detection at ground level of the produced neutrons with the results on the literature, as well as the neutron and proton production, although there is no record of proton detection yet. The results shown a comparable production of protons and neutrons, a concentration of the detected neutrons at a radius of 0.5 km from the simulation symmetry axis and a photon signature (with energy in the order of 1 MeV) on ground that is produced by the neutrons movement toward the ground due to collisions with the air.

SUMMARY

1	INTRODUCTION	1
2	ATMOSPHERICAL ELECTRIC DYNAMICS	4
2.1	ATMOSPHERIC PLASMA	4
2.2	ELECTRICAL DISCHARGES	6
2.3	HIGH ENERGY EMISSIONS	7
2.4	GLOBAL ELECTRIC CIRCUIT	9
3	MONTE CARLO METHOD IN THE MOTION OF PARTICLES	11
3.1	RANDOM NUMBERS	11
3.1.1	SAMPLING RANDOM NUMBERS PROCESS	12
3.1.2	CROSS SECTIONS	12
3.2	MOTION ALGORITHM	14
4	DIFFERENT MONTE CARLO CODES – A COMPARISON	16
4.1	INTRODUCTION	16
4.1.1	THE MULTIPLE SCALES IN ENERGY AND LENGTH	17
4.1.2	THEORETICAL UNDERSTANDING OF RREAs	18
4.2	FIELD-FREE COMPARISON	21
4.3	OVERVIEW OF INTERACTIONS AND APPROXIMATIONS	22
4.3.1	ELECTRONS AND POSITRONS	23
4.3.2	FRICTION (OR STOPPING-POWER) FOR ELECTRONS AND POSITRONS	23
4.3.3	STRAGGLING	24
4.3.4	CONTINUOUS SLOWING DOWN APPROXIMATION	25
4.3.5	PHOTON INTERACTIONS	26
4.3.6	PHOTON ATTENUATION	26
4.4	OVERVIEW OF CODES	27
4.4.1	EGS5	27
4.5	FIELD FREE COMPARISON SET UP	29
4.5.1	THE NUMBER OF PARTICLES VERSUS DISTANCE (ATTENUATION)	30
4.5.2	SPECTRAL ANALYSIS	31
4.5.3	PERFORMANCE BENCHMARK	31
4.6	RESULTS	32
4.6.1	STRAGGLING	32
4.6.2	OPENING ANGLE	32
4.6.3	BREMSSTRAHLUNG	33
4.6.4	OTHER DIFFERENCES	33

4.6.5	PERFORMANCE	34
4.7	THE EFFECT OF ELECTRIC FIELDS	34
4.8	ELECTROMAGNETIC STUDY AND MODEL REDUCTIONS	37
4.9	ELECTROMAGNETIC COMPARISON: MODEL DESCRIPTIONS	38
4.9.1	GEANT4	38
4.9.2	GRRR	39
4.9.3	REAM	40
4.10	STEPPING METHODOLOGY.....	40
4.10.1	GENERAL METHOD	40
4.10.2	THE CASE OF GEANT4	41
4.11	PROBABILITY OF GENERATING RREA.....	42
4.12	CHARACTERISATION OF RREA SHOWERS	44
4.12.1	AVALANCHE TIME AND LENGTH SCALES	47
4.12.2	EVOLUTION TO SELF-SIMILAR STATE.....	48
4.12.3	RREA SPECTRA	52
4.12.4	OTHER DIFFERENCES	56
4.13	CONCLUSIONS	58
5	ELECTRONS ON LOW ENERGY REGIME.....	60
5.1	INTRODUCTION.....	60
5.1.1	THE CONCEPT OF THE FRICTION CURVE	60
5.1.2	VALUE AND VALIDITY OF THE FRICTION CURVE IN DIFFERENT ENERGY REGIMES.....	62
5.1.3	THIS WORK	64
5.2	METHODOLOGY	64
5.2.1	SOFTWARE FRAMEWORK	64
5.2.2	SETUP OF SIMULATIONS	65
5.3	RESULTS AND DISCUSSION	67
5.3.1	STEADY STATE ELECTRON ENERGY DISTRIBUTIONS IN DIFFERENT FIELDS AND THE FRICTION CURVE	67
5.3.2	ELECTRON RUN-AWAY IN ELECTRIC FIELDS BELOW THE RUN-AWAY THRESH- OLD.....	70
5.4	CONCLUSION.....	72
6	DETECTION AND EFFECTS OF ATMOSPHERIC NEUTRONS	74
6.1	INTRODUCTION.....	74
6.1.1	NEUTRONS AS A FOOTPRINT OF THUNDERSTORMS	74
6.1.2	NEUTRON PRODUCTION THROUGH TGFs AND GAMMA-RAY GLOWS	74
6.1.3	NEUTRON EMISSIONS FROM THUNDERSTORMS MEASURED WITH DIF- FERENT DETECTORS	75
6.1.4	NEUTRON PROPAGATION TO GROUND	76

6.1.5	EARLIER SIMULATIONS	76
6.2	SIMULATIONS.....	77
6.3	SETUP OF THE SIMULATIONS	77
6.4	SIMULATED NEUTRON EFFECT IN THE ATMOSPHERE	78
6.4.1	PHOTON YIELD BY NEUTRON	81
6.4.2	THE PREDICTED SIGNAL	81
6.4.3	SUMMARY OF PREDICTIONS FOR TGF AFTERGLOW	81
6.4.4	POSSIBLE OBSERVATIONS	84
6.5	SIMULATED PHOTON AND NEUTRON DISTRIBUTIONS IN SPACE, TIME AND ENERGY AT SEA LEVEL.....	84
6.5.1	NEUTRON NUMBER AND DISTRIBUTION AT SEA LEVEL AS A FUNCTION OF SOURCE ALTITUDE	85
6.5.2	ENERGY SPECTRA OF PHOTONS AND NEUTRONS AT SEA LEVEL.....	85
6.5.3	DISTRIBUTION OF ARRIVAL TIMES OF PHOTONS AND NEUTRONS AT SEA LEVEL	87
6.5.4	INTERPRETATION OF THE SIMULATIONS AND THE SHAPE OF THE EF- FECTIVE NEUTRON SOURCE	88
6.5.5	SECOND PHOTON PULSE AND TIME DEPENDENT NEUTRON SPECTRA....	90
6.6	NEUTRON DETECTION ON GROUND AS A FUNCTION OF SPECTRUM AND ALTITUDE OF THE PHOTON SOURCE	90
6.6.1	CONSTRUCTION OF AN ARBITRARY PHOTON SOURCE SPECTRUM	90
6.6.2	RESULTS FOR DIFFERENT RREA SPECTRA AND SOURCE ALTITUDES....	92
6.6.3	ARBITRARY PHOTON SOURCES AND DETECTION ALTITUDES	93
6.7	DISCUSSION.....	94
6.8	CONCLUSIONS AND OUTLOOK.....	95
7	MODELLING THE ATMOSPHERIC HADRONIC PRODUCTION	97
7.1	INTRODUCTION.....	97
7.2	MODEL.....	98
7.2.1	CROSS SECTIONS AND THE MONTE CARLO PARTICLE CODE FOR LEP- TONS, PHOTONS AND HADRONS	98
7.2.2	NEUTRON CROSS SECTIONS	100
7.2.3	ALTITUDE AND ATMOSPHERIC DEPTH.....	103
7.3	RESULTS.....	104
7.3.1	THE MOTION OF MONOENERGETIC NEUTRON BEAMS THROUGH THE AT- MOSPHERE	105
7.3.2	THE MOTION OF PHOTONS THROUGH THE ATMOSPHERE AND THE SUB- SEQUENT PRODUCTION AND MOTION OF LEPTONS AND HADRONS	112
7.3.3	THE MOTION OF ELECTRONS IN THE ELECTRIC FIELD OF A NEGATIVE STEPPED LIGHTNING LEADER	113
7.4	CONCLUSIONS AND OUTLOOK.....	117

8	FINAL REMARKS	118
9	REFERENCES.....	121

Figure List

2.1	Yearly lightning rate around the globe. FROM: Christian <i>et al.</i> , 2003.	7
2.2	Time scales, Source: Turqueti <i>et al.</i> , 2016	10
3.1	Illustration of rejection sampling method. The sampled points are shown with color; the green point indicates an acceptance while the blue point is rejected.....	13
4.1	Friction $F_k(\varepsilon_{\text{cut}}, \varepsilon_1)$ for electrons per interaction (Bremsstrahlung in red and ionization in blue), for two different low energy cut-offs, $\varepsilon_{\text{cut}} = 50$ keV (solid line) and $\varepsilon_{\text{cut}} = \varepsilon_{\text{max}}$ (dashed line). The total friction is the sum of the two contributions, which in the energy regime of HEAP the total is dominated by the ionization (please, note the log-scale). The data are from Cullen <i>et al.</i> (1997) and Perkins <i>et al.</i> (1991) for an air density of 1.293×10^{-3} g cm ⁻³ corresponding to 1 bar and 273 K as used in this study.	25
4.2	Products of a beam of 400 keV electrons after a propagation distance of 0.5 times their CSDA range which is 1.9 m in air at 1 bar and 273 K. The electrons have now a maximal energy of 250 to 300 keV depending on the code, and additional electrons and photons have been produced.	33
4.3	The same as in Fig. 4.2, but now for 40 MeV electrons. The propagation distance of 0.5 times their CSDA range is now 63.8 m. Now not only electrons and photons, but also positrons have been produced.	34
4.4	Products of a beam of 10 MeV photons at a distance of $1/(0.5 \mu)$ which corresponds to 756 m. Particle number per primary as a function of the radial distance from the symmetry axis (above), and of arrival time (below).....	35
4.5	Products of a beam of 40 MeV electrons, as detected by 12 detectors at 10 to 120 m distance. The detectors are impenetrable to hinder backscattering; therefore a new simulation is run for every detector distance.....	36
4.6	Relativistic avalanches probabilities calculated from Geant4 simulations, for specific point $\{\epsilon = 75$ keV, $E = 0.80$ MV/m $\}$ (illustrated by a cross in figure 4.7) and for two stepping settings. (a) : Avalanche probability versus α_R setting for Geant4 O4 and Geant4 O1. $\delta\ell_{\text{max}}$ is set to the default value of 1 kilometer. (b) : Avalanche probability versus maximum step setting ($\delta\ell_{\text{max}}$) for Geant4 O4 and Geant4 O1. The parameter α_R is set to the default value of the models, that is 0.8 for O1 and 0.2 for O4.....	45

4.7	<p>(a): Relativistic avalanche probability comparison between GRRR, REAM, O4 and O1. It shows three contour lines at 10%, 50% and 90%, as function of seed (primary) energy ϵ and electric field magnitude E. These contours are derived from the full probability scan, that are presented in the paper supplementary Material (section 5, available at: https://www.geosci-model-dev.net/11/4515/2018/). The cross at $\{\epsilon = 75 \text{ keV}, E = 0.80 \text{ MV/m}\}$ highlights the point where we studied the effect of the simulation stepping parameters (for the O4 and O1) on the probability, see figure 4.6. (b): Five contour lines indicating the 0%, 10%, 50%, 90% and 100% probabilities to generate a relativistic electron avalanche (RREA) as function of ϵ and E, for the Geant4 O4 model for which we could run a very large number of initial electrons ($> 50,000$) to obtain curves with a very low noise level.</p>	46
4.8	<p>Top : Avalanche multiplication length as function of ambient electric field, for each of the codes included in this study. Bottom : The relative difference of all other models with respect to REAM. Table 4.2 indicates the values of the fit parameters.</p>	49
4.9	<p>Top : Avalanche multiplication time as function of ambient electric field, for each of the codes included in this study. Bottom : The relative difference of all other models with respect to REAM. Table 4.2 indicates the values of the fit parameters.</p>	49
4.10	<p>Top : time to self-similar state as function of ambient electric field, for each of the codes included in this study. Bottom : relative difference with respect to REAM. ...</p>	51
4.11	<p>Mean electron energies at self-similar state (for distance record), for different electric field magnitudes. The data points are fitted with the model presented in section 4.12.3, equation 4.28. The values of the fitted parameters are presented in Table 4.3. To highlight the importance of including step limitations, Geant4 O1 values are presented for two different max step ($\delta\ell_{\text{max}}$) settings: one that is not acceptable (1 cm) and one that is acceptable (1 mm). The parameter α_R is set to its default value of 0.8 for O1 and 0.2 for O4.</p>	52
4.12	<p>Top : Electron (kinetic) energy spectra of Geant4 (O4 and O1), REAM and GRRR, for $E = 0.80 \text{ MV/m}$, recorded at $z = 128 \text{ m}$. The RREA is generated from 200 seed electrons of $\epsilon = 100 \text{ keV}$. Bottom : relative difference between REAM and the three other models. The error bars are calculated from the Poisson statistics.</p>	55
4.13	<p>Top : Photon energy spectra of Geant4 (O4 and O1) and REAM for $E = 0.80 \text{ MV/m}$, recorded at $z = 128 \text{ m}$. Bottom : relative difference between Geant4 (O1 and O4) and REAM. The error bars are calculated from the Poisson statistics.</p>	57

5.1	The friction curve as function of electron energy in the range from 0.01 eV to 1 keV for artificial air (which is a mixture of 80% nitrogen with 20% oxygen, blue curve) and for pure nitrogen (red curve), calculated according to the definition of Moss <i>et al.</i> (2006), that is reproduced in equations (5.1) and (5.2). Both curves are calculated with the processes listed in Table 5.1, and for a density defined by 273 K and 1 bar. The electric forces on electrons in electric fields of 12 and 24 MV/m are indicated by horizontal dotted and dashed lines, respectively.	61
5.2	Statistical behaviour of the electron energies in air in the flux simulation: energy fluctuations of 2 electrons (red and blue) in a 26 MV/m electric field as a function of time; the left panel shows the time from 0 to 10 ps on linear scale, the right panel from 10 ps to 10 ns on logarithmic scale.....	67
5.3	Results of the bulk simulation for the steady-state electron energy distributions in constant electric fields ranging from 10^3 to 3.5×10^7 V/m (equivalent to 1 kV/m to 35 MV/m). Left panel: Mean electron energy as a function of the electric field for artificial air (blue) and for pure nitrogen (red). (The electric field is plotted on the y-axis and applies to all three panels.) Middle panel: Electron energy distribution in air in color coding as a function of the electric field. Right panel: The same as in the middle panel, but for pure nitrogen. The color code indicates the electron count per (logarithmic) energy bin, normalized by the total number of particles. The blue or red dashed lines in the middle and the right panel are the mean electron energies that are shown on the left panel as well. The white curves in the middle and the right panel are the respective friction curves from Figure 5.1 divided by the elementary charge, hence they have dimension of electric field and can be identified with the equilibrium points of the net force for each electric field, as discussed in the introduction.	68
5.4	Selected electron energy distributions from Figure 5.3 for air. The legend displays the electric field in two different units, in MV/m for reference to the present results, and in Td for comparison with Colman <i>et al.</i> (2010).	69
5.5	Results of the flux simulation for electrons starting with 200 eV in electric fields from 16 to 34 MV/m where lines of different color refer to different fields. Top panel: probability $P(t)$ that an electron in air attaches to oxygen up to time t , as a function of time (for 10 ps to 100 ns). Bottom panel: probability $P(t)$ that an electron in air (dotted lines) or pure nitrogen (dashed lines) reaches 1 keV, again as a function of field (color coded) and time. The numbers in the plots express the applied electric field in multiples of MV/m.	71

6.1	Evolution of the TGF afterglow generated by the primary TGF as a function of the logarithm of time. (top and middle) Contour figures of the photon and neutron density, on a logarithmic scale; contours represent half a decade (i.e., a factor of $10^{0.5}$). The contour lines (red, yellow to white) are photons above 10 keV, the filled contours (blue to white) are neutrons. In Figure 6.1 (top) the density is horizontally integrated. Figure 6.1 (middle) gives the density profile as a function of radius at 3 km altitude, the density is averaged over rings around the symmetry axis. (bottom) Two quantities: on the left y axis in purple, the total particle number $N_i(t)$ of photons (diamonds) and neutrons (crosses), per initial photon $N_\gamma(0)$, with their approximations given by equations 6.2–6.4; on the right y axis in blue, the average neutron energy is drawn as a solid line, together with the minimal and the maximal neutron energy as dashed lines.	79
6.2	The same as in Figure 6.1, but now for the TGF afterglow that started from a neutron source at 10 km directed downward. In this figure time is plotted only from 10^3 s onward, focusing on the TGF afterglow. Figure 6.2 (bottom) does not represent the total particle number as some escaped out of the system at the upper boundary at 18 km. The decay rates, that is, the fits of the purple dashed lines, are the same as in Figure 6.1, adapted to the lower air density (at 10 km compared to 3 km).....	82
6.3	(a, b) Simulated counts of gamma radiation from the simulation presented in Figures 6.1 and 6.2. (c, d) Taken from Gurevich <i>et al.</i> (2011), in which it is denoted there as event “6.” Figures 6.3a to 6.3c are gamma ray counts per 200 μ s interval on a detector of 475 cm ² , at 3, 10, and 3.8 km, respectively. Figure 6.3d gives the measured fast electric field variation (20 μ s sampling rate measured by the capacity sensor, see Gurevich <i>et al.</i> , 2011 for more details).	83
6.4	Photon energy spectra at the ground for different source altitudes. The gray shade indicates low statistics.	86
6.5	Neutron energy spectra at the ground for different source altitudes. The gray shade indicates low statistics. The vertical line marks the energy range at 10 keV. ...	87
6.6	Distribution of arrival times of (a) neutrons and (b) photons on ground per primary. The different source altitudes are indicated by the legend. The vertical line marks the end of the primary photon pulse at 0.1 ms. The gray shade indicates low statistics.	88
6.7	Illustration of the effective neutron source geometry due to a point-like initial photon beam directed downward. The beam of high energy (primary) photons (in red) diverges slightly. Within this beam, individual photons move on straight lines and can create neutrons (in blue) by a photonuclear reaction. The created neutrons diffuse isotropically while they cool down. Photon lines ending without a (blue) neutron, have mostly created electron positron pairs; these pairs as well as lower energy photons are not drawn. The spatial dimension is of the order of a kilometer.	89

6.8	Energy distributions of photons (top row) and neutrons (bottom row) as in figures 6.4 and 6.5, but now differentiated between arriving before 0.1 ms (left column) or after 0.1 ms (right column).	91
6.9	Neutron number on ground per primary photon as a function of source altitude. The lines refer to the four different energy ranges of 10-15 MeV; 15-20 MeV; 20-25 MeV; 25-30 MeV, as indicated in the legend.	92
6.10	Neutron number per primary at the ground, n_γ , plotted as a function of the source photon spectrum for different source altitudes. The source spectrum is parameterized by an RREA spectrum (6.7) with exponential cutoff energy E_{th} . The curves for 5 and 6 km are multiplied by scaling factors of 30 or 100 in order to display all curves in the same plot.	93
7.1	a) The simulation results and NIST data of the average length ν until full energy loss of electrons for different initial energies E_0 at ground pressure. b) The simulation results and NIST data of the mean free path Λ of photons in air as a function of the initial photon energy E_0 . c) The relative error $(\nu_{NIST} - \nu_{Simulation})/\nu_{Simulation}$ as a function of E_0 . d) The relative error $(\Lambda_{NIST} - \Lambda_{Simulation})/\Lambda_{Simulation}$ as a function of E_0	99
7.2	a) The total cross section for elastic and inelastic scattering off nitrogen molecules as well as for the capture of neutrons on nitrogen molecules as a function of the energy $E_{kin,n,i}$ of the incident neutron. b) The cumulative cross section of elastic and inelastic scattering in air as well as the inverse column density $1/N_{int}$, (black lines), at altitude ranges of 0-16 km, 13-16 km, 16-19 km and 16-500 km.	101
7.3	The ratio $E_{kin,n,f}/E_{kin,n,i}$ of the neutron energy in the final state $E_{kin,n,f}$ and in the initial state $E_{kin,i}$ after elastic scattering as a function of the scattering angle Θ . Different lines show different initial energies and nucleon numbers η ($\eta = 32$ for O_2 , $\eta = 28$ for N_2 and $\eta = 2$ for H_2).	102
7.4	The energy loss ΔE of neutrons after exciting air molecules (solid line) and the ratio of the energy loss to the incident neutron energy $E_{kin,n,i}$ (dotted line) as a function of the incident neutron energy.	103
7.5	The simulation results and the data by Nakamura and Kosako (1981) for the flux $r \cdot \Phi(r)$ of neutron beams of different energies E_0 as a function of distance r	104
7.6	The spatial distributions of neutrons after 1 ms for different initial energies E_0 and altitudes H_0 . The color code on the right shows the kinetic energy. Note that the spatial scales are different for different panels. The current neutron number is given in brackets.	106
7.7	The energy distribution $dn_n/dE_{kin,n}$, i.e. the number of neutrons per energy bin, after different time steps for different initial energies E_0 and altitudes H_0 . All simulations were initiated with 600 neutrons.	107

7.8	a) The normalized neutron number N/N_0 for the same cases as in Figs. 7.6 and 7.7 as a function of atmospheric layer ΔX . Here $\Delta X = 0$ refers to the initial altitude and $\Delta X \neq 0$ denotes the air package in g/cm^2 which a neutron passes where a negative sign of ΔX denotes the altitudes in the initial direction of the neutron beam. Panels b) - f) show N/N_0 for the different cases in a) distinguishing for different threshold energies $E_{kin,n}$ passing the air package ΔX (first xlabel) and equivalently the altitude H (second xlabel).....	109
7.9	The time-integrated normalized cross section area $\langle A \rangle = 1/N \cdot \sum_{i=1}^N (x_i^2 + y_i^2)$ as a function of atmospheric layer ΔX and equivalently of the altitude H . x_i and y_i are the positions of the i -th neutron (out of N) parallel to the xy plane. The solid line at $\Delta X = 0$ indicates the source altitude of the neutron beam. Panel a) shows all simulated cases whereas panels b) - f) show $\langle A \rangle$ for different threshold energies $E_{kin,n}$ for different initial altitudes and different initial energies.	110
7.10	Electric field strength (color coded) in the vicinity of the tip for a leader of 1 km length in an ambient field of -0.5 kV/cm. Cylindrical coordinates ($\varrho = \sqrt{x^2 + y^2}, z$) are used, and the upper leader tip lies at the origin of the coordinate system. The black level lines indicate fixed values of the electric field strength from 5 to 1000 kV/cm as indicated.....	112
7.11	The spatial distribution of a) electrons, b) photons, c) positrons, d) neutrons and e) protons after approximately 1 μs projected onto the xz plane (for all y) in the electric field of a leader of 1 km length and of 1 cm curvature radius in an ambient field of -0.5 kV/cm (as indicated by the black line). The color code shows the (kinetic) energy of all particles above 1 MeV on a logarithmic scale. The numbers in brackets give the particle numbers.	114
7.12	The energy distribution of electrons, photons, positrons, neutrons and protons after 1 μs (panels a and b) and 0.5 ms (panels c and d). Panels a) and c) are obtained in the absence of any field and panels b) and d) in the field of a leader.	115
7.13	The energy distribution of electrons, photons, positrons, neutrons and protons after a) 28 ns and b) 0.5 ms in the same field as in Figure 7.11.	116

Table List

4.1	Summary of the performance (completion time). Method explained in Sect. 4.5.3. N_{user} is the normalization factor used to multiply simulation time (on the specific architecture).....	27
4.2	Values of the parameters of the fits (with 95 % confidence intervals) for the simulations data for avalanche scale in space and time, using the models described by equations 4.24 and 4.25. See figure 4.8 and 4.9 for the corresponding curves.	48
4.3	Mean energy variation with electric field. For evaluated codes we fitted by equation 4.28, with $F = 0.28$ MV/m. Figure 4.11 shows the corresponding curves.....	53
5.1	List of the electron-molecule interactions included in the simulations. Different excitation types of the molecules are indicated as rot for rotations, v for vibrations, and all other symbols refer to electronic excitations, SUM is the sum over all singlet states. All cross section data are retrieved from the lxcat databank and refer to Phelps' compilation of measurements.....	65
6.1	Number and lateral spreading of the neutrons at sea level as a function of the altitude of the photon source. For each source altitude, 4×10^7 primary photons were used, with a uniform energy distribution between 10 and 30 MeV. The neutron spreading on ground is defined as the standard deviation from the beam axis. The fourth column contains the neutron number per primary photon, with an error estimated as the root of the neutron number. The last column is the average neutron flux density towards the ground calculated with a reference circular area with 1 km radius and a reference time of 0.5 s.	85
6.2	Interpolated values for the parameters ℓ_i and I_i in equation (6.5) for the different energy ranges of the source photons.	92
6.3	Number of neutrons at sea level per primary by different authors.	94
7.1	The fluence $N_n/(\Delta t \cdot A)$ of neutrons at different altitudes for different initial conditions calculated from the simulations as in Fig. 7.6 (600 initial neutrons) and the flux $N_{n,TGF}/\Delta t$ for a typical TGF event (10^{15} neutrons at source altitude) for different initial conditions.....	111

ACRONYM LIST

CG	Cloud to Ground
IC	IntraCloud
GEC	Global Electric Circuit
TLE	Transient Luminous Events
TGF	Terrestrial Gamma ray Flash
TNB	Terrestrial Neutron Burst
OTD	Optical Transient Detector
BATSE	Burst and Transient Source Experiment
RHESSI	Reuven Ramaty High Energy Solar Spectroscope Imager
AGILE	Astro-Rivelatore Gamma a Immagini Leggero
CWI	Centrum Wiskunde & Informatica
MHD	Magnetic-hidroynamics
COESA	Committee on Extension to the Standard Atmosphere
HEAP	High Energy Atmospheric Physics
CGRO	Compton Gamma-Ray Observatory
VHF	Very High Frequency
VLF	Very Low Frequency
ULF	Ultra Low Frequency
HF	High Frequency
LMA	Lightning Mapping Array
RREA	Relativistic Runaway Electron Avalanche
LASA	Los Alamos Sferic Array
WWLLN	World Wide Lightning Location Network
TEC	Total Electronic Content
NOAA	National Oceanic and Atmospheric Administration
TECU	Total Electronic Content Unit

1 INTRODUCTION

Earth is an electromagnetic active and dynamic system. From the interaction with Sun, through the atmospheric particles ionization and reception of energetic radiation; electric currents at high altitudes such as 100 km; winds and thunderstorms at low altitude (10 km); electromagnetic waves propagation between the ground and high atmosphere and electrical discharges such as lightning, Transient Luminous Events (TLEs) and High Energy Atmospheric Phenomena (HEAP). The later being the focus of this work.

The atmosphere can be divided according to the temperature behaviour with the altitude: up to approximately 15 km the temperature decreases with altitude, this is the Troposphere; this layer stops with the Tropopause where is an inflexion point on the temperature and it begins to increase with the beginning of the Stratosphere, where the ozone layer is deposited, up until 50 km; at higher altitudes, there is the Mesosphere with a decrease in temperature again up until the next inflexion point at approximately 85 km where the Thermosphere is extending up to 600 km with increasing temperature ending at the Exosphere, the final layer that limits the atmosphere reaching 1000 km. Details on each layer can be explored further in the literature such as Kirchoff (1991) and Rakov (2002).

There is an atmospheric layer with high free charge density compared with the whole atmosphere – the Ionosphere. It behaves as a plasma with non uniform electric distribution. The Ionosphere has its base at approximately 100 km but this altitude varies across the globe and also varies from the day and night side of the Earth. The daily variation happens due to the different solar exposition that provokes ionization in this layer promoting the free electron density. As the day side is continuously bombarded with radiation, its electron density is higher than the night side one.

The ground can be considered as a conductor plate if compared with the atmospheric air. Thus, a system can be modelled with the air as a resistor and the ground with the Ionosphere a pair of conductors. As a first approximation, this is the Global Electric Circuit (GEC) which involves factors as the wind, atmospheric composition, landscape and other that originate the whole electrodynamic phenomenology in air (TURQUETTI, 2016).

In particular, the thunderclouds have a fundamental role in this dynamics. They are composed by water, in its three physical states, and aerosols – microscopic dust particles. The thundercloud particles collide due to the wind dynamics and become charged promoting a reservoir of charges in the troposphere and a variety of interactions between different layers of the atmosphere and also between the atmosphere and the ground.

The thunderclouds, also known as *cumulonimbus*, are the origin of the phenomenology studied in this work. However, they can not produce a sufficiently high electric field to promote the lightning (COORAY, 2014). Cosmic rays, majorly from the Sun, hit the thundercloud particles

and promote an avalanche of energetic electrons within the clouds that breaks the air dielectricity and starts the whole lightning.

Lightnings can occur in many forms. They may be between the clouds (interclouds, IC) and between the cloud and the ground (cloud-to-ground, CG); they can have both positive and negative polarity that it is determined by the charge polarity that is transferred. Specifically, the CG lightnings can also happen both downwards and upwards (COORAY, 2014).

The final stage of the lightning process is called the return stroke. After building the plasma channel and connecting two different points in the atmosphere, a circuit is built in which charges flow free (COORAY, 2014).

This plasma channel is opened by a series of accelerated charges avalanches forming a plasma structure called leader that can independently grow in kilometer scale and moves through the ionized path (KÖHN, 2014). The leader may also have positive and negative polarity that is characterized by the net charge in its tip.

The positive and negative leader propagate differently due the difference between the mobility of negative and positive charges (RAKOV, 2002). The positive leader ionizes the air continuously because it attracts free electron from the air to the plasma channel promoting its growth. But the negative leader repels the free electrons and can not grow through the positive ions due to their large mass.

The negative leader intensely accelerates the free electrons, nearby its tip, that ionize the air locally and produce a small isolated plasma structure called stem (CELESTIN *et al.*, 2012) that connects to the leader promoting a step-wise propagation.

The step-wise propagation of the negative leader is the source of an intense bremsstrahlung radiation with a wide spectrum that may reach MeV energies (KÖHN *et al.*, 2017). The literature connects these emissions with a possible origin of the Terrestrial Gamma-ray Flashes (TGFs) that are gamma radiation in the scale of milliseconds related with the thunderclouds (DWYER, 2013; FISHMAN *et al.*, 1994).

TGFs have a broad spectrum that includes the window of 10-30 MeV. In this energy window the photons can interact with the air molecules through Giant Dipole Resonance that makes the nuclei vibrate to the point of atomic fission and liberate neutrons and protons (BALDWIN, 1947). There are several ground detections of neutrons related with thunderstorms and lightning (e.g., SHAH *et al.*, 1985; SHYAM *et al.*, 1999; MARTIN *et al.* 2010; STARODUBTEV *et al.* 2012; GUREVICH *et al.*, 2012; TSUICHYIA *et al.*, 2012; CHILINGARIAN *et al.*, 2012; KOZLOV *et al.*, 2013; TOROPOV *et al.*, 2013), but there are none proton detections related with these phenomena up to this date (KÖHN *et al.*, 2017).

This work analyses the TGF phenomenon from two different perspectives: the acceleration of electrons to the required energies and the chain hadronic production starting from the energetic photons in the window of the GDR interaction. Both analyses are done by different Monte Carlo simulations.

This thesis is organized as the following: the chapter two characterizes the environment in which these phenomena occur differentiating from the laboratory, the chapter three details the Monte Carlo analysis process, the chapter four presents a comparison between different Monte Carlo softwares used to this application. The chapter five is an statistical study on the acceleration of electrons from thermal energies to the required energies and the chapter six shows the details of the hadronic production.

2 ATMOSPHERICAL ELECTRIC DYNAMICS

2.1 ATMOSPHERIC PLASMA

Plasma is a state of matter compounded by a mixture of free electrons and ions, it can be achieved by heating enough a gas so that the electrons are liberated from the neutral molecules. It can be fully ionized, as the solar plasma, or partially ionized as in laboratories (PIEL, 2010).

The plasma mathematical treatment inherits characteristics of the neutral gas formalism. There are many degrees of freedom in plasma state. But, the electromagnetic forces between the particles themselves and between particles and the external fields imply in a series of particularities.

The existence of free charges promotes a highly dynamic ambient. Impact ionization and photoionization act as source of free charges while recombination may neutralize particles acting as a sink mechanism for free charges (PIEL, 2010).

The time evolution of a distribution function is described by Equation 2.2, the Boltzmann equation,

$$\frac{df}{dt} = \frac{\partial f}{\partial t} + \frac{\partial f}{\partial x_i} \frac{\partial x_i}{\partial t} + \frac{\partial f}{\partial v_i} \frac{\partial v_i}{\partial t}; \quad (2.1)$$

$$\frac{df}{dt} = \frac{\partial f}{\partial t} + (\mathbf{v} \cdot \nabla) f + (\mathbf{a} \cdot \nabla) f = 0. \quad (2.2)$$

for such, f is the distribution function which is relative to time (t), space (x) and velocity (v).

The total derivative consists of a partial derivative of the function f in time, a term with the particles velocities and another term with the particles acceleration. The later includes external forces. Here, differently from the neutral gas, the forces are the sum of any mechanical external force and the Lorentz terms. The Equation 2.2, including electromagnetic acceleration, is the Vlasov equation and represents a non-collisional plasma with zero variation on the number of particles.

The equations of continuity, momentum and energy conservation can be derived from 2.2. These equations are respectively the statistical moments of zero, first and second order (BITTENCOURT, 2004).

As in the neutral gas formalism, the statistical mechanics approach is important in plasma. Results can be obtained based in variations of the Maxwell-Boltzmann distribution 2.3 which is the equilibrium solution for the Boltzmann equation,

$$f_M(v_x, v_y, v_z) = \frac{1}{Z} \exp\left(-\frac{mv^2}{2k_B T}\right). \quad (2.3)$$

where Z is a normalization factor, T is the gas temperature, k_B is the Boltzmann constant; v_i are the velocity components of the gas and m , the particles mass. The Maxwell-Boltzmann distribution is often used to describe the free particles velocities (PIEL, 2010). Adaptations can be made to charge particles.

Although the particles react collectively to the electromagnetic forces, a shielding process occurs due to the thermal movement in plasma. The Debye mean free path, λ_D , measures how distant the particles can be, on average, and still behave as neutral and free, i.e., without a significant electromagnetic interaction between themselves. λ_D can be derived from the the distribution function and is different to electrons and ions as shown in Equations 2.4 and 2.5,

$$\lambda_{Di} = \left(\frac{\epsilon_0 k_B T_i}{n_{i0} e^2} \right)^{1/2}; \quad (2.4)$$

$$\lambda_{De} = \left(\frac{\epsilon_0 k_B T_e}{n_{e0} e^2} \right)^{1/2}. \quad (2.5)$$

The subindex 'i' is referred to ion while the subindex 'e' refers to electrons; n is the particles densities within the plasma. ϵ_0 and e are respectively, the electric permissivity of vacuum and electron charge.

A collision term included at Equation 2.1 presents the necessity to specify its form which varies with the problem context. The distribution 2.3 satisfy the Vlasov equation, thus it is an usual tool to approximations on the collision term through the Krooks formalism (BITTEN-COURT, 2004), represented by Equation 2.6:

$$\frac{df}{dt} = \left(\frac{\partial f}{\partial t} \right)_{col} \approx \frac{f - f_{max}}{\tau}; \quad (2.6)$$

$$f(t) = f_{max} + (f(0) - f_{max}) \exp\left(\frac{-t}{\tau}\right). \quad (2.7)$$

In this approximation, the collision term is treated as a small variation from the equilibrium function, f_{max} , resulting into the form 2.7. An arbitrary distribution function is given by this small perturbation $f(0)$ which decays with a characteristic time τ into the equilibrium function.

There are plasmas in diverse conditions along the atmosphere. The ionosphere, at 100 km high, have a total density in the order of $10^{-10} \text{ g.cm}^{-3}$ (MSIS-E-90¹) and a Total Electronic Content (TEC) to the order of 10^{16} m^{-2} (National Oceanic and Atmospheric Administration, NOAA²) which represents an unit of TEC called Total Electronic Content Unit (TECU). Those characteristic density numbers allow the ionospheric plasma to be treated as non-collisional which differ greatly from other phenomena in GEC.

¹https://cohoweb.gsfc.nasa.gov/vitmo/msis_vitmo.html

²<http://www.noaa.gov/>

Electrical discharges, such as TLEs and lightning, are produced by collisional processes and are highly dynamic with a small time scale (COORAY, 2014). Those characteristics impose difficulties to the traditional MHD treatment to plasma channel physics.

The Krooks approach is not adequate to treat such phenomena due the number of variables that they depend. Thus, more accurate techniques are necessary. The Monte Carlo process is then adopted by several works to describe the initial moments of the discharge.

2.2 ELECTRICAL DISCHARGES

Lightning are electrical discharges that may occur in the low atmosphere when the electric field produced by the charges within the thundercloud is high enough to break the dielectricity of air, the so called electrical breakdown

Dubinova *et al.* (2015) showed that the electrical discharge may start with electric fields below the breakdown threshold due to the time scale of electric field variations and the response time of the ice particles that is not fast enough to resist the air breakdown.

The lightning initial stages are the construction of a ionized path to the electrical current flow through the plasma channel. A structure called streamer begins the path ionization. It is a self propagating discharge that ionize the air due to the intense electric field in its tip establishing a conducting channel to the leader propagation (KÖHN, 2014).

IC discharges represent 90% of all lightning and may extend through several tens of kilometers as shown by radio waves mapping. On the other hand, CG discharges have a estimated length of 5 km which is the average cloud to ground distance (RAKOV, 2002).

Within the number of CG discharges, 90% are negative and the remaining 10% are dominated by positive discharges; both from the clouds to the ground. A small fraction occurs from the ground to the clouds. The upward discharges require a high object as a TV tower (SABA *et al.*, 2016) that stimulates the creation of the conducting plasma channel from its tip to the cloud base (RAKOV, 2002).

The lightning process has a time scale of milliseconds. IC discharges are observed to have continuous and long current with peaks of some kA. Most of negative CG discharges present a short signal of continuous current followed by several peaks due to a discharge multiplicity that flows through the opened plasma channel. Meanwhile, the positive CG discharges usually present a single intense peak of continuous current. The discharges from the ground to the clouds show a long and intense continuous current with few peaks (COORAY, 2014).

The Optical Transient Detector (OTD) is a global satellite system launched in 1995 to record the lightning global rate. The observations showed an average yearly rate of 44.5 flash per second. The Figure 2.1 shows the flash density around the globe with a peak at the Congo Basin. 78% of the recorded flashes occur between 30° south and 30° north in latitude with a ratio of 10:1

between the discharges at continent and ocean (CHRISTIAN *et al.*, 2003).

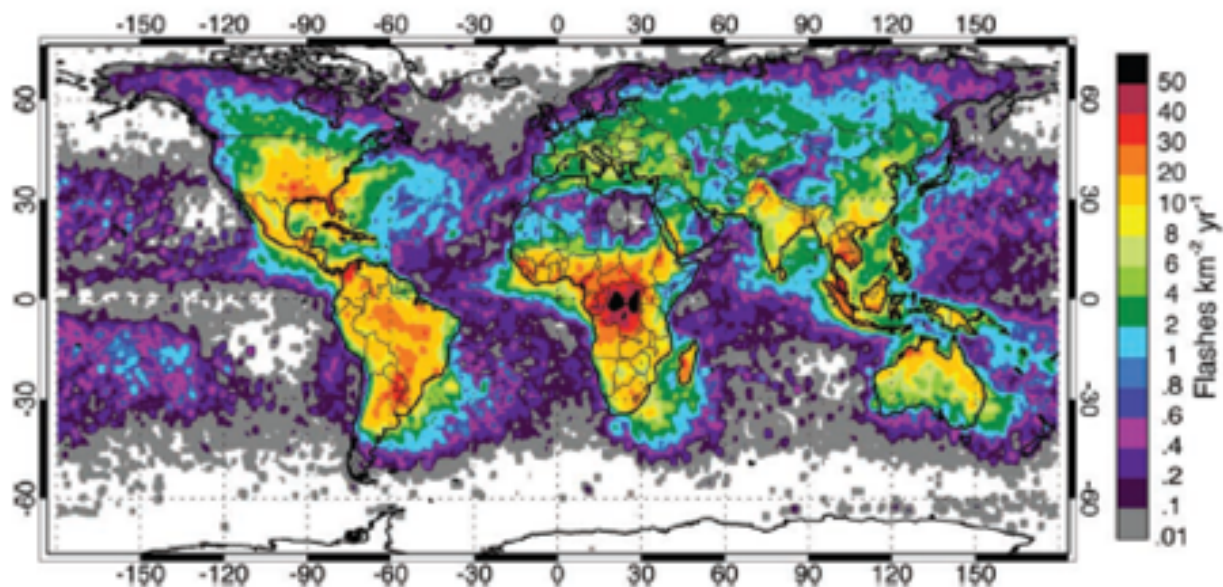


Figure 2.1: Yearly lightning rate around the globe.
FROM: Christian *et al.*, 2003.

2.3 HIGH ENERGY EMISSIONS

In 1925, C.T.R. Wilson proposed that thunderstorms could emit a "measurable amount of extremely penetrating radiation of β or γ type" (WILSON, 1925), about 60 years before such radiation was observed from the atmosphere and from space (PARKS *et al.*, 1981; FISHMAN *et al.*, 1994; WILLIAMS, 2010). This, and subsequent observations and modeling are now being investigated with the field of High Energy Atmospheric Physics (HEAP). A review is provided by Dwyer *et al.* (2012).

Observationally different types of high energy emissions have been identified coming from thunderclouds, naturally categorized by duration. Microsecond-long burst of photons, which were first observed from space (FISHMAN *et al.*, 1994; GREFENSTETTE *et al.*, 2008; MARISALDI *et al.*, 2014; ROBERTS *et al.*, 2018), are known as Terrestrial Gamma-ray Flashes (TGFs). TGFs also produce bursts of electron and positrons (DWYER *et al.*, 2008; BRIGGS *et al.*, 2011; SARRIA *et al.*, 2016) that follow the geomagnetic field lines into space and show longer durations. Two space missions specifically designed to study TGFs and related phenomena will provide new observations in the near future : ASIM (Atmosphere-Space Interaction Monitor) (NEUBERT *et al.*, 2006), successfully launched in April 2018; and TARANIS (Tool for the Analysis of Radiation from lightning and Sprites) (LEFEUVRE *et al.*, 2009; SARRIA *et al.*, 2017).

Seconds to minutes or even hours long X and gamma radiation have been observed on ground, from balloons and aircraft, by (MCCARTHY AND PARKS, 1985; EACK *et al.*, 1996; TORII

et al., 2002; TSUCHIYA *et al.*, 2007; ADACHI *et al.*, 2008; CHILINGARIAN *et al.*, 2010, 2011; KELLEY *et al.*, 2015; DWYER *et al.*, 2015; KOCHKIN *et al.*, 2017, 2018), which are called gamma-ray glows or thunderstorm ground enhancements. Some modeling attempts of both gamma ray and electron observations are also presented in Chilingarian *et al.* (2012).

TGFs were predicted to create a neutron emission on the millisecond duration, with associated isotope production (BABICH, 2006). Such emission was observed from the ground (BOWERS *et al.*, 2017; TERUAKI *et al.*, 2017). A similar phenomenon was modeled at higher altitudes by (RUTJES *et al.*, 2017), that also proposed to call it "TGF afterglow".

Following the idea of Wilson (1925), high energy X and gamma radiation are created by runaway electrons, which may further grow by the effect of Møller scattering in the form of so called relativistic runaway electron avalanches (RREAs) (GUREVICH *et al.*, 1992). For the multiplication to occur, a threshold electric field of $E_{th} = 0.28$ MV/m (at STP) is required (BABICH *et al.*, 2004A; DWYER, 2003).

The difference in duration between TGFs and gamma-ray glows can be explained by two possible scenarios to create runaway electrons, which is traditionally illustrated using the average energy-loss or friction curve (see, e.g., figure 1 of Dwyer *et al.*, 2012). In this curve, there is a maximum at around $\varepsilon \approx 123$ eV, illustrating the scenario that for electric fields higher than a critical electric field, of $E_c \approx 26$ MV/m at standard temperature and pressure (STP), thermal electrons can be accelerated into runaway regime, described in the so-called Cold Runaway theory (GUREVICH, 1961). The effective value of E_c may be significantly lower, as electrons could overcome the friction barrier due to their intrinsic random interactions (LEHTINEN *et al.*, 1999; LI *et al.*, 2009; LIU *et al.*, 2016; CHANRION *et al.*, 2016) Cold Runaway could happen in the streamer phase (MOSS *et al.*, 2006; LI *et al.*, 2009; CHANRION AND NEUBERT, 2010) or leader phase (CELESTIN AND PASKO, 2011; CELESTIN *et al.*, 2012; CHANRION *et al.*, 2014; KÖHN *et al.*, 2014, 2017; KÖHN AND EBERT, 2015) of a transient discharge, explaining the high energy electron seeding that will evolve to RREAs and produce gamma-rays by *bremstrahlung* emission from the accelerated electrons. The cold runaway mechanism may be further investigated with laboratory experiments, in high voltage and pulsed plasma technology, and may be linked to the not fully understood x-ray emissions that have been observed during nanosecond pulsed discharges and the formation of long sparks, (RAHMAN *et al.*, 2008; DWYER *et al.*, 2008; SHAO *et al.*, 2011; KOCHKIN *et al.*, 2016, and references therein), with different possible production mechanism that were proposed and tested using analytical modeling (COORAY *et al.*, 2009) and computer simulations (IHADDADENE AND CELESTIN, 2015; LUQUE, 2017; LEHTINEN AND ØSTGAARD, 2018). Alternatively, the relativistic feedback discharge model is also proposed to explain TGF production using large scale and high potential electric fields (DWYER, 2012), where the RREA initial seeding may be provided by cosmic-ray secondaries, background radiation, or cold runaway (DWYER, 2008).

For fields significantly below the thermal runaway critical electric field $E_c \approx 26$ MV/m but above the RREA threshold electric field of $E_{th} = 0.28$ MV/m (at STP), runaway behaviour is

still observed in detailed Monte Carlo studies (see Dwyer *et al.*, 2012, and references therein). At thundercloud altitudes, cosmic particles create energetic electrons that could runaway in patches of the thundercloud where the electric field satisfies this criterion. RREAs are then formed if space permits and could be sustained with feedback of photons and positrons creating new avalanches (BABICH *et al.*, 2005; DWYER, 2007, 2012). Gamma-ray glows could be explained by this mechanism, as they are observed irrespectively of lightning or observed to be terminated by lightning (MCCARTHY AND PARKS, 1985; CHILINGARIAN *et al.*, 2015; KELLEY *et al.*, 2015; KOCHKIN *et al.*, 2017). The fact that gamma-ray glows are not (necessarily) accompanied by classical discharges, results in the conclusion that the electric fields causing them are usually also below the conventional breakdown. The conventional (or classical) breakdown field, of $E_k \approx 3.0$ MV/m (at STP), is where low energy electrons (< 123 eV) exponentially grow in number, as ionisation overcomes attachment.

2.4 GLOBAL ELECTRIC CIRCUIT

There are spatially local and global parts in GEC. While thunderstorms and lightnings are local with lengths of some kilometers, there are radio waves emitted by lightning that surrounds the globe through the conducting cavity between the ground and ionosphere; electric currents due the charge movement in the ionosphere (so called ionospheric currents) that have a global length scale.

The geometry formed by the ground and the ionosphere allows the system to be seen as a spherical capacitor providing a characteristic time scale due the air resistance. Phenomena with a faster time scale are considered in the regime of alternate current while events with a longer time scale are considered in the continuous current regime (TURQUETTI *et al.*, 2016).

The phenomena classification can be seen in the Figure 2.2. The vertical line indicates the spherical capacitor characteristic time scale and processes to the left are considered in the alternate current regime while to the right the continuous current regime.

A large energy window is covered in the CEG. Lightning emits from radio waves to gamma-rays. The pairs electron-positron present in TGFs reach the ionosphere and are capable of following the magnetic field lines and may be detected far away from the emission point. Thus, there are energies from the sub-thermal regime (less than 0.025 eV) up to energies in which anti-matter creation or nuclear fission are possible, reaching up to 100 MeV (TAVANI *et al.*, 2011). The cosmic rays present energies that reaches 10^{21} eV though the average cosmic ray energies have 10^{15} eV (KOTERA *et al.*, 2011).

The Sun radiation is responsible for a large portion of the ionosphere free charge density. The air density and composition vary significantly with the altitude promoting differences in the TEC profile and creates different layers in the ionosphere (BRUM, 2005).

Those layers are marked by peaks in TEC (SHUNK, 2009). The ionosphere constitutes an

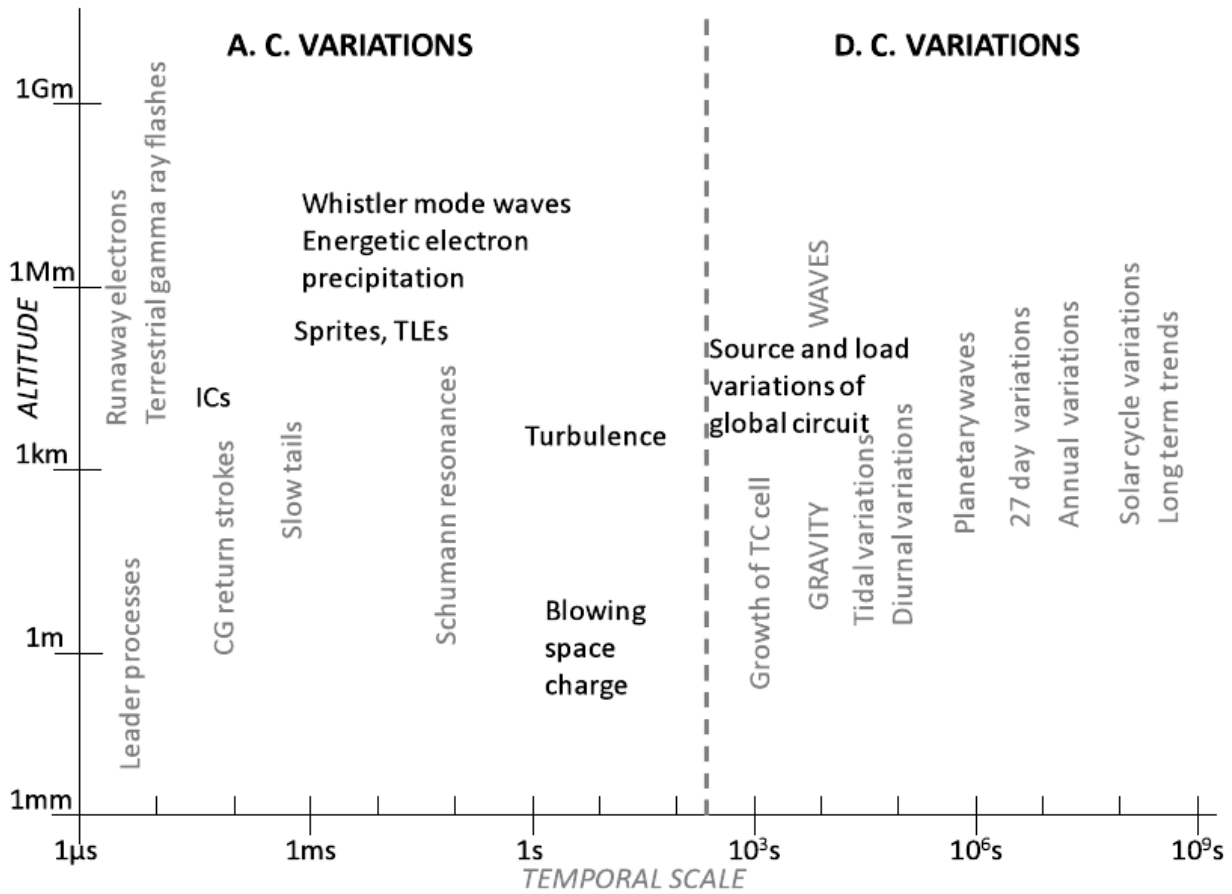


Figure 2.2: Time scales, Source: Turquetti *et al.*, 2016

anisotropic environment with non-homogeneous conductivity creating diverse electrical current patterns through the globe that produce effects in the geomagnetic field (KIRCHOFF, 1991).

Different bands of the electromagnetic spectrum penetrate the ionosphere down to different altitudes. The lowest layer, so called D, is characterized by the presence of negative ions and the lowest TEC peak; the E layer located upper presents a high conductivity and the F layer (uppest of all) is characterized by three sublayers (F1, F2, F3). F1 Being a transition layer between E and F due to differences on the TEC; F2 shows the largest TEC peak with an ion dominance of atomic oxygen and F3 which is a layer that appear at regions of low and medium latitudes due to a radiation peak in those regions (BATISTA *et al.*, 2003).

The electronic density profile presents an intense daily cycle since the sun acts as a source. At the night side there is a large decay in the electronic density that vanishes the D and E ionospheric layers and all the sublayers (F1, F2, F3) become a single F layer. An effect that also changes the whole electrical current dynamics in the atmosphere.

3 MONTE CARLO METHOD IN THE MOTION OF PARTICLES

The Monte Carlo method is a technique to simulate a mathematical or physical experiment based on statistics and sampling random numbers from probability functions. In this work, several Monte Carlo programs have been used to simulate the motion and collisions of neutral and charged particles in a given ambient. The randomness, in this background, comes from the interactions that each particle is able to do with the environment. Each interactions has a probability to occur related to the respective cross section. The sum of all cross sections is inversely proportional to the particles mean free path which dictates how much space it is going to be travelled between collisions (here, the code would be space-oriented), this distance can also be interpreted as time between collisions if, instead of the mean free path, the collision frequency is used making the code be time-oriented.

Results from Monte Carlo methods comes from a large statistical sample and require a considerable experimental repetition or, in this case, a considerable number of primary particles. Since it is based on probability, a variety of outcomes is possible and a small statistical sample may not show rare events.

3.1 RANDOM NUMBERS

It is important to understand the concept of random variable to be able to make better use of Monte Carlo methods as the core of these methods is this kind of variable. They may be discrete or continuous, a random variable X will be discrete if it can assume values from a countable set with certain probability and will be continuous if it can assume any value in an interval of real numbers, a countless set, with certain probability (MAGALHÃES, 2004). The random variables in the simulations are the pseudo-random numbers generated computationally in the sampling process.

A function that determines for each of its variables a probability is the probability function, these functions follow a set of axioms of always be positive or equal to zero, i.e., there is not a negative probability and the sum of the probabilities of all possible results is equal to 1. Since the probabilities are normalized and 1 basically represents a event that will happen for sure and 0 probability represents an event that will not happen, in the discrete case this sum is straight forward but in the continuous case the sum is done by a normalized integral over all the real numbers, i. e., from minus to plus infinity.

The cross sections play a central role as they will be the main term of the probability distribution function to determine the collision occurrence and its parameters. Since the microscopical

cross sections do not carry information about the medium density, which plays a significant role in the collisions determination, it is required a function involving these both concepts in order to do this evaluation.

3.1.1 Sampling random numbers process

In the codes used there is an intrinsic need to extract random numbers from distributions, this can be used for example as a way to randomly decide the occurrence of a collision in a particle code if the cross sections are used as part of the probability distributions in this case.

In order to draw random numbers within a determined distribution is commonly used the rejection method. It is based on the comparison between a point of the distribution and a random point on the plane, the distribution point determination has to be random so it is done by drawing a random number within the distribution range in the abscissa axis which will correspond to a ordinate value of the distribution forming a (x, y) pair.

Since the x point is randomly determined, there is a need to randomly determine a y_r point to be compared with the y value of the distribution, this is done by finding the maximum value of the distribution to have a range of possible values for the distribution and y_r is drawn from this range. Finally the points (x, y) and (x, y_r) are compared and if (x, y_r) is below (x, y) the number is accepted and count as a hit, there is no need to normalize the distribution but is required that the distribution be positive at all points and with no anomalous point in the set range.

The Figure 3.1 illustrates the rejection method in both situations, in this case, the point 2 is rejected and the point 1 is accepted as a hit as the point 1 is below to the point (x, y) and the point 2 is above the point (x', y') , both x and x' coordinate are randomly drawn within the valid range of the function and the coordinates y_r and y_r' are randomly drawn between zero and the maximum value of the function.

This method is very well spread because of its simplicity, as no integration is need and if the distribution is given the method is immediate. The downside of this process is the low efficiency, in a series of iterations only a small fraction count as a success in this method.

Through the rejection method, several parameters will be determined in this work. It will be extensively used together with the cross sections and another probability distribution functions to promote all the particle propagation through the simulation and it will coordinate the particles interaction.

3.1.2 Cross sections

The particle code implies in several collisions, to simulate the neutron's path through the atmosphere it is necessary to have a comparative measure of how much the neutrons collide in each energy. Scattering cross section (σ) of a system is defined by its ability on scatter particles for a given flux (ψ) in Equation 3.1 (CELOTTA *et al.*, 1986), as the flux is defined as the number

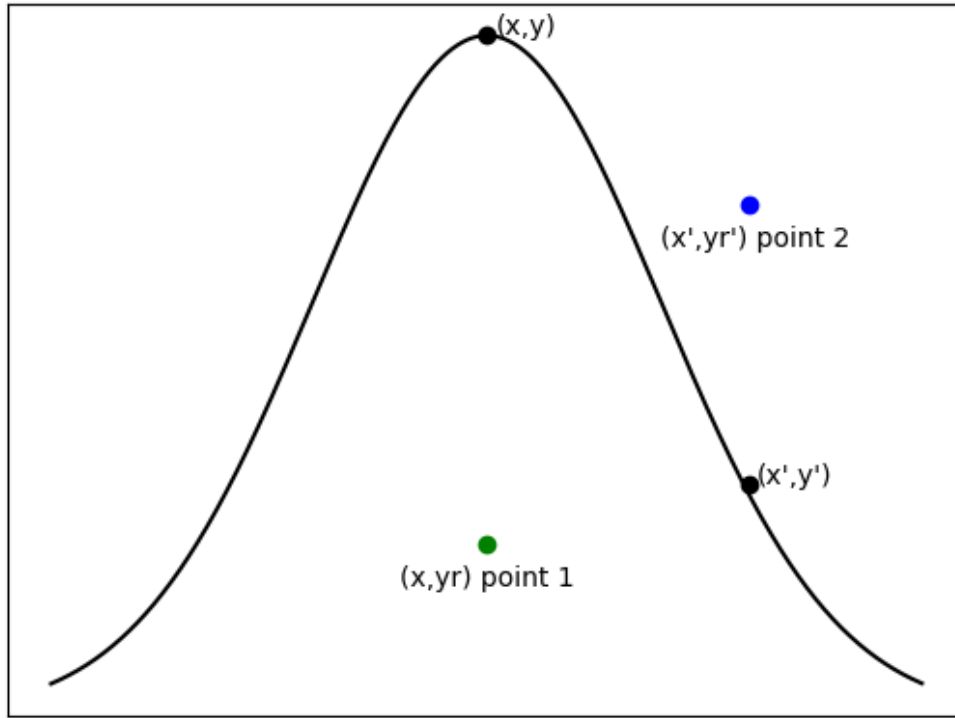


Figure 3.1: Illustration of rejection sampling method. The sampled points are shown with color; the green point indicates an acceptance while the blue point is rejected.

of particles reaching the surface per second per surface area perpendicular to the particles beam direction.

$$\sigma = \frac{N}{\psi}. \quad (3.1)$$

The cross section has dimension of area, thus N is the number of particles scattered per second, since it represents the system it is called the total cross section which depends on the size of the system. In the case of this work it is used cross section data of interactions between neutrons, photons, electrons and atmospheric gases represented by nitrogen gas and oxygen gas. This measure is available in data-bases such as the ENDF-7 library¹, Lxcat² and in the GEANT4 (CARLSON, 2010) and others (BERMAN, 1975) these data are used in the Monte Carlo approach to evaluate the occurrence of a collision and its angular distribution.

It is important to have information about the scattering angular dependence, for this purpose it is employed the differential cross section which can be defined with Equation 3.2 (CELOTTA

¹<http://www.nndc.bnl.gov/exfor/>

²https://fr.lxcat.net/data/set_type.php

et al., 1986), following the idea of differential cross sections it is also important to see the cross section energy dependence, which can be shown as Equation 3.3 the partial differential cross section (CELOTTA *et al.*, 1986)

$$\frac{d\sigma}{d\Omega} = \frac{N_{d\Omega}}{\psi d\Omega}, \quad (3.2)$$

$$\frac{d^2\sigma}{d\Omega dE} = \frac{N_{d\Omega, dE}}{\psi d\Omega dE}. \quad (3.3)$$

It is clear the statistical nature of the cross sections and their differentials, here $N_{d\Omega}$ is Number of particles scattered per second into solid angle $d\Omega$ and $N_{d\Omega, dE}$ is Number of particles scattered per sec with energy in $[E, E+dE]$ into solid angle $d\Omega$, they are used in the Monte Carlo method as part of the probability distribution functions that will be sampled in order to allow or not a random collision to happen. They are also used to determine in a random manner the characteristics of the collision outcome such as scattering angle and final energy of the particles in the interaction.

3.2 MOTION ALGORITHM

Particles will always move accordingly the external forces. In our environment, the charged particles will have influence of electromagnetic fields and collisions while the neutral ones scatter only due collision. It can be generalized in the motion Equations,

$$\frac{d^2\mathbf{x}}{dt^2} = \frac{\mathbf{F}}{m} \quad (3.4)$$

with

$$\mathbf{F} = q\mathbf{E} + q\mathbf{v} \times \mathbf{B} + \delta(\epsilon). \quad (3.5)$$

Where \mathbf{E} and \mathbf{B} are the electromagnetic field and δ is the generalized term for the random collisions as a function of energy ϵ . The need for relativistic corrections will happen and a particle's kinetic energy meets the condition,

$$\epsilon \gg m_r, \quad (3.6)$$

in which m_r is the rest energy.

Between collisions, at each computational step, the energies are updated according to the external forces. A collision is determined randomly based on the mean free path or collision frequency of each particle within the medium.

The totals mean free path and collision frequency are defined by the respective sum over all

possible interactions,

$$\lambda_T = \sum_j^a \sum_i^b \lambda_{i,j} = (\sum_j^a \sum_i^b \sigma_{i,j} n_j)^{-1} \quad (3.7)$$

and

$$\nu_T = \sum_j^a \sum_i^b \nu_{i,j} = \sum_j^a \sum_i^b \mathbf{v}(\epsilon) \lambda_{i,j}^{-1}. \quad (3.8)$$

Where λ and ν are, respectively, the mean free paths and the collision frequencies. The system in Equations 3.7 and 3.8 is for a medium with a gases and b possible interactions where n_j is the partial density for each gas.

Once there is a collision occur, the type of interaction is decided by a similar fashion with random numbers sampling based on the relative value of each cross section to the total cross section.

The simulation step can be based on the mean free path or the collision frequency and then it will be space-oriented (if based on the mean free path) or time-oriented (if based on the collision frequency). Hence the simulation step length can be determined with a random variable between 0 and 1 as follows:

$$l = -\ln(\eta)\lambda_T \quad (3.9)$$

and

$$\tau = -\ln(\eta)/\nu_T. \quad (3.10)$$

Where l and t are the step length in space and time respectively and η is the sampled random number.

Different Monte Carlo simulations can also define their step by a fixed value, generally smaller than the time step or mean free path of interest in the problem, and produce a large amount of data for each step; the so-called null collision method. The name null collision is given because, for computational purposes, the particles are all colliding in a fixed step but in some of these collisions there are no updates, necessarily. It is widely used to have more accuracy in the particles motion relatively to the geometric boundaries.

4 DIFFERENT MONTE CARLO CODES – A COMPARISON

1

4.1 INTRODUCTION

In this chapter, we benchmark the performance of the Monte Carlo codes Geant4, EGS5 and FLUKA developed in other fields of physics and of the custom-made codes GRRR and MC-PEPTITA against each other within the parameter regime relevant for high energy atmospheric physics. We focus on basic tests, namely on the evolution of monoenergetic and directed beams of electrons, positrons and photons with kinetic energies between 100 keV and 40 MeV through homogeneous air in the absence of electric and magnetic fields, using a low energy cutoff of 50 keV. We discuss important differences between the results of the different codes and provide plausible explanations. We also test the computational performance of the codes. Furthermore, we provide comparisons with active electric field for three codes used by the community: Geant4, GRanada Relativistic Runaway simulator (GRRR) and Runaway Electron Avalanche Model (REAM) – to simulate RREAs.

For the comparisons with active electric field, we first present our theoretical description of the RREA process, which is based on and incremented over previous published works. This analysis confirmed that the avalanche is mainly driven by electric fields and the ionisation and scattering processes determining the minimum energy of electrons that can run away, which was found to be above ≈ 10 keV for any fields up to the classical breakdown field. To investigate this point further, we then evaluated the probability to produce a RREA as a function of the initial electron energy and of the magnitude of the electric field. We found that the stepping methodology in the particle simulation has to be set up very carefully in Geant4. For example, a too-large step size can lead to an avalanche probability reduced by a factor of 10 or to a 40 % overestimation of the average electron energy. When properly set up, both Geant4 models show an overall good agreement (within ≈ 10 %) with REAM and GRRR. Furthermore, the probability that particles below 10 keV accelerate and participate in the high-energy radiation is found to be negligible for electric fields below the classical breakdown value. The added value of accurately tracking low-energy particles (< 10 keV) is minor and mainly visible for fields above 2 MVm^{-1} .

¹This chapter is a version and combination of such publications: Evaluation of Monte Carlo tools for high energy atmospheric physics, C. Rutjes, D. Sarria, A.B. Skeltved, A. Luque, G. Diniz, N. Ostgaard, U. Ebert, Geosci. Model Dev. 9, 3961 - 3974 (2016), doi:10.5194/gmd-9-3961-2016 and Evaluation of Monte Carlo tools for high-energy atmospheric physics II: relativistic runaway electron avalanches, David Sarria, Casper Rutjes, Gabriel Diniz, Alejandro Luque, Kevin M. A. Ihaddadene, Joseph R. Dwyer, Nikolai Ostgaard, Alexander B. Skeltved, Ivan S. Ferreira, Ute Ebert, Geosci. Model Dev. (GMD) 11, 4515-4535 (2018), doi: <https://doi.org/10.5194/gmd-11-4515-2018>,

In a second simulation set-up, we compared the physical characteristics of the avalanches produced by the four models: avalanche (time and length) scales, convergence time to a self-similar state and energy spectra of photons and electrons. The two Geant4 models and REAM showed good agreement on all parameters we tested. GRRR was also found to be consistent with the other codes, except for the electron energy spectra. That is probably because GRRR does not include straggling for the radiative and ionisation energy losses; hence, implementing these two processes is of primary importance to produce accurate RREA spectra. Including precise modelling of the interactions of particles below 10 keV (e.g. by taking into account molecular binding energy of secondary electrons for impact ionisation) also produced only small differences in the recorded spectra.

4.1.1 The multiple scales in energy and length

There are two basic problems for simulating these high energy phenomena in our atmosphere, related to the wide range of scales in energy and length. First, the models have to bridge energy scales from tens of MeV down to thermal energies of tens of meV ($300\text{ K} \rightarrow 0.03\text{ eV}$), i.e., over 9 orders of magnitude. At the upper edge of this energy range, models developed by the high energy physics community (e.g., for CERN) exist where it should be noted that they were originally developed for even higher particle energies, and for the interaction of energetic particles with metals rather than with air – though radiation medicine now also develops models for the penetration of energetic radiation into biological tissue (ANDREO,1991; SEMPAU *et al.*, 2001; CARRIER *et al.*, 2004), which consists mostly of similarly light molecules as air, but in the liquid rather than the gaseous state. In the low energy regime, models by the low temperature plasma physics community should be used, with cross sections listed, e.g., on the community web page (PANCHESHNYI *et al.*, 2012).

Second, in particular for cold runaway models, there are two widely separated spatial scales: the source region with high and time-dependent self-consistent electrodynamic fields where electrons are accelerated, and the wide propagation distances from the source to detectors in space or on the ground where electric fields can be neglected.

For the first comparison, without electric field, we focus on the second problem, namely the beam propagation towards detectors where the final products are characterized by energy spectra and arrival times, and the source properties must be reconstructed from this data, e.g., in the work by Østgaard *et al.* (2008). Accurately modeling the transport from the source to the very remote detector is, together with some knowledge of the source, thus very important to deduce production altitude, beaming angle or light curves of TGFs and associated electron beams from space data (DWYER AND SMITH, 2005; CARLSON *et al.*, 2007; HAZELTON *et al.*, 2009; DWYER *et al.*, 2008B; SARRIA *et al.*, 2016).

4.1.2 Theoretical understanding of RREAs

In the energy regime of a kilo-electronvolt (keV) to a hundred of mega-electronvolts (MeV), the evolution of electrons is mostly driven by electron impact ionisation (LANDAU *et al.*, 2013), as this energy loss channel is much larger than the radiative (bremsstrahlung) energy loss. However, the bremsstrahlung process does impact the shape of the electron energy spectrum, that can be understood by the straggling effect, that is discussed in the next section. When the electric field is below the classical breakdown $E_k \approx 3.0$ MV/m (at STP), the system can be simplified, because the effect of the electrons below a certain energy can be neglected, in particular the population that would otherwise (if $E > E_k$) multiply exponentially and have an important effect on the electric field. The part of the electron population that decelerates, and eventually attaches, cannot contribute to the production of the high energy radiation. Let ϵ_2^{\min} be the minimum energy for a secondary electron to have a chance to runaway, thus participate to the production of high energy radiation. The subscript index $i = 2$ indicates a secondary electron. A precise value of ϵ_2^{\min} will be evaluated in section 3 with the help of simulations, but, by looking at the friction curve, one can guess it is located in the keV to tens of keV energy regime (DWYER *et al.*, 2012). As almost all energy loss of ionisation is going into producing secondary electrons of lower energy ($\epsilon_2 \lesssim 200$ eV), it is reasonable to approximate that channel as a continuous energy loss, or friction.

In the case of electric fields above the RREA threshold ($E_{\text{th}} = 0.28$ MV/m at STP), the electrons, when considered as a population, will undergo avalanche multiplication. Some individual electrons do not survive (because there can be hard bremsstrahlung or ionisation collisions that will remove enough energy to get below ϵ_2^{\min}), but the ensemble grows exponentially as new electrons keep being generated from the ionisation collisions on air molecules, including a fraction with energy larger than ϵ_2^{\min} . The production of secondaries with energies much larger than the ionisation threshold (a few kilo-electronvolts being a reasonable value), can be described using the Møller cross section, which is the exact solution for a free-free electron-electron interaction (LANDAU *et al.*, 2013):

$$\frac{d\sigma_M}{d\delta_2} = Z \frac{2\pi r_e^2}{\gamma_1^2 - 1} \left[\frac{(\gamma_1 - 1)^2 \gamma_1^2}{\delta_2^2 (\gamma_1 - 1 - \delta_2)^2} - \frac{2\gamma_1^2 + 2\gamma_1 - 1}{\delta_2 (\gamma_1 - 1 - \delta_2)} + 1 \right], \quad (4.1)$$

where Z is the number of electrons in the molecule, the index $i = 1$ indicates the primary electron, $i = 2$ the secondary, γ_i is the Lorentz factor, $\delta_i = \gamma_i - 1 = \epsilon_i / (m_e c^2)$ is the kinetic energy divided by the electron rest energy (with rest mass m_e) and $r_e = \frac{1}{4\pi\epsilon_0} \frac{e^2}{m_e c^2} \approx 2.8 \times 10^{-15}$ m is the classical electron radius. In the case $\delta_2 \ll \gamma_1 - 1$ and $\delta_2 \ll 1$, we observe that the term $\propto 1/\delta_2^2$ is dominating. Thus, we can write equation 4.1 as:

$$\frac{d\sigma_M}{d\delta_2} \approx Z \frac{2\pi r_e^2}{\beta_1^2} \frac{1}{\delta_2^2}, \quad (4.2)$$

with $\beta_1 = v_1/c$ the velocity of the primary particle. Integrating equation (4.2) from δ_2 to the maximum energy ($\epsilon_1/2$) yields a production rate

$$\sigma_{\text{prod}} \approx Z \frac{2\pi r_e^2}{\beta_1^2} \frac{1}{\delta_2} \propto \frac{1}{\epsilon_2}, \quad (4.3)$$

using again $\epsilon_2 \ll \epsilon_1$. The remaining sensitivity of σ_{prod} in units of area to the primary particle is given by the factor β_1^2 which converges strongly to 1 as the mean energy of the primary electrons exceeds 1 MeV. In other words, as the mean energy of the electrons grows towards even more relativistic energies, the production rate σ_{prod} becomes independent of the energy spectrum.

For illustrative purposes, we now consider the one dimensional deterministic case, which results in an analytical solution of the electron energy spectrum. We make the system deterministic by assuming that the differential cross section is a delta-function at ϵ_2^{min} (the minimum energy at which a secondary electron can runaway) and use $\Lambda_{\text{prod}} = \frac{1}{N\sigma_{\text{prod}}}$ as the constant collision length, with N the air number density. In other words, every length Λ_{prod} a secondary electron of energy ϵ_2^{min} is produced. The derivation below is close to what was presented by Celestin and Pasko (2010), Dwyer *et al.* (2012), Skeltved *et al.* (2014) and references therein.

Consider a population of electrons in one dimension with space-coordinate z , a homogeneous and constant electric field E above the RREA threshold and a friction force $F(\epsilon)$. The minimum energy ϵ_2^{min} at which an electron can runaway is given by the requirement $F(\epsilon_2^{\text{min}}) \approx qE$ (where q is the elementary charge), that is to say $\epsilon_2^{\text{min}} = \text{function}(F, E)$ is constant. Assuming that the mean energy of the ensemble is relativistic results in a constant production rate $\Lambda_{\text{prod}} = \Lambda_{\text{prod}}(\epsilon_{\text{min}})$. Thus, in space, the distribution f_e grows exponentially as,

$$\frac{\partial f_e}{\partial z} = \frac{1}{\Lambda_{\text{prod}}} f_e. \quad (4.4)$$

While in energy, the differential equation is given by the net force,

$$\frac{d\epsilon}{dz} = qE - F(\epsilon). \quad (4.5)$$

Solving for steady state means,

$$\frac{df_e}{dz} = \frac{\partial f_e}{\partial z} + \frac{\partial f_e}{\partial \epsilon} \frac{d\epsilon}{dz} = 0, \quad (4.6)$$

and using equation 4.4 and 4.5 results in,

$$\frac{\partial f_e}{\partial \epsilon} = -\frac{1}{\Lambda_{\text{prod}}(qE - F(\epsilon))} f_e. \quad (4.7)$$

For the largest part of the energy spectrum, specifically above 0.511 MeV and below 100 MeV, $F(\epsilon)$ is not sensitive to ϵ (e.g. see Rutjes *et al.*, 2016). Only at around $\epsilon \approx 100$ MeV electron energy $F(\epsilon)$ starts increasing again because of the bremsstrahlung process. Thus, one may assume

$F(\epsilon) \approx F$ constant, which yields that the RREA energy spectrum $f(\epsilon)$ at steady state is given by,

$$f_e(\epsilon) = \frac{1}{\bar{\epsilon}} \exp\left(-\frac{\epsilon}{\bar{\epsilon}}\right), \quad (4.8)$$

with the exponential shape parameter and approximated average energy $\bar{\epsilon}(E)$ given by,

$$\bar{\epsilon}(E) = \Lambda_{\text{prod}}(qE - F). \quad (4.9)$$

Equivalently, in terms of collision frequency $\nu_{\text{prod}} = \frac{\beta c}{\Lambda_{\text{prod}}}$, equation 4.9 can be written as,

$$\bar{\epsilon}(E) = \frac{\beta c}{\nu_{\text{prod}}}(qE - F), \quad (4.10)$$

with β the velocity v/c of the RREA avalanche front. For the 1-d case there is no momentum-loss or diffusion, so $\beta \approx 1$. Note that Λ_{prod} depends on ϵ_2^{min} (the minimum energy at which a secondary electron can runaway), which depends on the electric field E as that determines the minimum electron energy that can go into runaway. In this analysis, we illustrate with equations 4.8 and 4.9, that the full RREA characteristics, such as the mean energy $\bar{\epsilon}$ or the collision length Λ_{prod} (directly related to the avalanche length scale λ discussed in section 4.12.1) are driven by processes determining ϵ_2^{min} .

In reality there are important differences compared to the one dimensional deterministic case described previously, which we propose to discuss qualitatively for understanding the Monte Carlo simulations evaluated in this study. During collisions, electrons deviate from the path parallel to E . Therefore in general, electrons experience a reduced net electric field as the cosine function of the opening angle θ , which reduces the net force to $qE \cos(\theta) - F$ and thereby the mean energy $\bar{\epsilon}$ of equation 4.9. In reality the 3D scattering (with angle parameter θ) changes of the path of the particle. Although the velocity remains still close to c (as the mean energy is still larger than several MeV), the RREA front velocity parallel to the electric field (\mathbf{E}) is reduced again because of the opening angle as function of its cosine:

$$\beta_{\parallel} = \beta \cos(\theta), \quad (4.11)$$

which also reduces the mean energy $\bar{\epsilon}$. Note that θ is not a constant and may change with each collision. Equivalently the avalanche scale length Λ_{prod} in 3-D changes to $\approx \Lambda_{\text{prod}} \times \cos(\theta)$. However, most importantly, the momentum-loss of the lower energetic electrons results in a significant increase of ϵ_2^{min} , as it is much harder for electrons to runaway. The increase of ϵ_2^{min} significantly increases Λ_{prod} and thereby increases the characteristic mean energy $\bar{\epsilon}$. On the other hand, the stochasticity creates an interval of possible energies ϵ_2^{min} that can runaway with a certain probability and for thin targets a straggling effect (RUTJES *et al.*, 2016). A recent article discussed the influence of the angular scattering of electrons on the runaway threshold in air (CHANRION *et al.*, 2016).

The effects discussed above prevent a straight forward analytical derivation of the RREA char-

acteristics in 3 dimensions, but what remains is the important notion that the physics is completely driven by the intermediate energy electron production. "Intermediate" means they are far above ionisation threshold ($\gg 123$ eV) but much below relativistic energies ($\ll 1$ MeV). The parametrisation of the electron energy spectrum, given by equation 4.9 turns out to be an accurate empirical fit, as it was already shown in Celestin and Pasko (2010), Dwyer *et al.* (2012), Skeltved *et al.* (2014) and references therein. Nevertheless in these works $\lambda^{\min}(E)$, or equivalently the velocity over collision frequency $\beta c/\nu_{\text{prod}}$, is fitted by numerical Monte Carlo studies and the final direct relation to ϵ_2^{\min} is not executed. Celestin *et al.* (2010) calculated that $\nu^{\text{prod}}(E) \propto E$, thus explains why $\bar{\epsilon}(E)$ must saturate to constant value. Celestin *et al.* (2010) argue that $\epsilon_2^{\min}(E)$ is given by the deterministic friction curve F , for which they use the Bethe's formula and an integration of a more sophisticated electron impact ionisation cross section (RBEB) including molecular effects, but that is only true in one dimension without stochastic fluctuations. Other attempts to simulate RREA by solving the kinetic equation instead of using Monte-Carlo methods are presented in Roussel *et al.* (1994), Gurevich *et al.* (1998), Babich *et al.* (2001) and references therein. An analytical approach is provided by Cramer *et al.* (2014).

4.2 FIELD-FREE COMPARISON

To model particle beams in air far from the source, some researchers use general purpose Monte Carlo (MC) codes developed by large collaborations like geant4 (used by CARLSON *et al.* (2011) and by SKELTVED *et al.* (2014)) or FLUKA (used by DUBINOVA *et al.* (2015)). On the other hand, to model, e.g., the radiation sources with their external or even self-consistent time dependent electric fields, other researchers develop custom made codes in small groups or as individuals, where the cross sections and numerical methods may come from already validated theory (e.g. SARRIA *et al.*, 2015), or include new physical insights (e.g. KOHN *et al.*, 2014).

While they are necessary for the understanding of the full physical phenomena, custom made codes are difficult to validate, especially if they are not made available by open access. Differences between one code and another may be explained by at least the following four factors:

- The choice of the included physics, as a compromise between correctness and feasibility.
- Cross sections, that can come from theory, measurements or both. In most cases the cross section data has a certain uncertainty.
- Numerical and coded implementation, e.g. numerical integrations, interpolations, roundoff errors and bugs.
- The performance, as faster codes can run more particles in the same time, which results in more accurate statistics.

Even if it is possible in principle to determine the differences between the physical models and between the numerical methods, it may be very complicated (if not impossible)

- to estimate the uncertainties associated with a certain choice of physical models,
- to estimate the uncertainty propagation and accumulation of all input through the full multiscale models, and
- to review all source codes (if available) to find any mistakes and possible numerical problems.

Therefore, we here strive to provide a comparison standard for the particle codes, as simple and as informative as possible, by only considering their physical outputs. We have chosen standard tests for the core parts of all codes: the evolution of monoenergetic and monodirectional beams of photons, electrons and positrons through homogeneous air and without electric or magnetic fields. We elaborate our standard tests in the methodology section 4.5.

The targeted energy interval for high energy atmospheric physics in this study is from tens of keV to tens of MeV, bounded above by the expected maximal energy in a TGF [REF]. The low energy cut-off is chosen for two reasons:

1. The codes developed for accelerator or cosmic-ray applications use typical energies well above 1 MeV, larger than the rest mass of electrons and positrons. For these energies relativistic approximations are accurate, ionization potentials are negligible, and electron impact ionization is essentially a free-free elastic collision (i.e., similar to a collision of two free electrons). These approximations limit the validity of the codes at lower energies.
2. The mean free path of particles decreases and the number of particles increases with decreasing energy. Simulating with or without a low energy cut-off can make a difference of minutes to months of simulation time. Therefore a low energy cut-off is wanted for computational reasons.

The different implementations of the low energy cut-off, as reviewed in Sect. 4.4 cause significant differences in the results, see Sect. 4.6. These differences increase when electric fields are added, see Sect. 4.7.

This comparison is organized as follows: Sects. 4.3 and 4.4 review the particle interactions and the codes included in this study. Sect. 4.5 describes the methodology we used to compare the codes. Sect. 4.6 contains a discussion of important differences between the results of the tested codes, and in Sect. 4.7 the implications of adding electric fields are discussed. Finally we conclude and give a list of recommendations for High Energy Atmospheric Physics simulations in Sect. 4.7.

4.3 OVERVIEW OF INTERACTIONS AND APPROXIMATIONS

In High Energy Atmospheric Physics (HEAP) it is usually assumed that the density of the considered high energy particles is too low to directly interact with each other, therefore they

only interact with the background medium which here are the air molecules. In addition for some ‘self-consistent’ codes, like GRRR (see Sect. 4.4.1), charged particles can interact non-locally due to the electric fields they produce. But for the present study these interactions are turned off, resulting in a linear problem. This means that the number of particles at the end of the beam is proportional to the particle number in the initial beam, and that different beams simply add up according to the superposition principle. Below we summarize the interactions considered for electrons, positrons and photons in HEAP. In these interactions the target molecule M and its resulting state are explicitly given, but for the MC model of the high energy particles, these molecules (or ions) act as a random background.

4.3.1 Electrons and positrons

Electrons and positrons above 50 keV (which is the low energy cut-off in our study) behave almost identically; they scatter elastically on molecules M , they ionize them, and they create bremsstrahlung on collisions with molecules:

$$e^{\pm} + M \rightarrow \begin{cases} e^{\pm} + M, & \text{elastic (Rutherford),} \\ e^{\pm} + e^{-} + M^{+}, & \text{ionization,} \\ e^{\pm} + \gamma + M, & \text{bremsstrahlung,} \end{cases} \quad (4.12)$$

with cross sections that only slightly dependent on the incoming particle type.

In addition, when positrons come to rest, they annihilate,

$$e^{+} + M \rightarrow 2\gamma + M^{+}, \quad \text{annihilation,} \quad (4.13)$$

and produce two photons of 511 keV. The standard implementation is that, when a positron drops below the low energy cut-off, it comes at rest immediately (in space and time). In reality the positron will come to rest over some distance and time, forming positronium (e.g. an $e^{-}e^{+}$ particle), before annihilation. The positronium has a lifetime depending on the spins of the positron and electron (KARSHENBOIM *et al.*, 2004), forming a singlet or triplet state with lifetimes of 124 ps or 139 ns, respectively.

In the eV regime, the interactions are getting more complex, as molecular excitations and dissociations need to be taken into account explicitly.

4.3.2 Friction (or stopping-power) for electrons and positrons

Usually, the energy transfer in an ionization collision of electrons and positrons with molecules is of the order of 10 eV, hence it causes only a small energy loss for a particle with energy above the keV range. By introducing a so-called low energy cut-off ε_{cut} , ‘high’ and ‘low’ energy particles and interactions can be decoupled. In this approximation, interactions producing secondary

particles below the low energy cut-off are approximated with a friction, while interactions with secondary particles above the cut-off are included explicitly.

Let ε_1 be the energy of the primary particle and ε_2 the energy of the secondary particle. The cross section $\sigma_k(\varepsilon_1)$ (in units of area) gives the probability of the primary particle to undergo an interaction labeled k . The differential cross section $d\sigma_k(\varepsilon_1, \varepsilon_2)/d\varepsilon_2$ (in units of area per energy) gives the probability of a primary particle to produce a secondary particle within the infinitesimal energy interval $[\varepsilon_2, \varepsilon_2 + d\varepsilon_2]$ for the interaction k .

The secondary energy ε_2 can take values between the minimum ε_{\min} (of the order of eV and the primary is not sensitive for the precise value) and the maximum ε_{\max} (of the order ε_1), depending on the interaction. For ionization $\varepsilon_{\max} = \varepsilon_1/2$ as the primary by convention is defined to be the final particle with the highest energy. For bremsstrahlung we have $\varepsilon_{\max} = \varepsilon_1$.

Now the energy range of the secondary particles is decomposed into two parts: the first part from ε_{\min} to ε_{cut} is implemented as a friction, and the second part from ε_{cut} to ε_{\max} is implemented by discrete collisions.

The friction F_k of interaction k is defined as

$$F_k(\varepsilon_{\text{cut}}, \varepsilon_1) = N \int_{\varepsilon_{\min}}^{\varepsilon_{\text{cut}}} \left(\varepsilon_{\text{loss}}(\varepsilon_2) \frac{d\sigma_k(\varepsilon_1, \varepsilon_2)}{d\varepsilon_2} \right) d\varepsilon_2, \quad (4.14)$$

where N is the number density of molecular collisions targets M , and $\varepsilon_{\text{loss}}$ the energy loss of the primary which is of the order of ε_2 plus the ionization energy. The total friction on the primary is given by the sum of all considered interactions,

$$F_{\text{tot}}(\varepsilon_{\text{cut}}, \varepsilon_1) = \sum_k F_k(\varepsilon_{\text{cut}}, \varepsilon_1). \quad (4.15)$$

For electrons and positrons in the energy regime important for HEAP, the total friction is almost completely determined by the ionization part, as illustrated in Fig. 4.1. Especially if only the friction below the low energy cut-off is considered (solid line), there the energy loss due to bremsstrahlung is more than two orders smaller than the energy loss due to ionization.

We remark that the friction is also frequently called the stopping-power for historical reasons, though it has the dimension of friction (energy/length) rather than of power (energy/time).

4.3.3 Straggling

In a simple implementation of the low energy cut-off, the primary particle suffers a uniform (and deterministic) friction $F_{\text{tot}}(\varepsilon_{\text{cut}}, \varepsilon_1)$, as given in Eq. (4.15). This means that now only the energy of the primary particle is altered, but not its direction. A greater concern is that the accuracy of the assumed uniform energy loss is a matter of length scale. If the scale is much smaller than $\varepsilon_1/F(\varepsilon_{\text{cut}}, \varepsilon_1)$, only a few interactions have taken place. On such a small length scale the real energy loss distribution (if one had considered all interactions explicitly) among the

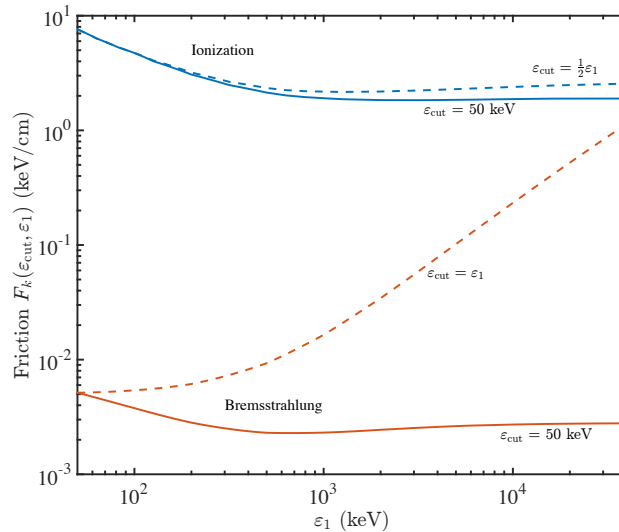


Figure 4.1: Friction $F_k(\varepsilon_{\text{cut}}, \varepsilon_1)$ for electrons per interaction (Bremsstrahlung in red and ionization in blue), for two different low energy cut-offs, $\varepsilon_{\text{cut}} = 50$ keV (solid line) and $\varepsilon_{\text{cut}} = \varepsilon_{\text{max}}$ (dashed line). The total friction is the sum of the two contributions, which in the energy regime of HEAP the total is dominated by the ionization (please, note the log-scale). The data are from Cullen *et al.* (1997) and Perkins *et al.* (1991) for an air density of 1.293×10^{-3} g cm^{-3} corresponding to 1 bar and 273 K as used in this study.

population would have a large spread. This effect is called straggling, and it was first studied by Bethe and Heitler (1934).

One way to mimic the real energy distribution is by implementing a stochastic friction, as is done in FLUKA and geant4L. Basically the energy loss of the primary particle is as if it would be modeled by real low energy collisions below the cut-off, but without creating the secondary particles and without altering the direction of the momentum. The different implementation of the low energy cut-off (i.e., different implementations of the friction) is one of the significant differences we see in the studied programs, as discussed in the results section 4.6.

4.3.4 Continuous Slowing Down Approximation

Using the friction equation (4.14) over the whole range of secondary particle energies, hence with $\varepsilon_{\text{cut}} = \varepsilon_{\text{max}}$, the expectation value of the maximal penetration depth of a primary particle into a medium can be calculated in the so-called the Continuous Slowing Down Approximation (CSDA). Integrating the friction over distance ℓ up to the point where the particle has lost all its primary energy ε_1 ,

$$\int_{\ell(\varepsilon_1)}^{\ell(0)} F_{\text{tot}}(\varepsilon_{\text{max}}, \varepsilon(\ell)) d\ell = \int_{\varepsilon_1}^0 F_{\text{tot}}(\varepsilon_{\text{max}}, \varepsilon) \frac{d\ell}{d\varepsilon} d\varepsilon = \varepsilon_1, \quad (4.16)$$

defines one CSDA range through

$$\text{CSDA}(\varepsilon_1) = \ell(\varepsilon_1) - \ell(0). \quad (4.17)$$

One CSDA range is thus the maximal length that primaries can penetrate into a material. Due to feedback from secondaries (e.g. electron \rightarrow photon \rightarrow electron) the complete avalanche can survive longer. As we describe in the methodology section 4.5, we choose half a CSDA range as the optimal detector distance to compare the differences in outputs of the codes as comprehensively as possible.

4.3.5 Photon interactions

The typical photon interactions are

$$\gamma + M \rightarrow \begin{cases} \gamma + M, & \text{elastic (Rayleigh),} \\ e^- + M^+, & \text{ionization (by absorption),} \\ \gamma + e^- + M^+, & \text{ionization (by Compton),} \\ e^+ + e^- + M, & \text{pair production.} \end{cases} \quad (4.18)$$

Photons have no charge, and therefore they lose energy much less gradually than electrons and positrons. In a typical inelastic interaction of a photon, the energy loss is significant.

4.3.6 Photon attenuation

The most important interaction for low energies (below 30 keV) is photo-absorption, and for the highest energies (above 40 MeV) it is pair production; in both cases the photon completely disappears. Inbetween, where Compton scattering is most important, the energy loss per interaction is still significant; the expectation value for the energy loss of the primary photon grows from 5% (at 30 keV) to above 90% (at 1 MeV). The Continuous Slowing Down Approximation is thus not appropriate for photons, as photons do not continuously lose small amounts of energy, in contrast to electrons and positrons, but they lose a substantial fraction of their energy after some free path. Consecutively, for most energies (certainly above 1 MeV and below 30 keV) the photon intensity I can be approximated by an exponential decay or attenuation,

$$I(\ell) = I(0) \exp(-\ell/\mu), \quad (4.19)$$

where $\mu(\varepsilon)$ is the attenuation-coefficient depending on energy (and material).

In this work we need to estimate an appropriate detector distance (the exponential decay does not appear explicitly in any model), and we use two e-folding lengths (i.e., the inverse of half the attenuation-coefficient) as the optimal detector distance to compare the output differences, as described further in the methodology section 4.5.

Table 4.1: Summary of the performance (completion time). Method explained in Sect. 4.5.3. N_{user} is the normalization factor used to multiply simulation time (on the specific architecture).

Code	GEANT4D	GEANT4L	MC-PEPTITA	EGS5	FLUKA	GRRR dt = 25 ps	GRRR dt = 2.5 ps
CPU	Q9650 3.0 GHz			Xeon E-3 1271 3.6 GHz		Xeon X7350 2.9 GHz	
N_{user}	1			1.95		0.85	
Time (s)	206	241	21 040	829	213	2 564	29 283

4.4 OVERVIEW OF CODES

In Table 4.1 we have summarized the codes used in this benchmark. In this chapter we give more detailed descriptions.

4.4.1 EGS5

EGS5 (Electron-Gamma Shower version 5, developed by Hirayama *et al.* (2005)) is a general purpose software package for the Monte Carlo simulation of the coupled transport of electrons, positrons and photons in an arbitrary geometry. It is the next version after EGS4 that was released by Nelson *et al.* (1985) with a history that dates back to 1960's. The user controls an EGS5 simulation by means of an input text file for settings and a written FORTRAN user code, to which the rest of the FORTRAN source files are appended and compiled as one. In the user code several subroutine calls create, establish and initiate the cascade. Two important subroutines HOWFAR & AUSBGAB, which should be written inside the user-code are to specify the geometry and the output of the results. EGS5 can simulate particles from a few keV up to several hundred GeV, depending on the material. There is a limited option for including magnetic fields, and no option to include electric fields. All interactions of equations (4.12), (4.13), and (4.18) are implemented, in this work with a low energy cut-off of 50 keV. In the user manual of Hirayama *et al.* (2005) a minimum low energy cut-off of 10 keV is advised, but we noticed that for the bremsstrahlung cross sections relativistic limits are applied, which results in a too low production of photons, see Sect. 4.6.3. Friction is implemented uniformly, without straggling effect (that is to say without fluctuations in the energy loss). The input file and user code, used in this work, can be found in the paper supplementary material (available at: <https://www.geosci-model-dev.net/9/3961/2016/>). Please see the documentation of Hirayama *et al.* (2005) for a detailed overview of the implemented physics.

FLUKA

FLUKA (developed by Ferrari *et al.* (2005), copyright to INFN and CERN 1989-2011), is a general purpose tool for calculations of particle transport and interactions with matter. FLUKA is able to simulate the interaction and propagation in matter of roughly 60 different particles, including photons from 100 eV and electrons and positrons from 1 keV to thousands of TeV, neutrinos,

muons of any energy, hadrons of energies up to 20 TeV (up to 10 PeV by linking FLUKA with the DPMJET code) and all the corresponding antiparticles, and neutrons down to thermal energies. FLUKA includes recent datasets, published by Bohlen *et al.* (2014). The program can handle magnetic and electric fields, although not self-consistently (i.e., the charged particles do not produce magnetic or electric fields). The program, written in FORTRAN, reads in so called user-cards, in which the user defines the geometry, materials and detectors. The user card, used in this work, can be found in the paper supplementary material (available at: <https://www.geosci-model-dev.net/9/3961/2016/>). All interactions of equations (4.12), (4.13), and (4.18) are implemented, in this work with a low energy cut-off of 50 keV. Friction in FLUKA is modeled with universal fluctuations, mimicking the straggling effect, meaning that the primary particle loses its energy as if it would undergo random collisions. But the direction of its momentum is not changed and no secondary particles are produced. Please see the documentation ‘FLUKA Manual’ at www.fluka.org for a detailed overview of the implemented physics.

GEANT4

GEometry ANd Tracking 4 (geant4) is an open source toolkit to simulate the passage of particles through matter, developed by a wide international collaboration lead by the CERN. It is coded in C++, following an object oriented philosophy. It can simulate the transport of almost all known particles, and can include electric and magnetic fields. We use the version 10.2 released in December 2015. In geant4, the user can choose between six main models for the treatment of electrons, positrons and photons, with different performances and accuracies. One can also specify the implementation of the friction, to take into account energy losses below the low energy cut-off. For this study we are using two geant4 configurations, that are detailed below. All geant4 codes are available in the paper supplementary material (available at: <https://www.geosci-model-dev.net/9/3961/2016/>). References and details for these models are presented in the ‘geant4 Physics reference manual’ available at <http://geant4.web.cern.ch>.

geant4D

geant4D uses the default model, but in addition we deactivated the fluctuations of the continuous energy loss, i.e. the energy losses are applied uniformly, without straggling effect. This choice is for benchmark purposes, to identify the effect of straggling.

geant4L

geant4L uses the Livermore model, which uses cross sections from the EPDL and EEDL databases, provided by the Lawrence Livermore National Laboratory. The detailed implementation is provided in Cullen *et al.* (1997) and Perkins *et al.* (1991). The ‘Universal fluctuation model’ is activated to include the straggling effect in the implementation of friction.

The GRanada Relativistic Runaway (GRRR) code

Developed by A. Luque at the Astrophysics Institute of Andalusia (IAA-CSIC), the GRanada Relativistic Runaway (GRRR) code was designed to investigate the self-consistent interaction between electrons in the limit of very intense Relativistic Runaway Electron Avalanches (RREA). This investigation, presented in Luque *et al.* (2014), concluded that due to the interaction between electrons in the avalanche RREAs saturate into a steady-state propagating Relativistic Runaway Ionization Front (RRIF). As the GRRR code was implemented with that specific goal in mind, its scope is narrower than the general purpose codes (EGS5, FLUKA, geant4) analyzed in this paper. It only follows the evolution of high-energy electrons, and includes a limited set of interactions between these electrons and the embedding medium. Electron ionization and Rutherford scattering are modeled discretely, and in this work down to a low energy cut-off of 50 keV. The friction for these interactions is uniform, without straggling effect. Bremsstrahlung collisions with nuclei are modeled deterministically by friction, in other words: as continuous radiative losses. The Supplemental Material of Luque *et al.* (2014) contains further details about the physical model underlying the GRRR code. The full source code for GRRR is available at <https://github.com/aluque/grrr>. However, presently the code is mostly undocumented so we advise potential users to contact the author.

MC-PEPTITA

The Monte Carlo model for Photon, Electron and Positron Tracking In Terrestrial Atmosphere (MC-PEPTITA) by Sarria *et al.* (2015) is a Fortran 90 code that simulates the propagations of TGF and associated electron/positron beams within the Earth environment, from the production altitude at 10 to 20 km to satellite altitude. To simulate the quasi-exponential atmospheric density profile and the Earth's magnetic field, it uses the NRLMSISE-00 and IGRF-11 models (CULLEN *et al.* (1997) AND PERKINS *et al.* (1991)). It is optimized to run in this environment, whereas some other codes (e.g., geant4) can only handle layers of constant density. Concerning the interactions between particles and matter, it mainly uses the EPDL and EEDL cross section sets (CULLEN *et al.* (1997) AND PERKINS *et al.* (1991)), except for inelastic scattering of electrons and positrons where the GOS model is used. The interactions are simulated similarly to PENELOPE (SALVAT *et al.*, 2011), with equivalent numerical methods. MC-PEPTITA does not include any continuous energy losses: the particles are followed discretely down to the lowest possible energies allowed by the models used, with exception of bremsstrahlung where the minimal energy is set to 100 eV.

4.5 FIELD FREE COMPARISON SET UP

We focus on the evolution of monoenergetic and directed beams of electrons, positrons and photons with kinetic energies between 100 keV and 40 MeV through homogeneous air in the

absence of electric and magnetic fields, using with a low energy cut-off of 50 keV. Assuming sufficiently low densities of high energy particles, arbitrary particle beams can be decomposed into such monoenergetic and directed beams.

The electron, positron and photon beams propagate through air, consisting of 78.085% nitrogen, 20.95% oxygen and 0.965% argon. We use a constant and homogenous air density of $1.293 \times 10^{-3} \text{ g cm}^{-3}$ which corresponds to 1 bar and 0 degree Celsius. For all programs we choose a low energy cut-off of 50 keV, below which all particles are removed. For most programs, this low energy cut-off is also the threshold to treat collisions discretely or continuously, with two exceptions: MC-PEPTITA handles all collisions explicitly, and GRRR uses continuous radiative loss (bremsstrahlung). During the simulation electrons, positrons or photons above the low energy cut-off can be created (except for GRRR, which only models electrons), and are then followed as well until they also drop below the low energy cut-off. If considered in the program, positrons dropping below the low energy cut-off can produce photons by annihilation above the low energy cut-off.

We use flat detectors, perpendicular to the primary particle beam. On a detector, the type, kinetic energy, position and arrival time of the arriving particles are recorded. After detection, the particles are removed from the program, thus we do not measure backscattered particles that have already been detected. Depending on the program, other secondary particles are created with a very low probability (e.g. neutrons by photo-nuclear interactions), but we do not record them in the output. First, we study the particle number of all particles as function of propagation distance (attenuation). Second, for one specific distance, (depending on particle type and initial energy) we proceed to a detailed analysis of energetic, spatial and temporal distribution. Complementarily we also benchmark the performance (i.e., the simulation completion time) of the programs used in this study.

4.5.1 The number of particles versus distance (attenuation)

We study the particle number of all particles as a function of beam propagation distance, up to of one CSDA range for electrons and positrons and of four times the inverse of the attenuation coefficient (four e-folding lengths) for photons. This range is divided in several distances (roughly 20) or data points. For each distance (or data point), we perform a new simulation. Each simulation with ten thousand particles in the initial beam, for beams of electrons, positrons and photons with energies of 0.1, 0.4, 1, 10 and 40 MeV. The particle numbers are therefore derived under the assumption that the detectors are impenetrable. This means that back scattering is excluded, and that the particle number therefore is lower than in a passing avalanche in air only.

We added a $\pm 1/\sqrt{n_i}$ relative error expected from the Monte Carlo methods (n_i being the number of counts in the i th bin). In this way we performed roughly 1800 simulations, namely circa 300 simulations per program: for 3 particle types, 5 initial energies and on average 20 distances per beam. GRRR only considers electrons while the energy loss due to production of photons is implemented as a continuous energy loss. The relevant results are given and discussed

in Sect. 4.6. In addition all data of this part are visualized and available in the paper supplementary material (available at: <https://www.geosci-model-dev.net/9/3961/2016/>).

4.5.2 Spectral analysis

We performed detailed simulations with 1 million particles per beam for one specific distance per beam. For electrons and positrons, the detection distance was chosen as half of the CSDA range. This gives most information in one plot, since the primary particles are still alive, while there is a significant number of secondary particles produced. For photons, the inverse of half the attenuation coefficient (two e-folding lengths) is chosen as the distance for the detailed study. At the detector we analyze the kinetic energy, the radial distance from the symmetry axis and the time of arrival. The spectra are binned using the Freedman–Diaconis rule in the log-domain and rescaled to numbers per primary. As also for the attenuation study, we added a $\pm 1/\sqrt{n_i}$ relative error expected from the Monte Carlo methods (n_i being the number of counts in the i th bin). We performed roughly 90 different simulations (circa 15 simulations per program: 3 particles and 5 initial energies). The relevant results are given and discussed in Sect. 4.6. In addition all data of this part are visualized and available in the paper supplementary material (available at: <https://www.geosci-model-dev.net/9/3961/2016/>).

4.5.3 Performance benchmark

As a complement, we also provide a test how much time codes need to complete the simulations. We do not pretend to do an in-depth performance benchmark of the codes, but we think this is an interesting piece of information for someone who is seeking for a code to be used in the HEAP context. Since the programs are written in different languages (Fortran, C++ and Python) and may be run on different machines with different architectures, we normalized the completion time with respect to a reference computer configuration.

As a reference, we calculate the normalization factor, using the c++ code ‘pidec.cpp’, written by Xavier Gourdon, and provided in the auxiliary material. It computes 8 digits of pi after a given digit position called n . It should be compiled using the GNU g++ compiler with no options, in particular no optimization options (eg ‘-O3’). The time taken to complete it with $n = 1000000$ (usually about 10-20 minutes). The code itself outputs it in the terminal, and it is equivalent to the ‘user time’ given by the ‘time’ bash command.

The simulation starting with one million 1 MeV electrons is used as the test case because it is feasible for all the evaluated codes, and as it takes a completion time that is neither too short, nor too long. If the considered code is parallelized, it should run on one single thread, but any compilation options can be used to make it as fast as possible. In any case, one should make several runs and get an average time to minimize the estimation error. The normalized results are discussed in Sect. 4.6. Further details of this benchmark can be found in the paper supplementary material (available at: <https://www.geosci-model-dev.net/9/3961/2016/>).

4.6 RESULTS

Most tests show similar outputs for the different codes, to within deviations of $\pm 10\%$, see the paper supplementary material (available at: <https://www.geosci-model-dev.net/9/3961/2016/>). Here we focus on important differences among the results of the codes, and we provide several plausible explanations.

4.6.1 Straggling

For electrons and positrons below 1 MeV, the data clearly show the effect of straggling, as discussed in Sect. 4.3.2). For example in the 400 keV electrons beam shown in Fig. 4.2, EGS5, geant4D and GRRR do not include straggling, therefore the maximal electron energy is too small and the drop of the energy spectrum towards this maximal energy too steep. geant4L, MCPEP and FLUKA show the correct spectrum, but for different reasons. MCPEP simulates without a low energy cut-off (and thus without friction). geant4L and FLUKA use a stochastic implementation of the friction called universal fluctuations. Basically the friction is not applied uniformly to all particles of the same energy equally, but a distribution of energy losses in time mimics the random nature of the collisions. Only the direction change is considered negligible.

The same effect is also seen for electron and positron beams with energy above 10 MeV, in the scenario where bremsstrahlung is treated as continuous. GRRR shows an unphysical drop in the electron spectrum at high energies, as illustrated in Fig. 4.3. The reason is that the energy loss by bremsstrahlung is mostly above the low energy cut-off, see Fig. 4.1, meaning that the energy loss of the electrons and positrons is mostly due to discrete ‘hard’ collisions and thus ill-approximated by uniform averaged friction. Nevertheless we found that the total integrated energy is similar. This approximation is also used by others in the community like Celestin *et al.* (2012) and Chanrion *et al.* (2014).

4.6.2 Opening angle

High energy photons penetrate the medium much deeper than electrons and positrons, and therefore small differences in opening angles after collisions are more important. In inelastic collisions photons always lose a significant amount of energy, as discussed in Sect. 4.3.5, and therefore they get a significant opening angle.

MCPEP simulates all collisions explicitly (others use a friction - which does not change the primary direction). The energy spectra agree between these codes, but Fig. 4.4 illustrates, that the radial and temporal spectra vary: MCPEP shows a wider photon beam and substantially later photon arrival times.

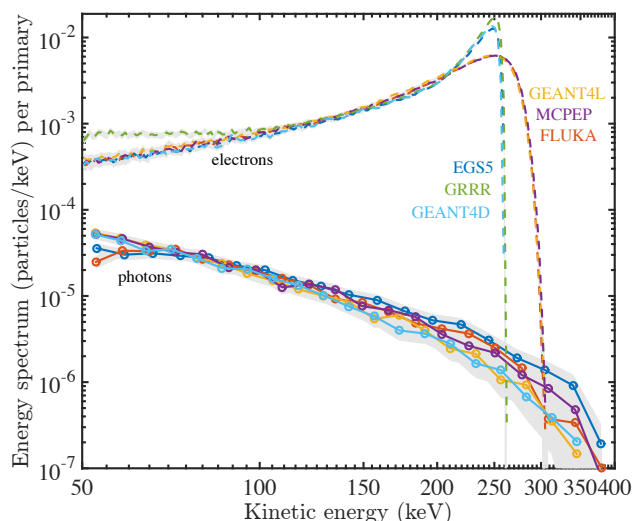


Figure 4.2: Products of a beam of 400 keV electrons after a propagation distance of 0.5 times their CSDA range which is 1.9 m in air at 1 bar and 273 K. The electrons have now a maximal energy of 250 to 300 keV depending on the code, and additional electrons and photons have been produced.

4.6.3 Bremsstrahlung

We saw that EGS5 uses an ultra-relativistic approximation in the treatment of bremsstrahlung and thereby we question the validity at lower energies, as discussed in Sect. 4.4.1). For the primary electron, in the energy regime important for HEAP, bremsstrahlung is negligible compared to ionization (see Fig. 4.1) and we thus do not see a difference there, but in the production of photons there is a significant difference, as can be seen in Fig. 4.5.

4.6.4 Other differences

Other differences we have found are listed below.

- For the electron and positron beams we see in the energy spectrum of FLUKA below 70 keV a dip in the number of photons. Fig. 4.3 shows an example.
- For the electron beams ≤ 1 MeV (but not in the positrons or photon beams) we see a difference in the longest arrival times (> 100 ns) for photons between the programs FLUKA and EGS5 compared to geant4D and geant4L. GRRR does not model photons, and MCPEP is completely different because of the opening angle, see Sect. 4.6.2.
- GRRR shows a slight higher count (less than 15% higher) than the other codes for the number of electrons in the avalanche as function of distance. Fig. 4.5 shows an example. In the energy spectrum we see that these electrons are in the low energy tail of the spectrum, see for example Fig. 4.2.
- For the electron and positron beams we see a difference in the shortest arrival times (< 1 ns) for electrons and positrons between the programs FLUKA, EGS5 and MCPEP compared to

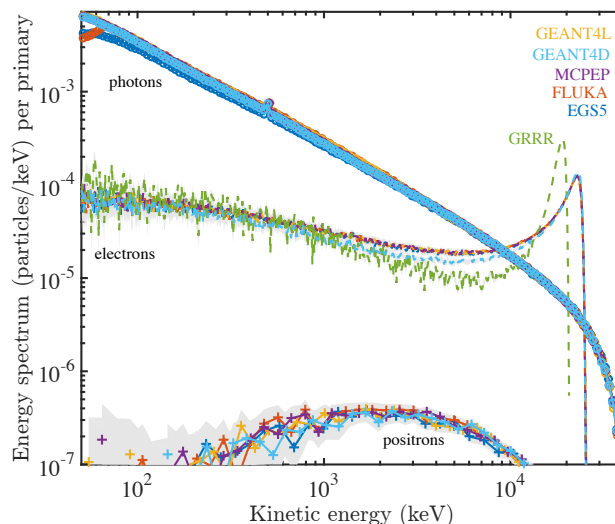


Figure 4.3: The same as in Fig. 4.2, but now for 40 MeV electrons. The propagation distance of 0.5 times their CSDA range is now 63.8 m. Now not only electrons and photons, but also positrons have been produced.

geant4D, geant4L and GRRR.

4.6.5 Performance

As said in the introduction the low energy cut-off is generally introduced to speed the simulation up. We therefore see a clear difference of completion time between MCPEP (simulations without low energy cut-off) and the rest, see Tab. 4.1. Also the choice to simulate all particles synchronously, to include self-consistent electric fields, slows the simulations significantly down, an example is GRRR.

The balance between performance and accuracy is important as for any Monte Carlo method the more simulations you do the better is the statistics. In a fixed amount of time the faster codes gain accuracy by simulating more particles.

4.7 THE EFFECT OF ELECTRIC FIELDS

In this study we have concentrated on the simplest case of particle beam evolution in air in the absence of electric fields, applicable to the wide distance from the particle source to detectors in space and on ground. However, as discussed in the introduction, the particles are initially accelerated by electric fields in the thunderstorm, either by weaker fields in larger regions in the Relativistic Feedback regime, or by strong and very localized self-consistent electric fields in the Cold Runaway regime. We here give a short outlook on the range of validity of the presented models in these cases. In general, it can be expected that electric fields will magnify all differences in choice and implementation of cross-sections to a certain extent, because particles not just lose energy and drop eventually below the energy cut-off, but charged particles can also be

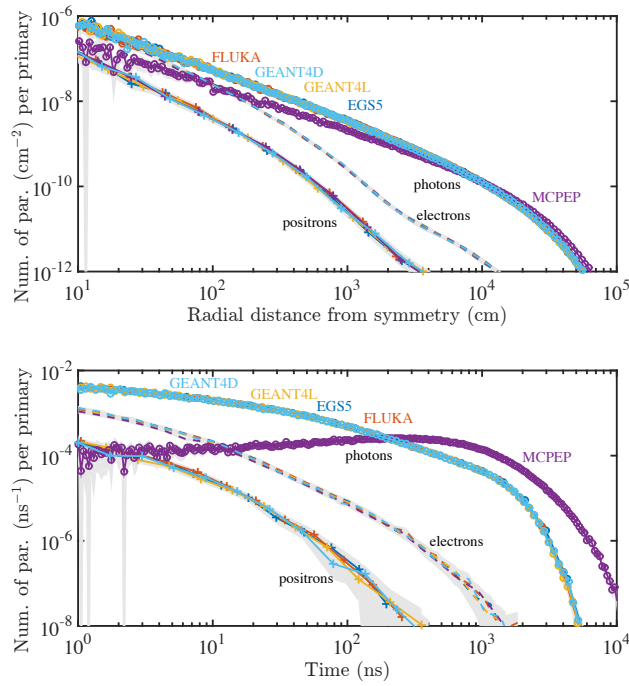


Figure 4.4: Products of a beam of 10 MeV photons at a distance of $1/(0.5 \mu)$ which corresponds to 756 m. Particle number per primary as a function of the radial distance from the symmetry axis (above), and of arrival time (below).

reaccelerated and reappear in the ensemble.

To be specific, we recall the definition of the three characteristic electric fields and electron energy regimes of the problem (giving field values for air at standard temperature and pressure (STP)). For electrons with energies in the eV regime, the classical breakdown field is $E_k \approx 32$ kV/cm. For higher fields electron avalanches are formed, but their energies typically do not exceed the range of several eV, as their friction increases with energy. The electron friction increases up to an electron energy of approximately 200 eV where the critical electric field $E_c \approx 260$ kV/cm is required to balance friction — as long as the approximation of the electron ensemble by classical friction is valid. For electron energies above 200 eV the friction decreases to a minimum that is balanced by an electric field of $E_b \approx 2.8$ kV/cm, called the break-even field, at an electron energy of about 1 MeV.

Clearly two limitations to using a particle model with a low energy cut-off are immediately visible. First, if the electric field is above the critical electric field of 260 kV/cm ($E > E_c$) in a sufficiently large volume, the two populations of electrons with energies below and above 200 eV are strongly coupled and essentially all electrons can be accelerated into the runaway regime, to 1 MeV and beyond. Second, if the electric field is below the critical field, but above the classical breakdown field ($E_k < E < E_c$), the population of electrons in the eV regime (the so-called thermal electrons) can grow strongly, and eventually ‘tunnel’ into the run-away regime; we will come back to this effect below.

On the other hand, for electric field strengths below the break-even field ($E < E_b$), all electrons, regardless of initial energy, will eventually stop as the friction force of air is stronger than

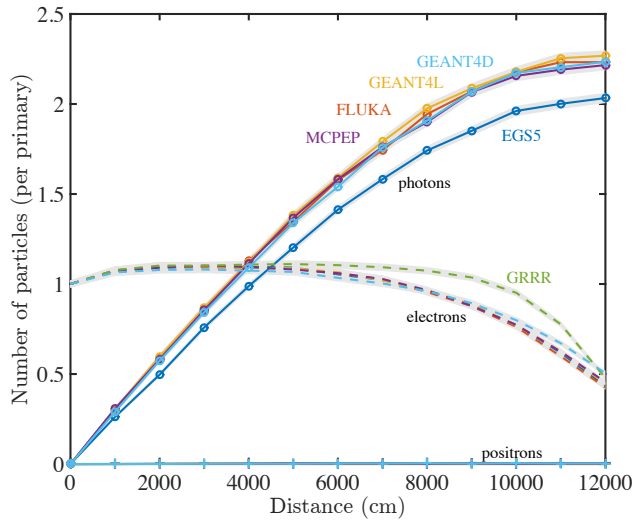


Figure 4.5: Products of a beam of 40 MeV electrons, as detected by 12 detectors at 10 to 120 m distance. The detectors are impenetrable to hinder backscattering; therefore a new simulation is run for every detector distance.

the accelerating force of the electric field.

Finally, when the electric field is above the break-even and below the classical breakdown field ($E_b < E < E_c$), the use of the energy cut-off of 50 keV (or even lower) can have strong implications: For an electron energy of 50 keV, friction and electric acceleration force balance each other when the field is 7.8 kV/cm. So in classical approximation one would estimate that at lower fields the inclusion of the cut-off is justified. However, this classical approximation neglects the stochastics of the actual process. Due to the randomness of free paths and scattering events, electrons actually can ‘tunnel’ into energy regimes that they could not reach in the classical approximation, an effect similar to the straggling effect discussed earlier.

Skeltved *et al.* (2014) have observed this effect: For all fields between 4 and 25 kV/cm, they found that energy spectrum and mean energy of runaway electrons depended on the low energy cut-off, even when it was chosen between 250 eV and 1 keV. They also found – not surprisingly – that the differences become most apparent when the electric field force approaches the friction force corresponding to the low energy cut-off.

A related observation was made by Li *et al.* (2009) when they found electron runaway from a negative streamer even though the maximal electric field at the leader tip was well below the critical field E_c .

Future studies on how to choose the low energy cut-off for given fields are desirable to optimize computations between efficiency and accuracy.

The goal of this work is to provide standard tests for comparing the core part of Monte Carlo simulations tools available for HEAP. We focused on the propagation of electrons, positrons and photons through air, in the absence of electric and magnetic fields. We compare the output at half the CSDA range for electrons and positrons, and at two e-folding lengths (the inverse of half the attenuation coefficient) for photons. We have run these tests for 0.1, 0.4, 1.0, 10 and 40

MeV initial energies for the several codes (geant4, EGS5, FLUKA, GRRR, and MC-PEPTITA) used by the co-authors. The outputs show equivalent results, but there are important differences one can identify. Especially the different implementations of the friction are causing observable effects. First we see that straggling is important in the energy regime of HEAP and should be included in the simulations. Secondly the opening-angle of photon beams are very sensitive to the low energy cut-off. Thirdly we noticed that EGS5 has an ultra-relativistic approximation for bremsstrahlung which is not appropriate in the energy regime of HEAP. Last but not least there is a big difference in completion time between programs, mainly depending on the low energy cut-off and the synchronous implementation of the code. Adding electric fields will only increase these differences further. All results are published as supplementary material (available at: <https://www.geosci-model-dev.net/9/3961/2016/>), and they can then be used by anyone in the community to benchmark his or her custom made codes.

4.8 ELECTROMAGNETIC STUDY AND MODEL REDUCTIONS

Apart from analytical calculations, the physics behind TGFs, TGF afterglows and gamma-ray glows are also studied with the help of experimental data, computer simulations, and often a combination of both. Simulations necessarily involve model reduction and assumptions. As we argued in the previous section, in scenarios where the electric field is below the classical breakdown field ($E_k \approx 3.0$ MV/m at STP), electrons below a certain energy can be neglected, because they will decelerate and eventually attach, thus not contributing to the production of the hard radiation. In Monte Carlo simulations it is therefore common to apply a so-called "low energy cutoff" (or threshold), noted ε_c , that is a threshold where particles with lower energy can be discarded (or not produced), to improve code performance. It is different from ε_2^{\min} (the minimum energy at which a secondary electron can runaway) as one is a simulation parameter and the other is a physical value. Ideally, ε_c should be set as close as possible to ε_2^{\min} . A second simplification can be made for the energetic enough particles that stay in the ensemble, by treating collisions that would produce particles below the low energy cutoff as a friction. Both simplifications can be implemented in different ways, leading to different efficiencies and accuracies.

As we indicated in section 4.1.2, the ionisation energy loss channel is much larger than the radiative (bremsstrahlung) energy loss, by a few orders of magnitude. However, this is only true for the average, and bremsstrahlung does have a significant effect on the electron spectrum because of straggling (RUTJES *et al.*, 2016). This straggling effect was first studied by Bethe and Heitler (1934). If it is not taken into account in the implementation of the low energy cut-off, the primary particle suffers a uniform (and deterministic) energy loss. This means that only the energy of the primary particle is altered, but not its direction. The accuracy of the assumed uniform energy loss is a matter of length scale : on a small length scale, the real energy loss distribution (if all interactions are considered explicitly) among the population would have a large spread. One way to obtain an accurate energy distribution is by implementing a stochastic friction

mimicking the straggling effect.

We chose not to use larger electric fields because that would produce an exponential growth of low energy electrons (< 123 eV) which would affect the electric field and therefore require a self-consistent simulation, that Geant4 is not capable of. We aim to provide a comparison standard for the particle codes able to simulate Relativistic Runaway Electron Avalanches, as simple and informative as possible, by only considering their physical outputs.

In section 4.1.2, we illustrated that the full RREA characteristics, such as the mean energy $\bar{\epsilon}$ or the collision length Λ_{prod} are driven by processes determining ϵ_2^{min} (the minimum energy at which a secondary electron can runaway). To prove this insight, and to benchmark codes capable of computing RREA characteristics for further use, we calculated the probability for an electron to accelerate into the runaway regime (see section 4.11), which is closely related to the quantity ϵ_2^{min} . From this probability study, it is directly clear that it is safe to choose the low energy cutoff ϵ_c higher than previously expected by Skeltved *et al.* (2014) and Rutjes *et al.* (2016), given an electric field $E < E_k$. In section 4.11, we will demonstrate that the probability for particles below 10 keV to accelerate and participate in the penetrating radiation is actually negligible. Thus, in practice an energy threshold value of $\epsilon_c \approx 10$ keV can be used for any electric field below E_k . However, in section 4.10, we will show that step-length restrictions are of major importance (e.g. it can lead to an underestimation of a factor of 10 of the probability to produce a RREA, in some cases). The results of the comparison of several parameters of the RREAs produced by the four tested codes is then presented in section 4.12. We conclude in section 4.13.

The test set-ups of the two types of simulations (RREA probability, and RREA characteristics) are described in the Supplementary Material (available at: <https://www.geosci-model-dev.net/11/4515/2018/>), together with the data we generated, and supplementary figures comparing several characteristics of the showers.

4.9 ELECTROMAGNETIC COMPARISON: MODEL DESCRIPTIONS

The data we discuss in the next sections were produced by the general-purpose code Geant4 (with several set-ups) and two custom-made codes (GRRR and REAM) which we describe below.

4.9.1 Geant4

The electromagnetic models can simulate the propagation of photons, electrons and positrons including all the relevant processes, and the effect of electric and magnetic fields. Geant4 uses steps in distance, whereas REAM and GRRR use time step. In the context of this study, three main different electromagnetic cross-section sets implementation are included : one based on analytical of semi-analytical models (e.g. uses the Møller cross section for ionisation and Klein-Nishina cross section for Compton scattering), one based on the Livermore data set (PERKINS

et al., 1991), and one based on the Penelope models (SALVAT *et al.*, 2011). Each of them can be implemented with a large number of different electro-magnetic parameters (binning of the cross section tables, energy thresholds, production cuts, maximum energies, multiple scattering factors, accuracy of the electro-magnetic field stepper, among others), and some processes have multiple models in addition to the main three, e.g. the Monash University model for Compton scattering (BROWN *et al.*, 2014). Skeltved *et al.* (2014) used two different physics list : LHEP and LBE. The first one, based on parametrisation on measurement data and optimized for speed, was deprecated since the 10.0 version of the toolkit. The LBE physics list is based on the Livermore data, but it is not considered as the most accurate electro-magnetic physics list in the Geant4 documentation, which is given by the Option 4 physics list (O4). This last uses a mix of different models, and in particular uses the Penelope model for the the impact ionisation of electrons. For this study, we will use two GEANT4 physics list options : Option 4 (referred as simply O4 hereafter) that is the most accurate one according to the documentation, and the Option 1 (referred as simply O1 hereafter) that is less accurate, but runs faster. In practice, O1 and O4 give very similar results for simulations without electric field and energies above 50 keV, as produced in our previous code comparison study (RUTJES *et al.*, 2016).

By default, Geant4 is following all primary particles down to zero energy. A primary particle is defined as a particle with more energy than a threshold energy ε_c^g (that is different from ε_c described before). By default, ε_c^g is set to 990 eV and was not changed to obtain the results presented in the next sections. The LBE Physics list used by Skeltved *et al.* (2014) uses a threshold down to 250 eV (i.e. more accurate than using 990 eV, in principle) and this parameter was thought to be responsible for a major change in the accuracy of the obtained RREA energy spectra. In section 4.11, we will argue that the most important factor able to effect the spectra obtained from Geant4 simulations is the accuracy of the stepping method for the tracking of the electrons, and not the low energy threshold. Actually, we found that the stepping accuracy of the simulation is indirectly improved by reducing ε_c^g , that explains why Skeltved *et al.* (2014) could make this interpretation.

4.9.2 GRRR

In the scope of this work, we want to point out three important features : 1. Electron ionisation and scattering processes are simulated discretely, and the friction is uniform and without a way to mimic the straggling effect. 2. Bremsstrahlung collisions are not explicit and are simulated as continuous radiative losses, without straggling. 3. GRRR uses a constant time-step Δt both for the integration of the continuous interactions using a fourth-order Runge-Kutta scheme and for determining the collision probability of each discrete process k as $\nu_k \Delta t$, where ν_k is the collision rate of process k . This expression assumes that $\nu_k \Delta t \ll 1$ and therefore that the probability of a particle experiencing two collisions within Δt is negligibly small. The collisions are sampled at the beginning of each time step and therefore the rate ν_k is calculated using the energy at that instant. In this work we used $\Delta t = 0.25$ ps for the avalanche probabilities simulations, and

$\Delta t = 1$ ps for the simulations used to characterise the RREA. For both cases, the time steps are small enough to guarantee a very accurate integration.

4.9.3 REAM

The REAM (Runaway Electron Avalanche Model) is a three dimension Monte Carlo simulation of Relativistic Runaway Electron Avalanche (also refereed as Runaway Breakdown), including electric and magnetic fields (DWYER, 2003, 2007; CRAMER *et al.*, 2016). This code is inspired by earlier work by Lehtinen *et al.* (1999) and takes accurately into account all the important interactions involving runaway electrons, including energy losses through ionisation, atomic excitation and Møller scattering. A shielded-Coulomb potential is implemented in order to fully model elastic scattering, and it also includes the production of X/gamma-rays from radiation energy loss (bremsstrahlung) and the propagation of the photons, by including photoelectric absorption, Compton scattering and electron/positron pair production. The positron propagation is also simulated, including the generation of energetic seed electrons through Bhabha scattering. The bremsstrahlung photon emissions from the newly produced electrons and positron are also included.

In the scope of this study, it is important to point out that REAM limits the time step size of the particles so that the energy change within one time step cannot be more than 10 %. The effect of reducing this factor down to 1 % was tested and did not make any noticeable difference in the resulting spectra. The comparative curves are presented in the paper supplementary material, section 10 (available at: <https://www.geosci-model-dev.net/11/4515/2018/>).

4.10 STEPPING METHODOLOGY

4.10.1 General method

In Monte Carlo simulations, particles propagate in steps, collide and interact with surrounding media by means of cross sections (and their derivatives). A step is defined by the displacement of a particle between two collisions. As it is presented in sections 4.11 and 4.12, the stepping methodology is responsible for most of the differences we observed between the codes we tested. Simulations can be either *space-oriented* or *time-oriented*, if the stepping is done in space or in time. By construction, space-oriented simulations are thus not synchronous in time. Usually, a single particle is simulated until it goes below the low energy threshold (ϵ_c), chosen by the user. But there are exceptions, like Geant4, that by default follows all primary particles down to zero energy. The advantage of asynchronous simulations is the ability to easily include boundaries, to have particles step as far as possible in the same material (minimizing the overhead due to null collisions), and smaller memory usage since there is no need to store all the particles alive at a given time (that may be a million or more). However, asynchronous simulations makes it

impossible to incorporate particle to particle interactions, such as a space charge electric field, or self-consistent electric fields.

During steps, charged particles can lose energy (and momentum) by collisions, and also change in energy (and momentum) when an electric fields is present. To guarantee accuracy, energies should be updated frequently enough. An accurate method would be to exponentially sample step lengths with

$$\delta\ell = \min_{\epsilon} \{(\sigma_t(\epsilon)N)^{-1}\}, \quad (4.20)$$

in space-oriented perspective, or

$$\delta t = \min_{\epsilon} \{(v(\epsilon)\sigma_t(\epsilon)N)^{-1}\}, \quad (4.21)$$

in time-oriented perspective. With v the velocity, σ_t the total cross section and N the number density of the medium. Then at each updated location (and energy), the type of collision must be sampled from probability distributions. The probability of doing a collision of the given process (pr) can be calculated with:

$$p_{pr} = 1 - \exp\left(-N \int_i^f \sigma_{pr}(\epsilon(\ell)) d\ell\right) \quad (4.22)$$

Where the index i refers to the beginning of the step, f to its end, ℓ is the step length variable along the trajectory, and $d\ell$ is an infinitesimal step length. For time oriented simulations, we have equivalently :

$$p_{pr} = 1 - \exp\left(-N \int_i^f v(\epsilon(t)) \sigma_{pr}(\epsilon(t)) dt\right) \quad (4.23)$$

Using these probabilities along a given step length or duration, there is a chance that no interactions happens, but the energy of the particle is guaranteed to be updated correctly.

4.10.2 The case of Geant4

In the Geant4 documentation, the stepping method presented in the previous section is referred as the "the integral approach to particle transport". This method is set up by default in Geant4 for impact ionisation and bremsstrahlung. However, the way it is implemented is not exactly following what was described in the previous section. The description of the exact implementation is out of the scope of this article, but is presented into details in Ivanchenko *et al.* (1991) and Apostolakis *et al.* (2009). The method relies on determining the maximum of the cross section over the step (σ_{max}), using a parameter α_R (called "dR over Range" in the Geant4 documentation), that is also used to determine the step lengths. Another related parameter is the maximum range parameter (ρ_{max}), set to the default values of 1 millimeter and 0.1 millimeter for O1 and O4 respectively, and was never changed in the scope of this study. The exact definition of these

parameters is given in Allison *et al.* (2016) and in the online Geant4 documentation (available at <http://geant4.cern.ch/support/userdocuments.shtml>). The default value of α_R is set to 0.80 for O1 and to 0.20 for O4. We found that both values are not low enough to be able to produce accurate results for the RREA probability simulations presented in the next section. To make Geant4 able to produce accurate RREA simulations using the multiple scattering algorithm, two methods are possible.

The first method is to tweak the value of the α_R parameter. Its value is set to 0.80 by default for O1, and 0.20 by default for O4. We found that these default values are way too high to be able to produce accurate RREA simulations, and values of $\alpha_R < 5.0 \times 10^{-3}$ should be used, as presented in the next section.

The second method is to implement a step limiter process (or maximum acceptable step). By default, this max step ($\delta\ell_{max}$) is set to one kilometer, and such a large value has no effect in practice, since the mean free path of energetic electrons in STP air is orders of magnitude smaller. Acceptable values of $\delta\ell_{max}$ depend on the electric field, and we found that it should be set to 1 millimeter or less to produce accurate RREA simulations, as presented in the next section. However, using this method results in relatively long simulation time required to achieve an acceptable accuracy, as the step is not adapted to the energy of the electrons.

4.11 PROBABILITY OF GENERATING RREA

As a first comparison test, we estimated the probability for an electron to accelerate into the runaway regime and produce a RREA, given its initial energy ϵ and some electric field magnitude E . Note that the momentum of the initial electrons is aligned along the opposite direction of the electric field, so that it gets accelerated. That gives maximum RREA probabilities, as other alignments reduce the chance to produce a shower (see, e.g., Lehtinen *et al.*, (1999)). We defined this probability as the fraction of initial (seed) electrons that created an avalanche of at least 20 electrons above 1 MeV. Once this state is reached, there is no doubt the RREA is triggered and can go on forever if no limits are set. The number 20 is arbitrary, to be well above 1 but small enough for computational reasons. For some initial conditions, we also tested requirements of 30 and 50 electrons above 1 MeV, that resulted in very similar probabilities. This study is somehow similar to the works presented in Lehtinen *et al.* (1999), Li *et al.* (2009), Liu *et al.* (2016) and Chanrion *et al.* (2016), but they all looked at the probability to have only one single runaway electron, whereas we used the criterion of $N = 20$ electrons above 1 MeV, that is a stricter constraint. The difference between the two criteria is mainly noticeable for low electric field (< 0.4 MV/m) and high seed energies (> 700 keV). A figure illustrating how the probability can change with N is presented in the paper supplementary material, section 5.3 (available at: <https://www.geosci-model-dev.net/11/4515/2018/>).

As a test case, we calculated the probability to produce RREAs as a function of α_R and

$\delta\ell_{max}$ (these parameters are presented in the previous section), for the configuration $\epsilon = 75$ keV, $E = 0.80$ MV/m. This case was chosen because it showed a particularly large sensitivity to the stepping methodology, as discussed later. The results are presented in figure 4.6. Although this configuration has a very low RREA probability for O1 and O4 by default (where α_R respectively equal to 0.80 and 0.20, and $\delta\ell_{max}$ is one kilometer for both), the probability increases as α_R decreases and converges to a value between 10 and 12 % for both models when $\alpha_R < 5.0 \times 10^{-3}$. The same effect is observed when reducing $\delta\ell_{max}$. In this case, the user should not set $\delta\ell_{max}$ below the maximum range parameter, set to 1 millimeter for O1 and 0.1 millimeter for O4 by default (and never changed in the scope of this article). When reducing the α_R parameter to arbitrarily small values, both Geant4 models converge to slightly different probabilities : 10.7 % for O1 and 11.7 % for O4. We think this small difference is not due to the stepping method, as reducing ρ_{max} or α_R further does not produce a significant difference. It is probability due to other factors, in particular the difference in the physical models and cross section sets used. We encourage other researchers to check if their simulations produce a RREA probability for this $\{\epsilon, E\}$ setting that is consistent with our result.

As explained in section 4.1.2, the final electron spectrum is essentially driven by the minimum energy ϵ_2^{\min} of electrons that can create a RREA. Here we can clearly see this probability is strongly affected by the choice of the α_R and $\delta\ell_{max}$ simulation parameters, affecting the accuracy of the stepping method, and that the values set by default for these parameters are not precise enough to obtain correct RREA probabilities. In order to help future researchers, we provide example Geant4 source codes where the α_R and $\delta\ell_{max}$ parameters can be changed and their effect to be tested.

In figure 4.7.a, we compare the contour lines of the 10%, 50% and 90% probability of triggering a RREA as function ϵ and E , for the four models : Geant4 O4 ($\alpha_R = 1.0 \times 10^{-3}$), Geant4 O1 ($\alpha_R = 1.0 \times 10^{-3}$), GRRR and REAM. The full RREA probability results in the (ϵ, E) domain for each model are presented in the paper supplementary material, section 5 (available at: <https://www.geosci-model-dev.net/11/4515/2018/>).

The most important difference between Geant4 and GRRR is present for energies > 200 keV and E-fields < 0.5 MV/m. At 1 MeV, the level curves are significantly different between the Geant4 models and GRRR: the 50% probability to trigger RREA for GRRR is approximately located at the 10 % probability for O4, and the 90 % probability to for GRRR is located at the 50 % probability for O1. The reason is probably similar to a point we raised in our previous study (RUTJES *et al.*, 2016) : GRRR does not include a way to simulate the straggling effect for the ionisation process. By looking at figure 2 of Rutjes *et al.* (2016), we can see that 200 keV is roughly the energy from where the difference in the spectrum of GRRR, compared to codes that simulate straggling, starts to become significant.

For low electron energy (< 40 keV) and high electric field (> 2 MV/m), GRRR and O4 present a good agreement, however O1 deviates significantly from O4. We investigated the effects of the stepping parameters (α_R , $\delta\ell_{max}$ and ρ_{max}) and it is clear that they were not involved in this

case. We think the Møller differential cross section (with respect to the energy of the secondary electron) used by O1 and extrapolated down to low energies leads to the production of secondary electrons with average energies lower than the Penelope model (used by O4), that includes the effects of the atomic electron shells, hence is probably more accurate. This hypothesis is confirmed by looking at the shape of the differential cross sections of impact ionisation, which plots are presented in the paper supplementary material, section 11.4 (available at: <https://www.geosci-model-dev.net/11/4515/2018/>).

The RREA probability data for REAM is also displayed in figure 4.7.a, as the red curves. The three REAM level curves show a significantly higher noise than the Geant4 data, mainly because the latter used 1000 electrons seeds whereas the former used only 100. The algorithms used to calculate the levels curves were also found to impact the noise level. Nevertheless, the noise level is low enough to be able to evaluate the consistency between the codes. REAM shows a consistency with Geant4 (O1 and O4) within less than 12% in the full parameter range, and less than 5 % in some part of it. The most apparent deviations between REAM and Geant4 O1/O4 can be noticed for a seed electron energy range between 50 and 300 keV, for the 50 % and 90% level curves, where there is a systematic, statistically significant difference in the probability for REAM compared to Geant4 (REAM requiring about 10% larger electric field or primary electron energy to reach the 90% or the 50% contour level). However, we do not expect such a small difference to significantly affect the characteristics of the RREA showers, such as the multiplication factors or the mean energies of the RREA electrons. To test this quantitatively, a detailed comparison of the most important characteristics of the RREA showers obtained with the four models is presented in the following section.

In Figure 4.7.b we show the 0 %, 10 %, 50 %, 90 % and 100 % probability contour lines for the Geant4 O4 model where we could run a very large number of initial electrons ("seeds") to obtain curves with a very low noise level. These are the most accurate probabilities we could obtain. From this figure, it is clear that the RREA probability for an electron of less than ≈ 10 keV is null for any electric field below $E_k \approx 3.0$ MV/m. Therefore 10 keV is a reasonable a lower boundary of ϵ_2^{\min} (the minimum energy at which a secondary electron can runaway), and any simulation with an electric field below $E_k \approx 3.0$ MV/m could use an energy threshold (ϵ_c) of this value while keeping accurate results. If electric fields with lower magnitude are used, it is also reasonable to increase this energy threshold by following the 0% level curve showed in Figure 4.7.b.

4.12 CHARACTERISATION OF RREA SHOWERS

We compared the output of the four models over 12 different electric field magnitudes from $E = 0.60$ MV/m to $E = 3.0$ MV/m. Two types of simulation were set : record in time, and record in distance (or space). This last choice was made because the resulting spectra can change significantly depending on the record method, as presented in figure 10 of Skeltved *et al.* (2014).

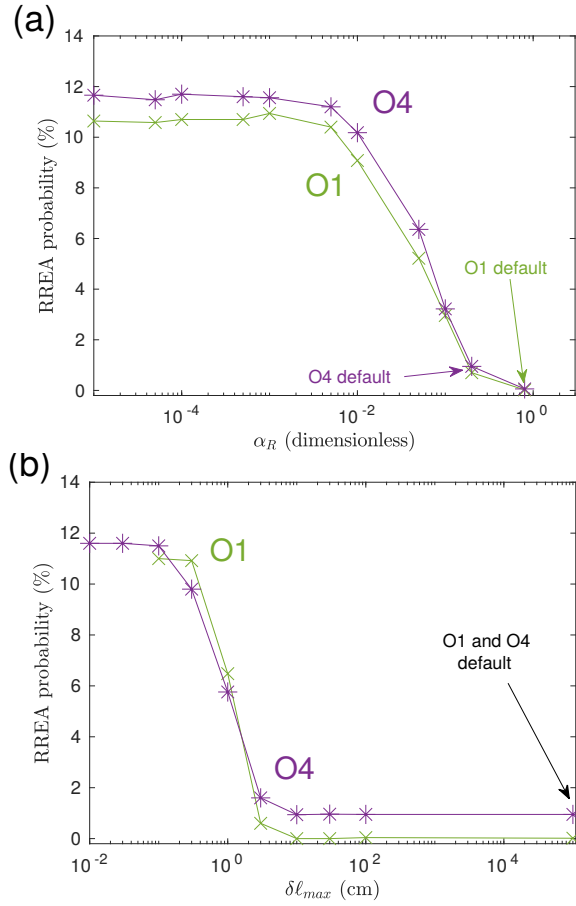


Figure 4.6: Relativistic avalanches probabilities calculated from Geant4 simulations, for specific point $\{\epsilon = 75 \text{ keV}, E = 0.80 \text{ MV/m}\}$ (illustrated by a cross in figure 4.7) and for two stepping settings. **(a)**: Avalanche probability versus α_R setting for Geant4 O4 and Geant4 O1. δl_{max} is set to the default value of 1 kilometer. **(b)**: Avalanche probability versus maximum step setting (δl_{max}) for Geant4 O4 and Geant4 O1. The parameter α_R is set to the default value of the models, that is 0.8 for O1 and 0.2 for O4.

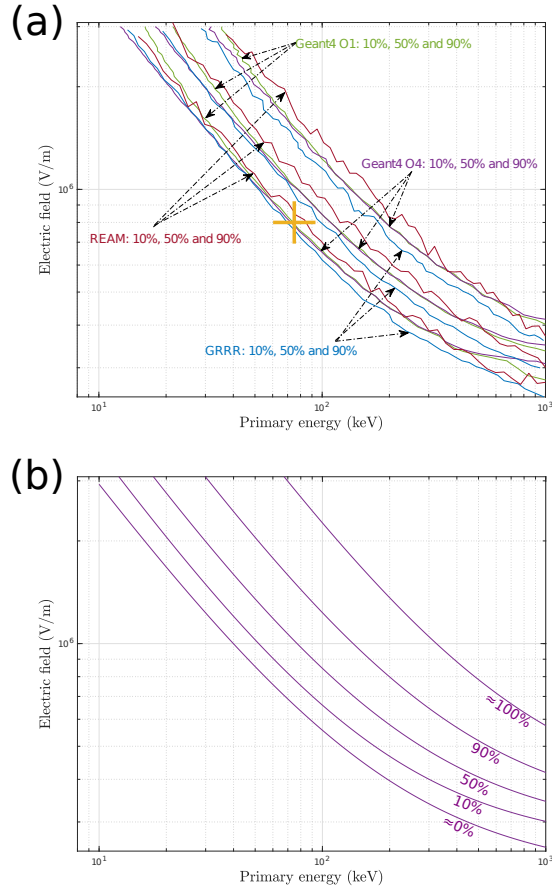


Figure 4.7: **(a)**: Relativistic avalanche probability comparison between GRRR, REAM, O4 and O1. It shows three contour lines at 10%, 50% and 90%, as function of seed (primary) energy ϵ and electric field magnitude E . These contours are derived from the full probability scan, that are presented in the paper supplementary Material (section 5, available at: <https://www.geosci-model-dev.net/11/4515/2018/>). The cross at $\{\epsilon = 75 \text{ keV}, E = 0.80 \text{ MV/m}\}$ highlights the point where we studied the effect of the simulation stepping parameters (for the O4 and O1) on the probability, see figure 4.6. **(b)**: Five contour lines indicating the 0%, 10%, 50%, 90% and 100% probabilities to generate a relativistic electron avalanche (RREA) as function of ϵ and E , for the Geant4 O4 model for which we could run a very large number of initial electrons ($> 50,000$) to obtain curves with a very low noise level.

All the curves presenting the simulation results are presented in the paper supplementary material (available at: <https://www.geosci-model-dev.net/11/4515/2018/>), as well as the complete details on how the simulation should be set up. In the following section, we discuss only the most important differences we found between the four codes. We show the comparison of avalanche scales in space and time in section 4.12.1 and in section 4.12.2 the evolution to self-similar state. Finally, in section 4.12.3 we show the comparison of the self-similar energy spectra of electrons and photons of the RREA.

4.12.1 Avalanche time and length scales

Figures 4.8 and 4.9 show the avalanche length and time scales as function of electric fields, for the four models, together with their relative difference with respect to REAM. Note that we could not compute any values for electric fields below 0.60 MV/m, as we only used 200 initial electron seeds of 100 keV, which could not produced enough showers. The choice of 200 initial electrons is purely due to computational limitations. The avalanches length and times of the different models agree within $\pm 10\%$. There is also a systematic shift of about 7 % between the two Geant4 models for both time and length scales. The Geant4 O4 model is in principle more accurate than the O1 model, since it includes more advanced models. For most of the electric fields, O1 tends to be closer to REAM and O4 tends to be closer to GRRR. Following Coleman *et al.* (2006), the avalanche length and time can be fitted by the empirical models,

$$\lambda(E) = \frac{c_1}{E - c_2}, \quad (4.24)$$

$$\tau(E) = \frac{c_3}{E - c_4} \quad (4.25)$$

where c_1 is in V, c_2 and c_4 in V/m and c_3 in s · V/m. The c_2 and c_4 parameters can be seen as two estimates of the magnitude of the electric field of the minimum of ionisation for electrons along the avalanche direction, and also of the electric field magnitude of the RREA threshold; both values being close. However, we note that these fits neglect the sensitivity of the mean energy and velocity to the electric field. These empirical fits are motivated from the relations presented in equation 4.9 and 4.10, derived for the one dimensional case. First results of such fits were presented in Babich *et al.* (2004) and Coleman *et al.* (2006); and they obtained consistent results. Here we will compare our results against Coleman and Dwyer.

The best fit values of the two models to the simulation data are given in table 4.2. The c_1 parameter is directly linked to the average energy of the RREA spectrum, though the definition of this average energy can be ambiguous as energy spectra change significantly if recorded in time or in space. The values given by all the code are located between 6.8 and 7.61 MV, and are all consistent with each other within a 95 % confidence interval, with the exception of O4 that slightly deviates from O1. Combining the four values gives :

Table 4.2: Values of the parameters of the fits (with 95 % confidence intervals) for the simulations data for avalanche scale in space and time, using the models described by equations 4.24 and 4.25. See figure 4.8 and 4.9 for the corresponding curves.

Code	Avalanche length		Avalanche time	
	c_1 (MV)	c_2 (kV/m)	c_3 (ns MV/m)	c_4 (kV/m)
REAM	7.43 ± 0.18	290 ± 9.5	27.6 ± 0.91	293 ± 13
G4 O1	7.50 ± 0.10	276 ± 5.6	27.6 ± 0.44	290 ± 6.3
G4 O4	6.93 ± 0.13	285 ± 7.5	25.9 ± 0.28	288 ± 4.2
GRRR	7.25 ± 0.30	266 ± 18	26.2 ± 0.76	282 ± 12

$$\bar{c}_1 = 7.28 \pm 0.10 \text{ MV} \quad (4.26)$$

By "combining", we mean that the four values are averaged and the rule $\sigma_{comb} = \sqrt{\sigma_1^2 + \sigma_2^2 + \sigma_3^2 + \sigma_4^2}/4$ is used to "combine" the four uncertainty ranges. The value \bar{c}_1 is consistent with the value of 7.3 ± 0.06 MV given in Coleman *et al.* (2006). And all the estimated values of the c_2 and c_4 are consistent with each other within a 95 % confidence interval. Combining all the values of c_2 and c_4 gives :

$$\begin{aligned} \bar{c}_2 &= 279 \pm 5.6 \text{ kV/m} \\ \bar{c}_4 &= 288 \pm 4.8 \text{ kV/m} \end{aligned}$$

And both value are also consistent with each other, leading to the final value of $\bar{c}_{2,4} = 283.5 \pm 3.69$ kV/m. These values slightly deviates from the value of 276.5 ± 2.24 obtained from Coleman *et al.* (2006) if the values they obtained for the fits of λ and τ are combined. The work of Coleman *et al.* (2006) used the REAM model too, in a version that should not have significantly changed compared to the one used here. Thus, we think this difference is purely attributed to differences in the methodology that was used to make these estimates from the output data of the code. Concerning the c_3 parameter, combining all the estimates gives $\bar{c}_3 = 26.8 \pm 0.32$ ns MV/m, that is slightly lower than the value of 27.3 ± 0.1 ns MV/m of Coleman *et al.* (2006), but none of the values are consistent within the 95 % confidence interval. For this case, we also think the slight difference can be attributed to differences in methodology. Furthermore, the ratio \bar{c}_1/\bar{c}_3 can also be used to determine an average speed of the avalanche $\approx \beta_{\parallel}c$ along the direction of the electric field (that also corresponds to the z direction), and we can estimate $\beta_{\parallel} \approx 0.90$, that is very close to what was found in previous studies.

4.12.2 Evolution to self-similar state

The photon and electron energy spectra of a relativistic runaway electron avalanche (RREA) is known to converge in time to a self-similar solution, where its shape is not evolving anymore,

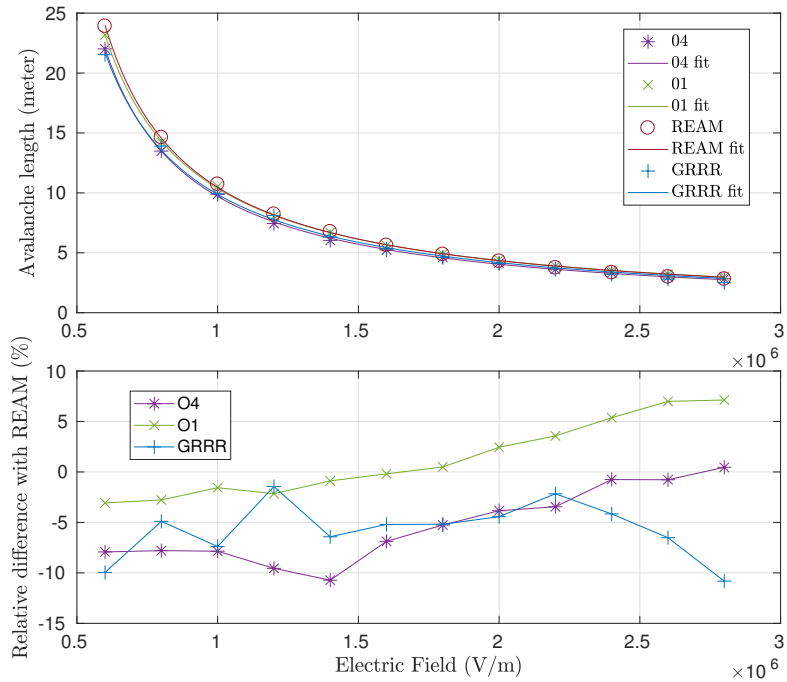


Figure 4.8: **Top** : Avalanche multiplication length as function of ambient electric field, for each of the codes included in this study. **Bottom** : The relative difference of all other models with respect to REAM. Table 4.2 indicates the values of the fit parameters.

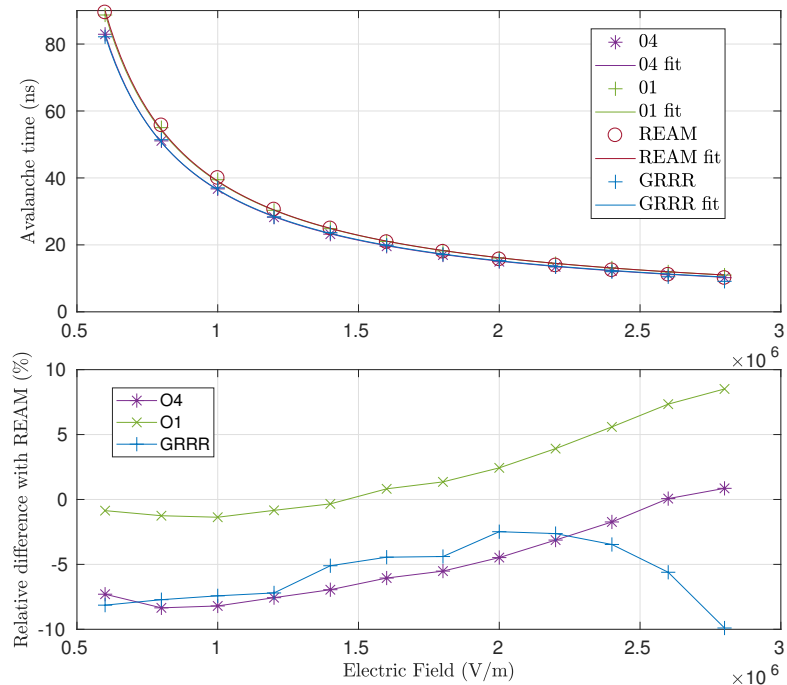


Figure 4.9: **Top** : Avalanche multiplication time as function of ambient electric field, for each of the codes included in this study. **Bottom** : The relative difference of all other models with respect to REAM. Table 4.2 indicates the values of the fit parameters.

even if the number of particles continues growing exponentially. It may also be referred as the "self-sustained state", or the "steady state" in the literature. At least 5 avalanche lengths (or avalanche times) are required to be able to assert that this state is reached. We propose to estimate this time by looking at the mean electron energy evolution as a function of time. Notice that, as already mentioned in the beginning of Section 4.12, this mean energy recorded in time is different from the one recorded in distance, used in the next section. We arbitrarily choose to evaluate this mean by averaging all the energies of each individually recorded electron from 10 keV and above. This choice of a 10 keV energy threshold (instead of a higher value, like 511 keV or 1 MeV) does not affect significantly the final estimate of this time to self-similar state. We started with a mono-energetic beam of 100 keV electrons, which is considered low enough compared to the self-similar state mean energy of 6 to 9 MeV. To define the time to self-similar state (T_s), we fitted the time evolution of the mean electron energy $\bar{\epsilon}$ with the model

$$\bar{\epsilon}(t) = b_1 - b_2 \times \exp(-t/b_3), \quad (4.27)$$

where b_1 and b_2 have dimension of energy, b_3 dimension of time, and we define $T_s = 5 b_3$, that is five e-folding times, i.e. converged to 99.3%. The evolution of electron spectra to self-similar state are illustrated for the Geant4 O4 model in the paper supplementary material (available at: <https://www.geosci-model-dev.net/11/4515/2018/>). The values of T_s we estimated for the different models are presented in figure 4.10, together with relative differences of the models with respect to REAM. The relatively high uncertainty (within 95 % confidence intervals) that can be seen on the estimate of T_s is due to a combination of the confidence interval from the exponential fit, from the statistics of the number of seed electrons that could produce a RREA, and from the statistics of the particle counts. For most case, 200 initial seed were used, but for REAM, only 16 seeds were simulated for $E \geq 2.2$ MV/m, and for GRRR, only 20 seeds were simulated above $E \geq 2.0$ MV/m, because of computation time limitations.

In figure 4.10, Geant O1, O4, GRRR and REAM show consistent times to reach the self-similar state, for all the E-fields. Notice that for them, $T(= T_s/5)$ is close to the avalanche time value τ given in the top panel of figure 4.9. For the low electric field of 0.60 MV/m, it seems to take about 5 times more to reach self-similar state. For this field, there were only three electrons seeds that could produce a RREA, giving a large uncertainty on the estimate of T_s , making it impossible to conclude on an inconsistency. From 0.60 MV/m to 1.8 MV/m, where all data from codes have good statistics, the times to self-similar state are consistent. From 2.0 MV/m to 2.4 MV/m, the two Geant4 models and REAM are consistent, but GRRR present lower times by about -20% to -50 %, but it is impossible to conclude an inconsistency, given the large confidence intervals. For E-field magnitudes of 2.6 MV/m to 2.8 MV/m, O1 and O4 present times to self-similar state lower than REAM by about 50 %, that is significant given the uncertainty intervals, whereas GRRR and REAM are consistent. We could not find a clear explanation for it.

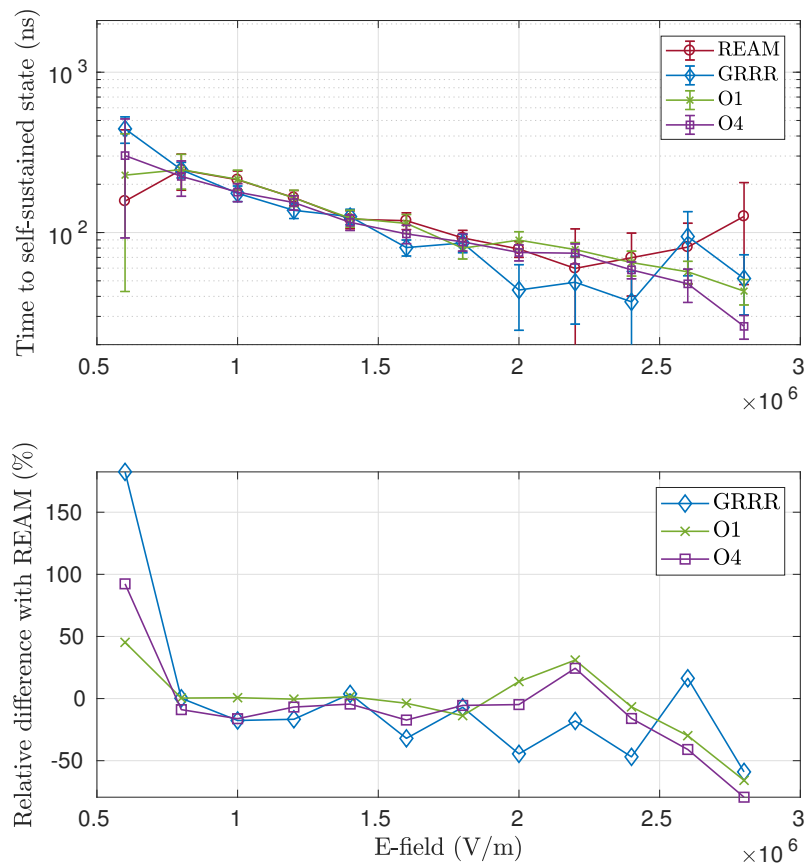


Figure 4.10: **Top** : time to self-similar state as function of ambient electric field, for each of the codes included in this study. **Bottom** : relative difference with respect to REAM.

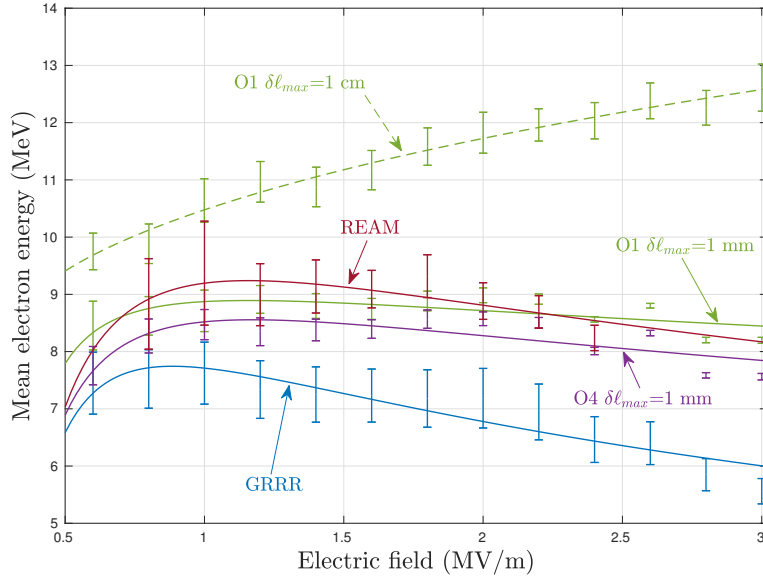


Figure 4.11: Mean electron energies at self-similar state (for distance record), for different electric field magnitudes. The data points are fitted with the model presented in section 4.12.3, equation 4.28. The values of the fitted parameters are presented in Table 4.3. To highlight the importance of including step limitations, Geant4 O1 values are presented for two different max step ($\delta\ell_{\max}$) settings: one that is not acceptable (1 cm) and one that is acceptable (1 mm). The parameter α_R is set to its default value of 0.8 for O1 and 0.2 for O4.

4.12.3 RREA spectra

In this section, we discuss the most important differences in the particles spectra we could find between the four models for the electric field between 0.60 MV/m and 3.0 MV/m.

Electrons

After the RREA electron spectra has reached self-similar state (that requires at least 5 avalanche lengths or times), we recorded the energy spectrum in a plane at a given distance (that is different for each electric field). Then we fitted it with an exponential spectrum model $\propto \exp(-\epsilon/\bar{\epsilon})$ (see also equation 4.8). Note that for an exponential distribution, the mean of the energy distribution is an estimator of its parameter $\bar{\epsilon}$, justifying the bar notation. We chose to evaluate the mean energy $\bar{\epsilon}$ for record at distances because, contrary to time records, it produces spectra that can be perfectly fit with an exponential distribution over the whole energy range (0 to 100 MeV). Therefore, in this case only the mean RREA electron energy is uniquely defined, and does not depend on an arbitrarily chosen energy threshold, or fitting method. The mean energy $\bar{\epsilon}$ of the exponential spectrum is calculated for the several codes as a function of electric field E , as presented in figure 4.11. For Geant4 O1 the whole simulations and analysis were done twice, for maximum allowed step length settings of $\delta\ell_{\max} = 1$ cm and $\delta\ell_{\max} = 1$ mm, to show that the first case generates totally incorrect spectra, that is consistent with having incorrect RREA probabilities (presented in section 3). In addition, values of the mean energy $\bar{\epsilon}$ for O1 with

Table 4.3: Mean energy variation with electric field. For evaluated codes we fitted by equation 4.28, with $F = 0.28$ MV/m. Figure 4.11 shows the corresponding curves.

CodeParameter	a_1 [10^6s^{-1}]	a_2	a_3 [10^6s^{-1}]
Geant4 O1 ($\delta\ell_{max} = 1$ mm)	6.17 ± 2.15	$1.14 \pm 7.3 \times 10^{-2}$	-4.31 ± 2.0
Geant4 O4 ($\delta\ell_{max} = 1$ mm)	5.17 ± 1.8	$1.23 \pm 8.2 \times 10^{-2}$	-1.93 ± 1.5
Geant4 O1 ($\delta\ell_{max} = 1$ cm)	10.8 ± 3.4	$0.782 \pm 3.9 \times 10^{-2}$	-10.7 ± 3.6
REAM	3.98 ± 2.1	1.31 ± 0.20	$-8.41 \times 10^{-2} \pm 2.1$
GRRR	4.24 ± 1.6	1.42 ± 0.11	-0.639 ± 1.16

$\alpha_R = 1.0 \times 10^{-3}$ and $\delta\ell_{max} = 1$ cm are presented in the paper supplementary material (available at: <https://www.geosci-model-dev.net/11/4515/2018/>).

The data of figure 4.11 was fit following the model,

$$\bar{\epsilon}_{\text{fit}}(E) = \lambda(E)(qE - F), \quad \lambda(E) = \beta c \left[a_1 \left(\frac{qE}{F} \right)^{a_2} + a_3 \right]^{-1}, \quad (4.28)$$

motivated by the facts that ϵ_2^{min} is roughly a power-law of E (see figure 4.7) and λ is a power-law of ϵ_2^{min} (see equation 4.3). It has three adjustable parameters a_1 , a_2 and a_3 . We set $F = 0.28$ MeV/m, that is approximately the RREA threshold. The speed β (rate between velocity and speed of light) is set constant, equal to 0.90, because the RREA velocity does not change of more than 5 % over the range of electric fields we tested. This model is in general agreement with the calculations of Celestin *et al.* (2012), where $\lambda(E)$ presents an approximately linear relation with the electric field. Table 4.3 gives the parameters' best fits (with confidence intervals) for the different models, and figure 4.11 shows the corresponding curves.

In figure 4.11, it is clear that the Geant4 O1 model with $\delta\ell_{max} = 1$ cm presents a significantly higher $\bar{\epsilon}(E)$ than the other codes, with values ranging from 9.5 MeV to 12.5 MeV. From the previous RREA probability simulations (see section 4.11), we know that this $\delta\ell_{max}$ parameter is not low enough, and so the results of this model can be disqualified. However, when $\delta\ell_{max}$ is reduced to 1 mm, the results of both Geant4 model are close. There seems to be a consensus between Geant4 (O1 and O4) and REAM, that gives a mean energy that is between 8 and 9 MeV and can vary up to 10 % depending on the electric field. For all electric field magnitudes, GRRR shows a smaller average energy, from about 10 % less at 1 MV/m to about 20 % less at 2.8 MV/m. The reason is certainly because GRRR only includes radiative energy losses as a continuous friction. This is actually a similar difference to what has been observed and discussed in Rutjes *et al.* (2016) concerning the high energy electron beams, and one can read the discussion therein for more details.

Figure 4.12 compares the electron spectra recorded at $z = 128$ meters (the electric field has a non-null component only in the z direction, so that electrons are accelerated towards positive z), for an electric field magnitude $E = 0.80$ MV/m, for a RREA generated from 200 initial ("seed")

electrons with $\epsilon = 100$ keV. This record distance was chosen because it corresponds to about 8.5 avalanche lengths, giving a maximum multiplication factor of about 5000, for which there is no doubt the RREA is fully developed and has reached self-similar state. This electric field of $E = 0.80$ MV/m was chosen because it is where we could observe the most interesting differences between the models, and it also happens to be the lowest for which we could build spectra with enough statistics on all the models to be able to present a precise comparison. The choice of 200 initial electrons is purely due to computational limitations.

In Figure 4.12, the error bars on the bottom panel represent the uncertainty due to the Poisson statistics inherent when counting particles. The four models are consistent within 10 % between 20 keV and 7 MeV. Below 20 keV, we think the discrepancy is not physical, and can be attributed to the recording methods set up for the different codes, that are not perfect and have a more or less important uncertainty range (that is not included in the display error bars, only based on Poisson statistics). Above 7 MeV, O1 remains consistent with REAM overall, but O4 and O1 deviate significantly : up to 50 % for O4 and up to 90 % for GRRR. For the last bin between 58 and 74 MeV, O4 and GRRR are inconsistent, that is explained by the fact that GRRR does not include straggling for Bremsstrahlung (i.e. either explicit bremsstrahlung collision or some stochastic fluctuations mimicking straggling). The deviations for the high energy part (>7 MeV) in the electron spectrum are significant for this particular field ($E = 0.80$ MV/m), however this is not true for all electric fields, where the codes are overall roughly consistent, as seen in the paper supplementary material (available at: <https://www.geosci-model-dev.net/11/4515/2018/>). In principle O4 should be more precise than O1 (ALLISON *et al.*, 2006), as it includes more advanced models, yet we cannot argue that O4 is more accurate than REAM. One way of deciding which model is the most accurate might be to compare these results with experimental measurements. but in the context of TGFs and Gamma-ray glows it is complicated to get a proper measurement of electron spectra produced by RREA. However, photons have much longer attenuation lengths than electron and can be more easily detected, e.g. from mountains, planes, balloons or satellites. In the next section we present and discuss the corresponding photon spectra.

Photons

In figure 4.13, the photon spectra recorded at $z = 128$ m (the electric field has a non-null component only in the z direction) for a magnitude $E = 0.80$ MV/m are given for Geant4 O1/O4 and REAM, together with the relative difference with respect to REAM. The reasons why these z and E values were chosen is given in the previous section.

The error bars in the relative differences represent the uncertainty due to the inherent Poisson statistics when evaluating particle counts. The Geant4 O1 and O4 models are consistent for the full energy range, except a small discrepancy below 20 keV, that can be attributed to different physical models, O4 being more accurate in principle. In this case, it cannot be attributed to recording methods, since they are exactly the same for both Geant4 models. At 10 keV the two Geant4 spectra are about 80 % larger than REAM. With increasing energy, the discrepancy

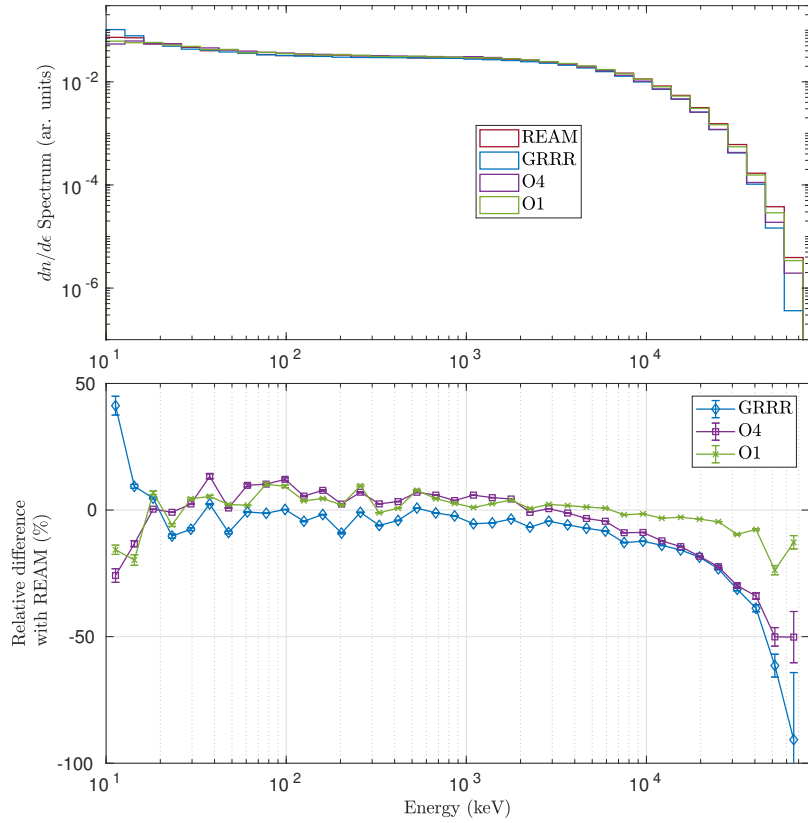


Figure 4.12: **Top** : Electron (kinetic) energy spectra of Geant4 (O4 and O1), REAM and GRRR, for $E = 0.80$ MV/m, recorded at $z = 128$ m. The RREA is generated from 200 seed electrons of $\epsilon = 100$ keV. **Bottom** : relative difference between REAM and the three other models. The error bars are calculated from the Poisson statistics.

reduces and reaches 0 % at 100 keV. Above 100 keV, the three models show consistent spectra. There may be some discrepancy above 30 MeV, but it is hard to conclude since the uncertainty interval is relatively large.

As just presented, the main noticeable discrepancy between O1/O4 and REAM is present below 100 keV. As far as we know, there is no reason to argue that Geant4 gives a better result than REAM in this range, or vice-versa. One way to find out which model is the most accurate could be to compare these results with real measurements. Are such measurement possible to obtain? Any photon that an instrument could detect has to travel in a significant amount of air before reaching detectors. The average path traveled in the atmosphere by a 100 keV photon in 12 km altitude air is 1540 ± 806 meters. It decreases for lower energies and is 671 ± 484 meters at 50 keV, and 63.0 ± 61.5 meters at 20 keV. Note that these lengths have been evaluated from precise Geant4 simulations, and are smaller than the attenuation lengths at the same energies, because photons gradually loose energy due to stochastic collisions. These average traveled paths are too small for the photons to have a reasonable chance to escape the atmosphere and to be detected by a satellite. But we cannot exclude that they may reach an airborne detector located inside or close to a thunderstorm. As a side note, we want to indicate that the vast majority (if not all) of the photons observed from space with energies below a few hundred of kilo-electronvolts (e.g., by the Fermi space telescope, see Mailyan *et al.* (2016)) had very likely more than 1 MeV when they were emitted. They lost some part of their energy by collisions (with air molecules in the atmosphere or/and with some part of the satellite) before being detected by the satellite. For information, a figure presenting the probability of a photon to escape the atmosphere as function of its primary energy for a typical TGF is presented in the paper supplementary material (available at: <https://www.geosci-model-dev.net/11/4515/2018/>).

4.12.4 Other differences

In addition to what is presented so far in this article, the following points should also be mentioned when comparing the results of the codes. The corresponding plots are available in the supplementary material (available at: <https://www.geosci-model-dev.net/11/4515/2018/>).

- The mean parallel (to the E-field direction) velocity β_{\parallel} of the avalanche is shown in section 4.2 of the paper supplementary material (labeled "mean Z velocity", available at: <https://www.geosci-model-dev.net/11/4515/2018/>). We observe that GRRR is giving β_{\parallel} faster than all the other codes, and O4 is systematically slower than REAM and O1, though the differences are less than 2 %. The variation of β_{\parallel} towards the electric field E is small, about 10 % for all codes. For increasing E-fields, electrons are less scattered and more focused in the field direction, hence slightly increasing β_{\parallel} .
- The electron to (bremsstrahlung) photon ratio $r_{e/p}$ was also calculated and compared for different distance record in the RREA shower, and the corresponding plots are presented in the paper supplementary material (available at: <https://www.geosci-model-dev.net/11/4515/2018/>),

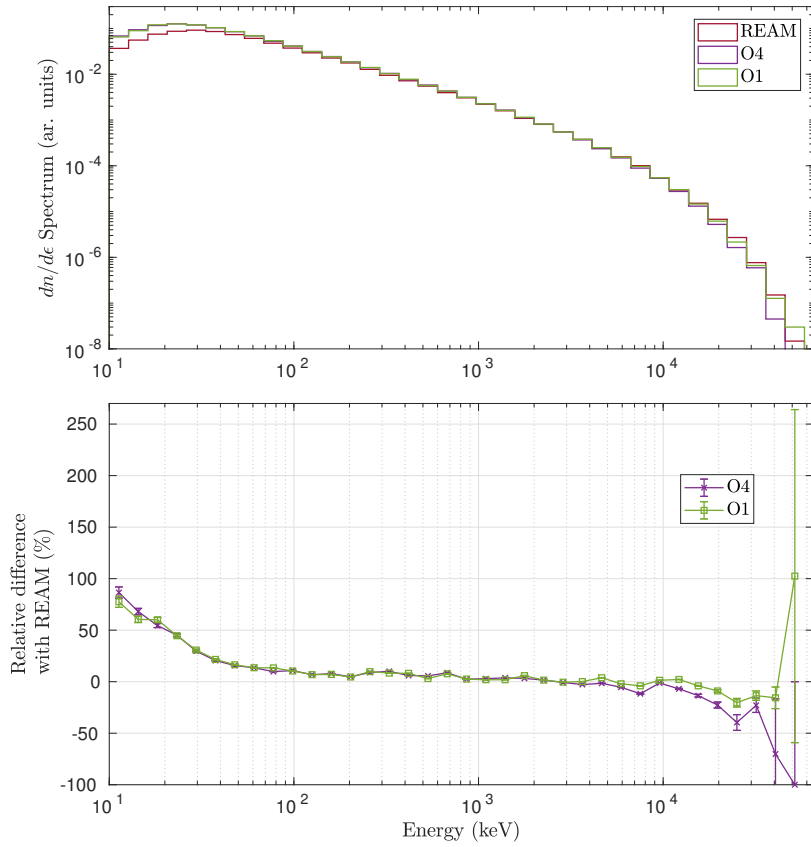


Figure 4.13: **Top** : Photon energy spectra of Geant4 (O4 and O1) and REAM for $E = 0.80$ MV/m, recorded at $z = 128$ m. **Bottom** : relative difference between Geant4 (O1 and O4) and REAM. The error bars are calculated from the Poisson statistics.

section 3. GRRR is excluded because it does not include photons. For any electric field, the same discrepancy is observed. At the beginning of the shower (<4 avalanche lengths), $r_{e/p}$ appears to be about 20 % larger for REAM compared to O1 and O4, then the three models are consistent at a given distance, and finally for more than about 4 avalanche lengths, the tendency is inverted and REAM presents a $r_{e/p}$ about 20 % smaller than Geant4. The magnitude of this discrepancy is largely reduced for increasing electric fields. We did not fully understand the reasons of these differences, and it may be due to the bremsstrahlung models used are involved. More investigations are required.

- The positron spectra have relatively low statistics (in the order of few hundreds particles recorded) and are all quite consistent within the relatively large uncertainties.
- In the photon spectra obtained from particle records at fixed times, REAM seems to show significantly less (at least a factor of 10) photon counts than the two Geant4 models for most of the electric fields magnitudes. For some fields, it even shows a lack of high energy photons, with a sharp cut at about 30 MeV. It seems to point out to a problem in the record method, explaining why we chose not to discuss these spectra in the main article. The spectra produced by the Geant4 O1 and O4 models for this case are consistent with one another for all the E-fields.

4.13 CONCLUSIONS

We have investigated the results of three Monte Carlo codes able to simulate Relativistic Runaway Electron Avalanches (RREA), including the effects of electric fields up to the classical breakdown field, which is $E_k \approx 3$ MV/m at STP. The Monte-Carlo codes REAM, GRRR and Geant4 (two models: O1 and O4) were compared. The main difference between the Geant4 O4 and O1 models is the inclusion of more precise cross sections for low energy interactions (< 10 keV) for O4.

We first proposed a theoretical description of the RREA process, that is based and incremented over previous published works. Our analysis confirmed that the relativistic avalanche is mainly driven by electric fields and the ionisation and scattering processes determining ϵ_2^{\min} , the minimum energy of electrons that can runaway. This is different from some of the previous works that speculated that the low energy threshold (ϵ_c), when changed from 1 keV to 250 eV, was the most important factor affecting the electron energy spectra (SKELTVED *et al.*, 2014; RUTJES *et al.*, 2016).

Then, we estimated the probability to produce a RREA from a given electron energy (ϵ) and a given electric field magnitude (E). We found that the stepping methodology is of major importance, and the stepping parameters are not set up satisfactorily in Geant4 by default. We pointed out which settings should be adjusted and provided example codes to the community. When properly set-up, the two Geant4 models showed a good overall agreement (within ≈ 10 %) with

REAM and GRRR. From the Geant4, GRRR and REAM simulations, we found that the probability for the particles below ≈ 10 keV to accelerate and participate in the penetrating radiation is actually negligible for the full range of electric field we tested ($E < 3$ MV/m). It results that a reasonable lower boundary of the low energy threshold (ε_c) can be set to ≈ 10 keV for any electric field below $E_k \approx 3$ MV/m (at STP), making it possible to have relatively fast simulations. For lower electric fields, it is possible to use larger ε_c , following a curve we provided (Figure 2.b).

The advantage of using more sophisticated cross sections able to accurately take into account low energy particles could be probed by comparing directly the O1 and O4 models. They showed minor differences that are mainly visible only for high E-fields ($E > 2$ MV/m), where low energy particles have more chance to runaway.

In a second part, we produced RREA simulations from the four models, and compared the physical characteristics of the produced showers. The two Geant4 models and REAM showed a good agreement on all the parameters we tested. GRRR also showed an overall good agreement with the other codes, except for the electron energy spectra. That is probably because GRRR does not include straggling for the radiative and ionisation energy losses, hence implementing these two processes is of primary importance to produce accurate RREA spectra. By comparing O1 and O4, we also pointed out that including precise modelling of the interactions of particles below ≈ 10 keV provided only small differences; the most important being a 5% change in the avalanche multiplication times and lengths. We also pointed out a discrepancy from Geant4 (O1 and O4) compared REAM, that is a 10% to 100% relative difference in the low energy part (< 100 keV) of the photon energy spectrum for an electric field of $E = 0.80$ MV/m. But we argued that it is unlikely to have an impact on spectra detected from satellites.

5 ELECTRONS ON LOW ENERGY REGIME

1

5.1 INTRODUCTION

There are two basically different types of high-energy electron sources in the atmosphere. The first type of sources are cosmic particles or radioactive decay, where the primary particles already have high energy. Cosmic particles impinge with high energy on to our atmosphere and create showers of more elementary particles and then secondary collision products. If the primary energy is as high as 10^{15} to 10^{17} eV, extensive air showers can create substantial densities of secondary particles that can play a role in lightning inception (DUBINOVA *et al.*, 2015). Air showers can be enhanced by high electric fields in thunderstorms, creating relativistic runaway electron avalanches (BABICH *et al.*, 2005; DWYER, 2007; DWYER *et al.*, 2008). Radioactive decay of atmospheric components is another direct source of high-energy particles (ENOTO *et al.*, 2017). The second type of sources are low-energy electrons (with energies in the eV range) that are accelerated in the fields of electric discharges like streamers or leaders into the so-called runaway regime where they can keep accelerating when the acceleration in a local electric field is larger than the energy losses due to collisions with air molecules. To reach this regime, they have to pass through some intermediate energy regime where the dynamic friction due to collisions is larger. The present chapter deals with this runaway process and the likelihood to pass through the friction barrier at intermediate energies toward runaway.

5.1.1 The concept of the friction curve

Electron run-away was first proposed by Wilson (1924) who suggested that thunderstorms could generate strong enough electric fields for electrons to continuously gain more energy than they lose through collisions with air molecules. This concept was further elaborated and quantified by Gurevich *et al.* (1992) who argued that the minimum of dynamic friction is at about 1 MeV electron energy in atmospheric air, and that an electric field above the threshold of 0.3 MV/m at standard temperature and pressure would maintain electron run-away at these energies. As discussed by Dwyer (2004), this dynamic friction curve for electrons with energies between 10 eV and 1 GeV can also be found in a report of the International Commission on Radiation Units and Measurements [ICRU 1984]. This is because dynamic friction acting on a particle is a common concept in high energy physics. E.g., a relativistic electron (with energy much above 1 MeV) on its path through matter loses energy mostly by creating many low energy particles while it es-

¹This chapter is published as: Cold electron run-away below the friction curve, Gabriel Diniz, Casper Rutjes, Ute Ebert, Ivan S. Ferreira, *J. Geophys. Res. - Atmospheres* 124, 189-198 (2019), DOI: 10.1029/2018JD029178

entially keeps its original direction; so it effectively loses energy continuously and experiences some friction force, known as a Continuous Slowing Down Approximation (CSDA), and it can be clearly distinguished by its high energy from the many liberated electrons in the eV regime. As discussed by Rutjes *et al.* (2016), this approximation is improved in some high energy codes by including the generation of all secondary particles below an energy threshold ε_{cut} into an effective friction force acting in the primary particle, while collisions where the primary particle loses more energy are treated explicitly and stochastically. In nuclear physics where one is interested in the thickness of some material needed to shield some particle radiation, the friction on the energetic particle is also called the stopping power of the material it penetrates.

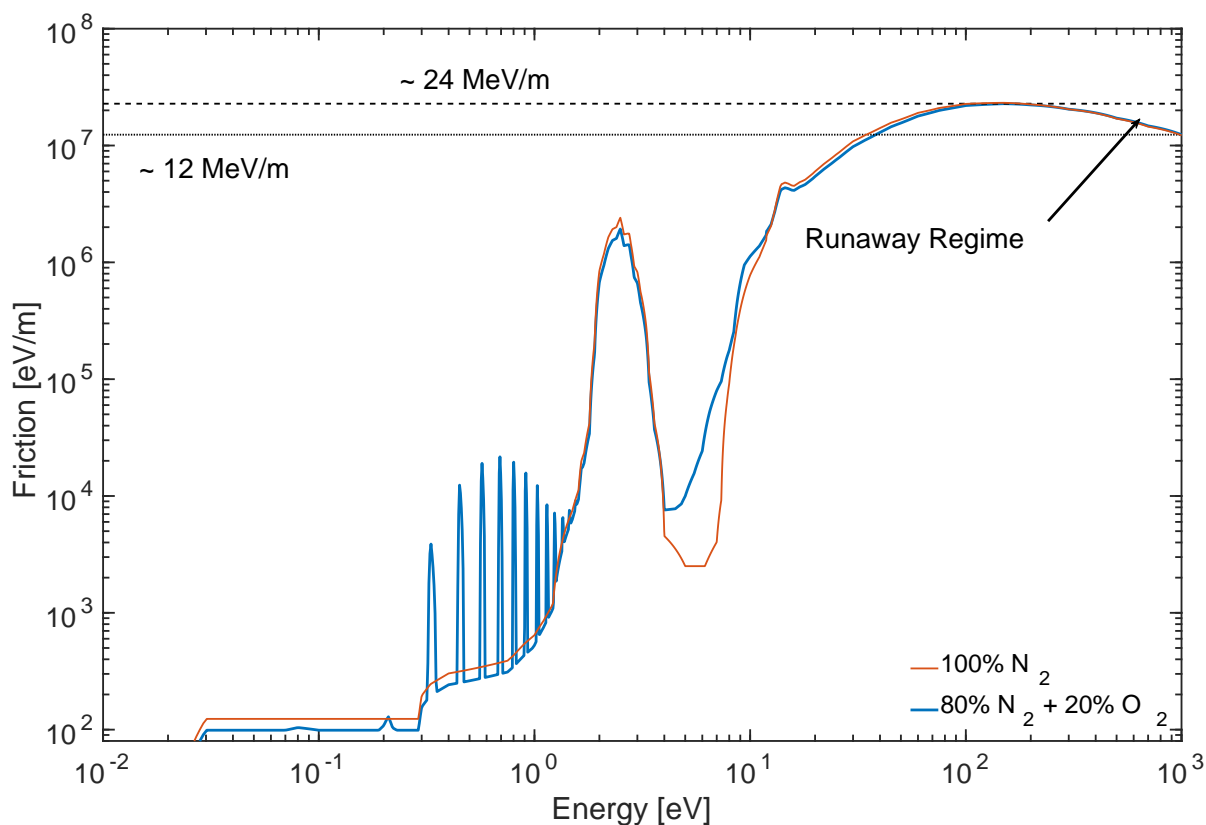


Figure 5.1: The friction curve as function of electron energy in the range from 0.01 eV to 1 keV for artificial air (which is a mixture of 80% nitrogen with 20% oxygen, blue curve) and for pure nitrogen (red curve), calculated according to the definition of Moss *et al.* (2006), that is reproduced in equations (5.1) and (5.2). Both curves are calculated with the processes listed in Table 5.1, and for a density defined by 273 K and 1 bar. The electric forces on electrons in electric fields of 12 and 24 MV/m are indicated by horizontal dotted and dashed lines, respectively.

While the friction concept is well based in high energy physics, Moss *et al.* (2006) have applied the concept to low energy electrons in the eV range as well, and, e.g., Colman *et al.* (2010) and Chanrion *et al.* (2016) use the same concept. Moss *et al.* (2006) define the dynamic

friction force $F_D(\epsilon)$ of an electron with energy ϵ through the equation²5.1

$$F_D(\epsilon) = \sum_{i,j} N_i \sigma_{i,j}(\epsilon) \delta\epsilon_{i,j}, \quad (5.1)$$

where N_i is the partial density of each air component i (nitrogen, oxygen, Argon etc.), $\sigma_{i,j}$ are the cross sections for an electron collision with a molecule of type i and collision type j (see Table 5.1), and $\delta\epsilon_{i,j}$ is the energy loss of the electron in the specific collision type. For an ionizing collision, the energy loss is the function $\delta\epsilon_{i,ion}(\epsilon)$ of the incident electron with energy ϵ is the ionization energy $\epsilon_{i,ion}$ plus the kinetic energy of the liberated second electron. In this case the average energy loss is calculated as

$$\delta\epsilon_{i,ion}(\epsilon) = \epsilon_{i,ion} + \frac{\bar{\epsilon}}{2 \arctan \frac{\epsilon - \epsilon_{i,ion}}{2\bar{\epsilon}}} \ln \left[1 + \left(\frac{\epsilon - \epsilon_{i,ion}}{2\bar{\epsilon}} \right)^2 \right], \quad (5.2)$$

where we used the empirical fit of Opal *et al.* (1971) with the constants $\bar{\epsilon} = 13.0$ eV for nitrogen and 17.5 eV for oxygen, and where we averaged over the energy distribution between the two outgoing electrons. Attachment cannot be taken into account in equation (1), as an attaching electron does not lose energy, but rather completely disappears from the ensemble. Also the second electron created in an impact ionization event cannot be incorporated into a friction force. In this sense, the friction concept is a flux concept that characterizes the behavior of individual particles, but does not take the dynamical change of the particle ensemble into account.

The friction curve as defined above is shown in Figure 5.1 as a function of electron energy. Results for artificial air and for pure nitrogen at 273 K and 1 bar are shown. For the lowest energies, there are only rotationally excited states that cause little friction. The peaks in the range from 0.3 to 1 eV are due to the vibrational states of oxygen in air, and absent in pure nitrogen. The electronic excitations above 1 eV create a local maximum of the friction at about 2.5 eV and are quite similar in air and in nitrogen. Also the global maximum of the friction at about 200 eV is quite similar for the two gases. Beyond 200 eV the friction decreases towards the run-away regime.

5.1.2 Value and validity of the friction curve in different energy regimes

Moss *et al.* (2006) interpret their friction force by direct comparison with the electric force. Thus the net force on an electron is approximated as the electric force minus the friction force. This interpretation leads to the notion of equilibrium points, where the net force of field acceleration and friction vanishes. These equilibrium points can be dynamically stable or unstable. When the friction increases with increasing electron energy, the electron will be driven back to a stable equilibrium point, and one would therefore expect that this point characterizes the mean electron energy in the given electric field. On the other hand, if the friction decreases for increas-

²Here we correct some notation error of the original paper of Moss *et al.* (2006) as one needs to sum over two indices, one for the molecule species and one for the collision types.

ing electron energy, the electron will move further away from the equilibrium point, and the point is unstable.

While this interpretation is correct for high energy electrons as they slow down almost continuously along a rather straight path as discussed above, it gives only a qualitative insight for electrons in the eV range and can lead to erroneous conclusions. This is the topic of the present work. The major short-comings of the deterministic friction approach in the eV regime are the following:

- A. For a direct comparison between electric and friction forces, they need to be aligned which is often not the case, as we exemplify below. The friction acts along any electron path, but electric acceleration acts only along the component of the path aligned with the electric field.
- B. In particular, there is no energy loss related to elastic scattering, but the elastic scattering plays an important role in changing the propagation direction of the electrons and hence the energy gain from the electric field. This effect is ignored in Equation (5.1).
- C. The collisions are discrete and stochastic; therefore there is no continuous energy loss, but rather there are discrete moments of time at which the electron loses a random amount of energy and attains a new random propagation direction.
- D. The deterministic friction approach cannot account for electron attachment to oxygen or other electronegative gas components, or for electron multiplication by impact ionization. In this sense, it is a flux quantity, characterizing the evolution of an ensemble with a fixed number of electrons. We will see that attachment has an important effect in a flux ensemble when comparing air with pure nitrogen. However, we will show that this effect is suppressed in a bulk ensemble where the electron number is changing continuously.

Points A and B are well explored by Chanrion *et al.* (2016) and Skeltved *et al.* (2014).

Point C makes it possible for electrons to enter the run-away regime in electric fields below the maximum of the friction curve; since the energy gain is continuous and the energy loss is stochastic, there is a chance for the electrons to gain enough energy between collisions to reach an energy region where the friction decreases. This possibility, was already observed by Li *et al.* (2009). We call this effect "tunneling through the friction curve".

Point D is here analyzed further, since the friction equation (BAKHOV *et al.*, 2000; CHANRION *et al.*, 2014, 2016; MOSS *et al.*, 2006) cannot include electron attachment or liberation. As said above, based on the similarity of the friction curves for pure nitrogen and for artificial air shown in Figure 5.1, one would expect similar run-away probabilities in both gases, but in a flux ensemble this is not seen.

5.1.3 This work

We have analyzed the electron motion through air and pure nitrogen in a range of electric fields with a focus on the stochasticity of the collisions. To do so, we use a Monte Carlo approach with a previously developed code to study the equilibrium or steady state between electric and friction forces in an electron ensemble, exposed to constant electric fields in the range from 1 kV/m to 35 MV/m. We have also simulated the random motion of electrons starting with an energy of 200 eV in electric fields of 16 to 34 MV/m, and their chance to run away.

5.2 METHODOLOGY

5.2.1 Software framework

We have simulated electrons in air or nitrogen with the Particle in Cell (PIC) Monte Carlo code `particle_core` that is described in Teunissen *et al.* (2016) and available on github³. The code follows the electron motion in a given electric field and their collisions with air molecules, where collision time and type are determined by a Monte Carlo procedure; hence the gas molecules are included as a random background of fixed density. The original code **particle_core** uses isotropic scattering of the electrons after collisions which is appropriate for electron energies up to the order of 20 eV, and the range of validity can be stretched by renormalizing the cross-sections; this is typically done for the cross-sections on the *lxcat.net* database⁴.

However, in order to study electron run-away, we have extended the code to 1 keV. Therefore we have modified the scattering model from an isotropic to an anisotropic algorithm as discussed below, and we have renormalized the elastic momentum transfer cross section according to Li *et al.* (2012). The cross sections for nitrogen are from Phelps and Pitchford (1985) and the oxygen data are from the Phelps compilation available in the *lxcat data bank*. All collision types with their energy losses are summarized in Table 5.1, they include attachment, elastic, excitation and ionization collisions.

We use the empirical fit of Opal *et al.* (1971) for the distribution of the energy between the two outgoing electrons after an ionization collision. The electron scattering angles after ionization are calculated as by Boeuf and Marode (1982). On the other hand, the scattering angle distribution of elastic and excitations collisions are the same and use the formula derived by Okhrimovskyy *et al.* (2002) for nitrogen and by Surendra *et al.* (1990) for oxygen.

³https://github.com/jannisteunissen/particle_core

⁴https://fr.lxcat.net/data/set_type.php

Table 5.1: List of the electron-molecule interactions included in the simulations. Different excitation types of the molecules are indicated as rot for rotations, v for vibrations, and all other symbols refer to electronic excitations, SUM is the sum over all singlet states. All cross section data are retrieved from the lxcat databank and refer to Phelps' compilation of measurements.

Result	Collision type	Energy loss [eV]	Result	Collision type	Energy loss [eV]
N_2	Elastic	0	O_2	Elastic	0
$N_2(\text{rot})$	Excitation	0.02	$O_2(\text{rot})$	Excitation	0.02
$N_2(\text{v1res})$	Excitation	0.29	$O_2(\text{v1})$	Excitation	0.19
$N_2(\text{v1})$	Excitation	0.291	$O_2(\text{v1res})$	Excitation	0.19
$N_2(\text{v2})$	Excitation	0.59	$O_2(\text{v2})$	Excitation	0.38
$N_2(\text{v3})$	Excitation	0.88	$O_2(\text{v2res})$	Excitation	0.38
$N_2(\text{v4})$	Excitation	1.17	$O_2(\text{v3})$	Excitation	0.57
$N_2(\text{v5})$	Excitation	1.47	$O_2(\text{v4})$	Excitation	0.75
$N_2(\text{v6})$	Excitation	1.76	$O_2(\text{a1})$	Excitation	0.977
$N_2(\text{v7})$	Excitation	2.06	$O_2(\text{b1})$	Excitation	1.627
$N_2(\text{v8})$	Excitation	2.35	$O_2(4.5\text{eV})$	Excitation	4.5
$N_2(\text{A3,v0-4})$	Excitation	6.17	$O_2(6.0\text{eV})$	Excitation	6
$N_2(\text{A3,v5-9})$	Excitation	7	$O_2(8.4\text{eV})$	Excitation	8.4
$N_2(\text{B3})$	Excitation	7.35	$O_2(9.97\text{eV})$	Excitation	9.97
$N_2(\text{W3})$	Excitation	7.36	O_2^+	Ionization	12.06 (Threshold energy)
$N_2(\text{A3,v10-})$	Excitation	7.8	O_2^-	3-body attach.	-
$N_2(\text{B'3})$	Excitation	8.16	$O^- + O$	Dissoc. attach.	-
$N_2(\text{a'1})$	Excitation	8.4	-	-	-
$N_2(\text{a1})$	Excitation	8.55	-	-	-
$N_2(\text{w1})$	Excitation	8.89	-	-	-
$N_2(\text{C3})$	Excitation	11.03	-	-	-
$N_2(\text{E3})$	Excitation	11.87	-	-	-
$N_2(\text{a"1})$	Excitation	12.25	-	-	-
$N_2(\text{SUM})$	Excitation	13	-	-	-
N_2^+	Ionization	15.6 (Threshold energy)	-	-	-

5.2.2 Setup of simulations

We performed two types of simulations, one in the bulk and one in the flux perspective. The distinction between these different statistical ensembles for reactive plasmas is described for instance in (BLEVIN FLETCHER, 1984; LI *et al.*, 2012; ROBSON, 1991). This distinction needs to be made here as well as free electrons appear and disappear during the discharge evolution.

Bulk: We studied an ensemble of electrons under the influence of a range of constant electric fields, i.e., we studied them in the bulk perspective (LI *et al.*, 2012) like an experiment does; the composition of the electron ensemble continuously changes as electrons are liberated by impact ionization and disappear due to attachment. The electrons started with vanishing energy, they accelerated initially, and then they converged in time to a stationary electron energy distribution. This analysis focusses on the energy distribution of the whole ensemble and allows to test the predictions of the deterministic friction curve concept.

Flux: Here we started with electrons with an initial energy of 200 eV aligned with the electric

field and investigated how they evolved in different electric fields. Focussing on "single" electrons, this analysis is done in the flux perspective (LI *et al.*, 2012), as needed in particle simulations. Differences between the electron behavior in air or pure nitrogen are highlighted by this setup, where we note significant differences in the probability of "tunneling" through the friction curve due to large energy fluctuations (see Figure 5.2) in combination with electron attachment to oxygen in air.

Both simulation types were performed without geometric boundary, in pure nitrogen or in a mixture of 80% nitrogen and 20% oxygen (artificial air), at a temperature of 273 K and a pressure of 1 bar.

The difference between bulk and flux perspectives highlights a possible source of error, if one does not pay attention on one's statistical framework, since both perspectives are valid in different contexts. The flux perspective is what happens with the individual particle while the bulk perspective shows the collective behavior of the whole particle ensemble.

5.2.2.1 Bulk simulations

The bulk simulations were performed with 10^5 electrons with an initial energy of 0 eV in constant electric fields. The electron number in the ensemble was kept constant by adding an electron at random from the instantaneous electron ensemble after an attachment reaction and by removing a random electron from the ensemble after an ionization reaction; in this way the ensemble averages stay the same, the ensemble develops on its intrinsic time scales, but the particle number stays both numerically manageable and sufficiently large to allow good averaging. We covered the range from 1 kV/m to 35 MV/m of electric fields in order to cover the whole domain of the friction curve represented in Figure 5.1.

Our energy range is up to 1 keV, and electrons that reach 1 keV in this set up are removed from the simulation and a random particle is added just like after an attachment reaction. Since the energy of the added particle is randomly chosen from the instantaneous distribution, the distribution does not change. However, in high electric fields the ensemble of electrons below 200 eV is strongly coupled to the ensemble with higher energies, therefore our distribution shows artifacts due to the removal of electrons above 1 keV. This can be seen in Figure 5.3 where the mean electron energy stops to increase for electric fields above 10 MV/m.

We considered 200 different electric fields values equally spread on a logarithmic scale, and we let the simulations run until the electron ensemble reached steady state. After 4 ns or less we noticed no significant changes of the mean energy and its standard deviation for all electric field values considered. And the standard deviation is always similar to the mean energy which reflects the broad energy distributions shown in the next section.

5.2.2.2 Flux simulations

The flux simulations start with 10^6 electrons with 200 eV energy. The electrons were launched in the direction opposite to the field, so they gain maximal initial acceleration. We let the electrons evolve for 100 ns in constant electric fields between 16 and 34 MV/m. When the electrons reach 1 keV or attach to oxygen, they are flagged and not followed further. When an ionization reaction occurs, the electron with the higher energy is kept, while the other one is removed. In this manner, we focus on those electrons most likely to run away, i.e., on those that might "tunnel" through the friction barrier.

We compute the probability that an electron reaches 1 keV up to time t , by accumulating the number of all electrons that reach 1 keV up to that time, divided by the total number of initial electrons. In the same manner, we define the cumulative probability of attachment up to time t as the ratio of the total number of attachments up to time t over the total number of initial electrons.

Figure 5.2 shows the particle energy fluctuations in the flux simulation. The energy varies by almost 5 orders of magnitude due to high collision frequency and high electric field. The two different colors in the figure represent two different particles, and we see that one particle disappears after some time due to an attachment collision.

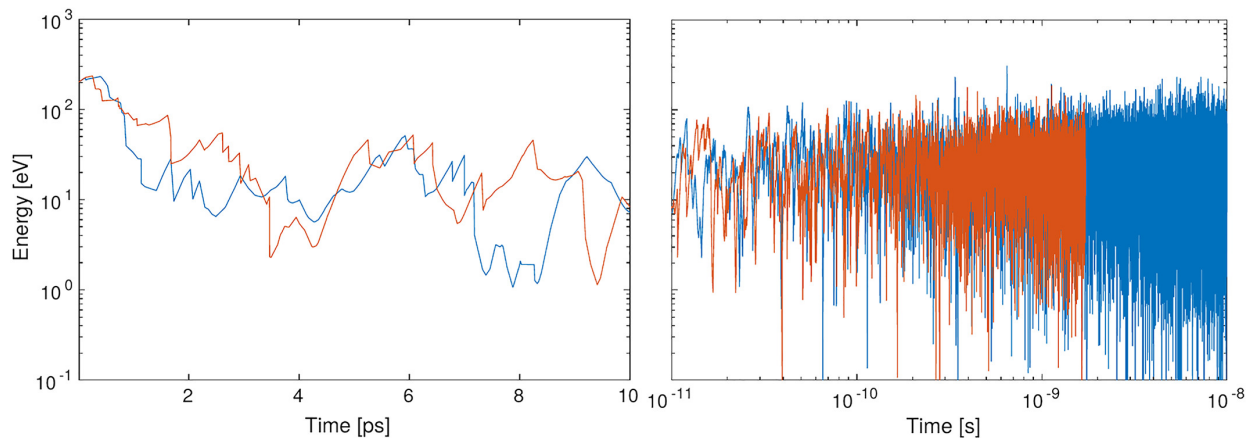


Figure 5.2: Statistical behaviour of the electron energies in air in the flux simulation: energy fluctuations of 2 electrons (red and blue) in a 26 MV/m electric field as a function of time; the left panel shows the time from 0 to 10 ps on linear scale, the right panel from 10 ps to 10 ns on logarithmic scale.

5.3 RESULTS AND DISCUSSION

5.3.1 Steady state electron energy distributions in different fields and the friction curve

5.3.1.1 The electron energy distributions

The electron energy distributions in steady state as a function of applied electric field are displayed in Figure 5.3. To share the same field axis with all three panels, the field is plotted on

the y-axis. It ranges from 1 kV/m to 35 MV/m which is well above the literature value for the electron run-away threshold of approximately 26 MV/m.

The left panel shows the mean electron energy in artificial air or pure nitrogen as a function of the electric field. The mean electron energy as a function of electric field is essentially the same for pure nitrogen or air, except for mean electron energies between 0.3 and 2 eV which correspond to electric fields between roughly 10^4 and 10^5 V/m (10 to 100 kV/m). There the mean electron energy in air is lower than in pure nitrogen. This effect can be attributed to electron energy losses due to the excitation of the vibrational states of oxygen, as also visible as the spikes around 1 eV of energy in the friction curve in Figure 5.1. The mean energy saturates when the electric field approaches 10^7 V/m. This is an artifact of the electron removal at 1 keV.

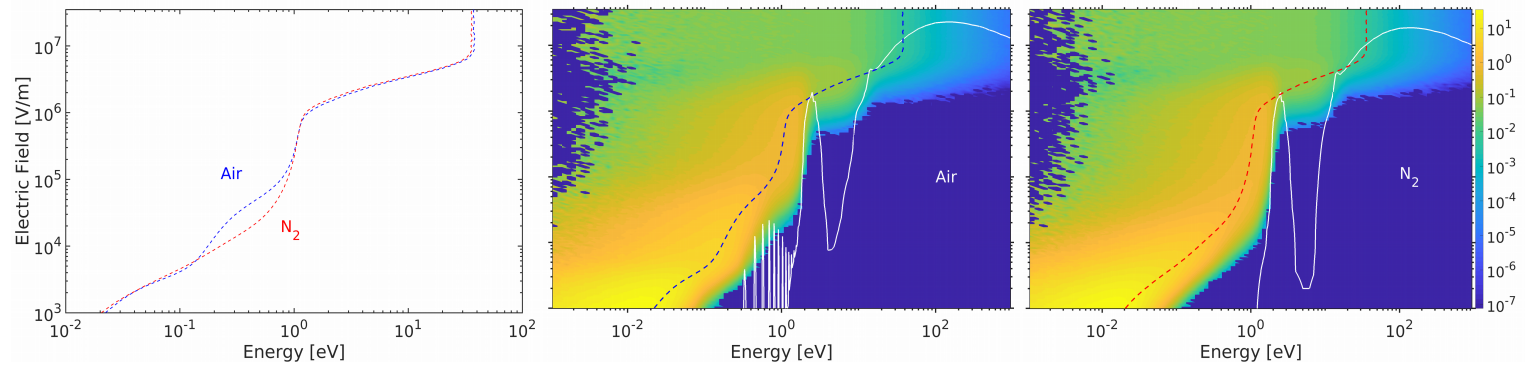


Figure 5.3: Results of the bulk simulation for the steady-state electron energy distributions in constant electric fields ranging from 10^3 to 3.5×10^7 V/m (equivalent to 1 kV/m to 35 MV/m). Left panel: Mean electron energy as a function of the electric field for artificial air (blue) and for pure nitrogen (red). (The electric field is plotted on the y-axis and applies to all three panels.) Middle panel: Electron energy distribution in air in color coding as a function of the electric field. Right panel: The same as in the middle panel, but for pure nitrogen. The color code indicates the electron count per (logarithmic) energy bin, normalized by the total number of particles. The blue or red dashed lines in the middle and the right panel are the mean electron energies that are shown on the left panel as well. The white curves in the middle and the right panel are the respective friction curves from Figure 5.1 divided by the elementary charge, hence they have dimension of electric field and can be identified with the equilibrium points of the net force for each electric field, as discussed in the introduction.

The middle and right panels show the electron energy distribution in air or nitrogen in color coding as a function of the electric field. The mean energy from the left panel is plotted as a dashed line in the middle and the right panel for the respective gas. Furthermore, the friction curves from Figure 5.1 are divided by the elementary charge and inserted as a white line in the panels for air or pure nitrogen. We will come back to this curve in the next subsection.

For better visualization of the data in Figure 5.3, we display the electron energy distributions in air for some selected electric fields between 180 kV/m and 4.27 MV/m in Figure 5.4. We note that as the electric field increases, the electron energy distribution shifts from a clear maximum below 2 eV to energies above 4 eV. A local minimum of the energy distribution around 3 eV develops in this case that reflects the local maximum of the collisional energy losses due to electronic excitations. A similar observation has been made by Colman *et al.* (2010).

For electric fields above roughly 3 MV/m, the electron energy distribution is already non-

zero up to electron energies of 1 keV. This means that electrons already have a non-vanishing probability to run away in such a field.

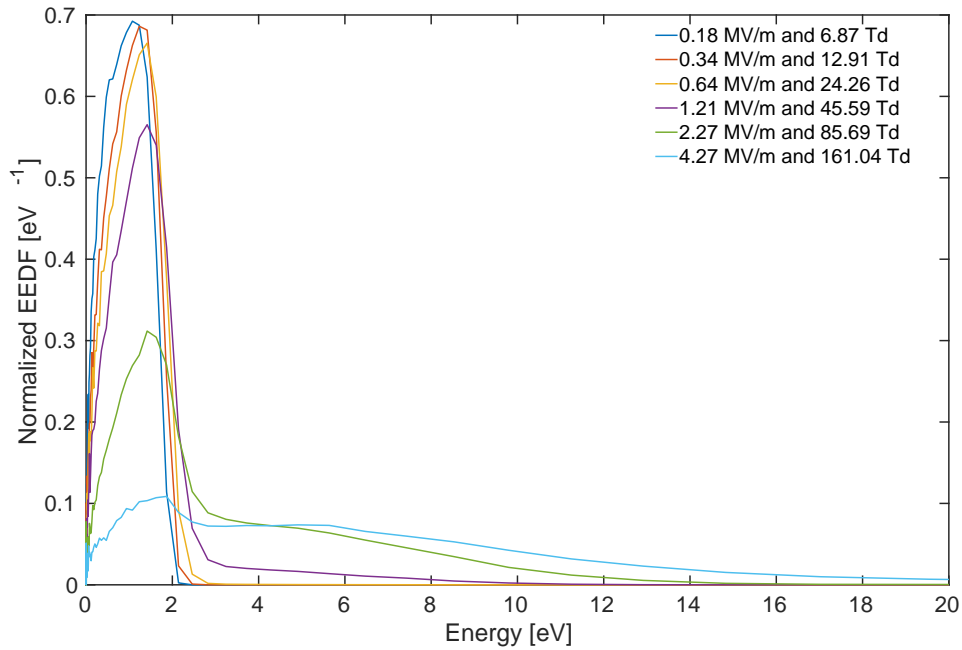


Figure 5.4: Selected electron energy distributions from Figure 5.3 for air. The legend displays the electric field in two different units, in MV/m for reference to the present results, and in Td for comparison with Colman *et al.* (2010).

5.3.1.2 The relation to the friction curve

The friction curve from Figure 5.1 is inserted in the middle and the right panel of Figure 5.3 as a white line. If it were a systematic approximation, then for each electric field, the intersection of the horizontal line of constant field with the friction curve would define an equilibrium point at this field — as described in the introduction. So if friction curve and electric field would fully characterize the electron energy in a deterministic manner, the electron energy distributions should fully collapse onto the friction curves in Figure 5.3. But obviously that is not the case. And we already have identified the four short-comings A to D of this approximation in the introduction.

A further analysis of the middle and right panels of Figure 5.3 shows the following: For fields up to 10^4 V/m, the friction curve is far above a wide electron energy distribution. For electric fields between 10 kV/m and 1 MV/m, the friction curve in practice seems to mark the upper limit of the electron energy distribution, or the energy range where the distribution function decays steeply.

For a large range of electric fields, there are several intersections with the friction curve, i.e., a number of equilibrium points. In a purely deterministic setting, one would expect electron energies to be localized at the stable equilibrium points, but that is also not the case. The small

dip of the energy distribution at about 3 eV for 4.27 MV/m is a small indication for such behavior.

When there are several stable equilibrium points of the electron energies in a deterministic interpretation, there can be transitions between them. We call this a tunneling effect. (Of course, this tunneling is due to stochastic fluctuations, and not to quantum mechanics.) We observe a tunneling process in two different energy and field regimes: first at the electronic excitation peak at about 2 eV, where the electron energy distributions start to tunnel through the friction curve for electric fields of about 1 MV/m; secondly, at the ionization region above 10 eV for electric fields near the classical breakdown value of 3 MV/m.

We finally remark that the electron energy distributions of air and pure nitrogen are quite similar, despite their differences in electron attachment and vibrational excitations.

5.3.2 Electron run-away in electric fields below the run-away threshold

5.3.2.1 An analysis in the flux perspective of single electrons

We now analyze the probability that an electron reaches the run-away regime as a function of the electric field when it starts out with an energy of 200 eV, and when it is optimally aligned with the electric field. This energy is chosen because the friction at this energy is maximal, see Figure 5.1. The electrons then have a high collision frequency and large energy losses per collision. The temporal evolution of the energy of two electrons starting with an energy of 200 eV in an electric field of 26 MV/m is shown in Figure 5.2.

A basic difference between air and pure nitrogen is that electrons in air can attach to oxygen. As they fluctuate through a large range of energies, electrons in air can reach energies where attachment is important, and then they will disappear, as is also illustrated in the right panel of Figure 5.2. In nitrogen this can not happen, and the probability that a given electron will run away is much larger.

This effect is quantified in Figure 5.5. The top panel shows the probability that an electron in air starts with 200 eV and attaches to oxygen up to time t . We can distinguish two different features: first, the probability of attachment reaches almost 100% after 0.1 μ s in all electric fields between 16 and 34 MV/m; second, the probability to attach diminishes with increasing electric fields. This is because the mean electron energy gain between collisions increases, and hence it is less likely that the electron will reach the low energies needed for attachment.

The bottom panel in Figure 5.5 shows the probability for an electron with initial 200 eV to reach 1 keV up to time t while it moves through air (dotted curves) or pure nitrogen (dashed curves). The colors of the lines indicate electric fields from 16 to 34 MV/m. Since nitrogen does not have attachment reactions, there is no sink mechanism for the electrons in the simulation, except that they are removed from the sample when they reach 1 keV, while electrons in air attach massively. Therefore single electrons in pure nitrogen reach 1 keV after maximally 100 ns with a probability of 50% in a field of 24 MV/m, while single electrons in air need more than 34 MV/m

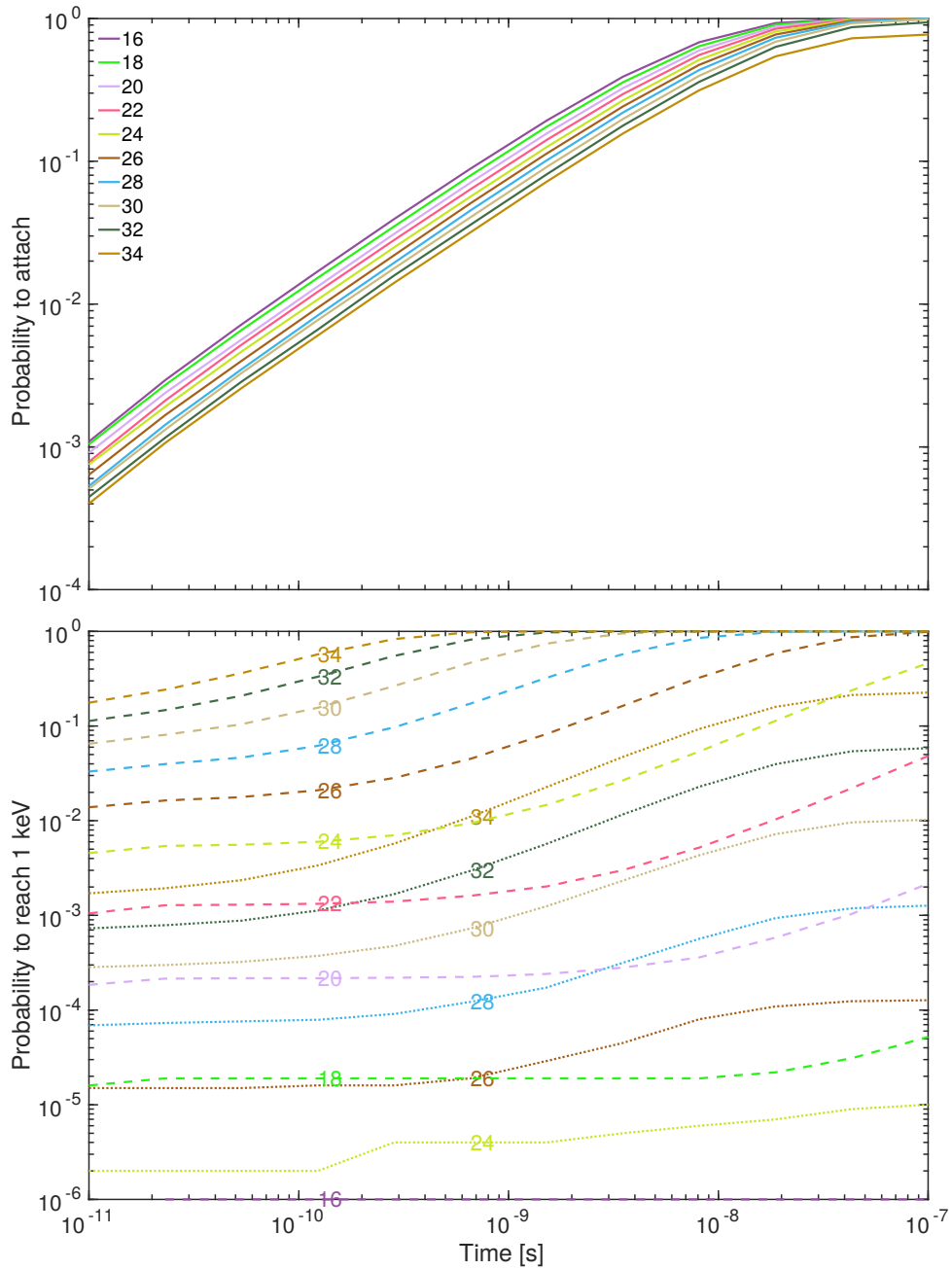


Figure 5.5: Results of the flux simulation for electrons starting with 200 eV in electric fields from 16 to 34 MV/m where lines of different color refer to different fields. Top panel: probability $P(t)$ that an electron in air attaches to oxygen up to time t , as a function of time (for 10 ps to 100 ns). Bottom panel: probability $P(t)$ that an electron in air (dotted lines) or pure nitrogen (dashed lines) reaches 1 keV, again as a function of field (color coded) and time. The numbers in the plots express the applied electric field in multiples of MV/m.

for a run-away probability above 50 %. In a field of 18 MV/m, single electrons in pure nitrogen already reach 1 keV within 100 ns with a probability of about 10^{-4} while in air they would need a field of 25 MV/m.

5.3.2.2 The bulk perspective on the electron ensemble

From the above analysis one might conclude that electron run-away is largely suppressed in an electronegative gas where electrons can attach. However, this is what happens in the flux perspective that focussed on the energy evolution of single electrons.

The energy fluctuations shown in Figure 5.2 indicate that electrons with initial energies as high as 200 eV play no very distinctive role in electron run-away, as they typically first explore a large range of lower energies before possibly running away.

In fact, Figure 5.3 clearly indicates that the electron energy distribution stretches to 1 keV for electric fields above 3 MV/m. This is the fact both for air and for pure nitrogen. The energy distribution of the whole electron ensemble is established collectively by all collision processes including electron loss due to attachment and electron gain due to impact ionization, and no major difference between air or pure nitrogen can be seen.

5.4 CONCLUSION

We have performed two different types of Monte Carlo simulations, both in pure nitrogen and in artificial air. In the bulk simulations, we have calculated the electron energy distributions of a dynamically changing electron ensemble in a wide range of electric fields. We have found that electrons can reach energies of 1 keV (which was the upper limit of the energies we explored) already in a field of about 3 MV/m, which is the classical break-down field.

We also have compared our results with predictions from the friction curve as calculated by Moss *et al.* (2006). In the introduction, we have already discussed that friction is a valid concept at high (relativistic) energies, but that there are short-comings when applied below 1 keV: in particular, the non-alignment of electron motion and electric field, due to the random electron scattering directions after electron molecule collisions is not taken into account, also the energy loss is not a continuous friction process, but happens in discrete stochastic events. And the dynamic change of the electron ensemble cannot be included either. For this reason, the friction curve in the energy range below 1 keV does not characterize the mean electron energies in a given electric field, but in practice it rather seems to act like the upper bound of a very broad electron energy distribution. Where the friction curve would predict the coexistence of two stable electron energies, the stochastic electron ensemble "tunnels" through the curve and creates a broad distribution. For the same reason, the maximum of the friction curve of 24 MeV/m is not a strict threshold to run-away, but electrons can reach energies of 1 keV in fields as low as 3 MV/m.

In a second Monte Carlo simulation, we have calculated the probability that a single electron starting with 200 eV reaches 1 keV or is being attached, in a range of electric fields. Here attachment is a major factor, and one might conclude that electron run-away below fields of 24 MV/m is suppressed by attachment in air, but not in pure nitrogen. However, this single electron (or

flux) perspective does not represent the behavior of the whole reactive electron ensemble in the ensemble (or bulk) perspective of the first Monte Carlo experiment, as discussed above. This first experiment shows that the electron ensemble can "tunnel through the friction curve" for electric fields well below the runaway threshold, in a similar manner in air and in pure nitrogen.

6 DETECTION AND EFFECTS OF ATMOSPHERIC NEUTRONS

1

6.1 INTRODUCTION

6.1.1 Neutrons as a footprint of thunderstorms

The relation between neutron and thunderstorm research has started with the radiocarbon studies of tree rings by Libby and Lukens (1973), as reviewed recently by Rutjes and Ebert (2017). Later Shah *et al.* (1985) proved a relative increase of neutron emissions over the cosmic background to be correlated with thunderstorms. The first attempts to explain neutron production by lightning focused on fusion, and dominated the literature for some decades, but this mechanism was disproven by Babich and Roussel-Dupré (2007). The fusion mechanism is not possible due to a too low energy and density of deuterium in air. Even for electric fields of 20 to 30 times the conventional breakdown field, the neutron yield from fusion remains small in comparison to the original estimates of Libby and Lukens (1973). Babich and Roussel-Dupré (2007) and in more detail Babich *et al.* (2010) proved that the correct explanation for the occurrence of neutrons in thunderclouds is the photonuclear reaction of gamma rays in the energy range from 10 to 30 MeV with nitrogen or oxygen nuclei. This photonuclear reaction is due to the so-called Giant Dipole Resonance (GDR) mechanism (BALDWIN KLAIBER, 1947; VARLAMOV *et al.*, 1999). Neutron observations are thus a diagnostic tool on ground for the occurrence of gamma rays with energies between 10 and 30 MeV in a thundercloud, a gamma-ray detector can provide a similar prove but the neutrons will then be a signature of gamma rays not present in the photon spectrum due to photonuclear reactions.

6.1.2 Neutron production through TGFs and gamma-ray glows

The photonuclear reaction mechanism requires a source generating gamma rays with energies above 10 MeV which is the approximate binding energy of neutrons in atmospheric nuclei. More precisely, the binding energies are 10.55 MeV for nitrogen, 15.66 MeV for oxygen, and 9.87 MeV for argon (Dietrich Berman, 1988). There are two known types of high energy atmospheric phenomena that can produce gamma rays above these thresholds, namely, Terrestrial Gamma-ray

¹This chapter is a version and combination of such publications: TGF afterglows: a new radiation type from thunderstorms, C. Rutjes, G. Diniz, I.S. Ferreira, U. Ebert, *Geophys. Res. Lett.* 44, 10702 - 10712 (2017), <https://doi.org/10.1002/2017GL075552> and Modeling neutron emissions in High Energy Atmospheric Phenomena, Gabriel Diniz, Casper Rutjes, Ute Ebert, Ivan S. Ferreira, Eliah Fernanda T. Sao Sabbas, *J. Geophys. Res. - Atmospheres* 123, 12726 - 12737, <https://doi.org/10.1029/2018JD028962>

Flashes (TGFs) and gamma-ray glows. TGFs are microsecond-long bursts of photons that were first observed from space (BRIGGS *et al.*, 2010; FISHMAN *et al.*, 1994); they can be accompanied by bursts of electron positron pairs (BRIGGS *et al.*, 2011; DWYER *et al.*, 2008), and they correlate with leader propagation. Glows, on the other hand, probably originate from relativistic runaway electron avalanches (RREA) in the field of the thundercloud and last much longer, for minutes; they have been observed on ground (where they are called terrestrial ground enhancements by some authors), from balloons and aircraft (ADACHI *et al.*, 2008; CHILINGARIAN *et al.*, 2010, 2011; EACK *et al.*, 1996; MCCARTHY PARKS, 1985; TORII *et al.*, 2002; TSUCHIYA *et al.*, 2007). Terrestrial ground enhancements have been found to be correlated with neutron detection as well (CHILINGARIAN *et al.*, 2017). The different properties of flashes and glows have been related to different physical mechanisms as explained by Dwyer *et al.* (2012) and Rutjes *et al.* (2016, 2017). While lightning leaders produce TGFs, lightning is observed to terminate gamma-ray glows (CHILINGARIAN *et al.*, 2015; KELLEY *et al.*, 2015; MCCARTHY PARKS, 1985; TSUCHIYA *et al.*, 2013).

6.1.3 Neutron emissions from thunderstorms measured with different detectors

Three main types of neutron detectors have been used by different researchers (CHILINGARIAN *et al.*, 2012; GUREVICH *et al.*, 2012; KOZLOV *et al.*, 2013; MARTIN ALVES, 2010; SHYAM KAUSHIK, 1999; STARODUBTSEV *et al.*, 2012; TOROPOV *et al.*, 2013; TSUCHIYA *et al.*, 2012): a thermal helium-based detector (^3He detector), a boron counter detector (^{10}B detector), and the Neutron Monitor NM-64. A thermal detector is most efficient for particles with energy of the order of 1 eV, a boron-based detector has a peak of efficiency at 2.45 MeV, while a Neutron Monitor NM-64 is focused on higher energies and has a small efficiency below the MeV energy range (reaching 10% for 3 MeV and 2% for 0.5 MeV). Hence, all three detector types operate in very distinct and narrow energy windows, which makes it difficult to analyze the whole spectrum. Recently, Bowers *et al.* (2017) measured a burst of neutrons after a lightning strike onto a wind turbine. The neutron detection was followed by a glow of gamma-ray photons which were presumably created by the neutrons themselves. Their detection system consists of three scintillation detectors (SmPI and LgPI, where PI stands for Plastic scintillator; and NaI(Tl)) and two additional electronics for noise control. The neutrons were detected through capture in LgPI that then releases photons with a characteristic energy of 2.223 MeV. The photons appeared on a millisecond time scale and with the characteristic energy signature of neutron capture, consistent with the TGF afterglow predicted by Rutjes *et al.* (2017). Enoto *et al.* (2017) also have measured the TGF afterglow during their measurements of neutrons and positron beams. They have observed gamma rays with time scale and energy cutoff consistent with the neutron capture process along with their decay record. Their detectors were based on BGO and NaI scintillation crystals and covered the energy range 0.2–48 MeV. Furthermore, they also found and identified the radioactive decay products of the nuclei that had been created by the photonuclear reaction, that is, isotopes such as ^{13}N .

6.1.4 Neutron propagation to ground

Neutrons interact with air through elastic and inelastic scattering and capture. The dominant process is elastic scattering for most of the relevant energy range below 20 MeV, while capture is the most rare process among the three (KÖHN *et al.*, 2017). But scattering only cools the neutrons down, while capture is the only loss process. Capture is the most efficient at low neutron energies. Therefore, the secondary gamma rays formed when a neutron is captured in a nucleus have energies of the order of a few MeV due to the energy released during capture. This is the mechanism of the TGF afterglow predicted by Rutjes *et al.* (2017), and first measured by Bowers *et al.* (2017) in a downward directed TGF.

6.1.5 Earlier simulations

Neutron emissions have been simulated by Babich *et al.* (2010), Carlson *et al.* (2010) and Köhn and Ebert (2015). Babich *et al.* (2010) conclude that there are 4.3×10^{-3} neutrons produced per photon, and that the neutron energy is in the range of 0 to 20 MeV both at production and at sea level altitude. The neutrons diffuse to distances of the order of km from the source axis, when reaching ground.

Carlson *et al.* (2010) assume an RREA spectrum to simulate an initial photon source and calculate neutron production and detection at sea level. Their results are in general agreement with Babich *et al.* (2010) concerning energy range and estimated production rate. Both papers predict the neutron pulse to last from the order of μs to seconds and conclude that the neutrons are produced along the photon trajectory through the atmosphere rather than from a point-like source, in contrast to Martin *et al.* (2010).

Köhn and Ebert (2015) simulate a negative lightning leader at the moment of stepping, where the lightning leader is simulated electrostatically as previously by Moss *et al.* (2006), Celestin and Pasko (2011), Celestin *et al.* (2012), and Xu *et al.* (2012). The accelerated electrons are the source of bremsstrahlung photons that produce neutrons. According to Köhn and Ebert (2015), these neutrons have energies up to 20 MeV at source altitude.

Bowers *et al.* (2017) perform Monte Carlo simulations of TGFs with GEANT4² to understand the neutron signature in the LgPI detector. A comparison between the measured 1-10 MeV photon spectrum and the GEANT4 simulations shows general agreement in the characteristic energy release on the capture reaction, hence confirming their observations. In their simulations they use an initial photon spectrum produced by a RREA, as parameterized by Dwyer *et al.* (2012), and they simulate neutron creation and propagation to ground. This ground signature is used as an input to filter the particles that reach the detector. Hence they can infer the number of TGF gamma-rays from the observed count rate in the detector on ground. They notice a longer signal of low energy neutrons in their simulations that is due to neutron thermalization in the ground, and not only in the air.

²<http://geant4.web.cern.ch/>

6.2 SIMULATIONS

In this chapter, we explore both the neutron effects in the atmosphere and their footprint at sea level. For such we performed three types of simulations:

- **For ground detection:** we split the relevant gamma-ray energies of 10 to 30 MeV into four intervals of 5 MeV width, so we investigate the energy intervals [10 MeV, 15 MeV], [15 MeV, 20 MeV], [20 MeV, 25 MeV], and [25 MeV, 30 MeV] separately. We assume that each energy interval has a flat spectrum of primary gamma rays and that all rays are directed in the same downward direction. This approach allows us to construct particle distributions for arbitrary gamma-ray sources by superposition, without further hypotheses on the initial energy spectrum. The source altitudes range from 300 m to 6 km. At higher source altitudes, too few particles reach sea level. So in total we performed 36 different simulations, namely for 9 different source altitudes and for 4 different energy ranges.
- **For TGF afterglow effect:** a simulation assuming that the TGF is at 8 km altitude and directed downward. It starts with 10^8 photons with uniformly distributed energies between 10 and 30 MeV. Using the results of Gjesteland *et al.* (2015), and assuming that 1% of the photons with energy above 1 MeV have an energy above 10 MeV, we should actually consider $10^{16\pm 1}$ photons above 10 MeV rather than 10^8 . But as the evolution outside the TGF source is linear, we can take this into account by multiplying the result of the evolution of 10^8 photons by a factor $10^{8\pm 1}$.
- **For TGF afterglow enhanced statistics:** the simulation starts directly with 10^8 neutrons at an altitude of 10 km. As photons with energies between 10 and 30 MeV are converted into neutrons with a probability of about 4×10^3 according to our calculations and to Babich *et al.* (2010), we have to multiply our simulation results for particle numbers now with a factor of $4 \times 10^{5\pm 1}$ to simulate a TGF with $10^{16\pm 1}$ primary photons in the required energy range.

6.3 SETUP OF THE SIMULATIONS

We simulate photons and neutrons in air by Monte Carlo simulation with the software package FLUKA (FERRARI *et al.*, 2005), which has a complete physics list for air in our energy regime (RUTJES *et al.*, 2016). FLUKA and other Monte Carlo simulation codes (GEANT4, EGS5, GRRR, MC-PEPTITA) were compared by Rutjes *et al.* (2016) where a standard input was used to test the effects of the different approximations and methods of each program on the output. The authors have noticed a general agreement between the programs, but differences due to the straggling effect and due to the implementation of friction were observable. The straggling effect is appropriately implemented in FLUKA. The photon interactions implemented in FLUKA are (FERRARI *et al.*, 2005): pair production, Compton scattering, photoelectric effect, Rayleigh

scattering, photon polarization, photonuclear reactions (GDR, Quasideuteron interactions, Vector Meson Dominance Model), and generation and transport of Cherenkov, scintillation and transition radiation. Since there is no energy gain in our simulations, the energy of the particles will always be below the initial energy, 10-30 MeV in this case.

Because at least 10 MeV are required to liberate neutrons in a photonuclear reaction from nitrogen or oxygen nuclei, the neutrons in our simulation always have energies below 20 MeV. In this energy range, FLUKA transports the neutrons with a multi-group algorithm using a cross-section library of 260 groups (FERRARI *et al.*, 2005). The angular probabilities are treated with a Legendre polynomial expansion of the actual scattering distribution. Further details on FLUKA physics can be found in the manual available at the official website <http://www.fluka.org/fluka.php>.

We use a low energy cutoff of 10 keV for photons and of 10^{-12} eV for neutrons which are the recommended minimum thresholds in FLUKA.

For this work, a cylindrical domain from sea level up to 19 km altitude and with a radius of 12 km was adopted. The atmospheric density profile of dry air was simulated by 76 layers of constant density with 250 m of height, consisting of 78.085 % N₂, 20.950 % O₂ and 0.965 % Ar. The atmospheric density in these layers was linearly interpolated from the density of the 1976 U.S. standard atmosphere, defined by the United States Committee on Extension to the Standard Atmosphere (COESA, 1976). The temperature, however, is constant and equal to 293 K everywhere. Each horizontal slab interface acts as an infinitely thin virtual detector, which detects any passing particle. The output that we record at these interfaces is as follows: the particle type and its kinetic energy, its position in the interface plane, and the time of passing.

6.4 SIMULATED NEUTRON EFFECT IN THE ATMOSPHERE

Figure 6.1 shows the evolution as function of the logarithm of time. Photons are included only if their energy exceeds 10 keV. The presented quantities are defined in section 2.1. Figure 6.1 (top), viewed from left to right, shows first the light cone of the developing TGF as non filled red to yellow contours. Photons moving upward have been backscattered or they are secondary, which implies that they have lost a significant amount of energy. Therefore, only the primary photons (that move downward), will be energetic enough to produce neutrons; hence, the neutron cloud appears only at lower altitudes in this configuration. The mean free path of the photonuclear reaction scales with density as $l = l_0 \frac{n_0}{n}$. For the integrated density (starting at 8 km downward), the mean free path of the photonuclear cross section equals 5 km, consistent with Figure 6.1.

When the neutrons are just created, their typical energy is of the order of 13 MeV (the energy of the maximum of the photonuclear cross section minus the neutron-binding energy in nitrogen nuclei); then the neutrons diffuse isotropically and cool down (the neutron energy is given in Figure 6.1, bottom). While cooling down, the intermediate neutrons do create some photons by inelastic scattering, visible in Figure 6.1 (top) at around 3 km, where the TGF envelope extends longer in

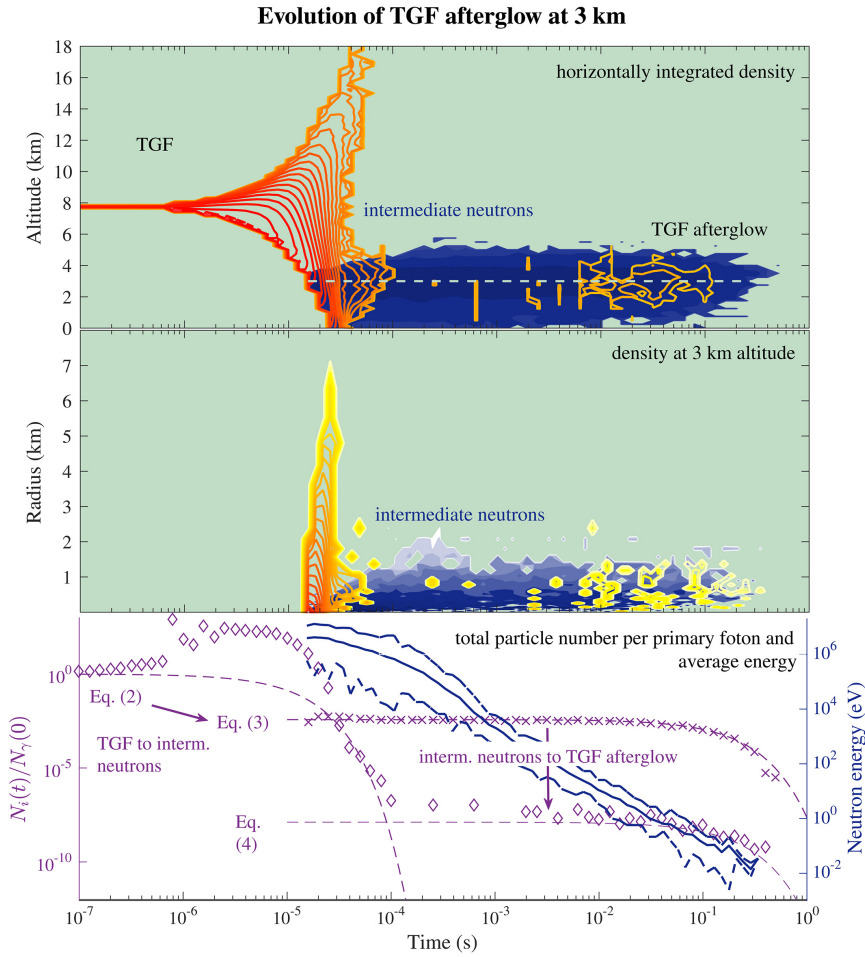


Figure 6.1: Evolution of the TGF afterglow generated by the primary TGF as a function of the logarithm of time. (top and middle) Contour figures of the photon and neutron density, on a logarithmic scale; contours represent half a decade (i.e., a factor of $10^{0.5}$). The contour lines (red, yellow to white) are photons above 10 keV, the filled contours (blue to white) are neutrons. In Figure 6.1 (top) the density is horizontally integrated. Figure 6.1 (middle) gives the density profile as a function of radius at 3 km altitude, the density is averaged over rings around the symmetry axis. (bottom) Two quantities: on the left y axis in purple, the total particle number $N_i(t)$ of photons (diamonds) and neutrons (crosses), per initial photon $N_\gamma(0)$, with their approximations given by equations 6.2–6.4; on the right y axis in blue, the average neutron energy is drawn as a solid line, together with the minimal and the maximal neutron energy as dashed lines.

time than at other altitudes, but after 10^4 s the secondary photons produced by inelastic scattering have energies below 10 keV and are thus not shown. The time for neutron thermalization scales as $t = t_0 \frac{n_0}{n}$. We see in Figure 6.1 (bottom) that around 3 km altitude the inter-mediate neutrons take 0.5 s to thermalize. Neutrons can (at any energy) be captured again, but the cross section for neutron capture increases for decreasing energy as $\sigma_{capture} \propto 1\sqrt{E_{neutron}} \propto 1v_{neutron}$, according to the so-called $1/v$ law (see chapter II of Blatt Weisskopf, 1979). Because of the $1/v$ law, the rate k_{capt} of neutron capture and hence of photon production in the TGF afterglow is constant for constant air density, as $k_{capt} = v_{neutron}\sigma_{capture}n_{air} \propto \frac{n}{n_0}$. Actually, the most significant capture pathway is not producing a high-energy photon, but of radiocarbon (i.e., $n + {}^{14}\text{N} \rightarrow {}^{14}\text{C} + p$). The cross section for this reaction is $\sigma_{capt} = 1.8 \times 10^{28} \text{m}^2$ (CHOI *et al.*, 2007) at thermal velocities (0.025 eV, 2200 m/s), yielding a neutron capture rate of $15.8 \text{ s}^{-1} \frac{n}{n_0}$. The TGF afterglow time scale

is thus (in seconds)

$$T_{afterglow}(h) = 1/k_{capt} \approx 0.063 \times \exp\left(\frac{h}{7km}\right) \quad (6.1)$$

if one assumes an exponential air density profile with a scale height of 7 km. Figure 6.1 (bottom) shows the total number of photons and neutrons. This number is the domain-integrated time-averaged density. The evolution can be explained in a simple way, with three species and four rates, where we for convenience neglect the altitude (i.e., air density) dependence of the reaction rates (as all frequencies scale as $f = f_0 \frac{n}{n_0}$). The first reaction is the absorption of high-energy photons,

$$N_\gamma(t) \approx N_\gamma(0) \exp[-k_{ph-absorp}t] \quad (6.2)$$

with the photon absorption rate $k_{ph-absorp} = \mu c \approx 2 \times 10^5 \text{ s}^{-1}$ at STP, (where μ is the photon attenuation coefficient; for a discussion see Rutjes *et al.*, 2016). The loss due to the production of neutrons, that is, the photonuclear reaction $k_{ph-nuc} = \sigma_{ph-nuc} c n_{air} \approx 8 \times 10^2 \text{ s}^{-1}$ can be neglected in equation 6.2 as $k_{ph-absorp} \gg k_{ph-nuc}$. In Figure 6.1 one sees that the photon number $N_\gamma(t)$ (displayed as diamonds) first increases, as the TGF beam creates also secondary photons, which are counted in the simulation, but equation 6.2 approximates only the number of high-energy photons (with energies sayge 1 MeV), see further discussion by Rutjes *et al.* (2016).

The photonuclear cross section for nitrogen and for photons between 10 and 30 MeV ranges from 1 mb to apeak value of 14 mb at photon energy of 23 MeV (Oblozinský, 2000). For the approximation of k_{ph-nuc} above, we took the average photonuclear cross section of nitrogen $\sigma_{ph-nuc} \approx 2 \text{ mb}$. The number of neutrons per TGFphoton (between 10 MeV and 30 MeV) can then be approximated as $\frac{k_{ph-nuc}}{k_{ph-absorp}} \approx 4 \times 10^{-3}$ (consistent with the result of 4.3×10^{-3} by Babich *et al.*, 2010). One may assume that all neutrons are generated, as this is limited by the photon absorption time scale $k_{ph-absorp}^{-1} \approx 5 \mu\text{s}$, efore they start to disappear by capture, which happens with a rate of $k_{capt} \approx 80(\text{ms})^{-1}$ at 3 km altitude.

As already mentioned above k_{capt} does not depend on energy, but only on altitude. For the number of intermediate neutrons this yields (for $t \gg k_{ph-absorp}^{-1}$)

$$N_n(t) \approx N_\gamma(0) \frac{k_{ph-nuc}}{k_{ph-absorp}} \times \exp[-k_{capt}t] \quad (6.3)$$

This equation is consistent with our simulated neutron number, indicated with crosses in Figure 6.1 (bottom). For the gamma radiation of the TGF afterglow we need to use the number of neutrons and the reaction rate from the most significant pathway producing high-energy photons, that is, $n + {}^{14}\text{N} \rightarrow {}^{15}\text{N} + \gamma$, which happens with a rate of $k_{n-ph} = 0.7 \text{ s}^{-1}$ as the cross section equals $7.98 \times 10^{30} \text{ m}^2$ (CHOI *et al.*, 2007) at thermal velocities (0.025 eV, 2200 m/s). Together this results in (for $t \gg k_{ph-absorp}^{-1}$)

$$N_{gamma-TGFafterglow}(t) \approx \frac{k_{ph-nuc}}{k_{ph-absorp}} N_n(t) \approx N_\gamma(0) \frac{k_{ph-nuc} k_{n-ph}}{k_{ph-absorp}^2} \times \exp[-k_{capt}t] \quad (6.4)$$

where $\frac{k_{ph-nuc}k_{n-ph}}{k_{ph-absorp}^2} \approx 1.3 \times 10^{-8}$, consistent with our simulated photon numbers, indicated with diamonds in Figure 6.1 (bottom).

6.4.1 Photon yield by neutron

The 10^8 neutrons of our simulation initially all have the most probable energy of 13 MeV, and they are directed downward, but they rapidly transit to isotropic diffusion. Figure 6.2 presents the evolution of neutrons and photons in a similar manner as Figure 6.1, but now focused on the TGF afterglow after 1 ms. Apart from the better statistics of neutron to photon conversion, there are major differences to the earlier simulation. As the air density n_{air} is 2.2 times lower, the neutrons cool down 2.2 times more slowly, and they spread 2.2 times more widely; hence, the TGF afterglow is much more extended in space and duration. At the altitude of 10 km, it lasts for more than 1 s, as the rate constant k_{capt} in equation (3) is now $k_{capt} \approx 5 \text{ s}^{-1}$.

The statistics of Figure 6.2 are much better than those of Figure 6.1, but unfortunately the simulated box was too small to keep all particles. Figure 6.2 (top) clearly indicates that many particles leave the system at its upper border at 18 km altitude. Therefore, the normalization rates of equations 6.1-6.4 do not apply in the same fashion, so we rescaled them to fit the data. The decay rate of particles, however, with a rate constant of 5/s at 10 km altitude represents a good fit.

6.4.2 The predicted signal

One question is whether the predicted TGF afterglow will be measurable above the cosmic background radiation. Figures 6.1 and 6.2 show that it will be hard to detect a TGF afterglow at sea level, if the neutrons are created above 3 km. We have calculated the predicted detector signal of the TGF afterglows for the simulation of Figure 6.1 at 3 km altitude and for the simulation of Figure 6.2 at 10 km altitude. The detector is the one of Gurevich *et al.* (2011) with an area of 475 cm², and we used a temporal bin size of 200 μs as in their published plots. We assume that it is hit by 2 cm²s⁻¹ or 9 cm²s⁻¹ cosmic background photons with energy above our threshold of 10 keV at 3 or 10 km altitude, based on Bazilevskaya *et al.* (2008). This Poisson-distributed background is added to the signal in Figure 6.3.

6.4.3 Summary of predictions for TGF afterglow

We have predicted a new thunderstorm radiation mechanism, the TGF afterglow. It is formed by the photo-nuclear production of neutrons by the TGF, neutron propagation, and cooling and the inverse reaction that creates gamma rays again. TGF afterglows are thus a signature of gamma rays above 10 to 30 MeV. A TGF afterglow can be distinguished from TGFs or gamma ray glows by the following criteria:

1. Duration: A TGF lasts not longer than 200 μs , or possibly 600 μs depending on the interpre-

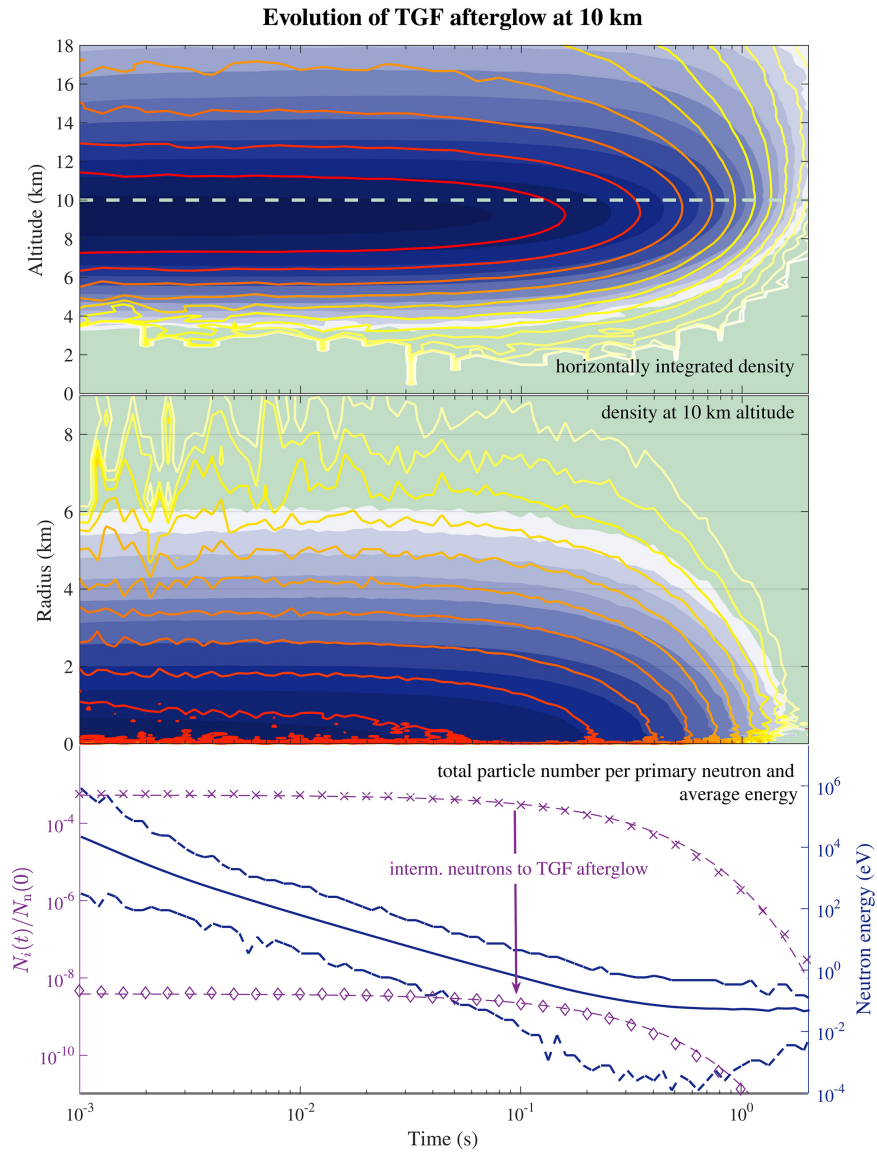


Figure 6.2: The same as in Figure 6.1, but now for the TGF afterglow that started from a neutron source at 10 km directed downward. In this figure time is plotted only from 10^3 s onward, focusing on the TGF afterglow. Figure 6.2 (bottom) does not represent the total particle number as some escaped out of the system at the upper boundary at 18 km. The decay rates, that is, the fits of the purple dashed lines, are the same as in Figure 6.1, adapted to the lower air density (at 10 km compared to 3 km).

tation of some observations as one or several flashes. A gamma ray glow lasts for seconds or more. A TGF afterglow lasts for 60 to 600 ms depending on the atmospheric altitudes crossed by the intermediate neutrons acting as their source, see equation 6.1.

2. Signal shape: Neutron and photon signal appear suddenly and decay in time, compared to the photon and neutron signal in a gamma ray glow which first swells and then decays.
3. Correlation with fast field changes: TGF afterglows are created by TGFs which are triggered by leader propagation and related to fast electric field changes. Gamma ray glows are seen before a discharge and can be terminated by one.

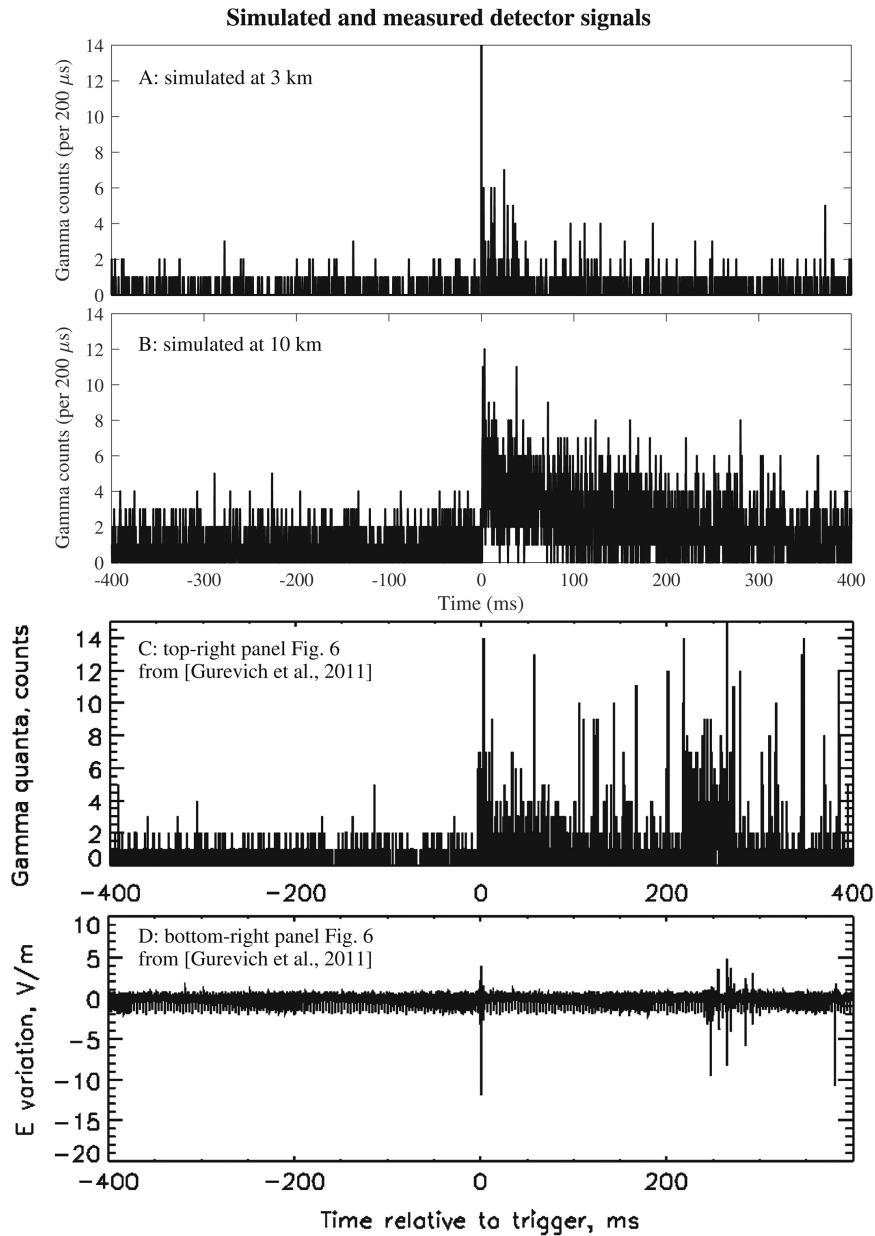


Figure 6.3: (a, b) Simulated counts of gamma radiation from the simulation presented in Figures 6.1 and 6.2. (c, d) Taken from Gurevich *et al.* (2011), in which it is denoted there as event “6.” Figures 6.3a to 6.3c are gamma ray counts per 200 μ s interval on a detector of 475 cm², at 3, 10, and 3.8 km, respectively. Figure 6.3d gives the measured fast electric field variation (20 μ s sampling rate measured by the capacity sensor, see Gurevich *et al.*, 2011 for more details).

4. Photon isotropy: The photons of a TGF afterglow are fairly isotropic, in contrast to the beams produced either in a TGF or in a gamma ray glow by the beamed motion of electrons and their beamed gamma ray emission by bremsstrahlung.
5. Energy range: The photon energy does not exceed the photon nuclear energy of 10 MeV for nitrogen, compared to many tens of MeV in a gamma ray glow or TGF.

6.4.4 Possible observations

As already mentioned in section 1, Gurevich *et al.* (2011) have reported gamma ray emissions lasting for 0.1 to 0.6 s. Clearly, the duration is significantly longer than any TGF detected or simulated, which should disappear within a millisecond, but the signals reported by Gurevich *et al.* (2011) are many orders longer. They occurred during the full duration of an atmospheric discharge at the Tien-Shan Cosmic Ray station at 3.3 to 3.9 km altitude, within the Tien-Shan mountains that reach up to almost 7.5 km altitude. Gurevich *et al.* (2011) found that the temporal distribution of gamma radiation intensity in a burst is quite nonuniform, with some time structures on the scale of millisecond strongly correlated with an electric field change during the discharge. Based on duration only, the measurements fall in the regime of TGF afterglows.

To illustrate how TGF afterglows would qualitatively appear in measurements, we added one event from Gurevich *et al.* (2011) to Figures 6.3 c and 6.3 d. The measured gamma ray counts in Figure 6.3 c appear suddenly at $t = 0$ ms, simultaneous with a fast field variation given in Figure 4d, after which it decays in time. This measured structure in Figure 4c, from 0 ms to 200 ms, shows similarities to our simulated TGF afterglow at 3 km. But, the observations are probably not produced by the specific TGF that we simulated (a TGF starting at 8 km and directed vertically downward), there could be other scenarios (different altitude, orientation, opening angle, and photon spectrum); in addition, also the number of photons per TGF varies by an order of magnitude.

The measurements of Gurevich *et al.* (2011) show also structures that would not fit in the description of a TGF afterglow. Namely, structures that first swell and then decay, centered around one or multiple fast field variations. An example of such a structure is also seen in Figures 6.3 c and 6.3 d, between 200 ms and 300 ms. We speculate that it fits in the description of a gamma ray glow, but a transient one with a much shorter lifetime than typically measured. It could be the result of field development by previous partial discharges, producing a transient patch of air with an electric field above runaway breakdown, until the patch itself is discharged by a leader.

There may be more candidates of gamma ray observations from thunderstorms which are actually TGF afterglows. We have summarized discriminators in section 2.5 to search for TGF afterglows and we invite other researches to look for their signatures in their millisecond time scale gamma ray measurements.

6.5 SIMULATED PHOTON AND NEUTRON DISTRIBUTIONS IN SPACE, TIME AND ENERGY AT SEA LEVEL

We have analyzed the photon and neutron distributions in space, time and energy at sea level as a function of the energy spectrum of the source photons and as a function of the source altitude where we assumed that the photons were emitted within one instantaneous burst in the downward direction. As said above, we divided the neutron relevant energy range from 10 to 30 MeV into

Table 6.1: Number and lateral spreading of the neutrons at sea level as a function of the altitude of the photon source. For each source altitude, 4×10^7 primary photons were used, with a uniform energy distribution between 10 and 30 MeV. The neutron spreading on ground is defined as the standard deviation from the beam axis. The fourth column contains the neutron number per primary photon, with an error estimated as the root of the neutron number. The last column is the average neutron flux density towards the ground calculated with a reference circular area with 1 km radius and a reference time of 0.5 s.

Source altitude	Lateral spreading	Neutron number on ground	Neutrons per primary photon	Flux density per primary [cm ⁻² s ⁻¹]
0.3 km	291 m	51777	$(1.294 \pm 0.006) \times 10^{-3}$	0.824×10^{-13}
1.0 km	396 m	24913	$(6.23 \pm 0.04) \times 10^{-4}$	0.396×10^{-13}
1.5 km	417 m	10666	$(2.67 \pm 0.03) \times 10^{-4}$	0.169×10^{-13}
2.0 km	427 m	4666	$(1.17 \pm 0.02) \times 10^{-4}$	0.074×10^{-13}
2.5 km	445 m	2018	$(5.1 \pm 0.1) \times 10^{-5}$	0.321×10^{-14}
3.0 km	408 m	917	$(2.29 \pm 0.07) \times 10^{-5}$	1.459×10^{-15}
4.0 km	413 m	227	$(5.7 \pm 0.4) \times 10^{-6}$	0.361×10^{-15}
5.0 km	373 m	81	$(2.0 \pm 0.2) \times 10^{-6}$	1.289×10^{-16}
6.0 km	347 m	13	$(3 \pm 1) \times 10^{-7}$	2.069×10^{-17}

4 intervals of 5 MeV width. We found that the spatial and temporal distributions of photons and neutrons on ground hardly depend on the energy of the source photons. Only the neutron production rate depends strongly on the photon energy. The results related to the total neutron number that depend on the source spectrum, will be discussed in the next section. In the present section we present the spectrum independent distributions, and we sum over the four energy intervals; so effectively we here present results for $4 \cdot 10^7$ source photons uniformly distributed over the energy interval of 10 to 30 MeV.

6.5.1 Neutron number and distribution at sea level as a function of source altitude

Table 6.1 shows the number of neutrons per primary photon at sea level and their spatial spread over the ground as a function of photon source altitude; the spatial spread is measured as the standard deviation from the beam axis. As expected, the neutron number strongly decreases with increasing source altitude. On the other hand, the spatial spread over the ground is fairly constant with radii ranging from 290 to 450 m. This can be understood based on the spatial distribution of neutron generation and propagation discussed below.

6.5.2 Energy spectra of photons and neutrons at sea level

The energy spectra of photons and neutrons at sea level are presented in Figures 6.4 and 6.5 as a function of energy for different source altitudes. The only dependence on the energy spectrum of the source photons lies in the fact that, e.g., photons in the energy range from 10 to 15 MeV only produce neutrons with energies below 5 MeV, and hence the spectrum of the produced neutrons has this upper energy limit. However, our simulations show that this initial energy difference of the neutrons rapidly disappears while they cool down through collisions with air molecules. For

the neutrons, there are 50 logarithmic bins from 0.1 eV to 20 MeV, while for the photons there are 100 logarithmic bins from 10 keV to 30 MeV, both equally spaced in logarithmic space.

The photon energy spectra recorded at sea level are shown in Figure 6.4. The source photon spectrum is a uniform distribution between 10 and 30 MeV as indicated in the figure as primary spectrum. This initial spectrum is still clearly visible on ground for source altitudes of 0.3 and 1 km, though attenuated, with a clear discontinuity toward the secondary photon spectrum at lower energies. This discontinuity diminishes for higher source altitudes due to multiple interactions where photons lose energy or disappear, and the discontinuity disappears above 4 km. There is a second discontinuity visible in the spectra at 511 keV which is the positron annihilation line. When photons with energies above 1.02 MeV are available, electron positron pairs can be produced, and the annihilation of the positrons creates the 511 keV line. It can be noticed that the shape of the photon spectrum for longer times and lower energies hardly changes. This is because the distribution is continuously refreshed by higher energy particles losing energy, and hence flowing into the lower energy regimes.

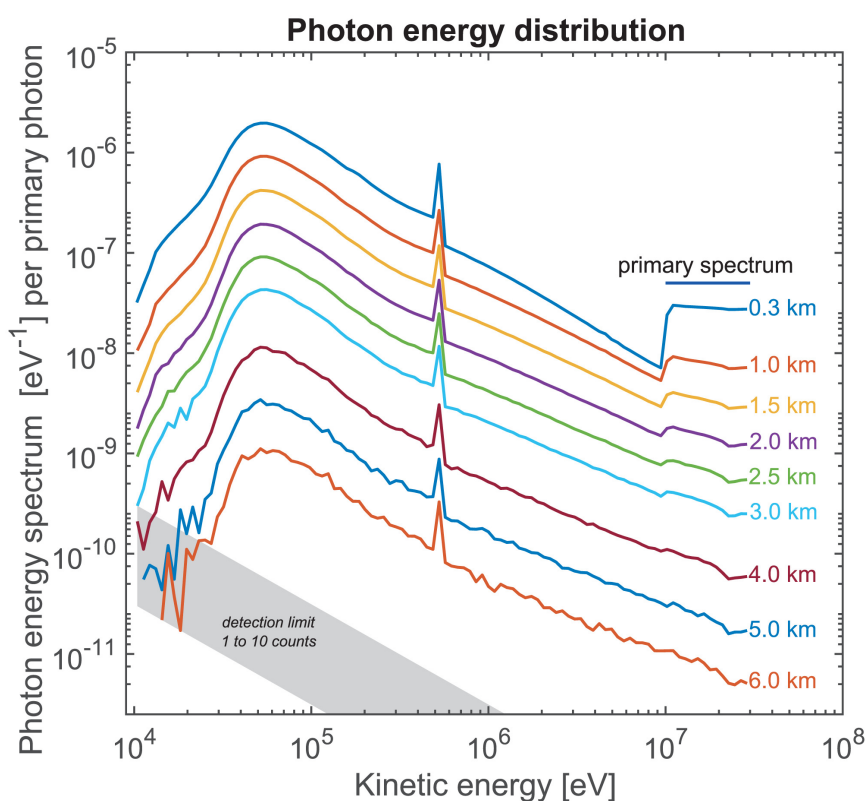


Figure 6.4: Photon energy spectra at the ground for different source altitudes. The gray shade indicates low statistics.

Figure 6.5 shows the energy spectra of the neutrons. There are two regimes visible: a spectrum with an index of approximately -0.8 for neutron energies up to 10 keV and an exponential cutoff in the MeV energy regime. The latter depends on the spectrum of the source photons as this determines the maximal neutron energy. However, the shapes of the neutron spectra on ground hardly depend on the source altitude. This is due to their actual places of generation and to their dynamics as we will explain further below. The neutron energy spectra below 10 keV become

noisy (i.e., they become as low as 1 to 10 counts per bin) with increasing source altitude, indicating that low energy neutrons do not reach the ground and rather thermalize in the air through inelastic scattering or capture. The neutron spectra for source altitudes of 4 km, 5 km and 6 km are very noisy and not shown. Due to the strong absorption for large source altitudes as also visible in Table 6.1, our simulations would have needed a much larger number of primaries ($\gg 10^7$) to identify the neutron spectrum on ground beyond the statistical noise.

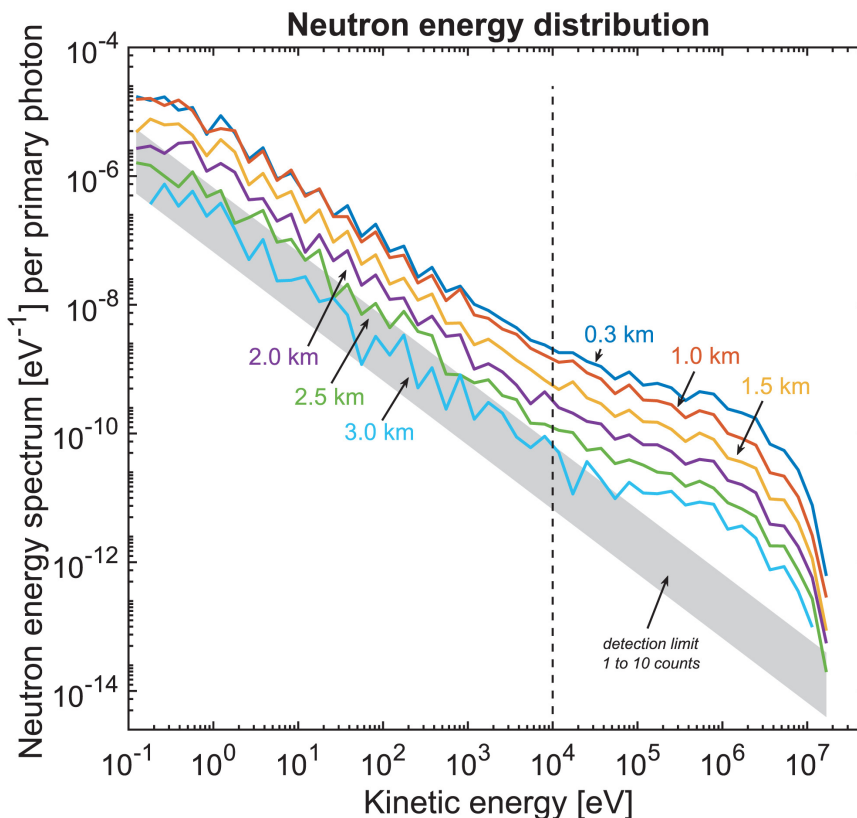


Figure 6.5: Neutron energy spectra at the ground for different source altitudes. The gray shade indicates low statistics. The vertical line marks the energy range at 10 keV.

6.5.3 Distribution of arrival times of photons and neutrons at sea level

We also investigated the arrival times of photons and neutrons at sea level, i.e., the number of particles arriving per primary per time as a function of time, again for different photon source altitudes. As before, the distribution of arrival times does not depend on the source spectrum.

The distribution of photon arrival times at sea level is shown in panel (b) of Figure 6.6; for all source altitudes this distribution exhibits two distinct pulses. The first pulse has a duration of less than 0.1 ms, it starts at the time a photon needs to travel from the source to the ground in a straight line. The photons arriving somewhat later have undergone some scattering along their path. The second photon pulse lasts up to about 500 ms. It appears when photons create neutrons by a photonuclear reaction, and these neutrons release photons at capture. This is the mechanism that creates a TGF afterglow after a TGF, as predicted by Rutjes *et al.* (2017).

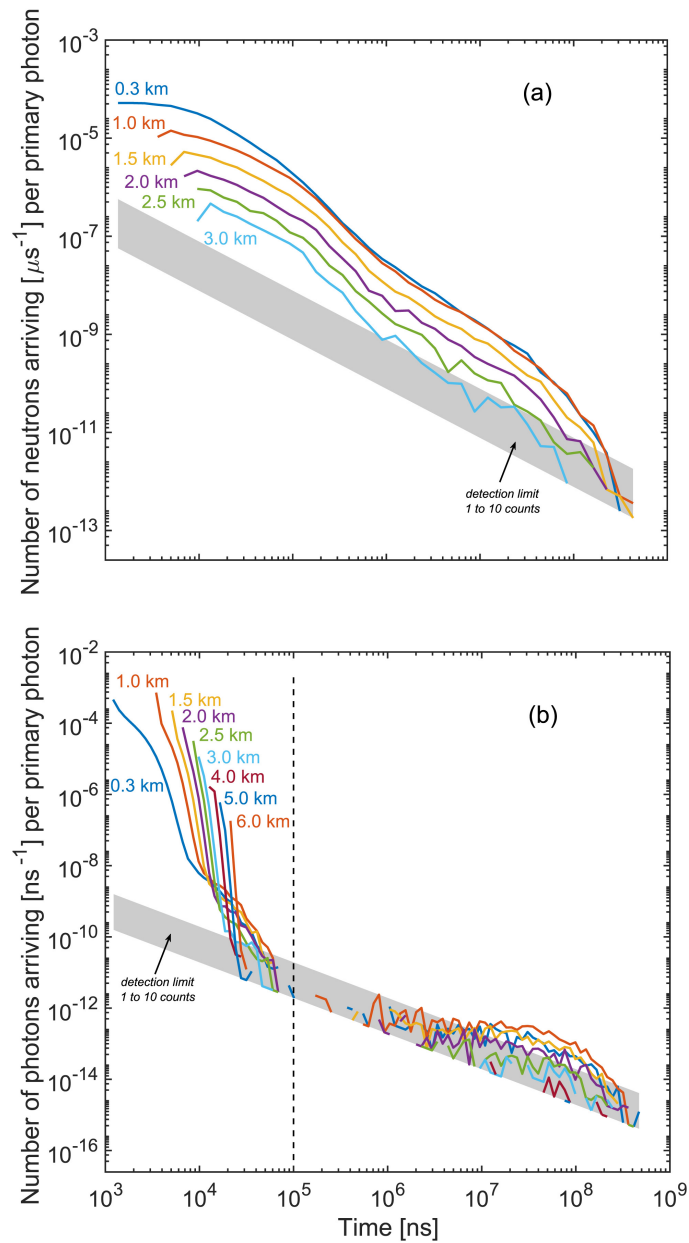


Figure 6.6: Distribution of arrival times of (a) neutrons and (b) photons on ground per primary. The different source altitudes are indicated by the legend. The vertical line marks the end of the primary photon pulse at 0.1 ms. The gray shade indicates low statistics.

The distribution of neutron arrival times per primary photon is shown in panel (a) of Figure 6.6. The first neutrons reach ground shortly after the first photons. They keep arriving up to times of 500 ms. But while the pulse of secondary photons forms, the neutron number decreases. The late neutrons arrive with lower energies than the fast ones, as will be discussed in more detail later.

6.5.4 Interpretation of the simulations and the shape of the effective neutron source

A photon traveling from a source altitude of 300 m straight down will reach ground within $1 \mu\text{s}$ (with the speed of light of 3×10^8 m/s). On the other hand, if the most energetic neutron with

a kinetic energy of 20 MeV would move straight to the ground without any interaction, it would need $5 \mu\text{s}$. But since the first neutrons arrive at ground level already after $\approx 1 \mu\text{s}$ as well, as shown in Figure 6.6(a), they must have been created along the photon trajectories near the ground and without many interactions with air particles.

Based on the relevant cross sections of photons and neutrons, the concept illustrated in Figure 6.7 can be developed for their distribution in space, time and energy: The photon source is assumed as a point-like instantaneous beam directed downward — from which other sources can be constructed by superposition. This photon beam broadens slightly, while losing energy; the attenuation length is $\sim 1.5 \text{ km}$ (RUTJES *et al.*, 2017) until the photon energy drops below 10 MeV and the photon cannot produce neutrons anymore. The neutrons are created everywhere along the trajectories of the sufficiently energetic photons, therefore the effective neutron source has a cone like structure of about kilometer length. The neutrons initially have energies in the MeV range. They diffuse isotropically while losing energy through collisions. Their attenuation length is $\sim 685 \text{ m}$ (KÖHN *et al.*, 2017). This concept is consistent with the simulated distribution of photons and neutrons in space, time and energy.

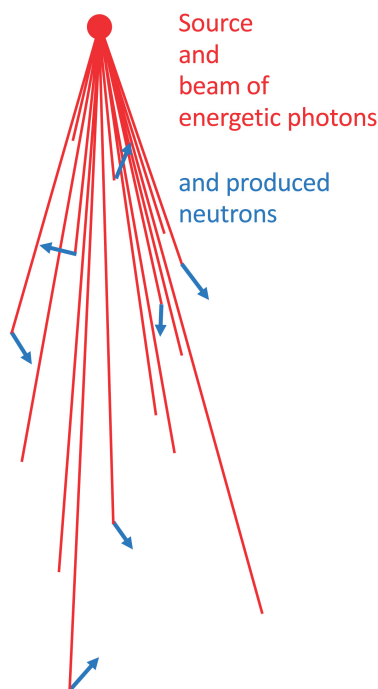


Figure 6.7: Illustration of the effective neutron source geometry due to a point-like initial photon beam directed downward. The beam of high energy (primary) photons (in red) diverges slightly. Within this beam, individual photons move on straight lines and can create neutrons (in blue) by a photonuclear reaction. The created neutrons diffuse isotropically while they cool down. Photon lines ending without a (blue) neutron, have mostly created electron positron pairs; these pairs as well as lower energy photons are not drawn. The spatial dimension is of the order of a kilometer.

6.5.5 Second photon pulse and time dependent neutron spectra

All neutrons that do not reach ground will eventually be captured, accompanied with the release of a high energy photon; this is the delayed photon signal visible in panel (b) of Figure 6.6. To better identify the relation between spectra and temporal delay, the data of Figures 6.4-6.6 are plotted in a different manner in Fig. 6.8: here the spectra of photons and neutrons arriving before or after 0.1 ms are plotted separately.

The majority of the photons arrives within the first photon pulse (before 0.1 ms), while the secondary pulse consists of a relatively small photon number with energy between 10 keV and some MeV, this feature is shown in the upper panels of Figure 6.8. The ratio of the photon number in the second pulse to the photon number in the first pulse is $\sim 10^{-5}$ for the different source altitudes. This ratio as well as the high energies of the second photon pulse are compatible with the hypothesis that the second photon pulse is created by the capture of neutrons that were created by a photonuclear reaction from the primary photons, see Rutjes *et al.* (2017) for a further discussion.

The spectra of the neutrons arriving before or after 0.1 ms are shown in the lower panels of Figure 6.8. The early arriving neutrons have much higher energies which is consistent with the concept that they were created by photons near the ground and have not collided much with air molecules. The neutrons arriving after 0.1 ms have mostly energies below 1 MeV, since they were created earlier when still many energetic photons were available, so they had more time to lose energy through collisions while diffusing through the atmosphere. These numerous and relatively cool "late" neutrons create the second photon pulse discussed above.

6.6 NEUTRON DETECTION ON GROUND AS A FUNCTION OF SPECTRUM AND ALTITUDE OF THE PHOTON SOURCE

We now investigate how the neutron production depends on the spectrum of the photon source.

6.6.1 Construction of an arbitrary photon source spectrum

In our simulations, we have divided the photon energy range into 4 intervals within the energy range relevant for neutron production: 10-15, 15-20, 20-25, 25-30 MeV; these four intervals are labeled as $i = 1, 2, 3, 4$ below. Figure 6.9 shows the total neutron count per primary as a function of photon source altitude for the 4 energy intervals of primary photons. Photons within the energy intervals from 20 to 25 MeV and from 25 to 30 MeV create about the same large number of neutrons on ground, and they do this for every source altitude. This is related to the fact that the photonuclear cross section of nitrogen has a maximum at 23 MeV (OBLOZINSKY, 2000). The photon energy range of 10-15 MeV, on the other hand, has the lowest neutron production for all source altitudes.

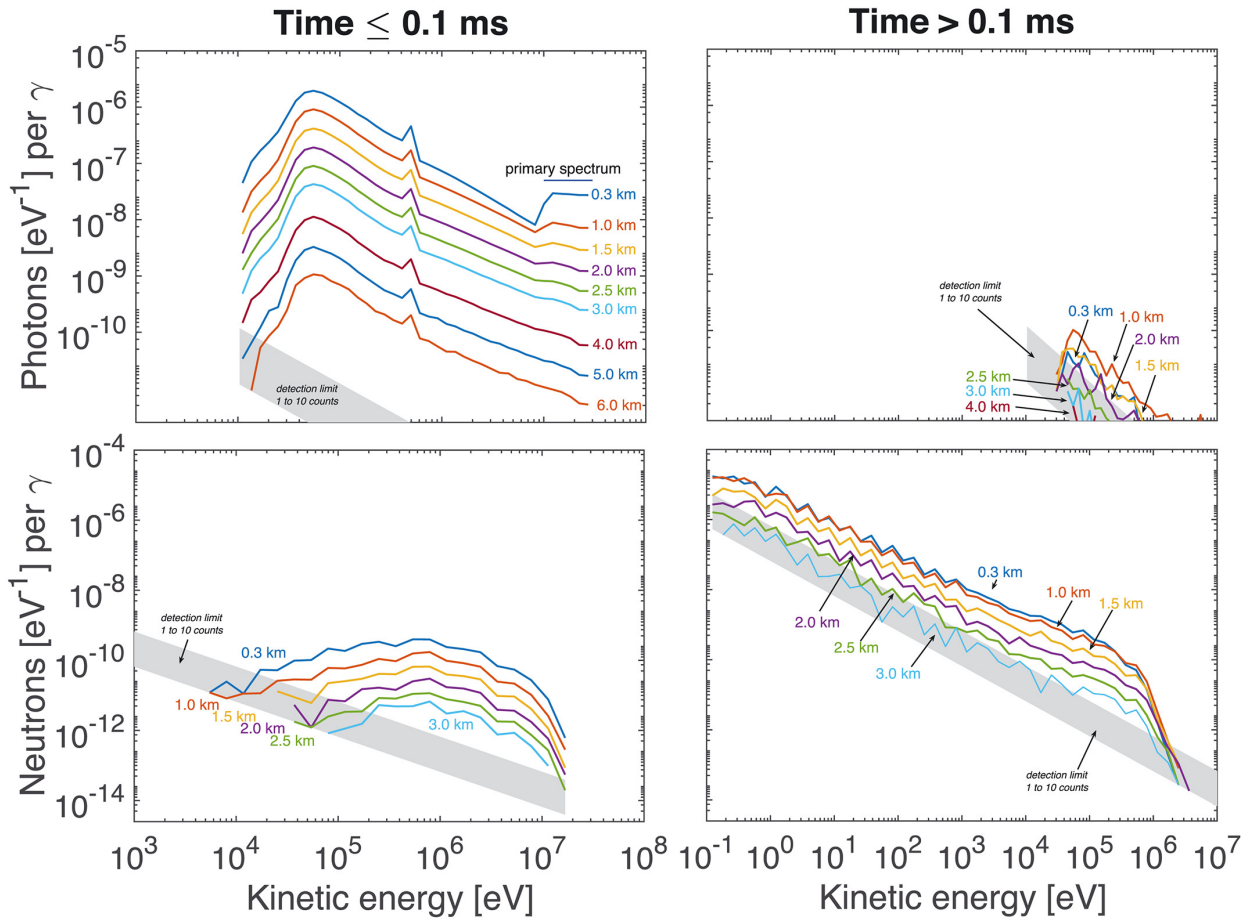


Figure 6.8: Energy distributions of photons (top row) and neutrons (bottom row) as in figures 6.4 and 6.5, but now differentiated between arriving before 0.1 ms (left column) or after 0.1 ms (right column).

The number of neutrons $N_i(h)$ on ground per primary photon in one of the four energy intervals $i = 1, 2, 3, 4$ can be approximated as a function of source altitude h as

$$N_i(h) = I_i e^{-h/\ell_i} \quad (6.5)$$

with the values of ℓ_i and I_i given in Table 6.2. The parameters were determined by interpolating the neutron number for the source altitude $h = 300$ m and for the highest source altitude with neutron counts for the respective energy interval i . (It should be noted that the exponential ansatz of the equation implicitly assumes a constant air density, therefore it is limited to altitudes below 5 or 6 km. For larger altitudes the variation of air density needs to be taken into account.)

In Table 6.2, it can be noted, that ℓ_i is not a monotonous function of the gamma-ray energy, and this has a physical reason. As the photonuclear cross section has a maximum at 23 MeV, photons in the energy range of 20 to 25 MeV liberate neutrons closer to the photon source, i.e. at a higher altitude. Therefore these neutrons have a lower probability to reach the ground, because effectively they have to traverse a larger distance. Based on this argument, one would expect ℓ_i to be largest for photons with 10-15 MeV, but then the neutrons have initial energies as low as 0-5 MeV and will not diffuse far before losing their energy.

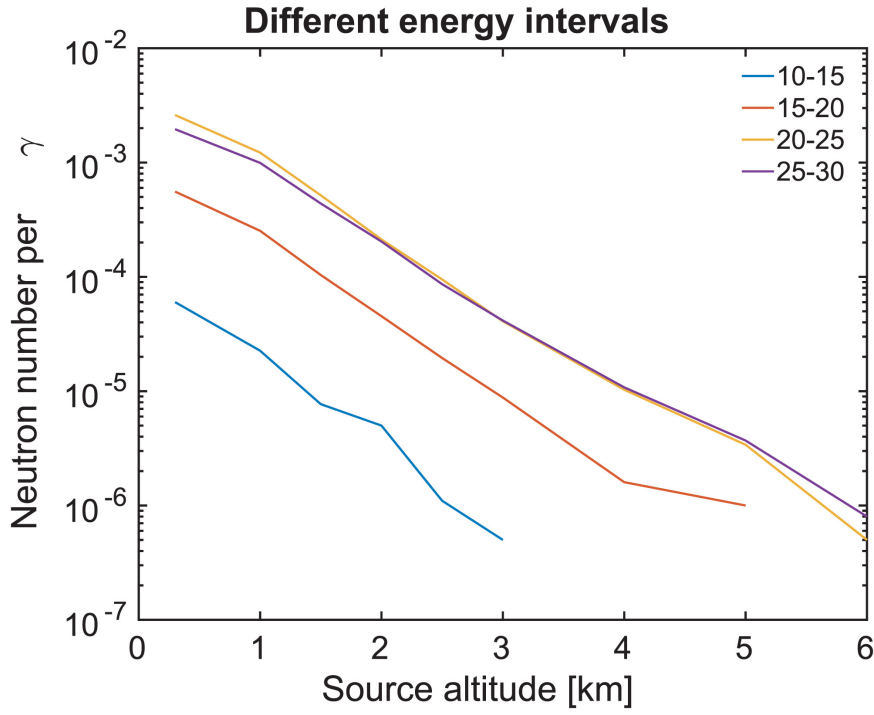


Figure 6.9: Neutron number on ground per primary photon as a function of source altitude. The lines refer to the four different energy ranges of 10-15 MeV; 15-20 MeV; 20-25 MeV; 25-30 MeV, as indicated in the legend.

Table 6.2: Interpolated values for the parameters ℓ_i and I_i in equation (6.5) for the different energy ranges of the source photons.

Label i	Energy Range	ℓ_i	I_i per primary
1	10 - 15 MeV	565 m	1.0×10^{-4}
2	15 - 20 MeV	740 m	8.3×10^{-4}
3	20 - 25 MeV	667 m	4.1×10^{-3}
4	25 - 30 MeV	735 m	2.9×10^{-3}

The neutron number n_γ per primary photon in the energy range of 10 - 30 MeV, for an arbitrary downward directed gamma-ray source with spectrum $f(E)$ at altitude h can now be approximately calculated as

$$n_\gamma \approx \sum_{i=1}^4 a_i N_i(h), \quad a_i = \int_{(5+5i)MeV}^{(10+5i)MeV} f(E)dE / \int_{10MeV}^{30MeV} f(E)dE, \quad (6.6)$$

where a_i is the number of photons in each energy interval i within the distribution $f(E)$.

6.6.2 Results for different RREA spectra and source altitudes

The photon spectrum is frequently assumed to be a stationary RREA spectrum (DWYER *et al.*, 2012) parameterized as

$$f(E) = \frac{1}{E} e^{-E/E_{th}} \quad (6.7)$$

with the exponential cutoff E_{th} . The number of photons with energy above the photonuclear reaction threshold increases with E_{th} .

Figure 6.10 shows the neutron production as a function of this exponential cutoff for source altitudes of 2.5, 5 and 6 km, calculated with equation (6.6). Two distinct features can be seen: First, for E_{th} varying from 6 to 10 MeV, the neutron detection on ground varies only by a factor of 1.5; this means that the neutron detection is fairly insensitive to this parameter for all source altitudes. On the other hand, the dependence on source altitude is quite strong; this is why we introduced the altitude dependent multiplication factors in the plot to display all curves. The neutron number on ground per primary photon in the right energy range is therefore characteristic for the source altitude.

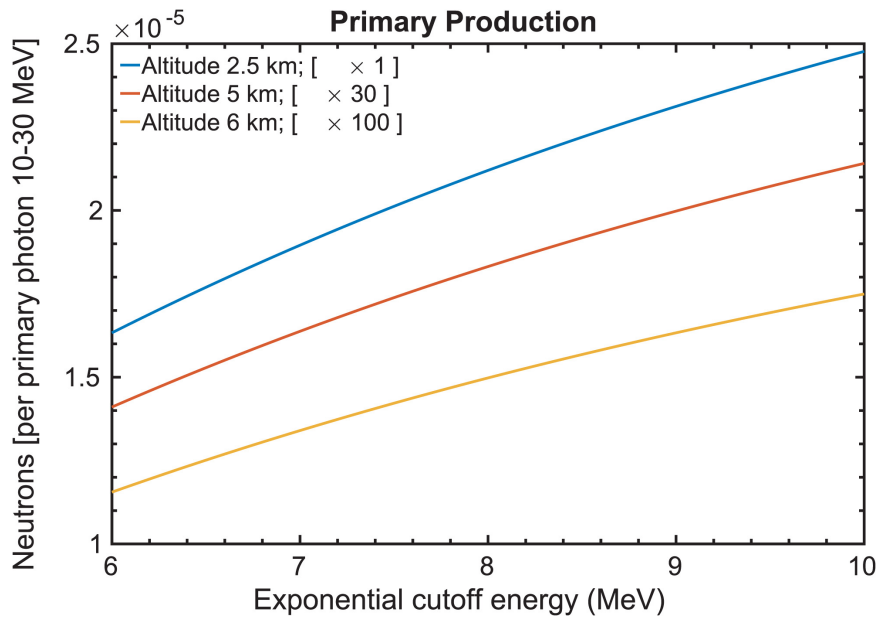


Figure 6.10: Neutron number per primary at the ground, n_γ , plotted as a function of the source photon spectrum for different source altitudes. The source spectrum is parameterized by an RREA spectrum (6.7) with exponential cutoff energy E_{th} . The curves for 5 and 6 km are multiplied by scaling factors of 30 or 100 in order to display all curves in the same plot.

6.6.3 Arbitrary photon sources and detection altitudes

Of course, the neutron number at sea level can be calculated in the same way as above for any other source spectrum and altitude.

If the detection is not at sea level, one has to consider that the results should be the same if the particles had the same probability to collide with air particles; this means that they must have crossed the same air density n integrated from start to end point.

Up to now, we have focussed on the products of a single instantaneous point-like photon beam directed downward. Beams with other distributions in space and time can be constructed from it by superposition.

6.7 DISCUSSION

Carlson *et al.* (2010) and Babich *et al.* (2010) have simulated neutron production from specific photon sources and altitudes. Carlson *et al.* (2010) used a measured TGF photon spectrum parameterized as in equation (6.7), their results are summarized in Table 6.3 and can be directly compared to Figure 6.10. In agreement with Carlson *et al.* (2010) and Babich *et al.* (2010), our results show that the effective neutron source is extended along the photon beam.

Source altitude	Carlson <i>et al.</i> (2010)	Babich <i>et al.</i> (2010)	present work
2.5 km	2.3×10^{-4}	n.a.	2.0×10^{-4}
5.0 km	6×10^{-6}	2.40×10^{-6}	8.1×10^{-6}

Table 6.3: Number of neutrons at sea level per primary by different authors.

Bowers *et al.* (2017) perform a similar analysis as we do. They simulate neutrons measured on ground that are generated by an instantaneous release of an RREA spectrum of gamma-rays moving downward, with $E_{th} = 6.5$ MeV. Source altitudes are 0.5, 1.0 and 1.5 km (for a Japanese winter thunderstorm). But, since they focus in a given spectrum, their work does not provide the possibility of generalization as the present work.

Toropov *et al.* (2013) have observed that lightning discharges and neutron bursts are well correlated; they registered several discharges, and some were accompanied by neutron burst of approximately 2 minutes duration. According to the present work, this suggests that there were multiple gamma-ray emissions during a single lightning discharge to generate the neutron pulse detected on ground as the neutron signal from an instantaneous gamma-ray pulse does not last longer than a fraction of a second when it arrives from 3 km altitude or less; for larger altitudes the signal would be very small, as we have calculated.

In our simulations, the vast majority of neutrons are concentrated in an area with less than 1 km radius around the beam axis, as shown in Section 6.5.1; and they arrive within some hundreds of milliseconds, as shown in Section 6.5.3. The average flux density can be calculated with these parameters; it is shown in the last column of Table 6.1 to allow an estimate whether it can be measured with a given detector.

Martin *et al.* (2010) measured a neutron area density of 20 cm^{-2} , but their detector was efficient only in the thermal part of the energy spectrum up to 1 eV; therefore they missed a great part of the neutron spectrum. They estimated that the initial neutron number was $10^{12} - 10^{13}$ assuming that they came from a point-like source and spread isotropically within a sphere of 1-2 km to their thermal detector.

Other measurements such as the flux of $4 \times 10^{-3} \text{ cm}^{-2}\text{s}^{-1}$ reported by Starodubtsev *et al.* (2012) took into account only neutrons with energy above 10 MeV. As our results show (Figure 6.8), neutrons with energy above 10 MeV reach the detection plane within 0.1 ms, so the flux

reported by Starodubtsev *et al.* (2012) may be a result of multiple emissions due the integration time in their measurements.

Considering that the integrated atmospheric density between 0-6 km is similar to the value between 6-400 km and taking into account that the number of neutron per primary at the ground is of the order of 10^{-7} for a source altitude of 6 km, a larger number of primary photons in the emission would be needed to generate detectable neutrons at the ground and at satellite altitudes. And as the neutrons travel to satellite altitudes, the particles have a lot more space to diffuse than during their motion to the ground, making neutron detection at satellite altitudes very difficult.

Recent TGF measurements (GJESTELAND *et al.*, 2015) have shown events that were estimated to have approximately $10^{17} - 10^{20}$ source photons with energy above 1 MeV. The measurements were done in the 25 keV - 17 MeV energy range, but the maximum detected energy was 11 MeV. Despite the large quantity of photons with energy above 1 MeV, the neutron binding energy in atmospheric nuclei is at least 10 MeV and the neutron production for 10-15 MeV is small compared to the peak values, as discussed in Section 6.5.2. In order for such events to produce ground detectable neutrons, the source energy must be higher than the detected energy. The energy range must cover at least the peak energy range of photonuclear cross section, i.e., 20-25 MeV. Since our results show that although the four energy intervals contribute with similarly shaped spectra and pulses, the absolute number of neutrons is dominated by the energy range 20-30 MeV by at least one order of magnitude, as can be seen in Figure 6.9.

6.8 CONCLUSIONS AND OUTLOOK

We simulated neutron footprints in space and time from gamma-ray point sources with initial photon energy between 10 MeV and 30 MeV; and we differentiated between four initial energy intervals of 5 MeV width. Clearly we see that even if the photons start from a point, neutrons do not originate from a point, but they are produced along the kilometer long paths of the high energy (primary) photons, as illustrated in Figure 6.7. This fact limits simple inverse approximations on the amount of photons needed to explain observed neutron fluxes. The fluxes provided here can be used for better estimations.

We observed that the neutron spectra for the four different gamma-ray energy intervals do not change significantly, but the number of neutrons produced depends on the gamma-ray energy. In other words, as the number of neutrons produced is so sensitive to the gamma-ray energy, the neutron yield depends on the initial gamma-ray spectrum. We calculated the number of neutrons as function of the characteristic (mean) energy cutoff of a steady state RREA for several altitudes, see Figure 6.10. This dependence can be used to calculate the original number of photons, e.g. in a gamma-ray glow, when the characteristic (mean) energy cutoff, E_{th} in Equation (6.7), can be approximated based for example on its sensitivity to electric field. Or in the other direction, knowing the total neutron to photon ratio results in the characteristic (mean) energy cutoff (assuming

RREA) and by that in a diagnostic for the ambient electric field.

From the energetic and spatio-temporal characteristics of the neutron signal, we conclude that the neutron source is spread in space by photon motion, as illustrated in Figure 6.7. There are neutrons arriving at sea level at the same time as the photons, indicating that the neutrons were produced at low altitudes so they could coincide with the pulse of primary photons, as shown in Figure 6.8; and also there are neutrons arriving at sea level after the pulse of photons from the source is gone, meaning that these neutrons were created at high altitudes or collided enough with air particles that their travel time to the ground is much longer. These neutrons have characteristically lower energies. In fact, the arrival times of gamma-rays and neutrons after a gamma-ray burst (as presented in Figures 6.6 and 6.8) depend in a characteristic manner on the source altitude, and allow its determination.

Since the photons can not have many interactions without leaving the energy range of photonuclear reaction, we estimate that most neutrons are created on a cone of kilometer length during the photon motion downward; and the neutrons' lateral spreading must be due to their collisions with air molecules. These neutron collisions with air molecules occur on a longer time scale than the time scale of the source particles and generate a second photon pulse constituting the TGF afterglow (RUTJES *et al.*, 2017).

7 MODELLING THE ATMOSPHERIC HADRONIC PRODUCTION

1

7.1 INTRODUCTION

It has been discussed that lightning flashes emit high-energy electrons, positrons, photons and neutrons with single energies of several tens of MeV.

In the first part of this chapter we study the absorption of neutron beams in the atmosphere. We initiate neutron beams of initial energies of 350 keV, 10 MeV and 20 MeV at source altitudes of 4 km and 16 km upwards and downwards and see that in all these cases neutrons reach ground altitudes, and that the cross section areas extend to several km². We estimate that for terrestrial gamma-ray flashes approximately between 10 and 2000 neutrons per ms and m² are possibly detectable at ground, at 6 km or at 500 km altitude.

In the second part of the chapter we discuss a feedback model involving the generation and motion of electrons, positrons, neutrons, protons and photons close to the vicinity of lightning leaders. In contrast to other feedback models, we do not consider large-scale thundercloud fields, but enhanced fields of lightning leaders. We launch different photon and electron beams upwards at 4 km altitude. We present the spatial and energy distribution of leptons, hadrons and photons after different times and see that leptons, hadrons and photons with energies of at least 40 MeV are produced. Because of their high rest mass hadrons are measurable on a longer time scale than leptons and photons. The feedback mechanism together with the field enhancement by lightning leaders yields particle energies even above 40 MeV measurable at satellite altitudes.

In section 7.2 we introduce our three-dimensional, relativistic Monte Carlo feedback model and put emphasis on the interaction of neutrons with air molecules. We will discuss the main neutron dissipation processes. Moreover, we will introduce the concept of atmospheric depths which gives a mean to estimate the absorption and energy loss of particle beams traveling at the same air package, but through different altitudes.

Finally, in section 7.3.1 we present simulation results of neutron beams with different initial energies originating at different altitudes and investigate the energy dissipation and how far they reach in the atmosphere.

In sections 7.3.2 and 7.3.3 we consider more general cases and analyze photon and electron beams of different energies. We explore the subsequent production and motion of electrons,

¹This chapter is a version: C. Köhn, G. Diniz and M.N. Harakeh, Leptons, hadrons and photons and their feedback close to lightning leaders *J. Geophys. Res. Atmos.*, vol. 122, pp. 1365-1383, doi:10.1002/2016JD025445

positrons, protons and neutrons and take into account the electromagnetic feedback of photons, positrons and electrons. For these cases we then present the spatial and energy distributions after different time steps.

Our conclusions are presented in section 7.4.

7.2 MODEL

7.2.1 Cross sections and the Monte Carlo particle code for leptons, photons and hadrons

We model the motion and production of leptons (electrons and positrons), neutrons and photons as well as the production of protons in air, i.e. in a mixture of N_2 (78.12%), O_2 (20.95%) and Ar (0.93%), with a three-dimensional, relativistic Monte Carlo code where we explicitly model the collision of electrons, positrons, photons and neutrons with air molecules.

For electrons we include elastic scattering off air nuclei (LXCat Database, 2014; JACOB, 1973; PHELPS and PITCHFORD, 1985; PHELPS, 1985; FIALA *et al.*, 1994; VAHEDI and SURENDRA, 1995), electron impact ionization (YONG-KIM and SANTOS, 2000), attachment to molecular oxygen (LUQUE and GORDILLO-VÁZQUEZ, 2011; PANCHESHNYI *et al.*, 2008; LAWTON and PHELPS, 1978), molecular excitations (LXCat Database, 2014; LAWTON and PHELPS, 1978), electron-electron Bremsstrahlung (KÖHN *et al.*, 2014) and electron-nucleus Bremsstrahlung (BETHE and HEITLER, 1934; KÖHN and EBERT, 2014). For positrons we include the same processes plus the annihilation of positrons at shell electrons of air molecules. This is justified since positrons and electrons behave alike (AGOSTINELLI *et al.*, 2003; KOTHARI and JOSHIPURA, 2011).

For photons we include photoionization (EPDL Database, 1997), Compton scattering (GREINER and REINHARDT, 1995; PESKIN and SCHROEDER, 1995) off shell electrons, the production of electron-positron pairs (KÖHN and EBERT, 2014) as well as the production of neutrons and protons (FULLER, 1985). Through the removal of neutrons from $^{14}_7N$ or $^{16}_8O$ by photons, the radioisotopes $^{13}_7N$ or $^{15}_8O$ are produced. However, as we have shown in (KÖHN and EBERT, 2015), this process is not significant enough to produce radioisotopes in large amounts.

For neutrons we include elastic scattering, excitations of air nuclei and charge-exchange reactions, i.e. $A(n,p)B$, where A is the nucleus of an air atom (target nucleus) and B is the nucleus formed by exchanging a proton by a neutron in the target nucleus. There we use different cross sections for nitrogen, oxygen and argon (MENDOZA *et al.*, 2012, 2014). The charge-exchange process can eventually produce radioisotopes, e.g. as through $^{14}_7N(n,p)^{14}_6C$. However, this process is a third-order process (after the production of photons and the subsequent production of neutrons) and thus it is negligible.

By implementing all the reactions mentioned above, we have automatically taken into account the feedback of electrons and positrons producing new photons through the Bremsstrahlung pro-

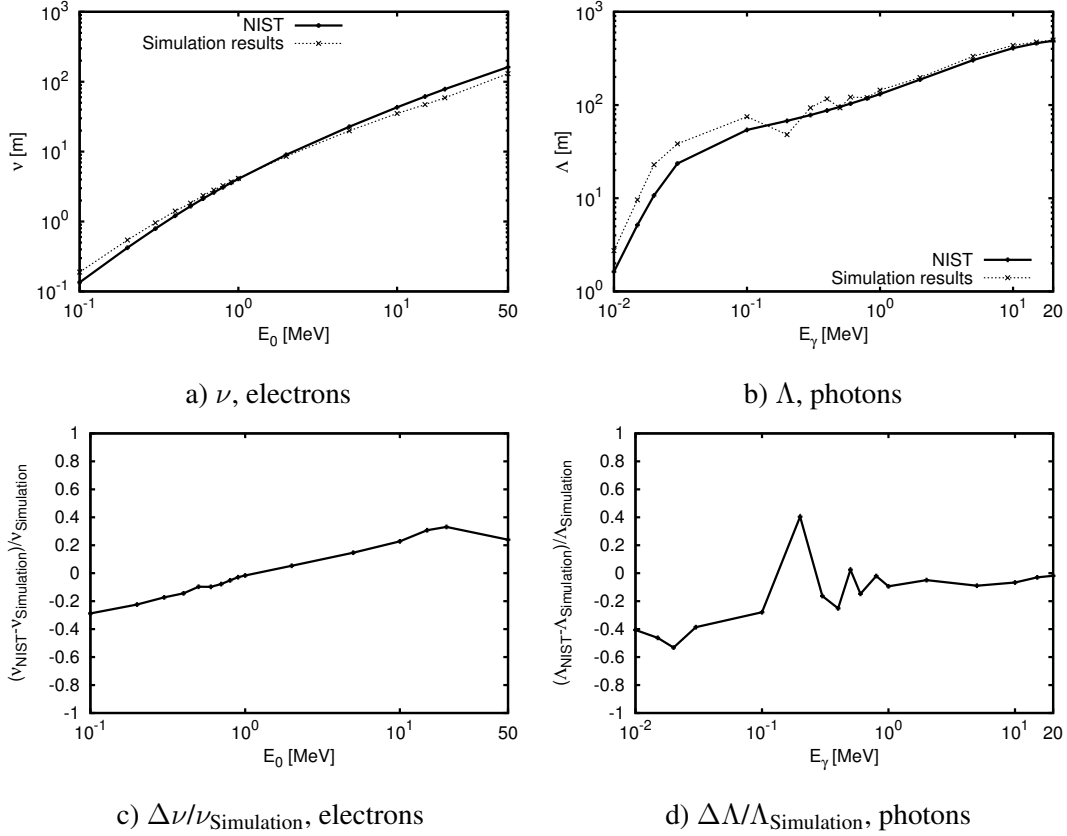


Figure 7.1: a) The simulation results and NIST data of the average length ν until full energy loss of electrons for different initial energies E_0 at ground pressure. b) The simulation results and NIST data of the mean free path Λ of photons in air as a function of the initial photon energy E_0 . c) The relative error $(\nu_{\text{NIST}} - \nu_{\text{Simulation}})/\nu_{\text{Simulation}}$ as a function of E_0 . d) The relative error $(\Lambda_{\text{NIST}} - \Lambda_{\text{Simulation}})/\Lambda_{\text{Simulation}}$ as a function of E_0 .

cess and through positron annihilation at shell electrons, as well as of photons producing leptons through Compton scattering, photoionization and pair production. The treatment of hadrons is not relevant for the feedback itself, but we have included them to complete the microphysical part as much as possible. However, once neutrons are liberated from air nuclei they can produce protons through charge-exchange reactions and, as such, enhance the proton signal.

We note here that this is the same microphysics as in Dwyer (2003) where new RREAs are initiated by electrons produced by photons or positrons. However, in our model we do not look into RREAs in homogeneous fields. Hence our feedback terminology differs slightly from the one used in Dwyer (2003) since we do not look into the feedback of photons and positrons on RREAs, but rather into the feedback of one species on another species.

The Monte Carlo code consists of two alternating steps: Between two steps the position and the velocity of the particles are updated according to the relativistic equations of motion in a given electromagnetic field. Afterwards we draw random numbers to determine if a collision, and if so, which collision takes place. For all species we use the same Monte Carlo algorithm as used by Li *et al.* (2012) fed with the above-mentioned cross sections for different species. The probability of a particle colliding with an air molecule is proportional to the air density which we control with the barometric formula. Details of the implementation of the electromagnetic processes can be

found in Köhn and Ebert (2014, 2015).

Parts of this Monte Carlo code were used to calculate the energy distributions of photons and positrons in the vicinity of a negative stepped lightning leader (KÖHN and EBERT, 2015), and the production of X-rays from meter long discharges (KOCHKIN *et al.*, 2016). We already validated our code up to energies of 1 MeV in (KOCHKIN *et al.*, 2016) by comparing the NIST data (BERGER *et al.*, 1998) with our simulation results for the average distance ν for full energy loss of an electron with initial energy E_0 . The NIST data is the so-called CSDA range which is “a very close approximation to the average path length traveled by a charged particle as it slows down to rest, calculated in the continuous-slowing-down approximation. In this approximation, the rate of energy loss at every point along the track is assumed to be equal to the total stopping power. Energy-loss fluctuations are neglected. The CSDA range is obtained by integrating the reciprocal of the total stopping power with respect to energy.” NIST CSDA, <http://physics.nist.gov/PhysRefData/Star/Text/appendix.html>) In the scope of this paper we extended this comparison up to 50 MeV, shown in Figure 7.1 a). Additionally, panel c) shows the relative error $(\nu_{\text{NIST}} - \nu_{\text{Simulation}})/\nu_{\text{Simulation}}$ indicating good agreement between the data and the simulations with a relative error of $\lesssim 0.2$ except for a small deviation for very small and very large energies. However, for intermediate energies where most of the electrons are in the energy distribution, the agreement is much better. As mentioned above, for positrons we use the same cross sections as for electrons in addition to the annihilation of positrons at shell electrons.

Fig. 7.1 b) compares the mean free path Λ of photons in air tabulated in the NIST database (BERGER *et al.*, 1998) and calculated with our Monte Carlo code; panel d) compares the relative difference $(\Lambda_{\text{NIST}} - \Lambda_{\text{Simulation}})/\Lambda_{\text{Simulation}}$. There are the deviations between the NIST data and our simulation results $\lesssim 0.4$ for photon energies below 1 MeV; for photon energies above 1 MeV, however, the relative error tends to zero. This is particularly the energy range we are interested in for the production of electron-positron pairs and of hadrons.

7.2.2 Neutron cross sections

In previous work, e.g. Dwyer *et al.* (2007) and Köhn and Ebert (2015), cross sections for electrons, positrons and photons, have carefully been investigated and documented. Here we revise cross sections for neutrons moving through the atmosphere.

Figure 7.2 a) shows the total cross sections of neutrons colliding with nitrogen molecules as a function of the incident neutron energy. The capture of neutrons is the least significant process, but its probability increases for decreasing energy; the main process for all relevant energies is elastic scattering whereas the probability for inelastic scattering (here this involves all reaction channels other than elastic scattering and capture, e.g. charge-exchange and transfer reactions) is in-between the one for capture and elastic scattering. Figure 7.2 b) shows the cross section for inelastic scattering and the cumulative cross section for elastic and inelastic scattering off air molecules as a function of the neutron energy. The black lines show the inverse column density

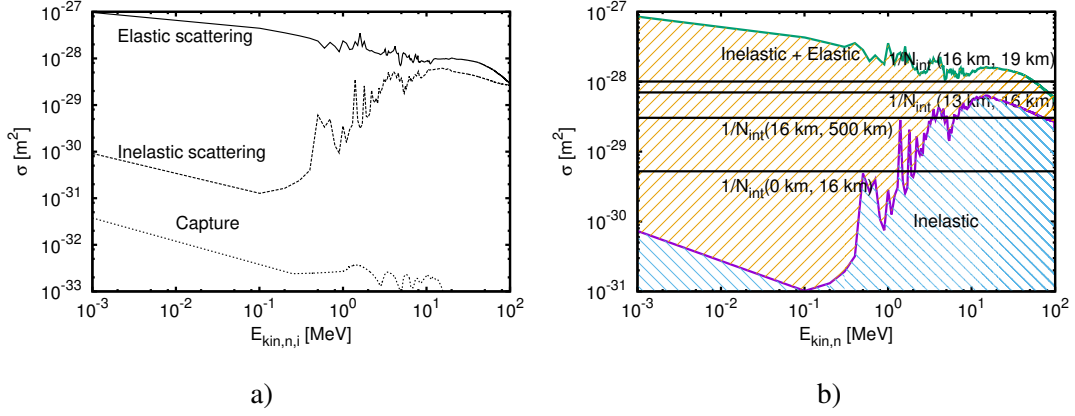


Figure 7.2: a) The total cross section for elastic and inelastic scattering off nitrogen molecules as well as for the capture of neutrons on nitrogen molecules as a function of the energy $E_{kin,n,i}$ of the incident neutron. b) The cumulative cross section of elastic and inelastic scattering in air as well as the inverse column density $1/N_{int}$, (black lines), at altitude ranges of 0-16 km, 13-16 km, 16-19 km and 16-500 km.

$1/N_{int}$ where

$$N_{int}(\mathbf{r}_1, \mathbf{r}_2) := \int_{\mathbf{r}_1}^{\mathbf{r}_2} d\ell n(\mathbf{r}) \quad (7.1)$$

is the air density integrated along the straight path ℓ . n is the density of air molecules given through $n(z) = n_0 \cdot \exp(-z/8.33 \text{ km})$ where $n_0 \approx 2.6 \cdot 10^{25} \text{ m}^{-3}$ is the air density at standard temperature and pressure. We have made a similar analysis for photons in Köhn and Ebert (2015). If $1/N_{int}(\mathbf{r}_1, \mathbf{r}_2) < \sigma$ for a process with cross section σ , a collision of a neutron with an air molecule is very likely. Figure 7.2 b) shows that for neutron energies above 2 MeV inelastic scattering is very probable for the motion of neutrons between 16 km and 500 km or between 16 km and 0 km; neutrons traveling between 16 km and 19 km scatter rather elastically than inelastically.

For elastic scattering the direction of the scattered neutron is determined by using the differential cross section $d\sigma/d\Omega$, $d\Omega = 2\pi \sin \Theta d\Theta$, (MENDOZA *et al.*, 2012, 2014) where Θ is the scattering angle. Once Θ is known, we can use the conservation of energy and momentum to determine the kinetic energy $E_{kin,n,f}$ of the neutron in the final state; it is

$$E_{kin,n,f} = -\frac{\beta}{2\alpha} + \sqrt{\left(\frac{\beta}{2\alpha}\right)^2 - \frac{\gamma}{\alpha}} \quad (7.2)$$

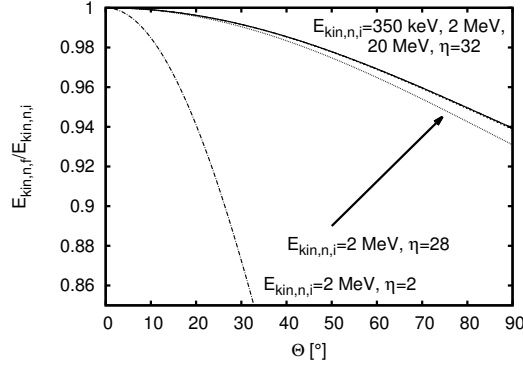


Figure 7.3: The ratio $E_{kin,n,f}/E_{kin,n,i}$ of the neutron energy in the final state $E_{kin,n,f}$ and in the initial state $E_{kin,i}$ after elastic scattering as a function of the scattering angle Θ . Different lines show different initial energies and nucleon numbers η ($\eta = 32$ for O_2 , $\eta = 28$ for N_2 and $\eta = 2$ for H_2).

with

$$\alpha := 4E_{kin,n,i}^2 \sin^2 \Theta + 4(\eta + 1)^2 m_n^2 c^4 + 8E_{kin,n,i}(\eta + 1)m_n c^2 - 8E_{kin,n,i}m_n c^2 \cos^2 \Theta \quad (7.3)$$

$$\beta := -8E_{kin,n,i}^2(\eta - 1)m_n c^2 - 8E_{kin,n,i}(\eta^2 - 1)m_n^2 c^4 - 8E_{kin,n,i}m_n c^2 \cos^2 \Theta - 16E_{kin,n,i}m_n^2 c^4 \cos^2 \Theta \quad (7.4)$$

$$\gamma := 4E_{kin,n,i}^2(\eta - 1)^2 m_n^2 c^4. \quad (7.5)$$

where $E_{kin,n,i}$ is the kinetic energy of the neutron in the initial state, $m_n \approx 1.67 \cdot 10^{-27}$ kg is the neutron mass, $c \approx 3 \cdot 10^8$ m/s is the speed of light and η is the nucleon number of the air molecule. Figure 7.3 shows the ratio $E_{kin,n,f}/E_{kin,n,i}$ as a function of the scattering angle for different initial energies and different nucleon numbers η . It shows that the energy loss increases with increasing scattering angle. Since the nucleon number of air molecules ($\eta = 28$ for N_2 and $\eta = 32$ for O_2) is larger than the rest mass of a neutron the energy loss of neutrons is at most 8% for initial neutron energies between 350 keV and 20 MeV. Thus, neutrons will hardly lose any energy through elastic scattering off air nuclei. For energies above 10 MeV (MENDOZA *et al.*, 2012, 2014) forward scattering is dominant and thus there is no significant energy loss through elastic scattering. For comparison, we also show $E_{kin,n,f}/E_{kin,n,i}$ for hydrogen. Since the mass of molecular hydrogen is close to the one of a neutron, the energy transfer from a neutron to a recoiling hydrogen molecule is significant, even for small scattering angles, and the neutron loses much more energy than through the collision with air molecules.

For energies above 10 MeV, the cross section of inelastic scattering approaches the cross section of elastic scattering. Inelastic scattering of neutrons can either be the excitation of air molecules, their nuclei or the production of charged nucleons through the (n,p) charge-exchange reaction. Figure 7.4 shows the average energy loss ΔE (solid line) for excitations as a function of the incident neutron energy. It shows that the energy loss grows linearly with the energy of the incident neutron. Additionally the dotted line shows the fraction of the energy loss to the incident neutron energy $E_{kin,n,i}$. On average more than 60% of the energy, much more than through elastic

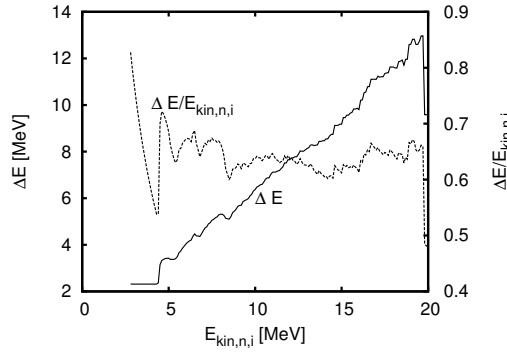


Figure 7.4: The energy loss ΔE of neutrons after exciting air molecules (solid line) and the ratio of the energy loss to the incident neutron energy $E_{kin,n,i}$ (dotted line) as a function of the incident neutron energy.

scattering, is lost through excitations.

The propagation of neutrons through the atmosphere is an interplay of inelastic and elastic scatterings. After neutrons have lost energy through inelastic scattering, the cross section for elastic scattering increases and the average scattering angle becomes larger. Thus the number of elastic scatterings per time unit increases and subsequently the energy loss through elastic scattering becomes more and more significant.

Section 7.3 not only presents the attenuation of neutrons in air, but will also show that the implementation of the above-mentioned cross sections and algorithms yields attenuation lengths comparable to those mentioned in literature. For further validation we compare with data provided by Nakamura and Kosako (1981). They calculate the total neutron flux $r \cdot \Phi(r)$ of an almost monoenergetic upwards directed neutron beam at distance r from the source for different initial energy groups where the flux $\Phi = N_n / (4\pi r^2)$ is defined as the number of neutrons N_n passing through a sphere with radius r . Fig. 7.5 shows the comparison of the flux of a neutron beam for different distances calculated with our simulation tool with the results presented in Fig. 8 of Nakamura and Kosako (1981). In Nakamura and Kosako (1981), they do not use distinct initial energies, but rather energy groups. We compare a 1.5 MeV beam with a beam in energy group 14 (1 - 2.02 MeV) and a 150 keV beam with energy group 16 (67.4 - 247 keV). We observe the same exponential decrease and a good agreement between our results and the ones by Nakamura and Kosako (1981). We see some deviations between our simulations and those of Nakamura and Kosako (1981) which might be related to the fact that they use energy groups rather than distinct initial energies.

7.2.3 Altitude and atmospheric depth

In addition to the different types of collisions it is essential for the understanding of the behavior of a particle beam to know how many air molecules a particle of that beam has encountered during its path through the atmosphere. Thus, the behavior depends not only on the initial altitude, but also on the integrated air density, and hence it is convenient to present results as a function of

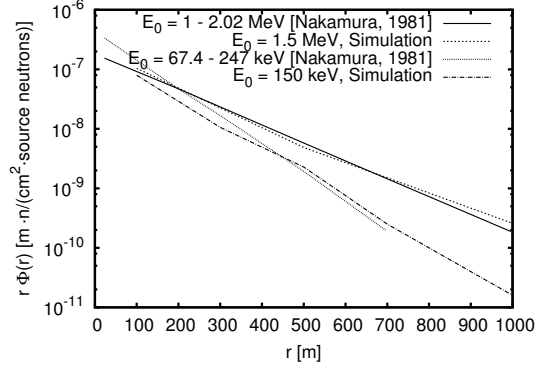


Figure 7.5: The simulation results and the data by Nakamura and Kosako (1981) for the flux $r \cdot \Phi(r)$ of neutron beams of different energies E_0 as a function of distance r .

the atmospheric depth X [g/cm^2] which is defined through (HECK D., *et al.*, 1998)

$$\frac{X(h)}{\text{g}/\text{cm}^2} := \begin{cases} -186.56 + 1222.66 \cdot e^{-\frac{h}{9.9 \text{ km}}}, & 0 \leq h/\text{km} < 4 \\ -94.92 + 1144.91 \cdot e^{-\frac{h}{8.8 \text{ km}}}, & 4 \leq h/\text{km} < 10 \\ 0.61 + 1305.59 \cdot e^{-\frac{h}{6.4 \text{ km}}}, & 10 \leq h/\text{km} < 40 \\ 540.18 \cdot e^{-\frac{h}{7.7 \text{ km}}}, & 40 \leq h/\text{km} < 100 \\ 0.01 - \frac{h}{10^4 \text{ km}}, & 100 \leq h/\text{km} < 112.8. \end{cases} \quad (7.6)$$

instead of using the altitude h . Two beams with different initial altitudes $H_{i,1/2}$, but with the same initial direction, traveling towards altitudes H_1 and H_2 , respectively, behave similar if they have passed through the same amount of air $\Delta X = X(H_1) - X(H_{i,1}) = X(H_2) - X(H_{i,2})$. We note here that the concept of using the atmospheric depth allows to study the similarity of the behaviour of particle beams at different altitudes, but that it does not capture the lateral dimensions.

7.3 RESULTS

We have simulated the motion of different initial monoenergetic particle beams of different species with different initial energies E_0 from different altitudes H_0 , i.e. air package $\Delta X = 0$, in the atmosphere and calculated the temporal evolution of the spatial and energy distributions of all relevant particles. We have chosen the sign of ΔX such that $\Delta X < 0$ refers to altitudes in the initial direction of the particle beam.

The following three subsections establish the feedback model in a piecewise manner. In section 7.3.1 we look into neutrons, in section 7.3.2 we look into photons which eventually produce neutrons and in section 7.3.3 we look into beams of electrons which can produce photons subsequently liberating neutrons from air nuclei.

The duration of the simulations of neutron beams was approximately two to three weeks on an “Intel(R) Xeon(R) CPU E3-1270 v3 @ 3.50GHz”; the simulations of the particle beams in the vicinity of lightning leaders took approximately six months on an “Intel(R) Xeon(R) CPU

7.3.1 The motion of monoenergetic neutron beams through the atmosphere

We simulated the motion of monoenergetic neutron beams originating at different altitudes upwards and downwards; all beams are initiated with 600 neutrons. We note here that we only regard some particular cases to cover the investigation of neutron beams in the keV and MeV range which is the energy range of neutrons as being produced by TGFs (KÖHN and EBERT, 2015). Hence, we get a broad insight into the properties of neutron beams in the atmosphere.

Figure 7.6 shows the spatial distribution of neutrons after 1 ms for initial energies of 350 keV (panel a), 10 MeV (panels b,c,d) and 20 MeV (panel e) for beams from 4 (panels a,b,e) and 16 km (panels c,d) altitude, upwards (panels a,d) and downwards (panels b,c,e). Figure 7.7 shows the energy distribution after 0.25 ms, 0.5 ms, 0.75 ms and 1 ms for the same cases. Neutrons with energies of 350 keV are rather scattered isotropically and travel less than 10 km in air; in the upwards directed beam (Fig. 7.7a) some of the neutrons are backscattered and reach the ground.

The color of the points as well as Fig. 7.7 a) show that there is a maximum in the energy distribution at 100 keV and also that there are still neutrons with 350 keV, thus keeping all their initial energy. As Figure 7.3 shows, inelastic scattering is not dominant for energies below 500 keV, and the only energy loss is through elastic scattering. Due to the randomness of neutrons scattering at air molecules, some neutrons will collide more frequently and lose more energy whereas a few of them will not collide too often and thus keep their energy.

Figures 7.6 and 7.7 b) and e) show that beams of 10 MeV and 20 MeV emitted from 4 km downwards behave similarly. After 1 ms neutrons populate altitudes from 0 km up to 8 km; because of the high probability of inelastic scattering for energies of 10 MeV and 20 MeV the neutrons lose a significant ratio of their initial energy and, hence, after 1 ms most neutrons have energies below 80 keV. The situation changes if the neutron beam was emitted at 16 km altitude (panels c and d). For both upwards and downwards emitted beams there are only a few neutrons reaching the ground. There is a cloud of neutrons close to the source altitude and also neutrons moving upwards. Panels c) and d) of Fig. 7.7 show that for the downwards emitted beam most neutrons have energies below 1 MeV whereas for the upwards emitted beam there is a significant number of neutrons with energies of approximately 10 MeV. While moving upwards, these neutrons have not undergone a considerable number of collisions in the early stage of the beam evolution and once the neutrons have passed a certain altitude, the air density has thinned out, thus collisions become less probable. For the downwards emitted beam neutrons, they have first to backscatter, before they can move upwards; since neutrons lose most of their energy when they are backscattered, the neutron energies are smaller than the ones for the upwards emitted beam.

Figure 7.8 shows the neutron number N normalized to the initial neutron number N_0 passing through altitude z . Panel a) shows an overview of all simulated cases. It shows that the neutron number decreases as the neutrons travel through the atmosphere. This is due to inelastic collisions

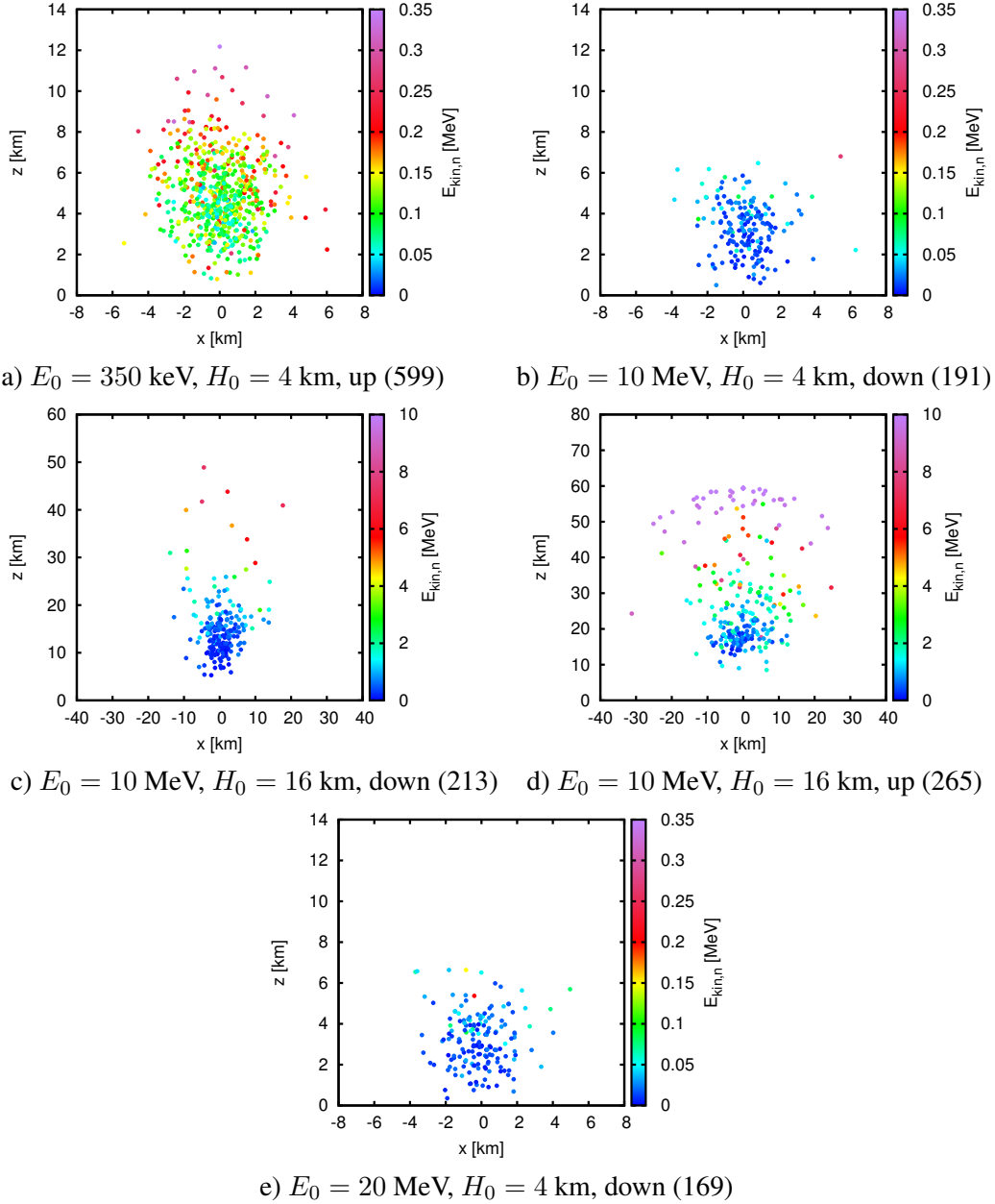


Figure 7.6: The spatial distributions of neutrons after 1 ms for different initial energies E_0 and altitudes H_0 . The color code on the right shows the kinetic energy. Note that the spatial scales are different for different panels. The current neutron number is given in brackets.

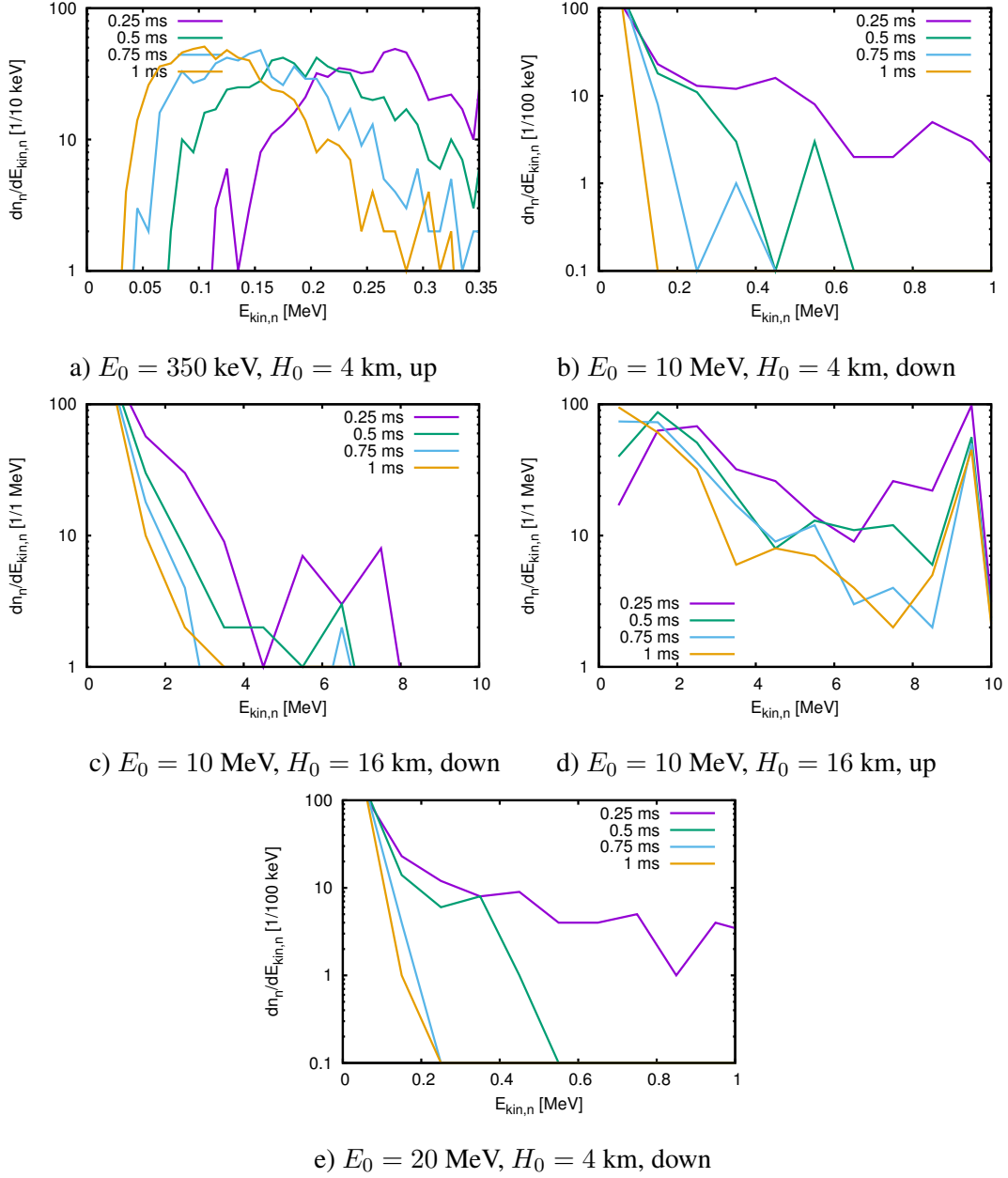


Figure 7.7: The energy distribution $dn_n/dE_{kin,n}$, i.e. the number of neutrons per energy bin, after different time steps for different initial energies E_0 and altitudes H_0 . All simulations were initiated with 600 neutrons.

and for all simulations there is a small probability of detecting neutrons on the ground according to Shah *et al.* (1985), Shyam and Kaushik (1999), Bratolyubova-Tsulukidze (2004), Tsuchiya and other (2012), and Kozlov *et al.* (2013). It also shows that for the same initial energy and altitude showers behave alike no matter whether they move upwards or downwards as long as they pass through the same air package ΔX . Note here that Eq. (7.6) is only valid for altitudes below 112.8 km; hence, the green line representing an upwards emitted beam of 10 MeV neutrons starting at an altitude of 16 km, is interrupted abruptly. $\Delta X = 0$ means no air layer at all and denotes the initial altitude of the neutron beam. Since we measure the flux of neutrons relative to $\Delta X = 0$, N/N_0 drops down to 0 at $\Delta X = 0$.

The attenuation length λ_{att} [g/cm²] is defined as the atmospheric depth where the neutron number has dropped to $1/e$ of the initial neutron number (in the initial direction). For 10 MeV neutrons, it is $\lambda_{att} \approx 74$ g/cm²; for 20 MeV neutrons it is $\lambda_{att} \approx 84$ g/cm² which is in agreement with the values presented by Shibata (1994) and Koi *et al.* (1999).

Panels b) - f) show details for all simulated cases. In each panel for different initial energies, different lines show the neutron number as a function of altitude/atmospheric depth for above different energies $E_{kin,n}$; in these panels $E_{kin,n} \geq 0$ means that all neutrons are taken into account, hence, showing the same line as in panel a). Panels b) - f) explicitly show that most neutrons move in their initial direction. Comparing panel a) with the others shows that for a 350 keV beam more neutrons move in the opposite direction than for beams of 10 MeV or above. Panel d) and e) show that for a 10 MeV beam emitted at 16 km altitude upwards or downwards, hardly any neutrons reach the ground, but move up to several tens of km. The different lines in panels b) - f) show that, regardless of the initial energy, there is a vanishing flux of high energy neutrons and that neutrons reach the ground after having lost a significant fraction of their initial energy. Because of the small neutron scattering cross section for high neutron energies, neutrons with higher energies travel further before losing their energy than low-energy neutrons which leads to the staircase structure in panels b) - f). The staircase structure is due to discretized output of our Monte Carlo simulation every 10 μ s. As such, especially for high neutron energies, we cannot plot the decrease of the neutron number accurately enough and sudden false stairs occur.

Figure 7.9 shows the normalized cross section area $\langle A \rangle(H) = 1/N(H) \cdot \sum_{i=1}^N (x_i^2(H) + y_i^2(H))$ as a function of H or atmospheric layer ΔX . $N(H)$ is the total neutron number at altitude H and $x_i(H)$ as well as $y_i(H)$ are the coordinates of the i -th neutron at altitude H parallel to the xy -plane. As in Fig. 7.8 panel a) shows an overview over all simulated cases whereas panels b) - f) show details for each simulation. Panel a) shows that for all beams from 4 km downwards and upwards the neutron beam covers an area of approximately 1 km² at $H \approx 0$. At the ground the 10 MeV beam from 16 km downwards covers an area of approximately 10 km² whereas the 10 MeV beam from 16 km upwards covers an area of approximately 50 km² because on their way downwards these neutrons scatter more than those initiated at 4 km altitude.

Figures 7.6 and 7.9 also show that for all simulated cases the neutron beams are much more widened for high altitudes in contrast to small altitudes. This is very well illustrated in Fig. 7.6

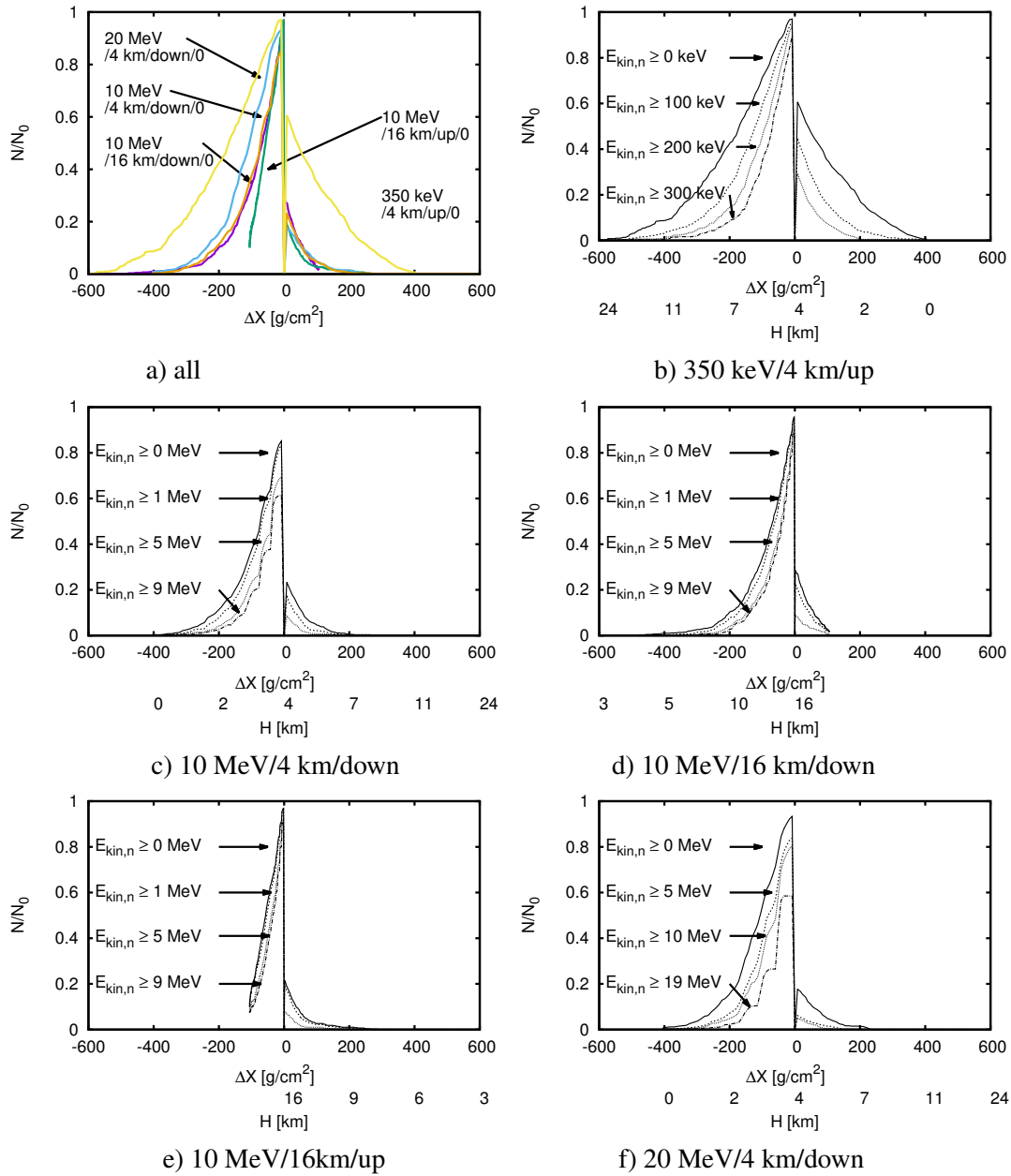


Figure 7.8: a) The normalized neutron number N/N_0 for the same cases as in Figs. 7.6 and 7.7 as a function of atmospheric layer ΔX . Here $\Delta X = 0$ refers to the initial altitude and $\Delta X \neq 0$ denotes the air package in g/cm² which a neutron passes where a negative sign of ΔX denotes the altitudes in the initial direction of the neutron beam. Panels b) - f) show N/N_0 for the different cases in a) distinguishing for different threshold energies $E_{kin,n}$ passing the air package ΔX (first xlabel) and equivalently the altitude H (second xlabel).

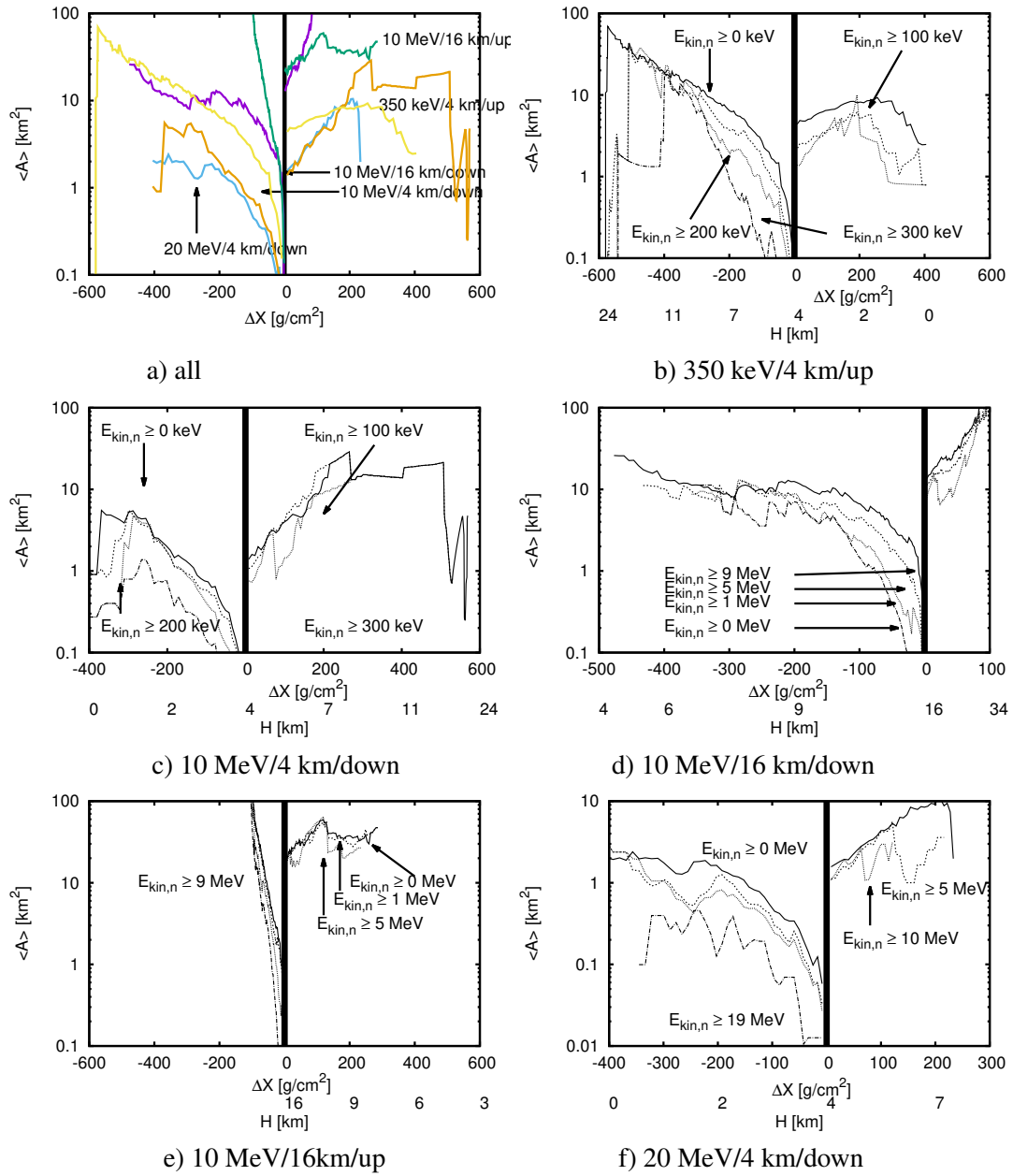


Figure 7.9: The time-integrated normalized cross section area $\langle A \rangle = 1/N \cdot \sum_{i=1}^N (x_i^2 + y_i^2)$ as a function of atmospheric layer ΔX and equivalently of the altitude H . x_i and y_i are the positions of the i -th neutron (out of N) parallel to the xy plane. The solid line at $\Delta X = 0$ indicates the source altitude of the neutron beam. Panel a) shows all simulated cases whereas panels b) - f) show $\langle A \rangle$ for different threshold energies $E_{kin,n}$ for different initial altitudes and different initial energies.

Initial condition	H [km]	$N_n/(\Delta t \cdot A)$ [1/(m ² ms)]	$N_{n,TGF}/\Delta t$ [1/ms]
350 keV/4 km/up	0	$< 10^{-9}$	< 1667
350 keV/4 km/up	6	$5 \cdot 10^{-9}$	8333
350 keV/4 km/up	500	$< 10^{-9}$	< 1667
10 MeV/4 km/down	0	$5 \cdot 10^{-9}$	8333
10 MeV/4 km/down	6	$5 \cdot 10^{-10}$	833
10 MeV/4 km/down	500	$< 10^{-10}$	< 167
10 MeV/16 km/down	0	$< 10^{-13}$	< 0.17
10 MeV/16 km/down	6	$3 \cdot 10^{-10}$	500
10 MeV/16 km/down	500	$< 2 \cdot 10^{-13}$	< 0.33
10 MeV/16 km/up	0	$< 10^{-11}$	< 17
10 MeV/16 km/up	6	10^{-10}	167
10 MeV/16 km/up	500	$< 2 \cdot 10^{-11}$	< 33
20 MeV/4 km/down	0	10^{-9}	1667
20 MeV/4 km/down	6	10^{-10}	167
20 MeV/4 km/down	500	$< 10^{-11}$	< 17

Table 7.1: The fluence $N_n/(\Delta t \cdot A)$ of neutrons at different altitudes for different initial conditions calculated from the simulations as in Fig. 7.6 (600 initial neutrons) and the flux $N_{n,TGF}/\Delta t$ for a typical TGF event (10^{15} neutrons at source altitude) for different initial conditions.

d) and Fig. 7.9 e). Close to the source location of the beam, neutrons scatter at air molecules and, hence, their direction changes; once the neutrons reach a region with a much smaller air density, they do not scatter any more and continue moving in the direction they obtained at lower altitudes. Neutrons moving downwards are confined because they keep on scattering at air molecules.

For all considered cases, Table 7.1 displays the fluence $\Psi = N_n/(\Delta t \cdot A)$ of neutrons at different altitudes, where N_n is the number of neutrons passing through the cross-section area A within the time interval Δt ; a small fluence is equivalent to a small neutron number or a large cross section area. Table 7.1 shows the fluence at ground (0 km), at typical balloon experiment altitudes (6 km) and at typical satellite altitudes (500 km); for those cases where our simulations stopped before neutrons reach the considered altitude or where all of the test neutrons are absorbed beforehand, we present upper bounds of the fluence. For almost all cases, the fluence lies between 10^{-11} and 10^{-9} per square meter and millisecond. The only outliers appear for the 10 MeV neutron beam initiated at 16 km altitude downwards; in that case the flux at ground and at satellite altitude is below approximately $10^{-13} \text{ m}^{-2} \text{ ms}^{-1}$.

The total number of neutrons detectable at altitude H per time interval related to a TGF event can be estimated through $\Psi \cdot N_{n,TGF}/600 \cdot A_{det}$ where $N_{n,TGF}$ is the number of neutrons produced during one TGF flash, 600 the initial number of neutrons in our simulations and A_{det} the size of the detector. Here, we choose $N_{n,TGF} = 10^{15}$ (BABICH *et al.*, 2007); for the detector size we choose approximately 1 m^2 for ground detectors (CHILINGARIAN *et al.*, 2010), for balloon experiments (MARSHALL *et al.*, 1995) and for detectors in satellites (MEEGAN *et al.*, 2009). Table 7.1 shows that for most relevant cases the number of neutrons passing through a detector per millisecond lies between 10 and 2000 with some outliers for a 350 keV beam initiated upwards (8333/ms) and for a 10 MeV beam initiated downwards at 16 km (0.17/ms).

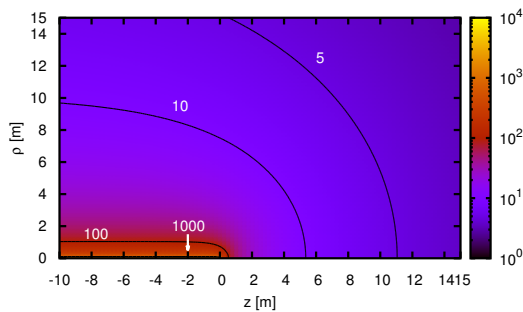


Figure 7.10: Electric field strength (color coded) in the vicinity of the tip for a leader of 1 km length in an ambient field of -0.5 kV/cm. Cylindrical coordinates ($\rho = \sqrt{x^2 + y^2}, z$) are used, and the upper leader tip lies at the origin of the coordinate system. The black level lines indicate fixed values of the electric field strength from 5 to 1000 kV/cm as indicated.

7.3.2 The motion of photons through the atmosphere and the subsequent production and motion of leptons and hadrons

This section is devoted to investigate the dissipation of already existing photons in the vicinity of an ideally conducting lightning leader. The full ab-initio calculation initiated with low-energy electrons will follow in the next section.

We initiate an upwards directed beam of 500 000 photons with energy distributions

$$n_\gamma(E_\gamma) \sim e^{-E_\gamma/3 \text{ MeV}} \quad (7.7)$$

as calculated in the vicinity of a lightning leader in previous work (KÖHN and EBERT, 2014) including electron-electron Bremsstrahlung; all initial photon energies are above 10 MeV since the production of electron and positron pairs as well as the production of neutrons and protons do not contribute significantly to the interaction of photons with air molecules below 10 MeV. As mentioned in section 7.2.1, we also include Compton scattering and photoionization of shell electrons.

We investigate three different cases: no ambient field at standard temperature and pressure (STP), a uniform, constant electric field of -100 kV/cm at STP and the field of a negative stepped lightning leader (KÖHN and EBERT, 2015) of 1 km length and 1 cm curvature radius whose tip is at 4 km altitude, in an ambient field of -0.5 kV/cm, as used by Xu *et al.* (2012); Köhn and Ebert (2015). Fig. 7.10 shows the electric field in the vicinity of the lightning leader as calculated by Köhn and Ebert (2015). There is a large field enhancement close to the leader tip which is enough to accelerate charged leptons into the run-away regime in the vicinity of the leader tip.

While propagating through the atmosphere, photons produce neutrons and protons as well as positrons and electrons producing new Bremsstrahlung photons. For the lightning leader configuration Figure 7.11 shows the detailed position and energy for all different species separately. We note here that we have not implemented collision processes for protons yet and, as such, on

their path through the atmosphere they are only affected by electric fields. In future work we will elaborate their correct motion, too.

There is a distinct beam of photons upwards. While moving upwards, they produce leptons and hadrons. In the presence of any electric field the motion of high-energy electrons is directed against the electric field lines whereas positrons and protons move along the electric field. Since hadrons are emitted isotropically, they move through the atmosphere in such an isotropic manner where the motion of protons is superposed by the electric field. Figure 7.11 demonstrates very well the higher mass of neutrons and protons relative to those of leptons and photons. Because of that distinction, hadrons move much more slowly through the atmosphere than leptons with the same energy. Depending on the electric field, there is the build-up of different layers of species. Dwyer (2003) already calculated this separation for electrons and positrons. Fig. 7.11 shows that in the presence of an electric field there is an additional separation due to the different charges of electrons on the one side and positrons as well as protons on the other side. Since in Fig. 7.11 the electric field is not uniform, negatively charged electrons are not only accelerated upwards, but also sideways. Likewise positively charged protons and positrons are accelerated not only downwards, but also sideways. Hence, charged particles are not beamed along the z axis.

Figure 7.12 shows the energy distribution of photons, leptons and hadrons after $1 \mu\text{s}$ (panels a and b) and after 0.5 ms (panels c and d) for energies above 5 MeV in the case of no electric field (panels a and c) and of the electric leader (panels b and d). Panels a) and b) show that in both cases after $1 \mu\text{s}$ there are leptons and hadrons with energies of up to approximately 30 MeV. Note that the fraction of photons converted to leptons and hadrons is small (EPDL Database, 1997; KÖHN and EBERT, 2014A; FULLER, 1985) and thus there are many fluctuations in the lepton and hadron numbers. Especially, for all simulated cases, there is a hole in the energy distribution of neutrons at approximately 11 MeV which we have already observed in previous work (KÖHN and EBERT, 2015); this hole is an artifact of the resonances to be found in the cross sections for neutron production (see Fig. 7a) in Köhn and Ebert, 2015). Panels c) and d) show that most photons have dissipated after 0.5 ms and that the number of leptons and hadrons has grown. In both cases there are even some rare events where we find hadrons with energies of up to 40 MeV. In the presence of an electric leader field, some few electrons have gained energies of up to 50 MeV. These electron energies are consistent with energies in recently observed electron beams (DWYER *et al.*, 2008); in addition Fig. 7.12 shows that a typical photon beam as the initial state of a TGF can produce neutrons of up to several tens of MeV.

7.3.3 The motion of electrons in the electric field of a negative stepped lightning leader

We also simulated the motion of a monoenergetic electron beam with initial energy of 0.1 eV upwards from 4 km altitude in the field of a leader of 1 km length and of 1 cm curvature at the tip, thus in the same leader field as in section 7.3.2. As we have seen in previous work (KÖHN and EBERT, 2015) and in Fig. 7.10 the enhancement of the electric field through the leader is large enough to overcome the friction of air and accelerate electrons into the run-away

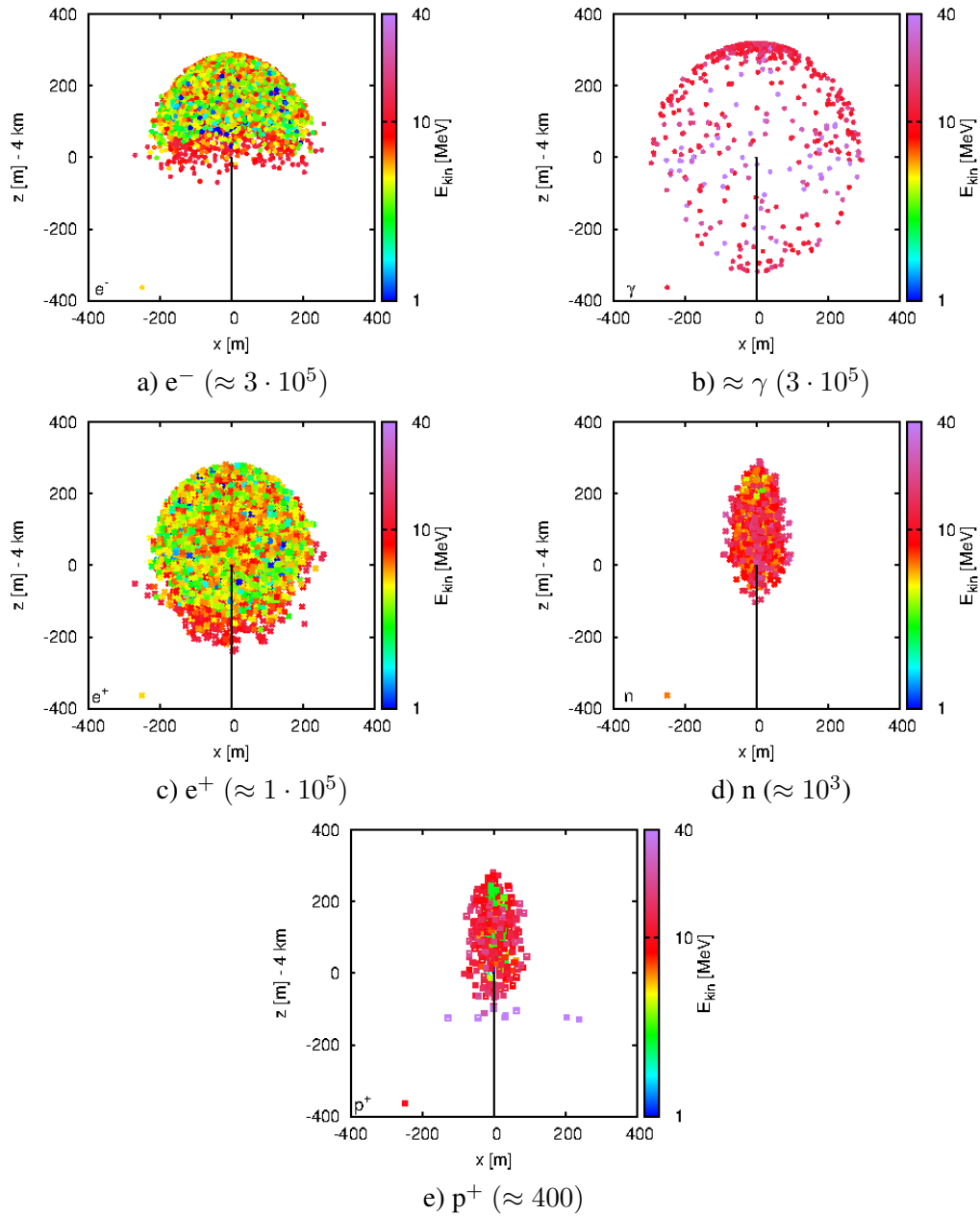


Figure 7.11: The spatial distribution of a) electrons, b) photons, c) positrons, d) neutrons and e) protons after approximately $1 \mu\text{s}$ projected onto the xz plane (for all y) in the electric field of a leader of 1 km length and of 1 cm curvature radius in an ambient field of -0.5 kV/cm (as indicated by the black line). The color code shows the (kinetic) energy of all particles above 1 MeV on a logarithmic scale. The numbers in brackets give the particle numbers.

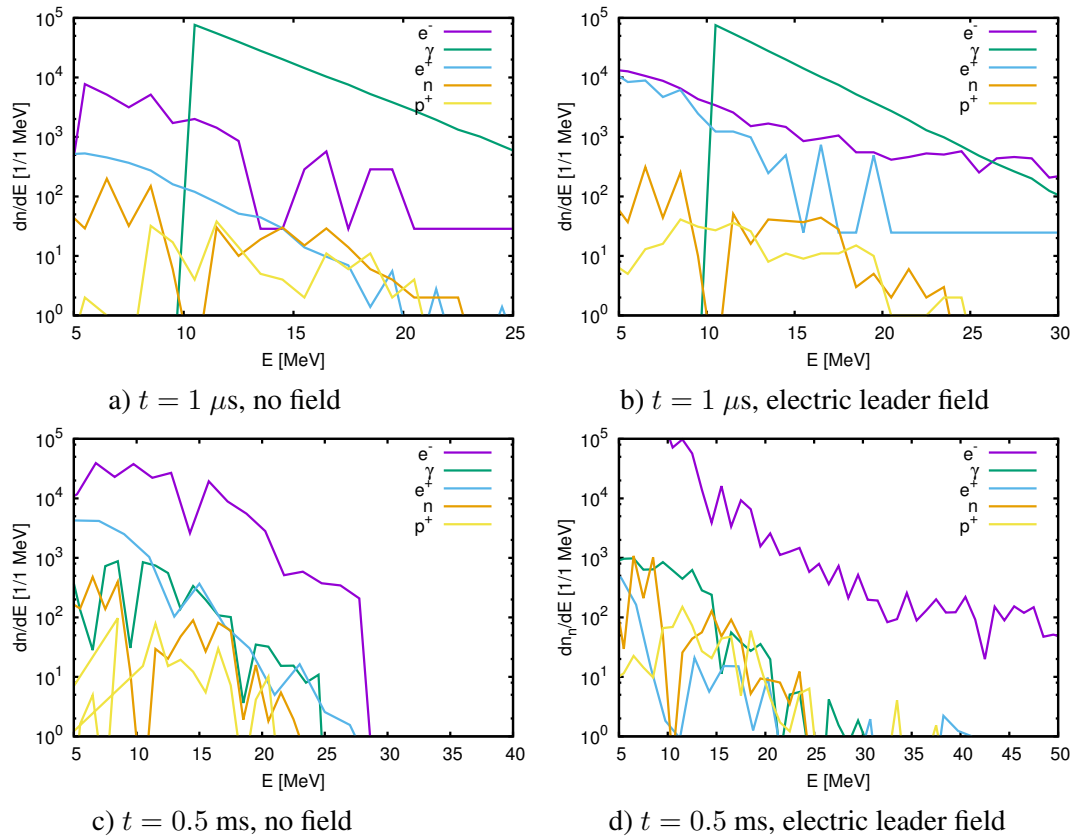


Figure 7.12: The energy distribution of electrons, photons, positrons, neutrons and protons after $1 \mu\text{s}$ (panels a and b) and 0.5 ms (panels c and d). Panels a) and c) are obtained in the absence of any field and panels b) and d) in the field of a leader.

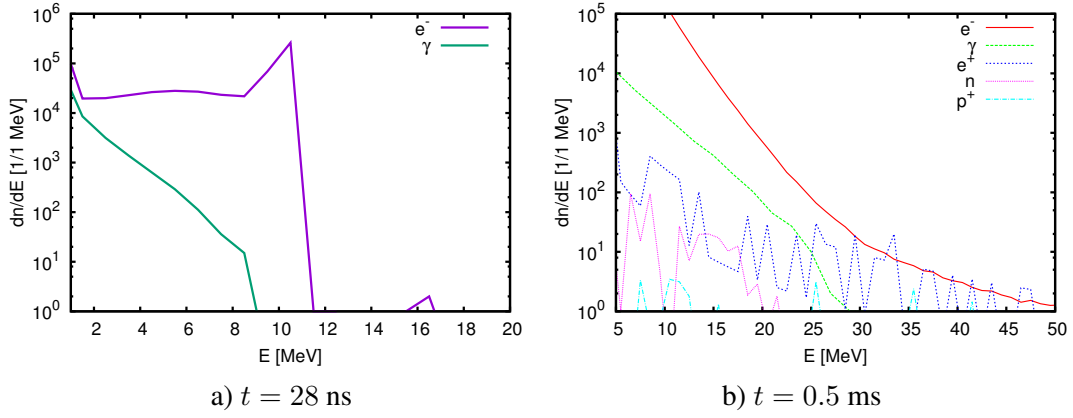


Figure 7.13: The energy distribution of electrons, photons, positrons, neutrons and protons after a) 28 ns and b) 0.5 ms in the same field as in Figure 7.11.

regime. As in Köhn and Ebert (2015) and in Xu *et al.* (2012), we use a simplified model where we do not take space charges into account. After they have gained enough energy, they produce photons through Bremsstrahlung which subsequently produce other species. Figure 7.13 shows the energy distributions after 28 ns and 0.5 ms. It shows that after 28 ns there are already electrons and photons with energies of up to 9 MeV and 16 MeV, respectively. After 0.5 ms electrons have reached energies of up to 50 MeV and there are even positrons with energies of up to 50 MeV. We note here that, as in section 7.3.2, the positron spectrum has a maximum at approximately 5-10 MeV as has been calculated in (Köhn and Ebert, 2015) and been measured by Fermi. Figure 7.13 also shows that there are single hadrons with energies of tens of MeV.

After 0.5 ms leptons, photons and hadrons have reached altitudes of up to 150 km and reached energies up to 50 MeV. Because of the thinning of the air density as a function of altitude, most of these leptons will continue moving upwards, following the geomagnetic field, and can be measured by satellites. Energies of particles in electron and positron beams as well as in TGFs are measured to reach to at least 40 MeV (BRIGGS *et al.*, 2010; MARISALDI *et al.*, 2010; TAVANI *et al.*, 2011) as is also in Fig. 7.13 b). Since in our model leptons can gain energies of above 40 MeV and since there is a small, but not-vanishing probability that these high-energy electrons, might produce Bremsstrahlung photons, even at higher altitudes, this sheds light on the fact that photons with energies above 40 MeV, possibly even of up to 100 MeV might reach satellite altitudes (M. MARISALDI, personal communication, 2015); this effect is not observable if we trace electrons only in the beginning, i.e. some meters in the vicinity of the leader tip although the leader field is still present several kilometers ahead of the leader tip, and not at the later stage of the simulation, or if we do not model the production of electrons by Bremsstrahlung photons at higher altitudes. We observe that these energies can be reached by initiating an electron beam at 4 km altitude. Additionally, as we have seen in section 7.3.1, there is also a small probability that neutrons which are produced by upwards moving photons can be detected not only at satellite altitudes, but also by ground-based instruments.

7.4 CONCLUSIONS AND OUTLOOK

In the course of this paper we investigated the motion of different beams of particles through the atmosphere.

The investigation of different neutron beams has shown that there is a small number of neutrons with energies of up to 20 MeV initiated upwards and downwards reaching the ground and also that upwards initiated neutron beams with energies above 10 MeV can be detected by satellites. However, we have seen that the cross-section areas of these beams are in the order of 0.1 - 100 km² which makes them harder to detect, especially for large cross-section areas. For an average terrestrial gamma-ray flash, producing 10^{15} neutrons, approximately 10 to 2000 neutrons per millisecond, depending on their initial energy and initial altitude, are detectable at ground, at 6 km or 500 km altitude. By analyzing cross-section data we have seen that most of the energy loss originates from inelastic channels whereas elastic collisions do not contribute significantly to the energy loss.

From the investigation of different initial photon and electron beams in different electric field configurations we conclude that in all relevant cases there is the production of leptons (electrons, positrons), photons and hadrons (protons and neutrons) with energies of up to several tens of MeV. Especially, in the case of a lightning leader of 1 km length, we have observed that electron or photon beams already initiated at 4 km altitude, can produce these energies. However, we have seen that in electric fields high-energy electrons and photons move much faster ahead than protons, neutrons and positrons. Positrons and protons are dragged into the opposite direction of the electrons because of their positive charge; even in the absence of any electric field, protons and neutrons move much more slowly than leptons because of their heavier rest mass. Hence we expect hadrons to be measured on a much longer time scale than leptons and photons.

In future work also cross sections for protons should be implemented into our Monte Carlo code to trace them through the atmosphere correctly. Additionally, the effect of space charges should be included in future work to study their effect on the low-energy part of the particle spectrum. Furthermore, our Monte Carlo code can be used to study how a particle signal at the ground or at satellite altitude changes if parameters like the initial particle energy, the relevant altitude or the electric field as well as the geometry of the leader are altered. This could potentially involve electron beams close to lightning leaders or monoenergetic neutron beams.

8 FINAL REMARKS

The HEAP conjunct was discovered in the early nineties. The recent studies still do not fully analyse those phenomena of such recent research field. This work displays different aspects of HEAP, which have distinct lengths and energy scales that may complicate the connection between the emission phases. Here, we investigate from the low energy and micrometer length to high energy and kilometer scale. This joint analysis allows us to see the current knowledge in perspective. The progress in the present work will guide further simulations and experimental research.

The analyzed phenomena produce a variety of particles, nevertheless there is still a number of possible reactions that can add branches in the particle production – such as the neutrinos produced by beta decay and the proton production (as well as its chain reactions) – which are reserved for future works.

This work as a whole is based on Monte Carlo methods, therefore we start with a comparison of several general purpose codes in Chapter 4. Here we investigate different aspects of such codes to determine the limitations and assets of each one using uniform tests. Providing recommendations and determining the best context for each program.

In Chapter 5, we have investigated low energy electrons moving through the air with several electric fields – the very beginning of an electrical discharge.

The results show that electrons can reach higher energies for electric fields below breakdown threshold than once thought because of its stochastic behaviour. This effect is highly composition dependent, i.e., different gases may provide different effects. Here, we provide background for the study of electric discharges in other atmospheres; in the future, it is planned to use similar technique to study atmospheres all over the solar system and beyond.

Different energy regimes provide new phenomena and Chapter 6 shows a complete study on photons and neutrons in the MeV energy range. This chapter provides two sets of number references to further research: reassuring the amount of neutron expected at the ground from the TGF phenomenon and we have predicted the, further confirmed, afterglow effect. The former result should guide experimental research by establishing reasonable possible numbers for detection and the latter provides an important connection between the TGF and long-lasting gamma-ray emissions by thunderclouds which is still not well understood by the community.

Lastly, the branches of particle production are investigated in Chapter 7 and we exploit all possible electron, photon and neutron reactions with the neutrals. In this work there is no ground detection but rather the very beginning of the TGF process during the step-wise lightning leader motion. The proton production in this work is still unexplored by the community because of its low production numbers, in comparison with other natural phenomena, which would complicate the experimental confirmation and because of lack of many cross section data which would facilitate the simulations in the future. Nevertheless, we connect the production numbers directly with the

lightning leader hypothesis providing clarity for further investigation.

We have performed Monte Carlo simulations in different energy regimes throughout the electric discharge context. The large particle number involved in the problem and the numerous possible reactions makes this method attractive but it depends on the computer power available. Nevertheless, the necessity for computer power may be lowered according to the simulations setup, the Chapter 3 provides a large comparison between general purposes codes. Such comparisons have the intention to explicit the limitations and differences of each code and help future research to match the code with the problem necessity. We provide here a series of recommendations for, firstly, the neutral problem and lastly the electromagnetic issue.

RECOMMENDATIONS

- Check where possible custom made codes to well established general purpose codes.
- Make your custom made code available to other researchers.
- For electrons and positrons below 1 MeV straggling should be included.
- For electrons and positrons above 10 MeV radiative loss should not be implemented with uniform friction.
- Photon production (due to bremsstrahlung) by electrons and positrons is under-estimated by EGS5.

From the experience of this study, we give the following general recommendations concerning RREA simulations :

- Codes should be checked / tested / benchmarked using standard test set-ups. In the papers supplementary material, we provide a precise description of such tests.
- Custom-made codes should be make available to other researchers, or at least the results they give for standard tests.
- In order to make it possible to compare results from different studies, the methodology used to derive a given quantity should be rigorously chosen, and presented clearly somewhere.
- Extending the recommendations of Rutjes et al. (2016), we concluded that to get an accurate RREA electron spectra above 10 MeV, radiative loss (bremsstrahlung) should not be implemented with uniform friction only: straggling should be included. Straggling should also be included for ionisation energy loses below the energy threshold.

Concerning the usage of Geant4 for simulating RREA :

- Default settings are not able to simulate RREA accurately. To get accurate RREA results, one of the following tweaks is possible :
 - Changing the α_R ("dR over Range") parameter of the electron/positron ionisation process to 5.0×10^{-3} or less. This solution gives the best ratio between accuracy and computation time. Leave the "final range" parameter to one millimeter (default value) or less.
 - Setting up a step limitation process (or a maximum acceptable step) to one millimeters or less. This will significantly increase the required computation time.
 - Using the single (Coulomb) scattering model instead of multiple scattering (the two previous tweaks relying on the multiple scattering algorithm). This will substantially increase the necessary computation time. This is because multiple scatterings algorithms were invented to make the simulation run faster by permitting to use substantially larger (usually >10 times) step lengths compared to a pure single scattering strategy, while keeping a similar accuracy.
- In section 3.7, of the papers supplementary material, we provide a link to Geant4 example source codes implementing these three methods.
- Compared to using the default Møller/Bhabha scattering models for ionisation, the usage of more accurate cross sections, e.g. taking into account the electrons' molecular binding energies (like done for the Livermore or Penelope models), only leads to minor differences.

These recommendations can guide further simulations using Monte Carlo simulations. Researches can also work by making their own program which is the case for Chapter 5 as well as the REAM and GRRR programs on Chapter 4.

9 REFERENCES

- ADACHI, T., TAKAHASHI, Y., OHYA, H., TSUCHIYA, F., YAMASHITA, K., YAMAMOTO, M., HASHIGUCHI, H., Monitoring of lightning activity in Southeast Asia: Scientific objectives and strategies, **Kyoto Working Papers on Area Studies: G-COE Series** (Vol. 11). Center for Southeast Asian Studies, Kyoto University, 2008.
- Agostinelli, S., Allison, J., Amakon, K., et al.: GEANT4: A simulation toolkit, **Nucl. Instrum. Meth.**, 506, 250–303, [https://doi.org/10.1016/S0168-9002\(03\)01368-8](https://doi.org/10.1016/S0168-9002(03)01368-8), 2003.
- ALLISON, J., AMAKO, K., APOSTOLAKIS, J., et al.: Geant4 developments and applications, **IEEE T. Nucl. Sci.**, 53, 270–278, <https://doi.org/10.1109/TNS.2006.869826>, 2006.
- ALLISON, J., AMAKO, K., APOSTOLAKIS, J., et al.: Recent developments in Geant4, **Nucl. Instrum. Meth.**, 835, 186–225, <https://doi.org/10.1016/j.nima.2016.06.125>, 2016.
- ANDREO, P.: Monte Carlo techniques in medical radiation physics, **Physics in medicine and biology**, 36, 861, 1991.
- APOSTOLAKIS, J., ASAI, M., BOGDANOV, A., et. al.: Geometry and physics of the Geant4 toolkit for high and medium energy applications, **Radiat. Phys. Chem.**, 78, 859–873, <https://doi.org/10.1016/j.radphyschem.2009.04.026>, 2009.
- ARNOLD, It. R., PIERCE, E.T. Leader and junction processes in the lightning discharge as a source of VLF atmospherics, **Radio Sci.**, 68D, 771-776, 1964.
- BABICH, L., Neutron generation mechanism correlated with lightning discharges. **Geomagnetism and Aeronomy**, 47(5), 664–670, 2007.
- BABICH, L. P., High-energy phenomena in electric discharges in dense gases: Theory, experiment and natural phenomena, **ISTC Sci. Technol. Ser.**, 2, 358, 2003.
- BABICH, L. P., Analysis of a new electron-runaway mechanism and record-high runaway-electron currents achieved in dense-gas discharges, **Phys. Usp.**, 48, 1015–1037, 2005.
- BABICH, L. P., Generation of neutrons in giant upward atmospheric discharges. **JETP Letters**, 84(6), 285–288, 2006.
- BABICH, L. P., Analysis of the experiment on the registration of X-rays of the stepped leader of the lightning discharge on the ground, **J. Geophys. Res. Space Physics**, 118,

2573–2582,

doi:10.1002/jgra.50236, 2013.

BABICH, L. P., ROUSSEL-DUPRÉ, R. A., Origin of neutron flux increases observed in correlation with lightning. **Journal of Geophysical Research**, 112, D13303.

<https://doi.org/10.1029/2006JD008340>, 2007

BABICH, L. P., BAKHOV, K. I., BALAKIN, V. A., DONSKOI, E. N., ZAVADA, N. I., ZELENSKII, K. F., IL'KAEV, R. I., KUTSYK, I. M., LOIKO, T. V., NEDOIKASH, Y. M., PAVLOVSKAYA, N. G., ROUSSEL-DUPRE, R. A., SYMBALISTY, E. M. D., AND SHAMRAEV, B. N., An Experimental Investigation of an Avalanche of Relativistic Runaway Electrons under Normal Conditions, **High Temperature**, 42, 1–11,

<https://doi.org/10.1023/B:HITE.0000020085.61526.40>, 2004a.

BABICH, L. P., BOCHKOV, E. I., KUTSYK, I. M., RASSOUL, H. K., Analysis of fundamental interactions capable of producing neutrons in thunderstorms. **Physical Review**, D, 89, 093010.

<https://doi.org/10.1103/PhysRevD.89.093010>, 2014.

BABICH, L. P., DONSKOY, E. N., IL'KAEV, R. I., KUTSYK, I. M., AND ROUSSEL-DUPRE, R. A.: Fundamental parameters of a relativistic runaway electron avalanche in air, **Plasma Phys. Rep.**, 30, 616–624,

<https://doi.org/10.1134/1.1778437>, 2004b.

BABICH, L. P., DONSKOY, E. N., KUTSYK, I. M., KUDRYAVTSEV, A. Y., ROUSSEL-DUPRE, R. A., SHAMRAEV, B. N., AND SYMBALISTY, E. M.: Comparison of relativistic runaway electron avalanche rates obtained from Monte Carlo simulations and kinetic equation solution, **IEEE T. Plasma Sci.**, 29, 430–438, 2001.

BABICH, L. P., E. BOCHKOV, J. R. DWYER, I. M. KUTSYK, AND A. N. ZALYALOV, Numerical analysis of 2010 high-mountain (Tien-Shan) experiment on observations of thunderstorm-related low-energy neutron emissions, **J. Geophys. Res. Space Physics**, 118, 7905–7912, doi:10.1002/2013JA019261, 2013.

BABICH, L. P., E. I. BOCHKOV, I. M. KUTSYK, AND A. N. ZALYALOV, On amplifications of photonuclear neutron flux in thunder storm atmosphere and possibility of detecting them, **JETP Lett.**, 6, 291–296, 2013.

BABICH, L. P., E. I. BOCHKOV, J. R. DWYER, AND I. M. KUTSYK, Numerical simulations of local thundercloud field enhancements caused by runaway avalanches seeded by cosmic rays and their role in lightning initiation, **J. Geophys. Res.**, 117, A09316, doi:10.1029/2012JA017799, 2012.

BABICH, L. P., et al., High-voltage nanosecond discharge in a dense gas at a high overvoltage with runaway electrons, **Sov. Phys. Usp.**, 33, 521–540, 1990.

- BABICH, L. P., et al., Self-sustained relativistic runaway electron avalanches in transverse field of lightning leader as a source of terrestrial gamma-ray flashes, **JETP Lett.**, 94, 606–609, 2011.
- BABICH, L. P., et al., Analysis of fundamental interactions capable of producing neutrons in thunderstorm atmosphere, **Phys. Rev. D**, 89, 093010, 2014.
- BABICH, L. P., et al., A model for electric field enhancement in lightning leader tips to levels allowing X- and γ -ray emissions, **J. Geophys. Res. Space Physics**, 120, 5087–5100, doi:10.1002/2014JA020923, 2015.
- BABICH, L. P., KUDRYAVTSEV, A. Y., KUDRYAVTSEVA, M., KUTSYK, I. , Terrestrial gamma-ray flashes and neutron pulses from direct simulations of gigantic upward atmospheric discharge. **JETP Letters**, 85(10), 483–487, 2007.
- BABICH, L. P.: Generation of neutrons in giant upward atmospheric discharges, **JETP letters**, 84, 285–288, 2006.
- BABICH, L., DONSKOY, E., KUTSYK, I., AND ROUSSEL-DUPRÉ, R., The feedback mechanism of runaway air breakdown, **Geophys. Res. Lett.**, 32, L09809, <https://doi.org/10.1029/2004GL021744>, 2005.
- BABICH, L., KUDRYAVTSEV, A. Y., KUDRYAVTSEVA, M., KUTSYK, I., Atmospheric gamma-ray and neutron flashes. **Journal of Experimental and Theoretical Physics**, 106(1), 65–76, 2008.
- BABICH, L.P., BOCHKOV, E. I., KUTSYK, I.M., ROUSSEL-DUPRÉ, R.A. Localization of the source of terrestrial neutron bursts detected in thunderstorm atmosphere. **JGR**, v. 115, doi: 10.1029/2009JA014750, 2010.
- BAKHOV, K. I., BABICH, L. P., KUTSYK, I. M., Temporal characteristics of runaway electrons in electron-neutral collision-dominated plasma of dense gases. Monte Carlo calculations. **IEEE Transactions on Plasma Science**, 28(4), 1254–1262. <https://doi.org/10.1109/27.893314>, 2000.
- BALDWIN, G.C., KLAIBER, G. S. Photo-fission in Heavy Elements. **Physical Review**, Volume 71, number 1, 1947.
- BASAGLIA, T., BELL, Z., DRESSENDORFER, P., LARKIN, A., AND PIA, M., Writing software or writing scientific articles?, in: Nuclear Science Symposium Conference Record, 2007. NSS'07. **IEEE**, vol. 1, pp. 219–226, IEEE, 2007.
- BATISTA, I. S., ABDU, M. A. , SILVA, A. M. , SOUZA, J. R., Ionospheric F3 layer: Implications for the IRI model. **Advances in Space Research**, v. 31, n.3, p. 607-611, 2003.

- BAZILEVSKAYA, G. A., USOSKIN, I. G., FLÜCKIGER, E. O., HARRISON, R. G., DES-ORGHER, L., BÜTIKOFER, R., ... KOVALTISOV, G. A., Cosmic ray induced ion production in the atmosphere. **Space Science Reviews**, 137, 149–173.
<https://doi.org/10.1007/s11214-008-9339-y>, 2008.
- BERGER, M. J., et al., **NIST Standard Reference Database. 8 XGAM NBSIR 87-3**. [Available at <http://physics.nist.gov/PhysRefData/Xcom/Text/XCOM.html>], 1998.]
- BERMAN, B.L. **Atlas of photoneutron cross sections obtained with monoenergetic photons. Atomic data and nuclear data tables**, v. 15, n. 4, p.319-390, 1975.
- BETHE, H, HEITLER, W. On the Stopping of Fast Particles and on the Creation of Positive Electrons. **The Royal Society**,
 doi: 10.1098/rspa.1934.0140, 1934.
- BITTENCOURT, J. A. **Fundamentals of plasma physics** . 3. ed. New York: Springer, 2004.
- BLATT, J. M., WEISSKOPF, V. F., **Theoretical Nuclear physics**. New York: Springer-Verlag, 1979.
- BLEVIN, H. A., FLETCHER, J., Transport and rate coefficients in townsend discharges. **Australian Journal of Physics**, 37, 593–600.
<https://doi.org/10.1071/PH840593>, 1984.
- BOEUF, J. P., MARODE, E. A Monte Carlo analysis of an electron swarm in a non-uniform field: The cathode region of a glow discharge in helium. **Journal of Physics D: Applied Physics**, 15(11), 2169–2187, 1982.
- BÖHLEN, T., CERUTTI, F., CHIN, M., FASSÒ, A., FERRARI, A., ORTEGA, P., ... VLA-CHOUDIS, V., **The fluka code: Developments and challenges for high energy and medical applications**. Nuclear Data Sheets, 120, 211–214, 2014.
- BOWERS, G. S., SMITH, D. M., MARTINEZ-MCKINNEY, G., KAMOGAWA, M., CUMMER, S., DWYER, J., WANG, D., STOCK, M., and KAWASAKI, Z.: Gamma Ray Signatures of Neutrons From a Terrestrial Gamma Ray Flash, **Geophys. Res. Lett.**, 44, 10063–10070, 2017.
- BRATOLYUBOVA-TSULUKIDZE, L., GRACHEV, E., GRIGORYAN, O., KUNITSYN, V., KUZHEVSKIJ, B., LYSAKOV, D., ... USANOVA, M. Thunderstorms as the probable reason of high background neutron fluxes at $L < 1.2$. **Advances in Space Research**, 34(8), 1815–1818, 2004.
- BRIGGS, M. S., CONNAUGHTON, V., WILSON-HODGE, C., PREECE, R. D., FISHMAN, G. J., KIPPEN, R. M., BHAT, P., PACIESAS, W. S., CHAPLIN, V. L., MEEGAN, C. A., VON KIENLIN, A., GREINER, J., DWYER, J. R., and SMITH, D. M.: Electron-positron beams from terrestrial lightning observed with Fermi GBM, **Geophys. Res. Lett.**,

38, L02808,

<https://doi.org/10.1029/2010GL046259>, 2011.

BRIGGS, M.S., et al., First results on terrestrial gamma ray flashes from the Fermi Gamma ray Burst Monitor. **JGR**, v. 115,

doi: 10.1029/2009JA015242, 2010.

BROWN, J. M. C., DIMMOCK, M. R., GILLAM, J. E., AND PAGANIN, D. M., A low energy bound atomic electron Compton scattering model for Geant4, **Nucl. Instrum. Meth. B**, 338, 77–88,

<https://doi.org/10.1016/j.nimb.2014.07.042>, 2014.a

BRUCE, C.E.R., GOLDE, R.H. The lightning discharge. **The journal of the institution of electrical engineers**, v. 88, n. 6, 1941.

BRUM, C. G. M. **Variabilidade da absorção de ruído cósmico via riômetro e modelagem numérica dos processos associados**, São José dos Campos, 2005.

CARLSON, B. E., et al., Terrestrial gamma ray flash production by active lightning leader channels, **J. Geophys. Res.**, 115,

doi:10.1029/2010JA015647, 2010.

CARLSON, B. E., GJESTELAND, T., and ØSTGAARD, N.: Terrestrial gamma-ray flash electron beam geometry, fluence, and detection frequency, *Journal of Geophysical Research (Space Physics)*, 116, A11217,

doi:10.1029/2011JA016812, 2011.

CARLSON, B. E., LEHTINEN, N. G. and INAN, U. S., Constraints on terrestrial gamma ray flash production from satellite observation, **GRL**, 34,L08809,

doi:10.1029/2006GL029229, 2007.

CARLSON, B.E., LEHTINEN, N.G., INAN, U.S., Neutron production in terrestrial gamma ray flashes. **JGR**, v.115,

doi: 10.1029/2009JA014696, 2010.

CARRIER, J.-F., ARCHAMBAULT, L., BEAULIEU, L., AND ROY, R., Validation of GEANT4, an object-oriented Monte Carlo toolkit, for simulations in medical physics, **Medical physics**, 31, 484–492, 2004.

CELESTIN, S. PASKO, V. P.: Energy and fluxes of thermal runaway electrons produced by exponential growth of streamers during the stepping of lightning leaders and in transient luminous events, **J. Geophys. Res.-Space**, 116, A03315,

<https://doi.org/10.1029/2010JA016260>, 2011.

CELESTIN, S. PASKO, V. P.: Soft collisions in relativistic runaway electron avalanches, *J. Phys. D*, 43, 315206,

<https://doi.org/10.1088/0022-3727/43/31/315206>, 2010.

CELESTIN, S., XU, W., PASKO, V.P. Terrestrial gamma ray flashes with energies up to 100 MeV produced by nonequilibrium acceleration of electrons in lightning. **JGR**, v.117, 2012. doi: 10.1029/2012JA017535.

CELOTTA, R., LEVINE, J. **Methods of experimental physics volume 23 –part A Neutron Scattering** Academic Press, Inc, 1986.

CHANRION, O. and NEUBERT, T.: Production of runaway electrons by negative streamer discharges, **J. Geophys. Res.-Space**, 115, A00E32, <https://doi.org/10.1029/2009JA014774>, 2010.

CHANRION, O., BONAVENTURA, Z., BOURDON, A., and NEUBERT, T.: Influence of the angular scattering of electrons on the runaway threshold in air, **Plasma Phys. Contr. F.**, 58, 044001, <https://doi.org/10.1088/0741-3335/58/4/044001>, 2016.

CHANRION, O., BONAVENTURA, Z., ÇINAR, D., BOURDON, A., NEUBERT, T., Runaway electrons from a “beam-bulk” model of streamer: Application to TGFs. **Environmental Research Letters**, 9, 55,003. <https://doi.org/10.1088/1748-9326/9/5/055003>, 2014.

CHEN, Q., CHEN, B., CAI, R., XU, B., **Numerical study of energy transport in expanding lightning return stroke channel**. Eighth International Conference on Computational Fluid Dynamics (ICCFD8), Chengdu, China, July 14-18, 2014.

CHILINGARIAN, A., BOSTANJYAN, N., VANYAN, L. Neutron bursts associated with thunderstorms. **Physical review D**, v. 85, doi: 10.1103/PhysRevD.85.085017, 2012.

CHILINGARIAN, A., CHILINGARYAN, S., KARAPETYAN, T., KOZLINER, L., KHANIKYANTS, Y., HOVSEPYAN, G., et al., On the initiation of lightning in thunderclouds. **Scientific Reports**, 7, 1371. <https://doi.org/10.1038/s41598-017-01288-0>, 2017.

CHILINGARIAN, A., et al., Ground-based observations of thunderstorm-correlated fluxes of high-energy electrons, gamma rays and neutrons, **Phys. Rev. D**, 82, 043009, 2010.

CHILINGARIAN, A., HOVSEPYAN, G., and HOVHANNISYAN, A.: Particle bursts from thunderclouds: Natural particle accelerators above our heads, **Physical review D**, 83, 062001, 2011.

CHILINGARIAN, A., HOVSEPYAN, G., KHANIKYANC, G., REYMERS, A., and SOGHOMONYAN, S.: Lightning origination and thunderstorm ground enhancements terminated by the lightning flash, **EPL (Europhysics Letters)**, 110, 49001, <https://doi.org/10.1209/0295-5075/110/49001>, 2015.

- CHILINGARIAN, A., MAILYAN, B., and VANYAN, L.: Recovering of the energy spectra of electrons and gamma rays coming from the thunderclouds, **Atmos. Res.**, 114, 1–16, <https://doi.org/10.1016/j.atmosres.2012.05.008>, 2012.
- CHOI, H., FIRESTONE, R., LINDSTROM, R., MOLNÁR, G. L., MUGHABGHAB, S., REVAY, Z., ... ZHOU, C., **Database of Prompt Gamma Rays from Slow Neutron Capture for Elemental Analysis**. Vienna: International Atomic Energy Agency, 2007.
- CHRISTIAN, H.J., BLAKESLEE, R.J., BOCCIPPIO, D.J., BOECK, W.L., BUECHLER, D.E., DRISCOLL, K.T., GOODMAN, S.J., HALL, J.M., KOSHAK, W.J., MACH, D.A., STEWART, M.F. Global frequency and distribution of lightning as observed from space by the Optical Transient Detector. **JGR**, v.108, doi: 10.1029/2002JD002347, 2003.
- COESA, U.S. **Standard atmosphere, 1976, U.S.**, U.S. Government Printing Office, Washington, D.C. 1976.
- COLEMAN, L. M. DWYER, J. R.: Propagation speed of runaway electron avalanches, **Geophys. Res. Lett.**, 33, L11810, <https://doi.org/10.1029/2006GL025863>, 2006.a, b, c, d, e, f
- COLMAN, J. J., ROUSSEL-DUPRÉ, R. A., TRIPLETT, L., Temporally self-similar electron distribution functions in atmospheric breakdown: The thermal runaway regime. **Journal of Geophysical Research**, 115, A00E16. <https://doi.org/10.1029/2009JA014509>, 2010.
- CONNAUGHTON, V., et al. Radio signals from electron beams in terrestrial gamma ray flashes, **J. Geophys. Res. Space Physics**, 118, 2313–2320, doi:10.1029/2012JA018288, 2013.
- COORAY, V. **The lightning flash**. London, United Kingdom: Institution of Engineering and Technology, 2010. IET power and energy series 69, 2014.
- COORAY, V., AREVALO, L., RAHMAN, M., DWYER, J., AND RASSOUL, H.: On the possible origin of X-rays in long laboratory sparks, **J. Atmos. Sol.-Terr. Phy.**, 71, 1890, <https://doi.org/10.1016/j.jastp.2009.07.010>, 2009.
- Cosmic Ray Conference**, vol. 7, edited by D. KIEDA, M. SALAMON, AND B. DINGUS, pp. 325, Under the auspices of the International Union of Pure and Applied Physics (IUPAP), Salt Lake City, Utah.
- CRAMER, E. S., DWYER, J. R., and RASSOUL, H. K.: Magnetic field modification to the relativistic runaway electron avalanche length, **J. Geophys. Res.-Space**, 121, 11261–11270, <https://doi.org/10.1002/2016JA022891>, 2016.

- CRAMER, E. S., DWYER, J. R., ARABSHAHI, S., VODOPIYANOV, I., LIU, N., RAS-SOUL, H.: An analytical approach for calculating energy spectra of relativistic runaway electron avalanches in air, **J. Geophys. Res.-Space**, 119, 7794–7823, 2014.
- CULLEN, D. E., HUBBELL, J. H., and KISSEL, L.: **EPDL97: the Evaluated Photon Data Library**, '97 Version, Accessed, 1997.
- CUMMER, S. A., BRIGGS, M. S., DWYER, J. R., XIONG, S., CONNAUGHTON, V., FISHMAN, G. J., LU, G., LYU, F., SOLANKI R. The source altitude, electric current, and intrinsic brightness of terrestrial gamma ray flashes, **Geophys. Res. Lett.**, 41, 8586–8593, doi:10.1002/2014GL062196, 2014.
- CUMMER, S.A., ZHAI, Y., HU, W., SMITH, D.M., LOPEZ, L.I., STANLEY, M.A. Measurements and implications of the relationship between lightning and terrestrial gamma ray flashes. **GRL**, v. 32, doi: 10.1029/2005GL022778, 2005.
- CUMMINS, K. L., MURPHY, M. J. An overview of lightning locating systems: History, techniques, and data uses, with an in-depth look at the U.S. NLDN , **IEEE Trans. Electro-magn. Compat.**, 51, pp. 499–518, doi:10.1109/TEMC.2009.2023450, 2009.
- DA SILVA, C., SÃO SABBAS, F.T. Consequences of the application of the streamer fluid model to the study of the sprite inception mechanism. **Advances in Space Research**, v. 51, p. 1902-1915, 2013.
- DIETRICH, S.S., BERMAN, B.L. **Atlas of photoneutron cross sections obtained with monoenergetic photons**, **Atomic Data and Nuclear Data Tables**, 38(2), 199-338.
- DINIZ, G. **High Energy Emissions from Thunderclouds: HEETs, from photons to neutrons toward the ground.**, Masters, São José dos Campos, 2016.
- DINIZ, G., RUTJES, C., EBERT, U., FERREIRA, I. S., SÃO SABBAS, E. F. T. Modeling detected neutrons related to High Energy Atmospheric Phenomena. **Journal of Geophysical Research**, 123, 12726 - 12737, <https://doi.org/10.1029/2018JD028962>, 2018.
- DROZDOV, A., GRIGORIEV, A., MALYSHKIN, Y., Assessment of thunderstorm neutron radiation environment at altitudes of aviation flights. **Journal of Geophysical Research: Space Physics**, 118, 947–955. <https://doi.org/10.1029/2012JA018302>, 2013
- DUBINOVA, A., RUTJES, C., EBERT, U. **Streamer discharge inception in a sub-breakdown electric field from a dielectric body with a frequency dependent dielectric permittivity.** In: INTERNATIONAL CONFERENCE ON REACTIVE PLASMAS, 9., 2015, Hawaii. Proceeding... Hawaii: AMS, 2015.

- DUBINOVA, A., RUTJES, C., EBERT, U., BUITINK, S., SCHOLTEN, O., and TRINH, G. T. N.: Prediction of Lightning Inception by Large Ice Particles and Extensive Air Showers, **Phys. Rev. Lett.**, 115, 015002, <https://doi.org/10.1103/PhysRevLett.115.015002>, 2015.
- DUNN, W.L., SHULTIS, J.K. **Exploring Monte Carlo methods**. Academic Press, 2012.
- DWYER, J. R., Implications of x-ray emission from lightning. **Geophysical Research Letters**, 31, L12102. <https://doi.org/10.1029/2004GL019795>, 2004.
- DWYER, J. R. and SMITH, D. M.: A comparison between Monte Carlo simulations of runaway breakdown and terrestrial gamma-ray flash observations, **GRL**, 32, L22804, doi:10.1029/2005GL023848, 2005.
- DWYER, J. R., CUMMER, S. A. Radio emissions from terrestrial gamma ray flashes, **J. Geophys. Res. Space Physics**, 118, 3769–3790, doi:10.1002/jgra.50188, 2013.
- DWYER, J. R., GREFENSTETTE, B. W., and SMITH, D. M.: High-energy electron beams launched into space by thunderstorms, **Geophys. Res. Lett.**, 35, L02815, <https://doi.org/10.1029/2007GL032430>, 2008.
- DWYER, J. R., SMITH, D. M., and CUMMER, S. A., High-Energy Atmospheric Physics: Terrestrial Gamma-Ray Flashes and Related Phenomena, **Space Sci. Rev.**, 173, 133–196, <https://doi.org/10.1007/s11214-012-9894-0>, 2012.
- DWYER, J. R., SMITH, D. M., HAZELTON, B. J., GREFENSTETTE, B. W., KELLEY, N. A., LOWELL, A. W., SCHAAL, M. M., RASSOUL, H. K.: Positron clouds within thunderstorms, **J. Plasma Phys.**, 81, 475810405, <https://doi.org/10.1017/S0022377815000549>, 2015.
- DWYER, J. R.: A fundamental limit on electric fields in air, **Geophys. Res. Lett.**, 30, 2055, <https://doi.org/10.1029/2003GL017781>, 2003.
- DWYER, J. R.: Relativistic breakdown in planetary atmospheres, **Phys. Plasmas**, 14, 042901, <https://doi.org/10.1063/1.2709652>, 2007.
- DWYER, J. R.: Source mechanisms of terrestrial gamma-ray flashes, **J. Geophys. Res.-Atmos.**, 113, D10103, <https://doi.org/10.1029/2007JD009248>, 2008.
- DWYER, J., SALEH, Z., RASSOUL, H., CONCHA, D., RAHMAN, M., COORAY, V., JERAULD, J., UMAN, M., and RAKOV, V.: A study of X-ray emissions from laboratory

sparks in air at atmospheric pressure, **Journal of Geophysical Research: Atmospheres**, 113, 2008a.

DWYER, J.R. et al. Energetic radiation produced by rocket-triggered lightning. **Science**, 299: 694–7, 2003.

DWYER, J.R. The relativistic feedback discharge model of terrestrial gamma ray flashes. **JGR**, v. 117, doi:10.1029/2011JA017160, 2012.

DWYER, J.R., RASSOUL, H.K., AL-DAYEH, M., CARAWAY, L., WRIGHT, B., CHREST, A., UMAN, M.A., RAKOV, V.A., RAMBO, K.J., JORDAN, D.M., JERAULD, J., SMYTH, C. A ground level gamma ray burst observed in association with rocket-triggered lightning. **GRL**, v. 31, doi: 10.1029/2003GL018771, 2004.

EACK, K. B., BEASLEY, W. H., RUST, W. D., MARSHALL, T. C., and STOLZENBURG, M.: Initial results from simultaneous observation of X-rays and electric fields in a thunderstorm, **J. Geophys. Res.-Atmos.**, 101, 29637–29640, <https://doi.org/10.1029/96JD01705>, 1996.

ENOTO, T., WADA, Y., FURUTA, Y., NAKAZAWA, K., YUASA, T., OKUDA, K., et al., Photonuclear reactions triggered by lightning discharge. *Nature*, 551, 481–484, 2017.

EPDL Database, **Photon and electron interaction data**, 1997. [Available at <http://www-609.nds.iaea.org/epdl97/>.]

FERRARI, A., SALA, P. R., FASSO, A., AND RANFT, J.: **FLUKA: A multi-particle transport code (Program version 2005)**, Tech. rep., 2005.

FERRARI, A., SALA, P.R., FASSÒ, A., RANFT, J., **FLUKA: a multi-particle transport code (program version 2014)**, Stanford, CA: CERN, 2014.

FIALA, A., L. C. PITCHFORD, and J. P. BOEUF, 2-dimensional, hybrid model of low-pressure glow-discharges, **Phys. Rev. E**, 49, 5607–5622, 1994.

FISHMAN, G.J., BHAT, P.N., MALLOZZI, R., HORACK, J.M., KOSHUT, T., KOUVELIOTOU, C., PENDLETON, G.N., MEEGAN C.A., WILSON, R.B., PACIESAS, W.S., GOODMAN, S.J., CHRISTIAN, H.J. Discovery of intense gamma ray flashes of atmospheric origin. **Science, new series**, v. 264, n. 5163, p.1313-1316, 1994.

FLEISCHER, R. L., PLUMER, J., CROUCH, K., Are neutrons generated by lightning?. **Journal of Geophysical Research**, 79(33), 5013–5017, 1974.

FULLER, E. G., Photonuclear reaction cross sections for 12 C, 14 N and 16 O, **Phys. Rep.**, 127, 185–231, 1985.

- GJESTELAND, T., ØSTGAARD, N., LAVIOLA, S., MIGLIETTA, M., ARNONE, E., MARISALDI, M., et al. (2015). Observation of intrinsically bright terrestrial gamma ray flashes from the Mediterranean basin. **Journal of Geophysical Research: Atmospheres**, 120, 12,143–12,156.
<https://doi.org/10.1002/2015JD023704>
- GREFENSTETTE, B. W., SMITH, D. M., HAZELTON, B. J., LOPEZ, L. I.: First RHESSI terrestrial gamma ray flash catalog, **J. Geophys. Res.-Space**, 114, A02314,
<https://doi.org/10.1029/2008JA013721>, 2009.
- GREINER, W., J. REINHARDT, **Quantenelektrodynamik**, Frankfurt am Main, Verlag Harri Deutsch, 1995.
- GRIFFITHS, D. **Introduction to Electrodynamics**. Prentice Hall, New Jersey, 1999.
- GRIGORIEV, A. V., et al., Thunderstorm neutrons in near space: Analyses and numerical simulation, **J. Geophys. Res.**, 115, A00E52,
[doi:10.1029/2009JA014870](https://doi.org/10.1029/2009JA014870), 2010.
- GUREVICH, A., On the theory of runaway electrons. **Soviet Physics JETP**, 12(5), 904–912, 1961.
- GUREVICH, A. ZYBIN, K.: Kinetic equation for high energy electrons in gases, **Phys. Lett. A**, 237, 240–246, 1998.a
- GUREVICH, A. V., A. N. KARASHTIN, Runaway breakdown and hydrometeors in lightning initiation, **Phys. Rev. Lett.**, 110(185005), 2013.
- GUREVICH, A., ANTONOVA, V., CHUBENKO, A., KARASHTIN, A., KRYAKUNOVA, O., LUTSENKO, V. Y., ... ZYBIN, K. P., The time structure of neutron emission during atmospheric discharge. **Atmospheric Research**, 164, 339–346, 2015.
- GUREVICH, A., CHUBENKO, A., KARASHTIN, A., MITKO, G., NAUMOV, A., PTITSYN, M., ... ZYBIN, K. P., Gamma-ray emission from thunderstorm discharges. **Physics Letters A**, 375(15), 1619–1625. 2011.
- GUREVICH, A., MILIKH, G., AND ROUSSEL-DUPRE, R., Runaway electron mechanism of air breakdown and preconditioning during a thunderstorm, **Phys. Lett. A**, 165, 463–468,
[https://doi.org/10.1016/0375-9601\(92\)90348-P](https://doi.org/10.1016/0375-9601(92)90348-P), 1992.
- GUREVICH, A.V., ANTONOVA, V.P., CHUBENKO, A.P., KARASHTIN,A.N., MITKO, G.G., PTITSYN, M.O., RYABOV, V.A., SHEPETOV, A.I., SHLYUGAEV, YU.V., VILDANOVA,L.I., ZYBIN, K.P. Strong flux of low-energy neutrons produced by thunderstorms. **PRL**, v.108, 125001,
[doi: 10.1103/PhysRevLett.108.125001](https://doi.org/10.1103/PhysRevLett.108.125001), 2012.

HAZELTON, B. J., GREFENSTETTE, B.W., SMITH, D. M., DWYER, J. R., SHAO, X.-M., CUMMER, S. A., CHRONIS, T., LAY, E. H., HOLZWORTH, R. H.: Spectral dependence of terrestrial gamma-ray flashes on source distance, **GRL**, 36, L01108, doi:10.1029/2008GL035906, 2009.

HECK, D., KNAPP, J., CAPDEVIELLE, J., SCHATZ, G., THOUW, T., et al.: **CORSIKA: A Monte Carlo code to simulate extensive air showers**, vol.6019, FZKA, 1998.

HIRAYAMA, H., NAMITO, Y., NELSON, W. R., BIELAJEW, A. F., WILDERMAN, S. J., and MICHIGAN, U.: **The EGS5 code system**, Tech. rep., United States. Department of Energy, 2005.

IHADDADENE, M. A. CELESTIN, S.: Increase of the electric field in head-on collisions between negative and positive streamers, **Geophys. Res. Lett.**, 42, 5644–5651, <https://doi.org/10.1002/2015GL064623>, 2015.

International Commission on Radiation Units and Measurements. **Stopping powers of electrons and positrons**, ICRU Rep. 37, Bethesda, Md, 1984.

IVANCHENKO, V. N., BUKIN, A. D., DUBROVIN, M. S., EIDELMAN, S. I., GROZINA, N. A., AND TAYURSKY, V. A.: **UNIMOD2: Universal Monte Carlo code for simulation of e+ e- experiments**, in: **MC 91: Detector and event simulation in high-energy physics**, Proceedings, Workshop, Amsterdam, the Netherlands, 8–12 April, 1991, 79–85, 1991.

JACOB, J. H., Multiple electron-scattering through a slab, **Phys. Rev. A**, 8, 226–235, 1973.

KARSHENBOIM, S. G.: Precision study of positronium: Testing bound state QED theory, **International Journal of Modern Physics A**, 19, 3879–3896, 2004.

KELLEY, N. A., SMITH, D. M., DWYER, J. R., SPLITT, M., LAZARUS, S., MARTINEZ-MCKINNEY, F., HAZELTON, B., GREFENSTETTE, B., LOWELL, A., RASSOUL, H. K.: Relativistic electron avalanches as a thunderstorm discharge competing with lightning, **Nat. Commun.**, 6, 7845, <https://doi.org/10.1038/ncomms8845>, 2015.

KIRCHOFF, V. **Introdução a geofísica espacial**. Brasil, USP, 1991.

KOCHKIN, P. O., VAN DEURSEN, A. P. J. and U. EBERT, U., Experimental study of the spatiotemporal development of metre-scale negative discharge in air, **J. Phys. D Appl. Phys.**, 47, 145203, 2015.

KOCHKIN, P. O., NGUYEN, C. V., VAN DEURSEN, A. P. J. and EBERT, U., Experimental study of hard X-rays emitted from metre-scale positive discharges in air, **J. Phys. D Appl. Phys.**, 45, 425202, 2012.

KOCHKIN, P., KÖHN, C., EBERT, U., and VAN DEURSEN, L.: Analyzing x-ray emissions from meter-scale negative discharges in ambient air, **Plasma Sources Science and Technology**, 25, 044 002, 2016.

KOCHKIN, P., SARRIA, D., SKEIE, C., DEURSEN, A. P. J., BOER, A. I., BARDET, M., ALLASIA, C., FLOURENS, F., AND ØSTGAARD, N., In-Flight Observation of Positron Annihilation by ILDAS, **J. Geophys. Res.-Atmos.**, 123, 8074–8090, <https://doi.org/10.1029/2018JD028337>, 2018.

KOCHKIN, P., VAN DEURSEN, A. P. J., MARISALDI, M., URSI, A., DE BOER, A. I., BARDET, M., ALLASIA, C., BOISSIN, J.-F., FLOURENS, F., and ØSTGAARD, N.: In-flight observation of gamma-ray glows by ILDAS, **J. Geophys. Res.-Atmos.**, 122, 12801–12811, <https://doi.org/10.1002/2017JD027405>, 2017.

KOCHKIN, P., VAN DEURSEN, A., and EBERT, U.: Experimental study on hard x-rays emitted from metre scale negative discharges in air, **Journal of Physics D: Applied Physics**, 48, 025 205, 2015.

KÖHN, C. **High-energy phenomena in thunderstorm and laboratory discharges**. 2014. PHD, Holstein, 2014.

KÖHN, C., and EBERT, U., Angular distribution of Bremsstrahlung photons and of positrons for calculations of terrestrial gamma-ray ashes and positron beams, **Atmos. Res.**, 135–136, 432–465, 2014a.

KÖHN, C., and EBERT, U., Calculation of beams of positrons, neutrons, and protons associated with terrestrial gamma ray flashes, **J. Geophys. Res. Atmos.**, 120, 1620–1635, [doi:10.1002/2014JD022229](https://doi.org/10.1002/2014JD022229), 2015.

KÖHN, C., and EBERT, U., The structure of ionization showers in air generated by electrons with 1 MeV energy or less, **Plasma Sources Sci. Techn.**, 23, 045001, 2014b.

KÖHN, C., CHANRION, O., NEUBERT, T., The influence of bremsstrahlung on electric discharge streamers in N₂, O₂ gas mixtures. **Plasma Sources Science and Technology**, 26(1), 15,006, 2016.

KÖHN, C., DINIZ, G., MUHSIN, N.H. (2017). Production mechanisms of leptons, photons, and hadrons and their possible feedback close to lightning leaders. **J. Geophys. Res. Atmos.**, 122, [doi:10.1002/2016JD025445](https://doi.org/10.1002/2016JD025445).

KÖHN, C., EBERT, U. and MANGIAROTTI, A., The importance of electron-electron Bremsstrahlung for terrestrial gamma-ray ashes, electron beams and electron-positron beams, **J. Phys. D: Appl. Phys. Fast Track Communication**, 47, 252001, 2014.

KOI, T., et al., **Attenuation of solar neutrons in the air determined by an accelerator experiment**, in Proceedings of the 26th International, 1999.

KOSTYRYA, I., TARASENKO, V., TKACHEV, A., YAKOVLENKO, S.: X-ray radiation due to nanosecond volume discharges in air under atmospheric pressure, **Technical physics**, 51, 356–361, 2006.

- KOTERA, K., OLINTO, A. The Astrophysics of Ultrahigh-Energy Cosmic Rays. *Annu. Rev. Astron. Astrophys.*,
doi: 10.1146/annurev-astro-081710-102620, 2011.
- KOTHARI, H. N., and JOSHIPURA, K. N., Total and ionization cross-sections of N₂ and CO by positron impact: Theoretical investigations, *Pramana - J. of Phys.*, 76, 477–488, 2011.
- KOZLOV, V.I., MULLAYAROV, V.A., STARODUBTEV, S.A., TOROPOV, A.A. Neutron Burst during Cloud-to-ground discharges of lightning. **Bulletin of the Russian Academy of Sciences, Physics**, v. 77, n. 5, p. 584-586, 2013.
- KRIDER, E. P., RADDI, G. J., NOGGLE, R. C. Regular radiation field pulses produced by intracloud lightning discharges, **J. Geophys. Res.**, 80, 3801–3804, 1975.
- KUTSYK, I. M., et al., Self-sustained relativistic-runaway-electron avalanches in the transverse field of lightning leader as sources of terrestrial gamma-ray flashes, E.N. **Jetp Lett.**, 94, 606,
doi:10.1134/S0021364011200094, 2011.
- KUZHEWSKIJ, B. M., Neutron generation in lightning, **Phys. Astron.**, 5, 14–16, 2004.
- LANDAU, L. D., BELL, J., KEARSLEY, M., PITAEVSKII, L., LIFSHITZ, E., AND SYKES, J.: **Electrodynamics of continuous media**, vol. 8, elsevier, 2013.
- LAWTON, S. A., and PHELPS, A. V., Excitation of b1 Σ + g state of O₂ by low-energy electrons, **J. Chem. Phys.**, 69, 1055–1068, 1978.
- LE VINE, D. Sources of the Strongest RF Radiation From Lightning. **JGR**, v. 85, n. C7, 1980.
- LEFEUVRE, F., BLANC, E., AND PINÇON, J. L.: TARANIS-a Satellite Project Dedicated to the Physics of TLEs and TGFs, **American Institute of Physics Conference Series**, 1118, 3–7,
<https://doi.org/10.1063/1.3137711>, 2009.
- LEHTINEN, N. G. ØSTGAARD, N.: X-ray Emissions in a Multiscale Fluid Model of a Streamer Discharge, **J. Geophys. Res.-Atmos.**, 123, 6935–6953,
<https://doi.org/10.1029/2018JD028646>, 2018.
- LEHTINEN, N. G., BELL, T. F., INAN, U. S.: Monte Carlo simulation of runaway MeV electron breakdown with application to red sprites and terrestrial gamma ray flashes, **J. Geophys. Res.**, 104, 24699–24712,
<https://doi.org/10.1029/1999JA900335>, 1999.
- LI, C., EBERT, U., and HUNDSDORFER, W.: 3D hybrid computations for streamer discharges and production of runaway electrons, **Journal of Physics D: Applied Physics**, 42, 202 003, 2009.

LI, C., et al., Spatially hybrid computations for streamer discharges: II. Fully 3D simulations, **J. Comput. Phys.**, 231, 1020–1050, 2012.

LIBBY, L. M., LUKENS, H. R., Production of radiocarbon in tree rings by lightning bolts. **Journal of Geophysical Research**, 78(26), 5902–5903.
<https://doi.org/10.1029/JB078i026p05902>, 1973.

LIU, C., BRENNAN, D. P., BHATTACHARJEE, A., and BOOZER, A. H.: Adjoint Fokker-Planck equation and runaway electron dynamics, **Phys. Plasmas**, 23, 010702,
<https://doi.org/10.1063/1.4938510>, 2016.

LU, G., BLAKESLEE, R. J., LI, J., SMITH, D. M., SHAO, X., MCCAUL, E. W., BUECHLER, D. E., CHRISTIAN, H. J., HALL J. M., CUMMER, S. A. Lightning mapping observation of a terrestrial gamma ray flash, **Geophys. Res. Lett.**, 37, L11806,
[doi:10.1029/2010GL043494](https://doi.org/10.1029/2010GL043494), 2010.

LU, G., CUMMER, S. A., LI, J., HAN, F., SMITH, D. M., GREFENSTETTE, B. W. Characteristics of broadband lightning emissions associated with terrestrial gamma ray flashes, **J. Geophys. Res.**, 116, A03316,
[doi:10.1029/2010JA016141](https://doi.org/10.1029/2010JA016141), 2011.

LUQUE, A., and GORDILLO-VÁZQUEZ, F. J., Mesospheric electric breakdown and delayed sprite ignition caused by electron detachment, **Nat. Geosci.**, 5, 22–25, 2011.

LUQUE, A.: Radio Frequency Electromagnetic Radiation From Streamer Collisions, **J. Geophys. Res.-Atmos.**, 122, 10497–10509,
<https://doi.org/10.1002/2017JD027157>, 2017.

LUQUE, A.: Relativistic Runaway Ionization Fronts, **Phys. Rev. Lett.**, 112, 045003,
[doi:10.1103/PhysRevLett.112.045003](https://doi.org/10.1103/PhysRevLett.112.045003), 2014.

LXCAT DATABASE, Electron scattering database, 2014.

Available at <http://www.lxcat.laplace.univ-tlse.fr>.

MAILYAN, B. G., BRIGGS, M. S., CRAMER, E. S., FITZPATRICK, G., ROBERTS, O. J., STANBRO, M., CONNAUGHTON, V., MCBREEN, S., BHAT, P. N., and DWYER, J. R.: The spectroscopy of individual terrestrial gamma-ray flashes: Constraining the source properties, **J. Geophys. Res.-Space**, 121, 11346–11363,
<https://doi.org/10.1002/2016JA022702>, 2016.

MAGALHÃES, M., **Noções de probabilidade e estatística**, USP, 2004.

MARCH, V., and MONTANYÁ, J., Influence of the voltage-time derivative in X-ray emission from laboratory sparks, **Geophys. Res. Lett.**, 37, L19801,
[doi:10.1029/2010GL044543](https://doi.org/10.1029/2010GL044543), 2010.

- MARISALDI, M., et al., Detection of terrestrial gamma ray flashes up to 40 MeV by the AGILE satellite, **J. Geophys. Res.**, 115, A00E13, doi:10.1029/2009JA014502, 2010.
- MARISALDI, M., **The first AGILE low-energy (< 30 MeV) terrestrial gamma-ray flashes catalog**. EGU General Assembly 2014, held 27 April - 2 May, 2014 in Vienna, Austria, id.11326, 2004.
- MARISALDI, M., FUSCHINO, F., TAVANI, M., et al.: Properties of terrestrial gamma ray flashes detected by AGILE MCAL below 30 MeV, **J. Geophys. Res.-Space**, 119, 1337–1355, <https://doi.org/10.1002/2013JA019301>, 2014.
- MARSHALL, T. C., et al., Rocket and balloon observations of electric field in two thunderstorms, **J. Geophys. Res.**, 100, 20,815–20,828, 1995.
- MARTIN, I.M., ALVES, M.A. Observation of a possible neutron burst associated with a lightning discharge?. **JGR**, 115, n. A2, doi:10.1029/2009JA014498, 2010.
- MCCARTHY, M. and PARKS, G.: Further observations of X-rays inside thunderstorms, **Geophys. Res. Lett.**, 12, 393–396, <https://doi.org/10.1029/GL012i006p00393>, 1985.
- MEEGAN, C., et al., The Fermi gamma-ray burst monitor, **Astrophys. J.**, 702, 791–804, 2009.
- MENDOZA, E., et al., **IAEA Tech. Rep. INDC(NDS)-0612**, Vienna, 2012. [Available at <http://www-nds.iaea.org/geant4>.]
- MENDOZA, E., et al., New standard evaluated neutron cross section libraries for the GEANT4 code and first verification, **IEEE Trans. Nucl. Science**, 61, 2357–2364, 2014.
- MEZENTVEV, A., et al. Radio emission from double RHESSI TGFs. **JGR**, doi: 10.1002/2016JD025111, 2016.
- MOSS, G. D., et al., Monte Carlo model for analysis of thermal runaway electrons in streamer tips in transient luminous events and streamer zones of lightning leaders, **J. Geophys. Res.**, 111, A02307, doi:10.1029/2005JA011350, 2006.
- NAKAMURA, T., AND KOSAKO, T., A systematic study on the neutron skyshine from nuclear facilities—Part I. Monte Carlo Analysis of neutron propagation in air-over-ground environment from a monoenergetic source, **Nucl. Sci. Eng.**, 77, 161–181, 1981.
- NELSON, W.R., HIRAYAMA, H., AND ROGERS, D.W., **EGS4 code system**, Tech.rep., Stanford Linear Accelerator Center, Menlo Park, CA (USA), 1985.

- NEUBERT, T., KUVVETLI, I., BUDTZ-JØRGENSEN, C., ØSTGAARD, N., REGLERO, V., and ARNOLD, N.: **The atmosphere-space interactions monitor (ASIM) for the international space station**, in: Proceedings of the ILWS Workshop, edited by: Gopalswamy, N. and Bhattacharyya, A., p. 448, 2006.a
- NGUYEN, C. V., VAN DEURSEN, A. P. J. and EBERT, U., Multiple X-ray bursts from long discharges in air, **J. Phys. D Appl. Phys.**, 41, 234012, 2008.
- NOGGLE, R., KRIDER, E., and WAYLAND, J., A search for X rays from helium and air discharges at atmospheric pressure, **Journal of Applied Physics**, 39, 4746–4748, 1968.
- OBLOZINSKÝ, P. **Handbook of photonuclear data for applications: Cross sections and spectra, International Atomic Energy Association Report IAEA-TECDOC-1178**, Vienna, Austria, 2000.
- OKHRIMOVSKYY, A., BOGAERTS, A., GIJBELS, R., Electron anisotropic scattering in gases: A formula for Monte Carlo simulations. **Physical Review**, E, 65, 037402. <https://doi.org/10.1103/PhysRevE.65.037402>, 2002.
- OPAL, C. B., PETERSON, W. K., BEATY, E. C., Measurements of secondary electron spectra produced by electron impact ionization of a number of simple gases. **Journal of Chemical Physics**, 55(8), 4100–4106. <https://doi.org/10.1063/1.1676707>, 1971.
- ØSTGAARD, N., GJESTELAND, T., STADSNES, J., CONNELL, P., AND CARLSON, B., Production altitude and time delays of the terrestrial gamma flashes: Revisiting the Burst and Transient Source Experiment spectra, **J. Geophys. Res.-Space**, 113, A02307, <https://doi.org/10.1029/2007JA012618>, 2008.
- PANCHESHNYI, S., BIAGI, S., BORDAGE, M., HAGELAAR, G., MORGAN, W., PHELPS, A., AND PITCHFORD, L., The LXCat project: Electron scattering cross sections and swarm parameters for low temperature plasma modeling, **Chemical Physics**, 398, 148–153, 2012.
- PANCHESHNYI, S., et al., **Computer code ZDPlasKin**, Univ. of Toulouse, LAPLACE, CNRS-UPS-INP, Toulouse, France, 2008. [Available at <http://www.zdplaskin.laplace.univ-tlse.fr>.]
- PARKS, G. K., MAUK, B. H., SPIGER, R., and CHIN, J., X-ray enhancements detected during thunderstorm and lightning activities, **Geophys. Res. Lett.**, 8, 1176–1179, <https://doi.org/10.1029/GL008i011p01176>, 1981.a
- PERKINS, S., CULLEN, D., and SELTZER, S., Tables and graphs of electron-interaction cross sections from 10eV to 100GeV derived from the LLNL Evaluated Electron Data Library (EEDL), Z=1–100, **Tech. rep.**, <https://doi.org/10.2172/5691165>, 1991.a

- PESKIN, M. E., and SCHROEDER, D. V., *An Introduction to Quantum Field Theory*, **West View Press**, Boulder, Colo, 1995.
- PETERSEN, D., BEASLEY, W., Microwave radio emissions of negative cloud-to-ground lightning flashes. **Atmospheric Research**, 135-136, 2014.
- PHELPS, A. V. , **JILA Information Center Report**, 28, 1985.
- PHELPS, A. V., and PITCHFORD, L. C., Anisotropic scattering of electrons by N₂ and its effect on electron transport, **Phys. Rev. A**, 31, 2932–2949, 1985.
- PIEL, A., **Plasma Physics: an introduction to Laboratory, Space and Fusion plasmas**. Springer, Berlin, 2010.
- VON KIENLIN, R. M., ET AL., First results on terrestrial gamma ray flashes from the Fermi Gamma-ray Burst Monitor, **Journal of Geophysical Research (Space Physics)**, 115, A07323, doi:10.1029/2009JA015242, 2010.
- RAHMAN, M., V., et al., X-rays from 80 cm long sparks in air, **Geophys. Res. Lett.**, 35, L06805, doi:10.1029/2007GL032678, 2008.
- RAIZER, Y. P., **Gas discharge physics**, vol. 2, Springer Berlin, 1997.
- RAKOV, V.A., UMAN, M.A., **Lightning: physics and effects**. Cambridge: University Press, 2002.
- REP'EV, A. AND REPIN, P., Spatio temporal parameters of the X-ray radiation from a diffuse atmospheric-pressure discharge, **Technical Physics**, 53, 73–80, 2008.
- ROBERTS, O. J., FITZPATRICK, G., STANBRO, M., MCBREEN, S., BRIGGS, M. S., HOLZWORTH, R. H., GROVE, J. E., CHEKHTMAN, A., CRAMER, E. S., AND MAI-LYAN, B. G., The First Fermi-GBM Terrestrial Gamma Ray Flash Catalog, **J. Geophys. Res.-Space**, 123, 4381–4401, <https://doi.org/10.1029/2017JA024837>, 2018.
- ROBSON, R. E., Transport phenomena in the presence of reactions: Definition and measurement of transport coefficients. **Australian Journal of Physics**, 44, 685–692. <https://doi.org/10.1071/PH910685>, 1991.
- ROUSSEL-DUPRE, R. A., GUREVICH, A. V., TUNNELL, T., AND MILIKH, G. M., Kinetic theory of runaway air breakdown, **Phys. Rev. E**, 49, 2257–2271, <https://doi.org/10.1103/PhysRevE.49.2257>, 1994.
- RUTJES, C., EBERT, U., A natural neutron source. **Physics World**, October 2017, 13–15, 2017.

RUTJES, C., DINIZ, G., FERREIRA, I. S., and EBERT, U., TGF afterglows: a new radiation mechanism from thunderstorms, **Geophys. Res. Lett.**, 44, 10702–10712, <https://doi.org/10.1002/2017GL075552>, 2017.

RUTJES, C., SARRIA, D., SKELTVED, A.B., LUQUE, A., DINIZ, G., OSTGAARD, N., EBERT, U., Evaluation of Monte Carlo tools for high energy atmospheric physics. **Geoscientific Model Development**, v. 0, issue 11, doi: 10.5194/gmd-9-3961-2016, 2016.

SABA, M., SCHUMANN, C. , WARNER, T. A. , FERRO, MARCO ANTONIO S. , DE PAIVA, AMANDA ROMÃO , HELSDON, JOHN , ORVILLE, R. E., Upward lightning flashes characteristics from high-speed videos. **Journal of Geophysical Research: Atmospheres**, v. 1, p. 1, 2016.

SALVAT, F., FERNÁNDEZ-VAREA, J. M., AND SEMPAU, J., **PENELOPE-2011: A Code System for Monte Carlo Simulation of Electron and Photon Transport**, 2011.

SARRIA, D., BLELLY, P.-L., AND FORME, F., MC-PEPTITA: a Monte Carlo model for Photon, Electron and Positron Tracking In Terrestrial Atmosphere. Application for a Terrestrial Gamma-ray Flash, **J. Geophys. Res.-Space**, 120, 3970–3986, <https://doi.org/10.1002/2014JA020695>, 2015.

SARRIA, D., BLELLY, P.-L., BRIGGS, M. S., AND FORME, F., Studying the time histogram of a terrestrial electron beam detected from the opposite hemisphere of its associated TGF, **Journal of Geophysical Research: Space Physics**, pp. n/a–n/a, doi:10.1002/2015JA021881, 2016.

SARRIA, D., LEBRUN, F., BLELLY, P.-L., CHIPAUX, R., LAURENT, P., SAUVAUD, J.-A., PRECH, L., DEVOTO, P., PAILOT, D., BARONICK, J.-P., and LINDSEY-CLARK, M., TARANIS XGRE and IDEE detection capability of terrestrial gamma-ray flashes and associated electron beams, **Geosci. Instrum. Method. Data Syst.**, 6, 239–256, <https://doi.org/10.5194/gi-6-239-2017>, 2017.

SARRIA, D., **Characterization of Relativistic Runaway Electron Avalanches (RREA) (GEANT4 based source code) (Version 1)**, **Zenodo**, <https://doi.org/10.5281/zenodo.1475220>, 2018d.

SARRIA, D., **Dataset used in the Article “Evaluation of Monte Carlo tools for high-energy atmospheric physics II: relativistic runaway electron avalanches” (Version 1) [Data set]**, <https://doi.org/10.5281/zenodo.1475209>, 2018a.

SARRIA, D., **MATLAB scripts for processing the dataset “Full RREA Dataset” (Version 1)**, **Zenodo**, <https://doi.org/10.5281/zenodo.1475245>, 2018b.

SARRIA, D., **Probability Evaluation of Relativistic Runaway Electron Avalanches (RREA) (GEANT4 based source code)**, Zenodo,

<https://doi.org/10.5281/zenodo.1475231>, 2018c.

SCHELLART, P., TRINH, T., BUITINK, S., CORSTANJE, A., ENRIQUEZ, J., FALCKE, H., HÖRANDEL, J., NELLES, A., RACHEN, J., ROSSETTO, L., et al., Probing atmospheric electric fields in thunderstorms through radio emission from cosmic-ray-induced air showers, **Physical review letters**, 114,165 001, 2015.

SCHUNK, R., NAGY, A., **Ionospheres: Physics, Plasmas physics, and Chemistry**. Cambridge, London, 2009.

SEMPAU, J., SANCHEZ-REYES, A., SALVAT, F., BEN TAHAR, H. O., JIANG, S., AND FERNÁNDEZ-VAREA, J., Monte Carlo simulation of electron beams from an accelerator head using PENELOPE, **Physics in medicine and biology**, 46, 1163, 2001.

SHAH, G.N., RAZDAN, H., BHAT, C.L., ALI, Q.M. Neutron generation in lightning bolts. **Nature**, n. 313, p. 773 – 775, doi:10.1038/313773a0, 1985.

SHAO, T., ZHANG, C., NIU, Z., YAN, P., TARASENKO, V. F., BAKSHT, E. K., BURAHENKO, A. G., AND SHUT'KO, Y. V., Diffuse discharge, runaway electron, and x-ray in atmospheric pressure air in an inhomogeneous electrical field in repetitive pulsed modes, **Appl. Phys. Lett.**, 98, 021503, <https://doi.org/10.1063/1.3540504>, 2011.a

SHAO, X.-M., HAMLIN, T., SMITH, D. M. A closer examination of terrestrial gamma-ray flash-related lightning processes, **J. Geophys. Res.**, 115, A00E30, doi:10.1029/2009JA014835, 2010.

SHIBATA, S., Propagation of solar neutrons through the atmosphere of the Earth, **J. Geophys. Res.**, 99, 6651–6665, 1994.

SHYAM, A., and KAUSHIK, T. C., Observation of neutron bursts associated with atmospheric lightning discharge, **J. Geophys. Res.**, 104, 6867–6869, 1999.

SKELTVED, B., et al., Modeling the relativistic runaway electron avalanche and the feedback mechanism with GEANT4, **J. Geophys. Res. Space Physics**, 119, 9174–9191, doi:10.1002/2014JA020504, 2014.

SMITH, D.M., LOPEZ, L.I., LIN, R.P., BARRINGTON-LEIGH, C.P. Terrestrial gamma ray flashes observed up to 20 MeV. *Science*, v. 307, n. 5712, p. 1085- 1088, doi: 10.1126/science.1107466, 2005.

STANKEVICH, Y. L., KALININ, V., Fast electrons and X radiation during the initial stages of an impulse spark discharge in air. **Doklady Akademii Nauk SSSR**, 177(Nov.-Dec. 1967), 72–73, 1967.

- STANLEY, M. A., SHAO, X., SMITH, D. M., LOPEZ L. I., PONGRATZ, M. B., HARLIN, J. D., STOCK, M., REGAN, A. A link between terrestrial gamma-ray flashes and intracloud lightning discharges, **Geophys. Res. Lett.**, 33, L06803, doi:10.1029/2005GL025537, 2006.
- STARODUBTEV, S.A., KOZLOV, V.I., TOROPOV, A.A., MULLAYAROV, V.A., GRIGOR'EV, V.G., MOISEEV, A.V. First experimental observations of neutron bursts under thunderstorm clouds near sea level. **JETP Letters**, v. 96, p. 188- 191, 2012.
- SURENDRA, M., GRAVES, D. B., JELLUM, G. M., Self-consistent model of a direct-current glow discharge: Treatment of fast electrons. **Physical Review**, A, 41, 1112–1125. <https://doi.org/10.1103/PhysRevA.41.1112>, 1990.
- TARASENKO, V. F., BAKSHT, E. K., BURACHENKO, A. G., KOSTYRYA, I. D., LOMAEV, M. I., AND RYBKA, D. V., Generation of supershort avalanche electron beams and formation of diffuse discharges in different gases at high pressure, **Plasma Devices and Operations**, 16, 267–298, 2008.
- TAVANI, M., et al., Terrestrial gamma-ray ashes as powerful particle accelerators. **Physical Review**, Letters, v. 106, n. 1, p. 018501, 2011.
- TERUAKI, E., WADA, Y., FURUTA, Y., NAKAZAWA, K., YUASA, T., OKUDA, K., MAKISHIMA, K., SATO, M., SATO, Y., NAKANO, T., UMEMOTO, D., and TSUCHIYA, H., Photonuclear reactions triggered by lightning discharge, *Nature*, 551, 481–484, <https://doi.org/10.1038/nature24630>, 2017.a
- TEUNISSEN, J., EBERT, U., 3D PIC-MCC simulations of discharge inception around a sharp anode in nitrogen/oxygen mixtures. **Plasma Sources Science and Technology**, 25, 044005, 2016.
- TORII, T., TAKEISHI, M., and HOSONO, T., Observation of gamma-ray dose increase associated with winter thunderstorm and lightning activity, **J. Geophys. Res.-Atmos.**, 107, 4324, <https://doi.org/10.1029/2001JD000938>, 2002.
- TOROPOV, A.A., KOZLOV, V.I., MULLAYAROV, V.A., STARODUBTSEV, S.A. Experimental observations of strengthening the neutron flux during negative lightning discharges of thunderclouds with tripolar configuration. **Journal of Atmospheric and Solar-Terrestrial Physics**, v. 94, p.13-18, 2013.
- TRAN, M.D., RAKOV, V.A. Initiation and propagation of cloud-to-ground lightning observed with a high-speed video camera. **Science**, doi: 10.1038/srep39521, 2016.

TRINH, T., SCHOLTEN, O., BUITINK, S., VANDEN BERG, A., CORSTANJE, A., EBERT, U., ENRIQUEZ, J., FALCKE, H., HÖRANDEL, J., KÖHN, C., et.al.:Influence of atmospheric electric fields on the radio emission from extensive air showers, **Physical Review**, D, 93, 023003, 2016.

TSUCHIYA, H., et al., Hardening and termination of long-duration rays detected prior to lightning. **Physical Review**, Letters, 111, 15001.
<https://doi.org/10.1103/PhysRevLett.111.015001>, 2013.

TSUCHIYA, H., ENOTO, T., YAMADA, S., YUASA, T., KAWAHARADA, M., KITAGUCHI, T., KOKUBUN, M., KATO, H., OKANO, M., NAKAMURA, S., and MAKISHIMA, K.: Detection of high-energy gamma rays from winter thunderclouds, **Phys. Rev. Lett.**, 99, 165002,
<https://doi.org/10.1103/PhysRevLett.99.165002>, 2007.

TSUCHIYA, H., HIBINO, K., KAWATA, K., HOTTA, N., TATEYAMA, N., OHNISHI, M., TAKITA, M., CHEN, D., HUANG, J., MIYASAKA, M., KONDO, I., TAKAHASHI, E., SHIMODA, S., YAMADA, Y., LU, H., ZHANG, J.L., YU, X.X., TAN, Y.H., NIE, S.M., MUNAKATA, K., ENOTO, T., MAKISHIMA, K. Observation of thundercloud-related gamma rays and neutrons in Tibet. **Physical review** D,85, 092006, 2012.
[doi:10.1103/PhysRevD.85.092006](https://doi.org/10.1103/PhysRevD.85.092006), 2006.

TURQUETTI, G., FERREIRA, I.S. Um estudo do circuito elétrico atmosférico global. **Physicae Organum**, v. 2, n. 1, 2016.

UMAN, M., MCLAIN, D. Radiation Field and current of the lightning stepped leader. **JGR**, v. 75, n. 6, 1970.

VAHEDI, V., and SURENDRA, M., A Monte Carlo collision model for the particle-in-cell method applications to argon and oxygen discharges, **Comp. Phys. Comm.**, 87, 179–198, 1995.

VARLAMOV, A., VARLAMOV, V., RUDENKO, D., STEPANOV, M., **Atlas of giant dipole resonances. Parameters and Graphs of Photonuclear Reaction Cross Sections.** INDC (NDS)-394 (pp. 1–311) IAEA NDS, Vienna, Austria, 1999.

VOLLAND, H. **Handbook of Atmospheric Electrodynamics.** New York, Springer, 1984.

WILLIAMS, E. R.: Origin and context of C. T. R. Wilson's ideas on electron runaway in thunderclouds, **J. Geophys. Res.-Space**, 115, A00E50,
<https://doi.org/10.1029/2009JA014581>, 2010.

WILLIAMS, E. The Schuman Resonance: A global thermometer, **Science**, 1992.

WILSON, C. T. R.: The Acceleration of beta-particles in Strong Electric Fields such as those of Thunderclouds, **PCPS-P. Camb. Philol. S.**, 22, 534,
<https://doi.org/10.1017/S0305004100003236>, 1925.

WILSON, C.: The electric field of a thundercloud and some of its effects, **Proceedings of the Physical Society of London**, 37, 32D, 1924.

WOUTER, B. **Modelling of Transient Phenomena in Gas Discharges**. Phd, Eindhoven, 2005.

XU, W., CELESTIN, S., PASKO, V.P. Source altitudes of terrestrial gamma-ray flashes produced by lightning leaders. **GRL**, v. 39, n. 8, doi: 10.1029/2012GL051351, 2012.

YONG-KIM, K., and SANTOS, J. P., Extension of the binary-encounter-dipole model to relativistic incident electrons, **Phys. Rev. A**, 62, 052710, 2000.